Cosmological simulations of large-scale structures in numerical relativity

Robyn Louise Munoz

Institute of Cosmology and Gravitation
University of Portsmouth
2023

The thesis is submitted in partial fulfilment of the requirements for the award of the degree of Doctor of Philosophy of the University of Portsmouth.

Whilst registered as a candidate for the above degree, I have not been registered for any other research award. The results and conclusions embodied in this thesis are the work of the named candidate and have not been submitted for any other academic award.

Ethical review number: ETHIC-2019-1452.
Approximate word count: 41924

Abstract

In the quest for relativistic effects in large-scale structures, we use numerical relativity simulations to describe the spacetime evolution during nonlinear structure formation. We explore how structures decouple from the expanding universe to collapse, finding criteria from the Top-Hat model to be robust estimators. Additionally, we characterise spacetime with gravito-electromagnetism, describing filaments as carrying a gravitational current, and the Petrov classification, invariantly identifying the generation of gravitational waves during this collapse.

A new Einstein Toolkit thorn `ICPertFLRW` was developed to generate the initial conditions. These are fully nonlinear based directly on the gauge invariant comoving curvature perturbation $\mathcal{R}_c$, commonly used to model early-universe fluctuations. Assigning a simple 3-dimensional sinusoidal structure to $\mathcal{R}_c$, we have a lattice of quasi-spherical over-densities representing idealised dark matter halos connected through filaments and surrounded by voids. This is implemented in the synchronous-comoving gauge, using a pressureless perfect fluid (dust) description of cold dark matter, set at an initial redshift $z \approx 300$ and then fully evolved with Einstein Toolkit.

With the simulation results, we look into whether the Top-Hat spherical and homogeneous collapse model provides a good description of the collapse of over-densities. We find that the Top-Hat is an excellent approximation for the evolution of peaks, where we observe that the shear is negligible and collapse occurs when the linear density contrast reaches the predicted critical value $\delta_C^{(1)} = 1.69$. Additionally, we characterise the turn-around boundary and show how its evolution depends on the initial distribution of matter, finding that it grows fastest in denser directions.

While relativistic cosmology can be formulated covariantly, one concern with numerical relativity simulations is gauge variance; although observables should be gauge-invariant, simulations do not necessarily focus on their computations. To address this issue, we consider invariants built from the Weyl tensor, notably the electric and magnetic parts and the Weyl scalars (gauge-invariant at first-order in cosmology), and invariants used for the Petrov classification. We then developed the `EBWeyl` post-processing code, which has been thoroughly tested on five analytic metrics and can be applied to any numerical spacetime in any gauge.

In the simulation data, we look at the distribution of the electric and magnetic parts of the Weyl tensor, finding that they are stronger along and around the filaments respectively. We find that the spacetime is of Petrov type I everywhere, so we introduce a method to dynamically classify different regions at different times of the simulation box in leading order Petrov types. Along the filaments, the leading order Petrov type is D, while the centre of the over-density remains conformally flat, type O, in line with the Top-Hat model. The surrounding region demonstrates a sort of peeling-off in action, with the spacetime transitioning between different Petrov types as non-linearities grow, with the production of gravitational waves.

Acknowledgements

I am grateful to every butterfly that created the path leading me here.

Thank you to my supervisors and teachers, all the knowledgeable individuals I was lucky enough to read, hear, and talk to; I am grateful for your guidance and support. I especially appreciate the mentoring I received from my PhD supervisor Marco Bruni.

Thank you to my parents, Jean-Michel and Louise, without whom none of this would be possible, and of course my family, friends and my loving partner James, for encouraging me in this endeavour and creating an environment that allowed me to thrive.

Dissemination

Papers

- **R. L. Munoz** and M. Bruni. In: *Classical and Quantum Gravity* 40.13 (June 2023), p. 135010.

  "EBWeyl: a Code to Invariantly Characterize Numerical Spacetimes".

  DOI: 10.1088/1361-6382/acd6cf. arXiv: gr-qc/2211.08133

  (Munoz and Bruni, 2023a) see Chapter 5.

- **R. L. Munoz** and M. Bruni. In: *Physical Review D* 107.12 (June 2023), p. 123536.

  "Structure formation and quasispherical collapse from initial curvature perturbations with numerical relativity simulations".

  DOI: 10.1103/PhysRevD.107.123536. arXiv: astro-ph/2302.09033

  (Munoz and Bruni, 2023b) see Chapter 6.

Codes

- `EBWeyl` GitHub

  (Munoz, 2022; Munoz and Bruni, 2023a), see Chapter 5

- `ICPertFLRW` GitHub

  (Munoz, 2023a; Munoz and Bruni, 2023b), see Section 6.1.3 and Appendix C

- `sphereint` GitHub

  (Munoz, 2023b; Munoz and Bruni, 2023b), see Appendix D

Contents

List of Figures

List of Tables

Notation

The speed of light and the gravitational constant are taken to be one: $c = G = 1$.
Greek indices are used for spacetime components $\{0,\ 1,\ 2,\ 3\}$,
while Latin indices are used for space components $\{1,\ 2,\ 3\}$.

General Relativity

Spacetime

τ	Proper time, $\frac{da}{d\tau} = \dot{a}$	Eq. (2.4)
$\delta_{\alpha\beta}$	Kronecker delta	
$g_{\mu\nu}$	Spacetime metric	Eq. (2.3), $\{-,\ +,\ +,\ +\}$
$A_{(\mu\nu)}$	Symmetrisation of the tensor $A_{\mu\nu}$	Eq. (2.7)
$A_{[\mu\nu]}$	Anti-symmetrisation of the tensor $A_{\mu\nu}$	Eq. (2.7)
$\bar{\bar{A}}^{\alpha}{}_{\beta}$ & $\tilde{\tilde{A}}^{\alpha}{}_{\beta}$	Tensor density & pseudo-tensor respectively	Eq. (2.8) & Eq. (2.9)
$\epsilon_{\alpha\beta\mu\nu}$	Levi-Civita tensor	Eq. (2.12)
∂_{α}	Partial derivative	$\partial_{\alpha} = \frac{\partial}{\partial x^{\alpha}}$
∇_{α}	Covariant derivative w.r.t. $g_{\mu\nu}$	Eq. (2.13)
$\Gamma^{\alpha}{}_{\mu\nu}$	Christoffel symbols	Eq. (2.14)
$R^{\alpha}{}_{\sigma\mu\nu}$	Riemann tensor	Eq. (2.19)
$R_{\alpha\beta}$ & R	Ricci tensor & Ricci scalar (also ${}^{(4)}R$)	Eq. (2.22) & Eq. (2.23)
$C_{\alpha\beta\mu\nu}$	Weyl tensor	Eq. (2.24)

Projection along or orthogonally to a vector

The superscript $\{v\}$ denotes a variable defined in the frame of said timelike vector v^{α}.
The pre-superscript (3) applies for 3-dimensional quantities built from the spatial metric $P^{\{v\}}_{\alpha\beta}$.
For simplicity, quantities with (3) are not given the $\{v\}$ superscript; instead, the relevant frame should be determined based on context.

$P^{\{v\}}_{\alpha\beta}$	Projection tensor of v^{α} or Spatial metric	Eq. (2.25), $\{+,\ +,\ +\}$
$A^{\{v\}}_{\langle\mu\nu\rangle}$	Spatially projected, symmetric and tracefree part of $A_{\mu\nu}$	Eq. (2.26)
$\mathcal{L}_v$	Lie derivative along the vector v^{α}	Eq. (2.27)
$D^{\{v\}}_{\alpha}$	Spatial covariant derivative w.r.t. $P^{\{v\}}_{\alpha\beta}$	Eq. (2.32)
$D^{\{v\}}\times$	Spatial curl operator	Eq. (2.34)
$\epsilon^{\{v\}}_{\beta\mu\nu}$	Spatial Levi-Civita tensor	Eq. (2.35)
${}^{(3)}\Gamma^{\alpha}{}_{\mu\nu}$	Spatial Christoffel symbols	
${}^{(3)}R^{\alpha}{}_{\sigma\mu\nu}$	Spatial Riemann tensor	Eq. (2.36)
${}^{(3)}R_{\sigma\nu}$ & ${}^{(3)}R$	Spatial Ricci tensor & scalar respectively	

Einstein's field equations

Λ	Cosmological constant	
$G_{\alpha\beta}$	Einstein tensor	Eq. (2.38)
κ	Einstein's gravitational constant	$\kappa = 8\pi G c^{-4} = 8\pi$
$T_{\alpha\beta}$	Energy stress tensor	Eq. (2.41)
T	Trace of the energy stress tensor	Eq. (2.42)

Matter

$\rho^{\{v\}}$	Energy density	Eq. (2.43)
$q_\alpha^{\{v\}}$	Energy flux or momentum density	Eq. (2.43)
$S_{\alpha\beta}^{\{v\}}$	Stress tensor	Eq. (2.43)
$S^{\{v\}}$	Trace of the stress tensor	Eq. (2.44)
$p^{\{v\}}$	Pressure	Eq. (2.44)
$\pi_{\alpha\beta}^{\{v\}}$	Anisotropic pressure	Eq. (2.44)
$\varrho^{\{v\}}$	Rest mass energy density	Eq. (2.45)
$\varepsilon^{\{v\}}$	Specific internal energy	Eq. (2.45)
$h^{\{v\}}$	Specific enthalpy	Eq. (2.46)

Kinematical rest-energy frame

All of the following are uniquely defined in the frame of the fluid flow u^α.

u^α	Fluid 4-velocity	
$h_{\alpha\beta}$	Projection tensor of u^α or Spatial metric	Eq. (2.49), $\{+,\ +,\ +\}$
$\Theta_{\alpha\beta}$	Expansion tensor	Eq. (2.50)
$\omega_{\alpha\beta}$	Vorticity tensor	Eq. (2.50)
a^α	Acceleration	Eq. (2.50)
Θ	Expansion scalar	Eq. (2.51)
$\sigma_{\alpha\beta}$	Shear	Eq. (2.51)

Weyl tensor

$E_{\alpha\beta}^{\{v\}}$	Electric part of the Weyl tensor in the frame v^α	Eq. (2.68)
$B_{\alpha\beta}^{\{v\}}$	Magnetic part of the Weyl tensor in the frame v^α	Eq. (2.68)
$Q_{\alpha\beta}^{\{v\}}$	Complex combination of $E_{\alpha\beta}^{\{v\}}$ and $B_{\alpha\beta}^{\{v\}}$	Eq. (2.71)
Ψ_0, Ψ_1, Ψ_2, Ψ_3, Ψ_4	Weyl scalars in the frame of the null tetrad $l^\alpha,\ k^\alpha,\ m^\alpha,\ \bar{m}^\alpha$	Eq. (2.80)
$I,\ J,\ L_B,\ M, \mathcal{S}, \mathcal{D}$	Frame independent invariants from $C_{\alpha\beta\mu\nu}$	Eq. (2.90, 2.93, 2.94, 2.95)
K, L, N	Frame dependent invariants from $C_{\alpha\beta\mu\nu}$	Eq. (2.96)

Numerical Relativity

γ_{ij}	Projection tensor of n^α or Spatial metric	Eq. (3.1), $\{+,\ +,\ +\}$
α	Lapse	
β^i	Shift	Eq. (3.2)
n^i	Timelike vector normal to γ_{ij}	Eq. (3.3)
$\mathfrak{a}^i$	Acceleration of n^i	Eq. (3.4)
t	Coordinate time	Eq. (3.8)
K_{ij}	Extrinsic curvature	Eq. (3.12)
K	Trace of extrinsic curvature	Eq. (3.14)
A_{ij}	Traceless part of the extrinsic curvature	Eq. (3.14)

Cosmology

Homogeneous & isotropic universe

The overhead bar identifies background quantities.

a	Scale factor	Section 4.1.4
η	Conformal time, $\frac{dg}{d\eta} = g'$	Eq. (4.2)
H	Hubble's scalar	Eq. (4.5)
$\mathcal{H}$	Conformal Hubble's scalar	Eq. (4.6)
z	Redshift	Eq. (4.8)
$\bar{\Theta}$	FLRW expansion scalar	Eq. (4.15)
$\bar{\rho}$	FLRW energy density in the u^μ frame	Eq. (4.17)
$\Omega_k, \Omega_m, \Omega_\Lambda$	Dimensionless density parameters of curvature, matter and dark energy	Eq. (4.19)

Perturbation theory & structure formation

The (1) superscript identifies a first-order perturbative term.

ϕ, ω, ψ, χ	Scalar perturbations to the spacetime metric	Eq. (4.30, 4.31, 4.32)
ω_i^S, χ_i^S	Vector perturbations to the spacetime metric	Eq. (4.30, 4.31, 4.32)
χ_{ij}^{TT}	Tensor perturbations to the spacetime metric	Eq. (4.30, 4.32)
δ	Density contrast	Eq. (4.33)
$\delta_C^{(1)}$	Linear density contrast a collapse	Eq. (4.75)
f_1	Growth factor	Eq. (4.57)
ϑ_{ij}	Deformation tensor	Eq. (4.34)
ϑ	Deformation scalar, trace of ϑ_{ij}	Eq. (4.34)
$\Box_{ij}$	Traceless operator	$\Box_{ij} = \partial_i\partial_j - \frac{1}{3}\delta_{ij}\delta^{kl}\partial_k\partial_l$
∇^2	Laplacian operator	$\nabla^2 = g^{\alpha\beta}\nabla_\alpha\nabla_\beta$
$\mathcal{R}_c$	Comoving curvature perturbation	Eq. (4.50)
ζ	Uniform-density curvature perturbation	Eq. (4.50)
Φ, Ψ	Bardeen potentials: Newtonian potential and conformal Newtonian curvature perturbation	Eq. (4.54)
$\langle\phi\rangle_{\mathcal{D}\{v\}}$	Average of ϕ on the domain $\mathcal{D}^{\{v\}}$ which is defined on the $P_{\alpha\beta}^{\{v\}}$ spatial hypersurface	Eq. (4.47)
$\mathcal{Q}_{\mathcal{D}\{u\}}$	Backreaction	Eq. (4.49)

Acronym

ADM	Arnowitt, Deser and Misner
BSSNOK	Baumgarte, Shapiro, Shibata, Nakamura, Ookara and Kojima
CDM	Cold Dark Matter
CMB	Cosmic Microwave Background
EdS	Einstein-de Sitter
FD	Finite Difference
FLRW	Friedmann Lemaître Robertson Walker
GR	General Relativity
LSS	Large-Scale Structure
LTB	Lemaître Tolman Bondi
NP	Newmann-Penrose
NR	Numerical Relativity
OD	Over Density
PDE	Partial Differential Equation
TA	Turn Around
UD	Under Density

1 - Introduction

Newton's theory of Gravity describes it as a force (Newton, 1687), which to a certain extent, in our everyday lives, is sufficient. However, when we look up to the stars and planets, we can start to see that there's more to it. Mercury's orbit was the first clue; its perihelion precession has been a mystery since ancient history, which was finally resolved once General Relativity was discovered. General Relativity (GR) (Einstein, 1916) is currently the best theoretical description of Gravity; it combines space, time and matter interwoven together through curvature.

The implications of GR are numerous, where all phenomena that the Newtonian theory of Gravity could not explain are called relativistic effects. These add amazement and wonder as we explore the universe, stimulating research and making the field of GR incredibly prolific in recent years. The wide variety of relativistic effects come with wildly different challenges for their observation.

❖ **Gravitational lensing**

In GR, the trajectory of light is curved around gravitational objects, which act as lenses. The first quest to observe this was during the solar eclipse of 1919, where the locations of stars on the sky passing close to the sun were found to be slightly offset. Observing this requires a light source to be behind a gravitational lens, like the sun or even galaxies. The likelihood of perfectly aligned objects is quite low, yet the progress of observational methods has given us the privilege of capturing images of this mesmerising effect. There are different lensing magnitudes; in the strong case, the source image is completely warped around the lens, and in the weak case, the source images show some form of alignment. A recent notable example of the strong case was with the observation of a supernova lensed by another galaxy (Goobar et al., 2023); such an object could be used to measure the universe's expansion. On the other hand, the weak case is typically seen when clusters of galaxies are the lens and all the galaxies behind them appear aligned around the cluster (Tyson, Valdes, and Wenk, 1990). All the matter surrounding us has the capacity to warp light rays, including matter that does not emit light.

❖ **Black holes**

Some objects have such a strong gravitational field that they bend the trajectory of light so much that it can't escape, leaving what appears to be a black hole. They can then only be seen with matter going around what appears to be nothing. This was first directly observed with stars orbiting a black hole at the centre of our galaxy (Gillessen et al., 2009), and in more recent years, with exemplary collaborative work, an accretion disk has been observed around a black hole at the centre of the M87 galaxy and our own Milky Way galaxy (The Event Horizon Telescope Collaboration, 2019a, 2022). These images were compared to simulations in full

GR, which are called Numerical Relativity (NR) simulations, to know what accretion around a black hole would look like.

❖ **Gravitational waves**

Any event that is not spherically symmetric creates ripples in the fabric of spacetime, called gravitational waves or gravitational radiation. To observe these, we first consider the "loudest" events, such as objects with strong gravitational fields (black holes or neutron stars) merging. Through technological prowess, bringing together experts from various fields, gravitational wave detectors were built and made their first detection of gravitational waves generated by two black holes merging together (LIGO Scientific Collaboration and Virgo Collaboration, 2016). This was made possible as the predicted signal can be recognised within the noise of the various detectors, where the theoretical signal is provided based on post-Newtonian theory, NR simulations, and black hole perturbation theory. Nowadays, there have been enough detections such that the sample is large enough to consider a statistical analysis that can inform on the universe's expansion (Gair et al., 2023). Even more recently, considering a different gravitational wave frequency range, with the ingenious method of monitoring the variation in pulsar timings, the gravitational wave background has been detected (Agazie et al., 2023; Antoniadis et al., 2023; Reardon et al., 2023; Xu et al., 2023). This could be generated by various sources, notably inspiralling supermassive black hole binaries, but also early universe mechanisms and some dark matter models; disentangling this will provide key insight into our universe.

All of the phenomena described above, and many more (Will, 2014), test GR's accuracy, showing that it remains robust so far. We can consider the impact of these effects on individual astronomical systems, but as was gradually suggested, these impact the universe as a whole and how we perceive it as studied by the field of Cosmology. See Chapter 4 for a historical introduction to Cosmology and the current standard model. In understanding the universe, there are numerous open questions, such as notably the origin of its dark content (Bull et al., 2016), and how relativistic effects impact our universe and our observations of it (Macpherson and Heinesen, 2021; Umeh, 2022; Bonvin et al., 2023; Umeh, 2023).

Simulations in NR have been a powerful tool in exploring GR in scenarios that escape our analytical capacities. This has been demonstrated by their contribution to understanding black hole observations and gravitational wave detection (Boyle, Hemberger, et al., 2019; The Event Horizon Telescope Collaboration, 2019b). Thus, we seek to bring this machinery to the field of cosmology, specifically considering cosmological structure formation. We explored initial conditions satisfying Einstein's field equations and how the resulting structure grows. One challenge with NR simulations is gauge-variance; so extracted results should be interpreted based on invariants and, if possible observable invariants. Therefore, we consider invariants characterising spacetime constructed from the Weyl tensor.

1.1 Structure

The structure of this thesis is split in two, with background chapters being Chapter 2, 3 and 4, while the original work contributed in this thesis is described in Chapter 5 and 6 that are based on Munoz and Bruni (2023a) and Munoz and Bruni (2023b) respectively[1].

The background chapters have been given a somewhat repetitive structure to simplify cross-referencing. The spacetime, matter and constraint and evolution equations of GR are described in Chapter 2 in their most general form, then made specific to NR in Chapter 3 and to cosmology both in the homogeneous case in Section 4.1 and inhomogeneous case in Section 4.2. See each topic's spacetime, matter, and constraint and evolution equation sections below.

	Spacetime	Matter	Constraint and evolution equations
General Relativity	2.1	2.3	2.4
Numerical Relativity	3.1	3.2	3.3
Homogeneous cosmology	4.1.1	4.1.2	4.1.3
Inhomogeneous cosmology	4.2.1	4.2.2	4.2.4

Another repeated structure can be found within each constraint and evolution equation section. Indeed, three main equations govern the system: Einstein's field equations, the Ricci identity and the conservation equations; a subsection is then dedicated to each.

Once this system of equations is understood, it can be evolved with the numerical methods described in Section 3.6. Then in the simulation analysis, two main axes are being pursued: studying structure formation and invariantly characterising spacetime. For structure formation, Section 4.3 first describes the linear evolution based on perturbation theory, then the nonlinear evolution with the Top-Hat homogeneous and spherical collapse model, which is used as a key point of comparison in Chapter 6. We additionally describe the Top-Hat model from different perspectives, reinforcing its versatile role and emphasising its relevance for the mass function.

In the second axis, we characterise the spacetime based on two different decompositions of the Weyl tensor. The first is done covariantly, considering the electric and magnetic parts of the Weyl tensor, also known as gravito-electromagnetism. This is generally presented in Section 2.5.1 and in terms of NR in Section 3.5. In a homogeneous universe, the Weyl tensor is zero, but not in an inhomogeneous one; see the form the electric and magnetic parts take for scalar perturbations at first order in Section 4.2.4 making quantities are gauge invariant at first order, as discussed in Section 4.2.6. The second decomposition is based on the Newmann-Penrose formalism leading to the invariant classification of spacetime into Petrov types. Gravito-electromagnetism and the Petrov classification are described in Section 2.5 where invariant scalars are defined, to be later extracted from simulations.

All of these concepts were introduced to then be applied in Chapter 5 and Chapter 6, which are based on Munoz and Bruni (2023a,b). Chapter 5 presents two post-processing codes that were created to extract the electric and magnetic parts of the Weyl tensor, as well as various invariants.

[1] Some parts of those papers dedicated to the theoretical background have been moved to the background chapters; notably, Section 2.5, 3.1, 3.5, and 4.2.6 have been extracted from (Munoz and Bruni, 2023a) and extended, and Section 2.3.1, 2.4.4, 4.1.4.4, 4.1.4.5, 4.2.4, 4.3.4, and 4.3.5 have been extracted from (Munoz and Bruni, 2023b) and extended.

Their application were demonstrated on a Λ-Szekeres spacetime, and the code tests concluded that of the two, the code henceforth called `EBWeyl` shows the best performance; we then applied it to simulation results.

Chapter 6 contains the main original contributions from this work, presenting the simulations and their results. The initial conditions and the corresponding code `ICPertFLRW` are described in Section 6.1, and the simulation analysis is described in Section 6.3.

2 - General Relativity

General Relativity (GR) is a gravitational theory (Einstein, 1916) that describes spacetime and matter interwoven together such that matter curves spacetime and the shape of spacetime dictates the trajectory of matter. Here we will then describe each of these, spacetime in Section 2.1 and matter in Section 2.3, with the two related through Einstein's field equations

$$G_{\alpha\beta} = \kappa T_{\alpha\beta}, \tag{2.1}$$

elaborated upon in Section 2.2 see Eq. (2.39) with spacetime on the left and matter on the right. $G_{\alpha\beta}$, in particular, is solely composed of local curvature information, in Section 2.5 we will see what further non-local behaviour is contained in the spacetime namely in the Weyl tensor (Weyl, 1918).

GR was built on key expressions determining how spacetime and matter are defined as given by the Ricci identity (Ricci and Levi-Civita, 1900), and the conservation equations

$$2\nabla_{[\mu}\nabla_{\nu]}u^{\alpha} = R^{\alpha}{}_{\beta\mu\nu}u^{\beta}, \qquad \nabla_{\alpha}T^{\alpha\beta} = 0, \tag{2.2}$$

see Eq. (2.18) and Eq. (2.40) respectively. What these three expressions imply for a perfect fluid is described in Section 2.4 as these will become the backbone of how spacetime and matter are evolved.

2.1 Spacetime

2.1.1 Coordinates & tensors

Spacetime combines the three dimensions of space, left/right, forward/backward and up/down, and the one dimension of time, past/future. How to measure and describe these different dimensional directions, in whatever geometrical shape they may take, is key to describe spacetime, see the textbook references (Weinberg, 1972; Wald, 1984; D'Inverno, 1992; Misner, Thorne, and Wheeler, 2017) for more detail. To describe these dimensions, we work with coordinates $\mathbf{x}$, for example $\mathbf{x} = \{t,\ x,\ y,\ z\}$ for Cartesian coordinates, or $\mathbf{x} = \{t,\ r,\ \theta,\ \phi\}$ for spherical coordinates; but in what observer frame are these coordinates defined? An inertial frame has a constant velocity (Newton, 1687), therefore these are observer-dependent coordinates. Yet, these mathematical constructs have no bearing on the gravitational phenomena, meaning that should we go from one set of observer-dependent coordinates to another the physical phenomena does not change, GR is invariant under coordinate transformation (Einstein, 1916). Observer-independent quantities then need to be constructed, using rods to measure intervals in space and clocks to measure intervals in time (Wald, 1984). Depending on the observers' position in spacetime and their velocity, different observers may

disagree on the time dt or space dx interval between two events. However, they will agree on the spacetime interval, as measured by the infinitesimal squared distance between the two events

$$ds^2 = g_{\mu\nu} dx^\mu dx^\nu, \tag{2.3}$$

where Einstein's summation convention is used from here on out (omitting the summation symbols that sum each repeated index over the spacetime dimensions). Greek indices (α, β, μ, ν...) go from 0 for time and 1, 2, and 3 for the spatial dimensions, while Latin indices (i, j, k...) go from 1 to 3 only spanning spatial dimensions.

$g_{\mu\nu}$ is the spacetime metric tensor that corresponds to the variation in the spacetime path as measured by the coordinates. It quantifies observer-independent properties of spacetime and maps those to the observer-dependent coordinates separation dx^μ. We additionally define g the determinant of $g_{\mu\nu}$, $g^{\mu\nu}$ its inverse, and $g^\alpha{}_\beta$ corresponding to the Kronecker delta $g^{\alpha\mu} g_{\mu\beta} = g^\alpha{}_\beta = \delta^\alpha{}_\beta$, meaning that the contraction of the metric corresponds to the number of dimensions of the spacetime: $g^\alpha{}_\alpha = \delta^\alpha{}_\alpha = 4$. With the notation convention used here, the metric signature is $\{-,\ +,\ +,\ +\}$, so $g < 0$ and the speed of light c is set to one $c = 1$. The simplest type of spacetime is provided by the Minkowski metric where $g_{\alpha\beta} = \eta_{\alpha\beta} = diag(-1,\ 1,\ 1,\ 1)$ in Cartesian coordinates which is a flat spacetime.

The separation between two events ds^2 is timelike if $ds^2 < 0$, lightlike if $ds^2 = 0$, and spacelike if $ds^2 > 0$ meaning that to connect these events, the observer needs to have a speed slower, equal, and faster than the speed of light respectively. This defines causally connected $ds^2 \leqslant 0$ and unconnected $ds^2 > 0$ events. An observer that is at rest will measure on their clock their proper time such that $ds^2 = -d\tau^2$. We will use the symbol τ for proper time, and derivatives with respect to τ are denoted with an overhead dot

$$\dot{a} = \frac{da}{d\tau} \tag{2.4}$$

Coordinates whose time is evolving according to each grid position's proper time are synchronous coordinates, and the metric tensor's time components are $g_{0\mu} = g_{\mu 0} = \{-1,\ 0,\ 0,\ 0\}$.

As we discuss tensors, let us define them as a collection of functions applied to the coordinate points that are transformed into a different set of coordinates according to the tensor transformation law Eq. (2.6). A tensorial quantity, say A, is given indices in accordance with its rank, rank 0 for a scalar A, rank 1 for a vector A^μ, rank 2 $A^{\mu\nu}$ and so on with indices up being contravariant and indices down covariant. The two are related through the spacetime metric, such that covariant and contravariant indices can be raised and lowered with the spacetime metric:

$$A_\mu = g_{\mu\nu} A^\nu, \qquad A^\mu = g^{\mu\nu} A_\nu. \tag{2.5}$$

Going from a set of coordinates x^μ to another $\tilde{x}^\mu$, the rank 2 tensor $A^\alpha{}_\beta$ with one contravariant index and one covariant index is transformed according to the tensor transformation law

$$\tilde{A}^\mu{}_\nu = \frac{\partial \tilde{x}^\mu}{\partial x^\alpha} \frac{\partial x^\beta}{\partial \tilde{x}^\nu} A^\alpha{}_\beta, \tag{2.6}$$

where $\partial x^\beta / \partial \tilde{x}^\nu$ is the Jacobian matrix of the coordinate change. With a rank of at least two, tensors can be split into symmetric and anti-symmetric parts

$$\begin{gathered} A_{\mu\nu} = A_{(\mu\nu)} + A_{[\mu\nu]}, \\ A_{(\mu\nu)} = \tfrac{1}{2}\left(A_{\mu\nu} + A_{\nu\mu}\right), \qquad A_{[\mu\nu]} = \tfrac{1}{2}\left(A_{\mu\nu} - A_{\nu\mu}\right), \end{gathered} \tag{2.7}$$

where $(...)$ and $[...]$ respectively indicate a symmetrisation and anti-symmetrisation. A symmetric tensor $A_{\mu\nu} = A_{(\mu\nu)}$ is identical under index permutation $A_{\mu\nu} = A_{\nu\mu}$, while an antisymmetric tensor $B_{\mu\nu} = B_{[\mu\nu]}$ has a sign change $B_{\mu\nu} = -B_{\nu\mu}$. The contraction of a symmetric tensor with an antisymmetric tensor cancels out $A^{(\mu\nu)}B_{[\mu\nu]} = 0$.

We can further define tensor densities $\bar{\bar{A}}^{\alpha}{}_{\beta}$ and pseudo-tensors $\tilde{\tilde{A}}^{\alpha}{}_{\beta}$ as quantities that transform as (Plebański and Krasiński, 2006)

$$\bar{\bar{\tilde{A}}}^{\mu}{}_{\nu} = det\left(\frac{\partial\tilde{x}^{\lambda}}{\partial x^{\sigma}}\right)^{\mathcal{W}} \frac{\partial\tilde{x}^{\mu}}{\partial x^{\alpha}}\frac{\partial x^{\beta}}{\partial\tilde{x}^{\nu}}\bar{\bar{A}}^{\alpha}{}_{\beta}, \tag{2.8}$$

and

$$\tilde{\tilde{\bar{A}}}^{\mu}{}_{\nu} = sign\left(det\left(\frac{\partial\tilde{x}^{\lambda}}{\partial x^{\sigma}}\right)\right)\frac{\partial\tilde{x}^{\mu}}{\partial x^{\alpha}}\frac{\partial x^{\beta}}{\partial\tilde{x}^{\nu}}\tilde{\tilde{A}}^{\alpha}{}_{\beta}, \tag{2.9}$$

respectively. In the first case, for tensor densities, the Jacobian determinant is in powers of $\mathcal{W}$, which is the weight. A normal tensor has no weight $\mathcal{W} = 0$.

An example of a pseudo-tensor is the Levi-Civita symbol which is completely anti-symmetric, meaning that permuting any index will lead to a sign change. Should there be 4 dimensions, then it is

$$\begin{aligned}\tilde{\tilde{\varepsilon}}_{\alpha\beta\mu\nu} &= \begin{cases} 1 \text{ for even permutation of } (0,\ 1,\ 2,\ 3) \\ -1 \text{ for odd permutation of } (0,\ 1,\ 2,\ 3) \\ 0 \text{ otherwise} \end{cases} \\ &= \text{sign}(\beta-\alpha)\ \text{sign}(\mu-\alpha)\ \text{sign}(\nu-\alpha)\ \text{sign}(\mu-\beta)\ \text{sign}(\nu-\beta)\ \text{sign}(\nu-\mu)\end{aligned} \tag{2.10}$$

while if there are 3 dimensions (where indices go from 1 to 3), then it is

$$\tilde{\tilde{\varepsilon}}_{kij} = \text{sign}(i-k)\ \text{sign}(j-k)\ \text{sign}(j-i), \tag{2.11}$$

such that all temporal components of $\tilde{\tilde{\varepsilon}}_{\alpha\mu\nu}$ are zero. To make this pseudo-tensor a tensor, the Levi-Civita symbol is multiplied by the metric determinant

$$\epsilon_{\alpha\beta\mu\nu} = \sqrt{|g|}\tilde{\tilde{\varepsilon}}_{\alpha\beta\mu\nu} \tag{2.12}$$

which is the Levi-Civita tensor and has the same antisymmetric properties as the Levi-Civita symbol.

2.1.2 Covariant derivative

Having defined the spacetime coordinates and the properties of coordinate transformable functions, one needs to define how to differentiate them such that the derivative of a tensor is also a tensor. This is the role of the covariant derivative (Ricci and Levi-Civita, 1900), for a scalar, a contravariant and a covariant tensor, this is applied as

$$\begin{aligned}\nabla_{\sigma}A &= \partial_{\sigma}A \\ \nabla_{\sigma}A^{\alpha} &= \partial_{\sigma}A^{\alpha} + \Gamma^{\alpha}{}_{\lambda\sigma}A^{\lambda} \\ \nabla_{\sigma}A_{\mu} &= \partial_{\sigma}A_{\mu} - \Gamma^{\lambda}{}_{\mu\sigma}A_{\lambda}\end{aligned} \tag{2.13}$$

where the first terms are simply the coordinate derivative of the tensor with $\partial_\sigma = \frac{\partial}{\partial x^\sigma}$, and the other terms depend on the Levi-Civita connection ${\Gamma^\alpha}_{\mu\nu}$ that brings this expression back to being tensorial, although the Levi-Civita connection itself is not a tensor.

Relating this expression to the metric $g_{\alpha\beta}$, the components of this connection are found to be the Christoffel symbols (Christoffel, 1869) expressed as

$$\Gamma_{\alpha\mu\nu} = \frac{1}{2}\left(\partial_\mu g_{\alpha\nu} + \partial_\nu g_{\mu\alpha} - \partial_\alpha g_{\mu\nu}\right), \qquad {\Gamma^\alpha}_{\mu\nu} = \frac{1}{2} g^{\alpha\beta}\left(\partial_\mu g_{\beta\nu} + \partial_\nu g_{\mu\beta} - \partial_\beta g_{\mu\nu}\right), \tag{2.14}$$

where the last two indices of ${\Gamma^\alpha}_{\mu\nu}$ are symmetric. In this case, the covariant derivative of the metric is zero, $\nabla_\sigma g_{\alpha\beta} = 0$. While the covariant derivative does not necessarily commute, product and additive rules apply.

2.1.2.1 Divergence & curl

The divergence of a vector or tensor corresponds to the contraction of its covariant derivative: $\nabla_\alpha A^\alpha$ or $\nabla_\alpha A^{\alpha\beta}$. For a vector in particular, this can be expressed as (Weinberg, 1972)

$$\nabla_\mu A^\mu = \frac{1}{\sqrt{|g|}} \frac{\partial}{\partial x^\mu}\left(\sqrt{|g|} A^\mu\right). \tag{2.15}$$

Then to compute the curl, one needs to define a vector with respect to which the curl is calculated; this is addressed in Section 2.1.4.3.

2.1.2.2 Geodesic

In a curved spacetime, geodesics are the lines that extremise the path providing the most direct trajectory between two events. It can be timelike for the trajectories of massive particles, null for massless particles or spacelike for causally disconnected events. In the timelike case, a generic timelike 4-velocity v^α is considered

$$v^\alpha = \frac{dx^\alpha}{d\tau}, \qquad v^\alpha v_\alpha = -1. \tag{2.16}$$

-1 for a timelike normalisation, 0 for null and $+1$ for spacelike. Since the geodesic provides a path of constant velocity, the geodesic equation is given by the 4-acceleration $\dot{v}^\alpha = v^\mu \nabla_\mu v^\alpha$ being set to zero

$$v^\mu \nabla_\mu v^\alpha = \frac{d^2 x^\alpha}{d\tau^2} + {\Gamma^\alpha}_{\mu\nu} \frac{dx^\mu}{d\tau}\frac{dx^\nu}{d\tau} = 0. \tag{2.17}$$

Solving these equations will provide the particle trajectory.

2.1.3 Curvature

To quantify the curvature of spacetime, one considers the deviation experienced by a vector v^α as it is parallel transported around the spacetime in a closed loop. This defines the Riemann tensor, ${R^\alpha}_{\sigma\mu\nu}$ (Riemann, 1868), according to the Ricci identity (Ricci and Levi-Civita, 1900)

$$\nabla_\mu \nabla_\nu v^\alpha - \nabla_\nu \nabla_\mu v^\alpha = {R^\alpha}_{\sigma\mu\nu} v^\sigma. \tag{2.18}$$

${R^\alpha}_{\sigma\mu\nu}$ essentially quantifies by how much the covariant derivative does not commute; it is then found to have the form

$${R^\alpha}_{\sigma\mu\nu} = \partial_\mu {\Gamma^\alpha}_{\sigma\nu} - \partial_\nu {\Gamma^\alpha}_{\mu\sigma} + {\Gamma^\alpha}_{\mu\lambda}{\Gamma^\lambda}_{\sigma\nu} - {\Gamma^\alpha}_{\lambda\nu}{\Gamma^\lambda}_{\mu\sigma}. \tag{2.19}$$

An N-dimensional tensor with 4 indices has N^4 components. Thankfully, given the symmetries of the Christoffel symbol, and the expression above, this tensor possesses certain symmetries, namely pairwise symmetry, and the indices within each pair are anti-symmetric

$$\begin{aligned} R_{\alpha\beta\mu\nu} &= R_{\mu\nu\alpha\beta}, \\ R_{\alpha\beta\mu\nu} &= -R_{\alpha\beta\nu\mu} = -R_{\beta\alpha\mu\nu} \end{aligned} \tag{2.20}$$

and $R^{\alpha}{}_{\sigma\mu\nu}$ satisfies the Bianchi identities (Voss, 1880; Bianchi, 1902)

$$\begin{aligned} R_{\alpha\beta\mu\nu} &= R_{\alpha\mu\beta\nu} + R_{\alpha\nu\mu\beta}, \\ \nabla_\sigma R_{\alpha\beta\mu\nu} &= \nabla_\mu R_{\alpha\beta\sigma\nu} + \nabla_\nu R_{\alpha\beta\mu\sigma}. \end{aligned} \tag{2.21}$$

All of these properties reduce the number of independent components in the Riemann tensor to $N^2(N^2-1)/12$, so 20 for 4-dimensions. $R^{\alpha}{}_{\sigma\mu\nu}$ can be split into the Ricci and Weyl tensors, each possessing 10 degrees of freedom. The Ricci tensor is obtained from the trace of the Riemann tensor

$$R_{\alpha\beta} = R^{\mu}{}_{\alpha\mu\beta} \tag{2.22}$$

which is symmetric. And the further trace of this term is the Ricci scalar,

$$R = R^{\mu}{}_{\mu} = g^{\mu\nu} R_{\mu\nu}. \tag{2.23}$$

Both quantify local curvature and are present in Einstein's field equation Eq. (2.39).

Then the Weyl tensor (Weyl, 1918) is the traceless part of the Riemann tensor. It is constructed by removing the Ricci tensor and scalar parts to the Riemann tensor,

$$C_{\alpha\beta\mu\nu} = R_{\alpha\beta\mu\nu} - \left(g_{\alpha[\mu} R_{\nu]\beta} - g_{\beta[\mu} R_{\nu]\alpha}\right) + \frac{1}{3} g_{\alpha[\mu} g_{\nu]\beta} R. \tag{2.24}$$

This is not present in Einstein's field equations Eq. (2.39) and it quantifies non-local gravitational effects whose impact on the fluid evolution can only be quantified with the Ricci identity Eq. (2.18) applied to the fluid 4-velocity, see Section 2.5.1. We also define the Weyl tensor's dual $C^*_{\alpha\beta\mu\nu} = \frac{1}{2} C_{\alpha\beta\lambda\sigma} \epsilon^{\lambda\sigma}{}_{\mu\nu}$ and its complex self-dual $\widetilde{C}_{\alpha\beta\mu\nu} = \frac{1}{4}(C_{\alpha\beta\mu\nu} - i C^*_{\alpha\beta\mu\nu})$, which by definition corresponds to its own dual: $\widetilde{C}_{\alpha\beta\mu\nu} = i \widetilde{C}^*_{\alpha\beta\mu\nu}$, see Stephani et al. (2003).

2.1.4 Projecting along or orthogonally to a vector

In relativity, special or general, the physical notions of the observers and that of the associated reference frames play a crucial role, where in practice, most often frame of reference is used interchangeably with the notion of coordinate system. However, it is sometimes useful, starting from a given tensor, to define new tensors by projecting on one or more vectors. Therefore, for the sake of clarity in this thesis, we use the word *frame* only in reference to a projection on a unit timelike vector, or on a tetrad of basis vectors, never in reference to coordinate systems. This is made explicit with the use of the notation $\{v\}$ when a given quantity is defined by projecting along or orthogonally to a given timelike vector v^μ; that will define the quantity in the frame v^μ.

This unit timelike 4-vector may have a corresponding spacelike hypersurface such that the two are orthogonal. The spatial hypersurfaces are layered along time and connected to one another through this projection vector v^μ; in other words, this foliates space through time (Arnowitt, Deser,

and Misner, 1959; Bruni, 1991; Alcubierre, 2008; Ellis, Maartens, and MacCallum, 2012). This concept is relevant in describing fluid terms and is key to NR, so we give introductory notions here that will be elaborated in Chapter 3.

Here we shall use v^α as the normal timelike 4-vector, so $v^\alpha v_\alpha = -1$, and

$$P^{\{v\}}_{\alpha\beta} = g_{\alpha\beta} + v_\alpha v_\beta \qquad P^{\{v\}\alpha}{}_\beta = \delta^\alpha{}_\beta + v^\alpha v_\beta \tag{2.25}$$

as its projection tensor. $P^{\{v\}}_{\alpha\beta}$ corresponds to the metric of this spatial hypersurface, its contraction $P^{\{v\}\alpha}{}_\alpha = 3$ shows that it describes a 3-dimensional space and so its determinant is positive, $P^{\{v\}} > 0$, and by definition, it is orthogonal to v^α: $v^\alpha P^{\{v\}}_{\alpha\beta} = 0$.

Any tensor, say $A_{\alpha\beta}$, can then be projected into this foliation such that:

- $A_{\alpha\beta}v^\alpha v^\beta$ is its temporal part,
- $P^{\{v\}\beta}{}_\alpha A_{\beta\mu}v^\mu$ its time and space part, and
- $P^{\{v\}\mu}{}_\alpha P^{\{v\}\nu}{}_\beta A_{\mu\nu}$ its spatial part.

Since these new tensors depend on the choice of projection vector v^α, this is made explicit with a $\{v\}$ superscript. So, for example, $P^{\{v\}\beta}{}_\alpha A_{\beta\mu}v^\mu = B^{\{v\}}_\alpha$ and $P^{\{v\}\mu}{}_\alpha P^{\{v\}\nu}{}_\beta A_{\mu\nu} = C^{\{v\}}_{\alpha\beta}$ where $B^{\{v\}}_\alpha$ and $C^{\{v\}}_{\alpha\beta}$ live on the $P^{\{v\}}_{\alpha\beta}$ surface and as such their indices are to be raised or lowered with $P^{\{v\}}_{\alpha\beta}$ and by definition they are is automatically orthogonal to v^α: $v^\alpha B^{\{v\}}_\alpha = 0$ and $v^\alpha C^{\{v\}}_{\alpha\beta} = 0$.

A useful operator that takes the spatial traceless part of $A_{\alpha\beta}$ is

$$A^{\{v\}}_{\langle\alpha\beta\rangle} = A^{\{v\}}_{(\alpha\beta)} - \frac{1}{3}P^{\{v\}}_{\alpha\beta}P^{\{v\}}_{\mu\nu}A^{\mu\nu} = P^{\{v\}\mu}{}_{(\alpha}P^{\{v\}\nu}{}_{\beta)}A_{\mu\nu} - \frac{1}{3}P^{\{v\}}_{\alpha\beta}P^{\{v\}}_{\mu\nu}A^{\mu\nu}. \tag{2.26}$$

If the tensor is already on this hypersurface, this operator simply takes the traceless part.

With this projection approach, a derivative along and orthogonally to v^α can be defined.

2.1.4.1 Lie derivative & Killing vectors

The Lie derivative (Lie, 1888) defines the derivative of a tensor along the vector v^σ. This derivative applied to a scalar, a contravariant, and a covariant tensor takes the form

$$\begin{aligned}
\mathcal{L}_v A &= v^\sigma\left(\partial_\sigma A\right) \\
\mathcal{L}_v A^\alpha &= v^\sigma\left(\partial_\sigma A^\alpha\right) - \left(\partial_\sigma v^\alpha\right)A^\sigma \\
\mathcal{L}_v A_\mu &= v^\sigma\left(\partial_\sigma A_\mu\right) + \left(\partial_\mu v^\sigma\right)A_\sigma
\end{aligned} \tag{2.27}$$

Considering a tensor density, an extra term is added (Alcubierre, 2008)

$$\begin{aligned}
\mathcal{L}_v \bar{\bar{A}} &= \left[\mathcal{L}_v \bar{\bar{A}}\right]_{\mathcal{W}=0} + \mathcal{W}\left(\partial_\sigma v^\sigma\right) \\
\mathcal{L}_v \bar{\bar{A}}^\alpha &= \left[\mathcal{L}_v \bar{\bar{A}}^\alpha\right]_{\mathcal{W}=0} + \mathcal{W}\bar{\bar{A}}^\alpha\left(\partial_\sigma v^\sigma\right) \\
\mathcal{L}_v \bar{\bar{A}}_\mu &= \left[\mathcal{L}_v \bar{\bar{A}}_\mu\right]_{\mathcal{W}=0} + \mathcal{W}\bar{\bar{A}}_\mu\left(\partial_\sigma v^\sigma\right)
\end{aligned} \tag{2.28}$$

where $[\mathcal{L}_v \ldots]_{\mathcal{W}=0}$ corresponds to the terms expressed in Eq. (2.27) and $\mathcal{W}$ is the weight of the tensor density, see Eq. (2.8).

Should the Lie derivative along a vector ξ^α of the spacetime metric tensor vanish, then the ξ^α field is called a Killing vector field (Killing, 1892) and identifies a symmetry of the spacetime. This field satisfies the Killing equation

$$\mathcal{L}_\xi g_{\alpha\beta} = 2\nabla_{(\alpha}\xi_{\beta)} = 0, \tag{2.29}$$

meaning that $\nabla_\alpha \xi_\beta$ is antisymmetric. A vector field v^α that follows the geodesic curve Eq. (2.17) $v^\mu \nabla_\mu v^\nu = 0$ contracted with a Killing vector vanishes

$$v^\mu \nabla_\mu \left(\xi_\nu v^\nu\right) = v^\mu v^\nu \nabla_\mu \xi_\nu = 0, \tag{2.30}$$

indeed a symmetric tensor contracted with an antisymmetric tensor is zero. Therefore $\xi_\nu v^\nu$ is a conserved quantity along the geodesic curve.

2.1.4.2 Spatial covariant derivative

Projecting the covariant derivative of the spacetime metric ∇_α, defines the covariant derivative of the spatial metric $D_\alpha^{\{v\}}$ (Alcubierre, 2008; Ellis, Maartens, and MacCallum, 2012). Applying this to the tensor $A_\beta^{\{v\}}$ that lives on $P_{\alpha\beta}^{\{v\}}$, it is

$$D_\alpha^{\{v\}} A_\beta^{\{v\}} = P^{\{v\}\mu}{}_\alpha \nabla_\mu A_\beta^{\{v\}} = \nabla_\alpha A_\beta^{\{v\}} + v_\alpha \dot{A}_\beta^{\{v\}}, \tag{2.31}$$

where $\dot{A}^\alpha = v^\mu \nabla_\mu A^\alpha$ is the derivative with respect to proper time τ. If A_β does not live on $P_{\alpha\beta}^{\{v\}}$ then it needs to be projected and the spatial covariant derivative only applies to the projected part

$$D_\alpha^{\{v\}} A_\beta = P^{\{v\}\mu}{}_\alpha P^{\{v\}\nu}{}_\beta \nabla_\mu A_\nu. \tag{2.32}$$

By definition this is orthogonal to v^α as $v^\alpha D_\alpha^{\{v\}} A_\beta = v^\beta D_\alpha^{\{v\}} A_\beta = 0$. In practice, this is equivalent to saying that $D_\alpha^{\{v\}}$ is the covariant derivative associated with $P_{\alpha\beta}^{\{v\}}$ where the Christoffel symbols, Eq. (2.14), are computed with $P_{\alpha\beta}^{\{v\}}$ instead of $g_{\alpha\beta}$.

2.1.4.3 Spatial divergence and curl

The spatial divergence is the contraction of the spatial covariant derivative $D_\alpha^{\{v\}}$ and the term being differentiated

$$D_\alpha^{\{v\}} A^\alpha = \nabla_\alpha A^\alpha + v_\alpha \dot{A}^\alpha \tag{2.33}$$

where this is composed of the spacetime divergence and the projected time derivative.

Then the curl (Ellis, Maartens, and MacCallum, 2012) is given by this spatial covariant derivative contracted with the Levi-Civita tensor on the hypersurface. For rank 1 and 2 tensors, this is

$$(D^{\{v\}} \times A)_\alpha = \epsilon^{\{v\}}{}_{\alpha\mu\nu} D^{\{v\}\mu} A^\nu, \qquad (D^{\{v\}} \times A)_{\alpha\beta} = \epsilon^{\{v\}}{}_{\mu\nu(\alpha} D^{\{v\}\mu} A_{\beta)}{}^\nu. \tag{2.34}$$

with $\epsilon^{\{v\}}{}_{\alpha\beta\mu}$ corresponding to the projected Levi-Civita tensor Eq. (2.12)

$$\epsilon^{\{v\}}{}_{\alpha\beta\mu} = v^\sigma \epsilon_{\sigma\alpha\beta\mu}. \tag{2.35}$$

The anti-symmetric nature of this tensor means that $\epsilon^{\{v\}}{}_{\alpha\beta\mu}$ is only spatial $v^\alpha \epsilon^{\{v\}}{}_{\alpha\beta\mu} = 0$. This is equivalent to saying $\epsilon^{\{v\}}{}_{\alpha\beta\mu}$ is the Levi-Civita tensor computed with $P_{\alpha\beta}^{\{v\}}$ such that

${\epsilon^{\{v\}}}_{\alpha\beta\mu} = \sqrt{P^{\{v\}}}\,\tilde{\tilde{\varepsilon}}_{\alpha\beta\mu}$, with the 3-Levi-Civita symbol given by Eq. (2.11). Note that should the vector be constructed from a scalar, say $A_\nu = \partial_\nu A$, then $D^{\{v\}\mu}A^\nu$ would be symmetric which contracted with the anti-symmetric Levi-Civita tensor would cancel out. Indeed the curl of a gradient is zero, meaning that only purely vectorial and tensorial quantities have a curl. Then reminding another vector calculus identity, the divergence of a curl is zero such that the result of a curl is purely vectorial and tensorial.

2.1.4.4 Spatial curvature

Now as the covariant derivative defines the 4-dimensional Riemann tensor ${R^\alpha}_{\sigma\mu\nu}$ via the Ricci identity Eq. (2.18). With this new spatial covariant derivative, we can construct a new 3-dimensional Riemann tensor ${}^{(3)}{R^\alpha}_{\sigma\mu\nu}$ with:

$$D^{\{v\}}_\mu D^{\{v\}}_\nu w^\alpha - D^{\{v\}}_\nu D^{\{v\}}_\mu w^\alpha = {}^{(3)}{R^\alpha}_{\sigma\mu\nu} w^\sigma \tag{2.36}$$

where w^α is an arbitrary vector. ${}^{(3)}{R^\alpha}_{\sigma\mu\nu}$ is the 3-Riemann tensor of the spatial hypersurface $P^{\{v\}}_{\alpha\beta}$, its contraction with $P^{\{v\}}_{\alpha\beta}$ then further provides the 3-dimensional Ricci tensor ${}^{(3)}R_{\alpha\beta}$ and scalar ${}^{(3)}R$. These can be obtained by using Eq. (2.14) and Eq. (2.19) where $P^{\{v\}}_{\alpha\beta}$ is used instead of $g_{\alpha\beta}$. By their definition, they exclusively live on the $P^{\{v\}}_{\alpha\beta}$ hypersurface. Following our notation, these terms should then be given the $\{v\}$ superscript however this is omitted for simplicity and we trust the reader to establish which spatial hypersurface is discussed based on the context.

The transition from the 4-dimensional to 3-dimensional Ricci identity, Eq. (2.18) and Eq. (2.36), applied to the projecting vector v^μ provides the Gauss-Codazzi equations, Eq. (3.25) and Eq. (3.26), that relate ${R^\alpha}_{\sigma\mu\nu}$ and ${}^{(3)}{R^\alpha}_{\sigma\mu\nu}$ as discussed in Section 3.1.1.

2.2 Einstein's field equations

The gravitational action of GR is provided by the Einstein-Hilbert action (Hilbert, 1915), which we express here with the cosmological constant Λ (Einstein, 1917) and the Lagrangian of the matter field $\mathcal{L}_M$ as

$$S = \int \left[\frac{1}{2\kappa}(R - 2\Lambda) + \mathcal{L}_M\right]\sqrt{-g}dx^4. \tag{2.37}$$

where R is the 4-dimensional Ricci scalar Eq. (2.23) of the metric $g_{\alpha\beta}$ whose determinant is g, and $\kappa = 8\pi G$ is Einstein's gravitational constant, with G the gravitational constant that we set to one $G = 1$. Varying Eq. (2.37), the stationary action principle, $\delta S = 0$, provides the equations of motion called Einstein's field equations Eq. (2.1) (Einstein, 1916). This relates the spacetime described with Einstein's tensor

$$G_{\alpha\beta} = R_{\alpha\beta} - \frac{1}{2}Rg_{\alpha\beta}, \tag{2.38}$$

to the matter field described with the energy-stress tensor $T_{\alpha\beta}$ addressed in Section 2.3, and including the cosmological constant Λ, Einstein's field equations are

$$\begin{aligned} G_{\alpha\beta} + \Lambda g_{\alpha\beta} &= \kappa T_{\alpha\beta}, \\ \Leftrightarrow R_{\alpha\beta} - \frac{1}{2}Rg_{\alpha\beta} + \Lambda g_{\alpha\beta} &= \kappa T_{\alpha\beta}, \\ \Leftrightarrow R_{\alpha\beta} - \Lambda g_{\alpha\beta} &= \kappa\left(T_{\alpha\beta} - \frac{1}{2}Tg_{\alpha\beta}\right) \end{aligned} \tag{2.39}$$

also written with $T = g^{\alpha\beta}T_{\alpha\beta}$ the trace of the energy-stress tensor.

The second Bianchi identity, Eq. (2.21), contracted twice, and since Λ is a constant, provides the conservation equation $\nabla_\alpha G^\alpha{}_\beta = 0$, meaning that the matter has the conservation equations

$$\nabla_\alpha T^\alpha{}_\beta = 0. \tag{2.40}$$

As presented this may be perceived as a consequence of the definition of spacetime, however, the fact that the energy-stress tensor is divergenceless is a well-known property that predates GR. Instead, this conservation equation was a key property in the definition of curvature.

2.3 Matter

In general for an imperfect fluid without charge or viscosity, the energy-stress tensor is (Bruni, 1991)

$$T_{\alpha\beta} = \rho^{\{v\}}v_\alpha v_\beta + 2q^{\{v\}}_{(\alpha}v_{\beta)} + S^{\{v\}}_{\alpha\beta}, \tag{2.41}$$

which is symmetric and has the trace

$$T = g^{\alpha\beta}T_{\alpha\beta} = 3p^{\{v\}} - \rho^{\{v\}}. \tag{2.42}$$

v^α is an arbitrary timelike 4-vector chosen to describe the fluid with its projection tensor $P^{\{v\}}_{\alpha\beta}$ Eq. (2.25). Projecting $T_{\alpha\beta}$ in the v^α frame provides the energy density $\rho^{\{v\}}$, energy flux $q^{\{v\}}_\alpha$ (also called momentum density) and stress tensor $S^{\{v\}}_{\alpha\beta}$

$$\begin{aligned}
\rho^{\{v\}} &= T^{\alpha\beta}v_\alpha v_\beta, \\
q^{\{v\}}_\alpha &= -P^{\{v\}\beta}{}_\alpha T_{\beta\mu}v^\mu, \\
S^{\{v\}}_{\alpha\beta} &= P^{\{v\}\mu}{}_\alpha P^{\{v\}\nu}{}_\beta T_{\mu\nu},
\end{aligned} \tag{2.43}$$

such that the trace and traceless parts of the stress tensor are respectively given by the pressure $p^{\{v\}}$, and anisotropic pressure $\pi^{\{v\}}_{\alpha\beta}$

$$\begin{aligned}
p^{\{v\}} &= \frac{1}{3}S^{\{v\}} = \frac{1}{3}P^{\{v\}\alpha\beta}S^{\{v\}}_{\alpha\beta} = \frac{1}{3}P^{\{v\}\mu\nu}T^{\{v\}}_{\mu\nu} = \frac{1}{3}\left(T + \rho^{\{v\}}\right), \\
\pi^{\{v\}}_{\alpha\beta} &= S^{\{v\}}_{\langle\alpha\beta\rangle} = S^{\{v\}}_{\alpha\beta} - P^{\{v\}}_{\alpha\beta}p^{\{v\}}.
\end{aligned} \tag{2.44}$$

The energy density $\rho^{\{v\}}$ is distinguished from the rest mass energy density $\varrho^{\{v\}}$ and its specific internal energy $\varepsilon^{\{v\}}$ as (Ellis, 2009)

$$\rho^{\{v\}} = \varrho^{\{v\}}\left(1 + \varepsilon^{\{v\}}\right) \qquad \text{with} \qquad \varrho^{\{v\}} = n^{\{v\}}m, \tag{2.45}$$

where $\varrho^{\{v\}}$ is expressed in terms of the particle number density $n^{\{v\}}$ and the rest average mass of the fluid particles m. The internal energy $\varepsilon^{\{v\}}$ and pressure $p^{\{v\}}$ together correspond to the thermodynamical total energy doing mechanical work as measured by the specific enthalpy of the fluid

$$h^{\{v\}} = 1 + \varepsilon^{\{v\}} + \frac{p^{\{v\}}}{\varrho^{\{v\}}}. \tag{2.46}$$

While v^μ is an arbitrary timelike vector, the fluid 4-velocity is denoted as u^μ which is used to define the particle flux (also called density current), $N^\alpha = \rho^{\{u\}}u^\alpha$, and entropy flux, S^α. Both N^α

and S^α have their own conservation equations: the conservation of current $\nabla_\alpha N^\alpha = 0$, also known as the continuity equation

$$\nabla_\mu \left(\rho^{\{u\}} u^\mu\right) = 0 \tag{2.47}$$

and the second law of thermodynamics $\nabla_\alpha S^\alpha \geqslant 0$. Should N^α be chosen as the observer this is called the particle frame. Another relevant frame that is always present and unique is the one provided by a vector E^α defined such that there is no energy flux $q_\alpha^{\{E\}} = 0$. This implies that the observer is at rest therefore this frame of reference is commonly called the energy or rest frame.

Should the fluid be a perfect fluid, the particle and energy frames are the same and are parallel to the entropy flux S^α (Bruni, Dunsby, and Ellis, 1992). In this case, the fluid flow has a unique 4-velocity u^α with $q_\alpha^{\{u\}} = \pi_{\alpha\beta}^{\{u\}} = 0$. The energy-stress tensor then only depends on the energy density $\rho^{\{u\}}$ and pressure $p^{\{u\}}$ that can be related through the equation of state. Should this be a barotropic fluid then it is expressed as

$$p^{\{u\}} = w\rho^{\{u\}}, \tag{2.48}$$

with $w = 0$ for dust, $w = 1/3$ for radiation, $w = -1$ for vacuum energy, and $w = 1$ for stiff matter[1]. For dust the energy-stress tensor is $T^{\mu\nu} = \rho^{\{u\}} u^\mu u^\nu$ where u^μ is its eigenvector with $\rho^{\{u\}}$ the eigenvalue. Should the coordinates be comoving with the fluid then the fluid flow and metric are related as $u^\alpha = g^{0\alpha}/\sqrt{|g^{00}|}$.

2.3.1 Kinematical rest-energy frame

The fluid flow 4-velocity u^α, corresponding to the energy frame/rest frame, is unique for perfect fluids and always present for imperfect fluids where one can opt for either the energy frame or the particle frame, see Bruni, Dunsby, and Ellis (1992) and Refs. therein. Physically, quantities that result from projecting tensors in this frame are unique[2], as they are rest-frame quantities, e.g. the energy density $\rho^{\{u\}}$. We, therefore, define a projection tensor specific to this fluid frame

$$h_{\mu\nu} = P_{\mu\nu}^{\{u\}} = g_{\mu\nu} + u_\alpha u_\beta. \tag{2.49}$$

The kinematics of the fluid flow can be established with the variation $\nabla_\nu u_\mu$. That is (Ellis and Elst, 1999; Ellis, 2009; Ellis, Maartens, and MacCallum, 2012) we can decompose $\nabla_\nu u_\mu$ in its irreducible parts Eq. (2.33) and Eq. (2.7)

$$\nabla_\nu u_\mu = \Theta_{\mu\nu} + \omega_{\mu\nu} - a_\mu u_\nu, \qquad \text{with} \qquad \begin{cases} \Theta_{\mu\nu} \equiv D_{(\mu}^{\{u\}} u_{\nu)} \\ \omega_{\mu\nu} \equiv D_{[\mu}^{\{u\}} u_{\nu]} \\ a^\mu \equiv u^\alpha \nabla_\alpha u^\mu = \dot{u}^\mu \end{cases} \tag{2.50}$$

where $\Theta_{\mu\nu}$ is the symmetric expansion tensor, $\omega_{\mu\nu}$ the anti-symmetric vorticity tensor and a^μ the 4-acceleration sourced by pressure gradients. We also define $\omega^2 = \omega_{\mu\nu}\omega^{\mu\nu}/2$ as the vorticity magnitude, and $\omega_\alpha = (D^{\{u\}} \times u)_\alpha/2 = \epsilon^{\{u\}}{}_{\alpha\mu\nu}\omega^{\mu\nu}/2$ as the vorticity vector which is essentially the

[1] Then of course, if there is no matter, only vacuum, $T_{\alpha\beta} = 0$.

[2] The same uniqueness applies in the case where there are different matter fields (Dunsby, Bruni, and Ellis, 1992), each with its own 4-velocity, as one can always define an average u^μ, say an average energy frame, or project tensorial quantities with respect to a specific u^μ, for instance that of pressureless matter, i.e. dust.

curl of the fluid velocity u^μ. Note that should vorticity be present, then it is not possible to create a smooth hypersurface orthogonal to the fluid flow $h_{\alpha\beta}$, then u^α in the expressions above would not correspond to the fluid flow, see the Appendix in Ellis, Bruni, and Hwang (1990). While each point of the spacetime may have its own local tangent space orthogonal to the vector field u^μ, the collection of these spaces only creates an integrable hypersurface if there is no vorticity. This can be avoided if instead of the local fluid velocity, one considers its average to create a smooth hypersurface.

The expansion tensor can be decomposed into its trace $\Theta = h^{\mu\nu}\Theta_{\mu\nu}$ and traceless part $\sigma_{\mu\nu} = \Theta_{\langle\mu\nu\rangle}$ Eq. (2.26), with $h_{\alpha\beta}$

$$\Theta_{\mu\nu} = \frac{1}{3}h_{\mu\nu}\Theta + \sigma_{\mu\nu}, \tag{2.51}$$

i.e. the expansion scalar $\Theta = D^{\{u\}}_\mu u^\mu = \nabla_\mu u^\mu$, because $u_\nu a^\nu = 0$, and the shear tensor $\sigma_{\mu\nu}$ with its magnitude defined as

$$2\sigma^2 = \sigma_{\mu\nu}\sigma^{\mu\nu} = \Theta_{\alpha\beta}\Theta^{\alpha\beta} - \frac{1}{3}\Theta^2. \tag{2.52}$$

Considering Eq. (2.15) and $h > 0$ as the determinant of $h_{\alpha\beta}$, the expansion scalar corresponds to the rate of change of the local fluid volume element

$$\Theta = \frac{1}{\sqrt{h}}\frac{\partial}{\partial x^\mu}\left(\sqrt{h}u^\mu\right) = \frac{\dot{V}}{V} \tag{2.53}$$

where $V = \sqrt{h}$. The expansion tensor used to quantify scale variations can also be expressed using variations to a relative distance $\delta l^{\{e\}}$ in the direction of the vector e^α:

$$\frac{\dot{\delta l^{\{e\}}}}{\delta l^{\{e\}}} = \frac{1}{3}\Theta + \sigma_{\alpha\beta}e^\alpha e^\beta. \tag{2.54}$$

2.4 Constraint & evolution equations of a perfect fluid

The constraint and evolution equations governing the fluid can all be derived from projecting key equations along or orthogonally to the fluid flow. Namely the conservation equation Eq. (2.40), the Ricci identity Eq. (2.18) applied to the fluid flow u^α, and Einstein's field equations Eq. (2.39) all projected in accordance to the description of Section 2.1.4. Here we will only express these equations for a perfect fluid in the particle flow frame, omitting all terms that include energy flux $q^{\{u\}}_\alpha$, and anisotropic pressure $\pi^{\{u\}}_{\alpha\beta}$.

2.4.1 Conservation equations

The first set of evolution equations comes from the conservation equations Eq. (2.40) (Ellis, Maartens, and MacCallum, 2012). One obtains the energy conservation and the momentum conservation equations by projecting Eq. (2.40) along and orthogonally to u^μ, respectively. So the energy conservation equation is obtained by expanding $u_\beta\nabla_\alpha T^{\alpha\beta} = 0$ and substituting with the fluid kinematical terms

$$\dot{\rho}^{\{u\}} + \left(\rho^{\{u\}} + p^{\{u\}}\right)\Theta = 0, \tag{2.55}$$

which provides the evolution equation of the energy density $\rho^{\{u\}}$. Then the momentum conservation equation is similarly obtained from $h^\mu{}_\beta\nabla_\alpha T^{\alpha\beta} = 0$

$$\left(\rho^{\{u\}} + p^{\{u\}}\right)a^\mu + D^{\{u\}\mu}p^{\{u\}} = 0, \tag{2.56}$$

which provides the evolution equation of the pressure $p^{\{u\}}$ simply indicating that the fluid only accelerates within the fluid frame if there is a pressure gradient, otherwise the fluid moves along geodesics.

2.4.2 Ricci identity

The next set of equations comes from the Ricci identity, Eq. (2.18), applied to the fluid flow 4-velocity u^α. Projecting with u^ν and then contracting α and μ, Eq. (2.18) can be simplified to obtain the Raychaudhuri equation (Raychaudhuri, 1955)

$$\dot{\Theta} + \frac{1}{3}\Theta^2 + 2(\sigma^2 - \omega^2) - \nabla_\alpha a^\alpha + \frac{\kappa}{2}\left(\rho^{\{u\}} + 3p^{\{u\}}\right) - \Lambda = 0, \tag{2.57}$$

which corresponds to the evolution equation of the expansion of the fluid. The Ricci tensor $R_{\alpha\beta}$ was replaced with fluid terms from Einstein's field equations Eq. (2.39). The presence of Einstein's gravitational constant κ and the cosmological constant Λ makes it evident that Einstein's field equations were used in the derivation.

Again projecting Eq. (2.18) with u^ν, then taking its spatial part, i.e. projecting with $h^\mu{}_\omega h^\beta{}_\alpha$, and substituting the Riemann tensor with the Weyl and Ricci tensors and scalar Eq. (2.24), the resulting expression can be split into a symmetric and anti-symmetric expression (Bruni, 1991; Ellis, Maartens, and MacCallum, 2012). The traceless part of the symmetric expression provides the evolution equation of the shear

$$\begin{aligned} &h^\mu{}_\alpha h^\nu{}_\beta \dot{\sigma}_{\mu\nu} - D^{\{u\}}_{(\alpha} a_{\beta)} - a_\alpha a_\beta + \omega_\alpha\omega_\beta + \sigma_{\alpha\mu}\sigma^\mu{}_\beta + \tfrac{2}{3}\Theta\sigma_{\alpha\beta} \\ &+\tfrac{1}{3}h_{\alpha\beta}\left(\nabla_\mu a^\mu - 2\sigma^2 - \omega^2\right) + C_{\alpha\mu\beta\nu}u^\mu u^\nu = 0. \end{aligned} \tag{2.58}$$

While the anti-symmetric part provides the evolution equation of the vorticity

$$h^\alpha{}_\mu \dot{\omega}^\mu + \frac{2}{3}\Theta\omega^\alpha - \sigma^{\alpha\mu}\omega_\mu - \frac{1}{2}\epsilon^{\{u\}\alpha\mu\nu}\nabla_\mu a_\nu = 0, \tag{2.59}$$

which can emerge only if there is acceleration.

2.4.3 Einstein's field equations

The last set of equations comes from Einstein's field equations Eq. (2.39). These require the 3-dimensional Ricci tensor and scalar, ${}^{(3)}R_{\alpha\beta}$ and ${}^{(3)}R$ respectively, of the spatial hypersurface $h_{\mu\nu}$ Eq. (2.49), see Section 2.1.4.4 and Section 3.1.1. If vorticity is present, it is not possible to create a smooth hypersurface orthogonal to the fluid flow. So here expressions are given in the vorticity free case, as well as perfect fluid, so $\omega^{\{u\}}_{\alpha\beta} = q^{\{u\}}_\alpha = \pi^{\{u\}}_{\alpha\beta} = 0$. While the spatial information from $R_{\alpha\beta}$ is retained in the intrinsic curvature ${}^{(3)}R_{\alpha\beta}$, the temporal information is kept in the extrinsic curvature, which in the case of this hypersurface orthonormal fluid corresponds to the expansion tensor $\Theta_{\alpha\beta} = \frac{1}{2}\mathcal{L}_u h_{\alpha\beta}$ (with a sign change). The derivation of these expressions requires the Gauss-Codazzi equations Eq. (3.25) and Eq. (3.26) that come from the Ricci identity and are introduced in Section 3.1.1 so as an over-simplification, for now, let us consider $G_{\alpha\beta} + \Lambda g_{\alpha\beta} - \kappa T_{\alpha\beta} = 0$ and project it with the three different types of projections along and orthogonally to the fluid flow

❖ $(G_{\alpha\beta} + \Lambda g_{\alpha\beta} - \kappa T_{\alpha\beta})\, u^\alpha u^\beta = 0$ is the Hamiltonian constraint equation,

$$ {}^{(3)}R + \frac{2}{3}\Theta^2 - 2\sigma^2 = 2\kappa\rho^{\{u\}} + 2\Lambda \tag{2.60} $$

❖ $h^\beta{}_\alpha\,(G_{\beta\mu} + \Lambda g_{\beta\mu} - \kappa T_{\beta\mu})\, u^\mu = 0$ are the Momentum constraint equations,

$$ \frac{2}{3}D^{\{u\}}_\alpha\Theta - D^{\{u\}}_\beta\sigma_\alpha{}^\beta = 0 \tag{2.61} $$

❖ and $h^\mu{}_\alpha h^\nu{}_\beta\,(G_{\mu\nu} + \Lambda g_{\mu\nu} - \kappa T_{\mu\nu}) = 0$ are the evolution equations,

$$ h^\mu{}_\alpha h^\nu{}_\beta\dot{\Theta}_{\mu\nu} + \Theta_{\alpha\beta}\Theta + {}^{(3)}R_{\alpha\beta} = \nabla_\alpha a_\beta + \Lambda h_{\alpha\beta} + \frac{\kappa}{2}h_{\alpha\beta}\left(\rho^{\{u\}} - p^{\{u\}}\right). \tag{2.62} $$

This naturally has a strong resemblance with the Raychaudhuri equation Eq. (2.57) without vorticity (by taking the trace and replacing ${}^{(3)}R$ with the Hamiltonian constraint) since Einstein's field equations are evolution equations for the spacetime and $h_{\alpha\beta}$ evolves according to $\mathcal{L}_u h_{\alpha\beta} = 2\Theta_{\alpha\beta}$ and $\Theta_{\alpha\beta}$ evolves according to Eq. (2.62).

2.4.4 Irrotational dust perfect fluid

The type of fluid used in this thesis is an irrotational dust perfect fluid. This is described as pressureless matter and this means that $p^{\{u\}} = q^{\{u\}}_\alpha = \pi^{\{u\}}_{\alpha\beta} = 0$ simplifying the energy-momentum tensor to $T_{\alpha\beta} = \rho^{\{u\}}u_\alpha u_\beta$. Having no pressure the fluid has no acceleration $a^\mu = 0$, fluid elements move along geodesics, and choosing the fluid to have no initial vorticity, its evolution equation Eq. (2.59) shows that it will not grow if it is not present. The constraint equations, Eq. (2.60) and Eq. (2.61), are the same while the non-trivial evolution equations that remain are then the energy conservation which coincides with the continuity equation Eq. (2.47)

$$ \dot{\rho}^{\{u\}} + \rho^{\{u\}}\Theta = 0, \tag{2.63} $$

and the evolution equations of the expansion Eq. (2.62)

$$ h^\mu{}_\alpha h^\nu{}_\beta\dot{\Theta}_{\mu\nu} + \Theta_{\alpha\beta}\Theta + {}^{(3)}R_{\alpha\beta} = \Lambda h_{\alpha\beta} + \frac{\kappa}{2}h_{\alpha\beta}\rho^{\{u\}}. \tag{2.64} $$

Which can be split into its trace, and traceless parts providing the Raychaudhuri equation Eq. (2.57)

$$ \dot{\Theta} + \frac{1}{3}\Theta^2 + 2\sigma^2 + \frac{\kappa}{2}\rho^{\{u\}} - \Lambda = 0, \tag{2.65} $$

and the shear evolution equation Eq. (2.58)

$$ h^\mu{}_\alpha h^\nu{}_\beta\dot{\sigma}_{\mu\nu} + \sigma_{\alpha\mu}\sigma^\mu{}_\beta + \frac{2}{3}\left(\Theta\sigma_{\alpha\beta} - h_{\alpha\beta}\sigma^2\right) + C_{\alpha\mu\beta\nu}u^\mu u^\nu = 0. \tag{2.66} $$

Notice that the source term here depends on the Weyl tensor $C_{\alpha\mu\beta\nu}$ which is absent in Eq. (2.64) which instead has the local curvature term ${}^{(3)}R_{\alpha\beta}$. This is because in this form it is derived from the Ricci identity following the logic described in Section 2.4.2 and not Eq. (2.64).

The continuity equation Eq. (2.63) with Eq. (2.53) can simply be integrated to give the conservation of proper mass M

$$ \rho^{\{u\}}V = M \tag{2.67} $$

where M is the proper mass of the local fluid element. An integral of this quantity in a given coordinate domain will give the proper mass contained within that domain, see Appendix D.

2.5 Weyl tensor

Now, let us focus on the information contained in $C_{\alpha\beta\mu\nu}$ Eq. (2.24) (Weyl, 1918). This tensor is traceless and has the same symmetries as the Riemann tensor, Eq. (2.20) and Eq. (2.21), and so possesses 10 independent components. In this section, we will consider two methods of extracting information from the Weyl tensor. The first is described in Section 2.5.1 and is based on projecting $C_{\alpha\beta\mu\nu}$ along a chosen timelike vector by analogy to electromagnetism (Maxwell, 1865), this will be the gravito-electromagnetic decomposition creating two rank 2 spatial symmetric and traceless tensors, each with 5 independent components. The second, discussed in Section 2.5.2, is based on projecting it along a null tetrad base according to the Newmann-Penrose (NP) formalism, providing the five complex Weyl scalars.

By the nature of these decompositions, the resulting quantities will depend on the metric coordinates and the projection frame used. We will see that in specific frames, the fluid frame for gravito-electromagnetism and the principal null directions for the Weyl scalars, these quantities will take particular physical meanings. While they remain coordinate-variant, and coordinate and frame-dependent, they can be used to construct coordinate-invariant, and coordinate and frame-independent quantities which will inform on the nature of the spacetime with the Petrov classification.

2.5.1 Gravito-electromagnetism

By projecting the Weyl tensor with an arbitrary timelike unit vector, say v^μ, the Weyl tensor can be decomposed into its electric and magnetic parts (Matte, 1953; Jordan et al., 1964; Hawking, 1966):

$$E^{\{v\}}_{\alpha\mu} = v^\beta v^\nu C_{\alpha\beta\mu\nu}, \qquad B^{\{v\}}_{\alpha\mu} = v^\beta v^\nu C^*_{\alpha\beta\mu\nu}, \tag{2.68}$$

where $C^*_{\alpha\beta\mu\nu} = \frac{1}{2} C_{\alpha\beta\lambda\sigma}\epsilon^{\lambda\sigma}{}_{\mu\nu}$ is the dual of the Weyl tensor. Note that these tensors depend on the choice of projection vector v^α and as such are frame dependent hence the $\{v\}$ superscript, see Section 2.1.4. We define their magnitude as $E^{\{v\}2} \equiv E^{\{v\}\alpha\beta}E^{\{v\}}_{\alpha\beta}$ and $B^{\{v\}2} \equiv B^{\{v\}\alpha\beta}B^{\{v\}}_{\alpha\beta}$.

Since the Weyl tensor is traceless and based on the symmetries of the Riemann tensor Eq. (2.20), $E^{\{v\}}_{\alpha\beta}$ and $B^{\{v\}}_{\alpha\beta}$ are then symmetric and traceless, and based on their definition Eq. (2.68), they are covariantly purely spatial, i.e. they live on a 3-dimensional space orthonormal to the chosen timelike vector:

$$v^\alpha E^{\{v\}}_{\alpha\mu} = 0, \qquad v^\alpha B^{\{v\}}_{\alpha\mu} = 0. \tag{2.69}$$

In particular for $B^{\{v\}}_{\alpha\mu}$ the trace vanishes due to the first Bianchi identity Eq. (2.21). In synchronous coordinates (where $g_{0\mu} = \{-1, 0, 0, 0\}$), and with $v^\mu = \{1, 0, 0, 0\}$ the specific expression is

$$R_{1023} - R_{2013} + R_{3012} = 0 \tag{2.70}$$

we will use this explicitly in Section 5.3.2.3.

A useful complex linear combination of $E^{\{v\}}_{\alpha\beta}$ and $B^{\{v\}}_{\alpha\beta}$ and its complex conjugate are

$$\begin{aligned} Q^{\{v\}}_{\alpha\beta} &= E^{\{v\}}_{\alpha\beta} + iB^{\{v\}}_{\alpha\beta}, \\ \overline{Q}^{\{v\}}_{\alpha\beta} &= 4v^\beta v^\nu \widetilde{C}_{\alpha\beta\mu\nu} = E^{\{v\}}_{\alpha\beta} - iB^{\{v\}}_{\alpha\beta}, \end{aligned} \tag{2.71}$$

where we use the complex self dual Weyl tensor $\widetilde{C}_{\alpha\beta\mu\nu} = \frac{1}{4}(C_{\alpha\beta\mu\nu} - iC^*_{\alpha\beta\mu\nu})$.

If one already has $E^{\{v\}}_{\alpha\beta}$ and $B^{\{v\}}_{\alpha\beta}$ but not the Weyl tensor $C_{\alpha\beta\mu\nu}$ itself and would rather have $E^{\{u\}}_{\alpha\beta}$ and $B^{\{u\}}_{\alpha\beta}$ projected along the fluid flow u^μ (a natural frame in cosmology), as will be the case in Section 5.1.2, then $C_{\alpha\beta\mu\nu}$ can be constructed using (Alcubierre, 2008)

$$C_{\alpha\beta\mu\nu} = 2\left(l_{\alpha[\mu}E^{\{v\}}_{\nu]\beta} - l_{\beta[\mu}E^{\{v\}}_{\nu]\alpha} - v_{[\mu}B^{\{v\}}_{\nu]\lambda}\epsilon^{\{v\}\lambda}{}_{\alpha\beta} - v_{[\alpha}B^{\{v\}}_{\beta]\lambda}\epsilon^{\{v\}\lambda}{}_{\mu\nu}\right), \tag{2.72}$$

with $l_{\mu\nu} = g_{\mu\nu} + 2v_\mu v_\nu$. Then, projecting along the fluid flow we get:

$$E^{\{u\}}_{\alpha\mu} = u^\beta u^\nu C_{\alpha\beta\mu\nu}, \qquad B^{\{u\}}_{\alpha\mu} = u^\beta u^\nu C^*_{\alpha\beta\mu\nu}, \tag{2.73}$$

and from these we obtain their magnitudes $E^{\{u\}2}$ and $B^{\{u\}2}$ in the fluid frame, c.f. (King and Ellis, 1973; Bruni, Dunsby, and Ellis, 1992; Bini, Carini, and Jantzen, 1995).

$E^{\{u\}}_{\alpha\beta}$ and $B^{\{u\}}_{\alpha\beta}$ represent the non-local gravitational tidal effects: if we think of the Riemann curvature tensor as made up of the Ricci and Weyl parts, as in Eq. (2.24), then the Ricci part is directly determined locally by the matter distribution through Einstein's field equations, Eq. (2.39), while the Weyl part can only be determined once the field equations are solved for the metric. $E^{\{u\}}_{\alpha\beta}$ and $B^{\{u\}}_{\alpha\beta}$ can then later be expressed in terms of the matter field with their divergence and curl presented in a Maxwell-like[3] form by using the second Bianchi identity, Eq. (2.21), the Ricci identity, Eq. (2.18) (applied to u^α), and Einstein's field equations, Eq. (2.39), to substitute for the Ricci tensor (Hawking, 1966; Wainwright and Ellis, 1997; Maartens and Bassett, 1998; Danehkar, 2009; Ellis, 2009; Ellis, Maartens, and MacCallum, 2012; Danehkar, 2022). For an irrotational dust perfect fluid the electric and magnetic parts are:

$$\begin{aligned} E^{\{u\}}_{\alpha\beta} &= -h^\mu{}_\alpha h^\nu{}_\beta \dot{\sigma}_{\mu\nu} - \sigma_{\alpha\mu}\sigma^\mu{}_\beta - \frac{2}{3}\left(\Theta\sigma_{\alpha\beta} + h_{\alpha\beta}\sigma^2\right), \\ B^{\{u\}}_{\alpha\beta} &= \left(D^{\{u\}} \times \sigma\right)_{\alpha\beta}, \end{aligned} \tag{2.74}$$

where the first of these equations actually corresponds to the shear evolution equation Eq. (2.66). Indeed, a key quantity in these expressions is the shear $\sigma_{\alpha\beta}$, since it is present in every term. Should shear be absent, the presence of an electric part of the Weyl tensor would then make it appear. The magnetic part is simply the curl of the shear, see Section 2.1.4.3. Since the curl of a scalar is zero, $B^{\{u\}}_{\alpha\beta}$, is solely sourced by purely vectorial or tensorial quantities. We finally note that if there is no magnetic part, the spacetime can be evolved only with ordinary differential equations (instead of partial) (Bruni, Matarrese, and Pantano, 1995b; Bolejko, 2018).

Then the divergence and curl of $E^{\{u\}}_{\alpha\beta}$ and $B^{\{u\}}_{\alpha\beta}$ are

$$\begin{aligned} D^{\{u\}\mu}E^{\{u\}}_{\alpha\mu} &= \frac{1}{3}D^{\{u\}}_\alpha\rho^{\{u\}} + \epsilon^{\{u\}}_{\alpha\mu\nu}\sigma^\mu{}_\beta B^{\{u\}\nu\beta}, \\ D^{\{u\}\mu}B^{\{u\}}_{\alpha\mu} &= -\epsilon^{\{u\}}_{\alpha\mu\nu}\sigma^\mu{}_\beta E^{\{u\}\nu\beta}, \\ \dot{E}^{\{u\}}_{\alpha\beta} - \left(D^{\{u\}} \times B^{\{u\}}\right)_{\alpha\beta} &= -\Theta E^{\{u\}}_{\alpha\beta} + 3\sigma_{\mu\langle\alpha}E^{\{u\}\mu}_{\beta\rangle} - \frac{1}{2}\rho^{\{u\}}\sigma_{\alpha\beta}, \\ \dot{B}^{\{u\}}_{\alpha\beta} + \left(D^{\{u\}} \times E^{\{u\}}\right)_{\alpha\beta} &= -\Theta B^{\{u\}}_{\alpha\beta} + 3\sigma_{\mu\langle\alpha}B^{\{u\}\mu}_{\beta\rangle}. \end{aligned} \tag{2.75}$$

[3] Further electromagnetic analogies can be pursued with the Bel-Robinson tensor (Bel, 1958; Maartens and Bassett, 1998).

See Eq. (2.26) for the traceless operator $A_{\langle\alpha\beta\rangle}$. Here again, we can see that the shear $\sigma_{\alpha\beta}$ is a crucial quantity but notable features are that the divergence of the electric part is also given by the energy density gradient, which in general will be a stronger effect than the shear, and the evolution of $E^{\{u\}}_{\alpha\beta}$ and $B^{\{u\}}_{\alpha\beta}$ are both strongly impacted by the expansion of the fluid.

2.5.2 Weyl scalars

An alternative method to decompose the Weyl tensor $C_{\alpha\beta\mu\nu}$ is with the Newman-Penrose (NP) formalism (Newman and Penrose, 1962; Stephani et al., 2003; Alcubierre, 2008; Shibata, 2015) which projects it with a null tetrad base to create the five complex Weyl scalars: Ψ_0, Ψ_1, Ψ_2, Ψ_3, and Ψ_4.

To obtain these, we will first present how to create a null tetrad base, starting by defining a set of four vectors:

$$v_0{}^\alpha = v^\alpha, \quad v_1{}^\alpha = \delta^\alpha{}_1/\sqrt{P^{\{v\}}_{11}}, \quad v_2{}^\alpha = \delta^\alpha{}_2/\sqrt{P^{\{v\}}_{22}}, \quad v_){}^\alpha = \delta^\alpha{}_3/\sqrt{P^{\{v\}}_{33}}, \tag{2.76}$$

where v^α is a unit timelike vector, that can be freely chosen and $P^{\{v\}}_{\alpha\beta}$ its projection tensor Eq. (2.25). This set of vectors are made orthonormal with the Gram-Schmidt method to obtain $\mathbf{e}_{(\alpha)}$, our orthonormal tetrad basis. We start this procedure by choosing $e_{(0)}{}^\alpha = v_0{}^\alpha = v^\alpha$ without normalising it such that it remains timelike. Then the Gram-Schmidt scheme makes the other vectors all orthogonal to $e_{(0)}{}^\alpha$ and each other with a spacelike normalisation. We distinguish tetrad indices with parenthesis and these are raised or lowered with the Minkowski metric $\eta_{\alpha\beta} = diag(-1,\ 1,\ 1,\ 1)$. As they are orthonormal they have the properties:

$$e_{(0)}{}^\alpha e^{(0)}{}_\alpha = -1, \quad e_{(i)}{}^\alpha e^{(i)}{}_\beta = \delta^\alpha{}_\beta, \quad e_{(i)}{}^\alpha e^{(j)}{}_\alpha = \delta^{(j)}{}_{(i)}, \quad e_{(0)}{}^\alpha e^{(j)}{}_\alpha = 0. \tag{2.77}$$

They span the metric as $g_{\alpha\beta} = -e_{(0)\alpha}e_{(0)\beta} + P^{\{v\}}_{\alpha\beta}$ where the projection tensor can be expressed as $P^{\{v\}}_{\alpha\beta} = \delta^{(i)(j)}e_{(i)\alpha}e_{(j)\beta}$ and $e_{(1)}{}^1 e_{(2)}{}^2 e_{(3)}{}^3 = det\left(P^{\{v\}}_{ij}\right)^{-1/2}$.

From these, four complex null vectors are defined [4]:

$$\begin{aligned} l^\alpha &= \left(e_{(0)}{}^\alpha + e_{(1)}{}^\alpha\right)/\sqrt{2}, \quad & k^\alpha &= \left(e_{(0)}{}^\alpha - e_{(1)}{}^\alpha\right)/\sqrt{2}, \\ m^\alpha &= \left(e_{(2)}{}^\alpha + ie_{(3)}{}^\alpha\right)/\sqrt{2}, \quad & \overline{m}^\alpha &= \left(e_{(2)}{}^\alpha - ie_{(3)}{}^\alpha\right)/\sqrt{2}, \end{aligned} \tag{2.78}$$

together referred to as a null NP tetrad corresponding to our null tetrad base. By definition their norm is zero, and while $l_\alpha k^\alpha = -m_\alpha \overline{m}^\alpha = -1$ all other combinations vanish. They span the metric as

$$g_{\alpha\beta} = -2l_{(\alpha}k_{\beta)} + 2m_{(\alpha}\overline{m}_{\beta)}. \tag{2.79}$$

Finally, this null tetrad base is used to project the Weyl tensor and obtain the Weyl scalars, defined as:

$$\begin{aligned} \Psi_0 &\equiv C_{\alpha\beta\mu\nu}l^\alpha m^\beta l^\mu m^\nu = \overline{Q}^{\{v\}}_{\alpha\beta} m^\alpha m^\beta \\ \Psi_1 &\equiv C_{\alpha\beta\mu\nu}l^\alpha k^\beta l^\mu m^\nu = -\overline{Q}^{\{v\}}_{\alpha\beta} m^\alpha e_{(1)}{}^\beta/\sqrt{2} \\ \Psi_2 &\equiv C_{\alpha\beta\mu\nu}l^\alpha m^\beta \overline{m}^\mu k^\nu = \overline{Q}^{\{v\}}_{\alpha\beta} e_{(1)}{}^\alpha e_{(1)}{}^\beta/2 = -\overline{Q}^{\{n\}}_{\alpha\beta} m^\alpha \overline{m}^\beta \\ \Psi_3 &\equiv C_{\alpha\beta\mu\nu}l^\alpha k^\beta \overline{m}^\mu k^\nu = \overline{Q}^{\{v\}}_{\alpha\beta} \overline{m}^\alpha e_{(1)}{}^\beta/\sqrt{2} \\ \Psi_4 &\equiv C_{\alpha\beta\mu\nu}k^\alpha \overline{m}^\beta k^\mu \overline{m}^\nu = \overline{Q}^{\{v\}}_{\alpha\beta} \overline{m}^\alpha \overline{m}^\beta, \end{aligned} \tag{2.80}$$

[4] Here we use Alcubierre's notation in Alcubierre (2008), the l^α and k^α vectors are swapped in comparison to the notation in Stephani et al. (2003).

where in the second equalities, the Ψs are related to $E^{\{v\}}_{\alpha\beta}$ and $B^{\{v\}}_{\alpha\beta}$ via $\overline{Q}^{\{v\}}_{\alpha\beta}$. Clearly, by construction, the Ψs are frame dependent, based on the choice of null tetrad whose construction was based on v^α. To express them as a function of $\overline{Q}^{\{v\}}_{\alpha\beta}$, we use Maple (Maplesoft, 2019) to substitute the Weyl tensor with Eq. (2.72) and make simplifications based on the tetrad and null vector properties, as well as ${e_{(0)}}^\alpha {e_{(1)}}^\beta m^\mu \bar{m}^\nu \epsilon_{\alpha\beta\mu\nu} = {e_{(1)}}^\beta m^\mu \bar{m}^\nu \epsilon_{\beta\mu\nu} = -i$, meaning that : ${e_{(1)}}^\beta m^\mu \epsilon_{\beta\mu\nu} = -i m_\nu$ and ${e_{(1)}}^\beta \bar{m}^\nu \epsilon_{\beta\mu\nu} = -i\bar{m}_\mu$ (Shibata, 2015).

Conversely, with the Weyl scalars one can express $\overline{Q}^{\alpha\beta\{v\}}$ by projecting Eq. (3.58) of (Stephani et al., 2003) along v^μ, obtaining (Barnes and Rowlingson, 1989; Stephani et al., 2003; Cherubini et al., 2004)

$$\begin{aligned}\overline{Q}^{\{v\}\alpha\beta} =& \Psi_2 e_C^{\alpha\beta} \\ &+ \frac{1}{2}(\Psi_0 + \Psi_4) e_{T+}^{\alpha\beta} - \frac{i}{2}(\Psi_0 - \Psi_4) e_{T\times}^{\alpha\beta} \\ &- 2(\Psi_1 - \Psi_3) e_{(1)}{}^{(\alpha} e_{(2)}{}^{\beta)} + 2i(\Psi_1 + \Psi_3) e_{(1)}{}^{(\alpha} e_{(3)}{}^{\beta)}.\end{aligned} \tag{2.81}$$

To build intuition on this expression, consider a spherical frame, ${e_{(0)}}^\alpha = v^\alpha$ is in the temporal direction, ${e_{(1)}}^\alpha$ would radially be pointing outward giving the longitudinal direction, and ${e_{(2)}}^\alpha$ and ${e_{(3)}}^\alpha$ along with m^α and $\bar{m}^\alpha$ would be the angular transverse directions. Thus Ψ_2 is the component on the Coulombian basis tensor

$$e_C^{\alpha\beta} = 3{e_{(1)}}^\alpha {e_{(1)}}^\beta - P^{\{v\}\alpha\beta} = 2{e_{(1)}}^\alpha {e_{(1)}}^\beta - {e_{(2)}}^\alpha {e_{(2)}}^\beta - {e_{(3)}}^\alpha {e_{(3)}}^\beta, \tag{2.82}$$

Ψ_0 and Ψ_4 are the components of the two transverse basis tensors

$$e_{T+}^{\alpha\beta} = {e_{(2)}}^\alpha {e_{(2)}}^\beta - {e_{(3)}}^\alpha {e_{(3)}}^\beta \quad \text{and} \quad e_{T\times}^{\alpha\beta} = 2{e_{(2)}}^{(\alpha} {e_{(3)}}^{\beta)} \tag{2.83}$$

Ψ_1 and Ψ_3 are the components on the two longitudinal basis tensors ${e_{(1)}}^{(\alpha} {e_{(2)}}^{\beta)}$ and ${e_{(1)}}^{(\alpha} {e_{(3)}}^{\beta)}$.

One can then express $E^{\{v\}\alpha\beta}$ and $B^{\{v\}\alpha\beta}$ using the Weyl scalars, as components on the above-defined tetrad basis, by using Eq. (2.71) and its complex conjugate taking the real $\Re$ and imaginary $\Im$ parts:

$$\begin{aligned}E^{\{v\}\alpha\beta} =& \Re(\Psi_2) e_C^{\alpha\beta} \\ &+ \frac{1}{2}\Re(\Psi_0 + \Psi_4) e_{T+}^{\alpha\beta} + \frac{1}{2}\Im(\Psi_0 - \Psi_4) e_{T\times}^{\alpha\beta} \\ &- 2\Re(\Psi_1 - \Psi_3) {e_{(1)}}^{(\alpha} {e_{(2)}}^{\beta)} - 2\Im(\Psi_1 + \Psi_3) {e_{(1)}}^{(\alpha} {e_{(3)}}^{\beta)},\end{aligned} \tag{2.84}$$

$$\begin{aligned}B^{\{v\}\alpha\beta} =& -\Im(\Psi_2) e_C^{\alpha\beta} \\ &- \frac{1}{2}\Im(\Psi_0 + \Psi_4) e_{T+}^{\alpha\beta} + \frac{1}{2}\Re(\Psi_0 - \Psi_4) e_{T\times}^{\alpha\beta} \\ &+ 2\Im(\Psi_1 - \Psi_3) {e_{(1)}}^{(\alpha} {e_{(2)}}^{\beta)} - 2\Re(\Psi_1 + \Psi_3) {e_{(1)}}^{(\alpha} {e_{(3)}}^{\beta)}.\end{aligned}$$

Note that $\overline{Q}^{\{v\}\alpha\beta}$, $E^{\{v\}\alpha\beta}$ and $B^{\{v\}\alpha\beta}$ are defined in terms of a generic v^μ frame, therefore the expressions in Eq. (2.81) and Eq. (2.84) are valid in any orthonormal frame with timelike vector ${e_{(0)}}^\mu = v^\mu$.

2.5.2.1 Null tetrad rotation

As the Ψs are frame dependent we may want to identify the frame that maximises the independence between the different scalars, i.e. the frame where the most number of Ψs vanish, this null tetrad frame is referred to as the principal null directions. There are three different types of null tetrad frame rotations available to find them.

- **Class I:** Using the complex scalar a and its complex conjugate, the frame is rotated such that l^α and Ψ_0 remain intact:

$$\begin{aligned} l^\alpha &\to l^\alpha & \Psi_0 &\to \Psi_0 \\ k^\alpha &\to k^\alpha + a\bar{a}l^\alpha & \Psi_1 &\to \Psi_1 + \bar{a}\Psi_0 \\ &\quad + \bar{a}m^\alpha + a\bar{m}^\alpha & \Psi_2 &\to \Psi_2 + 2\bar{a}\Psi_1 + \bar{a}^2\Psi_0 \\ m^\alpha &\to m^\alpha + al^\alpha & \Psi_3 &\to \Psi_3 + 3\bar{a}\Psi_2 + 3\bar{a}^2\Psi_1 + \bar{a}^3\Psi_0 \\ \bar{m}^\alpha &\to \bar{m}^\alpha + \bar{a}l^\alpha & \Psi_4 &\to \Psi_4 + 4\bar{a}\Psi_3 + 6\bar{a}^2\Psi_2 + 4\bar{a}^3\Psi_1 + \bar{a}^4\Psi_0 \end{aligned} \tag{2.85}$$

- **Class II:** Using the complex scalar b and its complex conjugate, the frame is rotated such that k^α and Ψ_4 remain intact:

$$\begin{aligned} l^\alpha &\to l^\alpha + b\bar{b}k^\alpha & \Psi_0 &\to \Psi_0 + 4b\Psi_1 + 6b^2\Psi_2 + 4b^3\Psi_3 + b^4\Psi_4 \\ &\quad + \bar{b}m^\alpha + b\bar{m}^\alpha & \Psi_1 &\to \Psi_1 + 3b\Psi_2 + 3b^2\Psi_3 + b^3\Psi_4 \\ k^\alpha &\to k^\alpha & \Psi_2 &\to \Psi_2 + 2b\Psi_3 + b^2\Psi_4 \\ m^\alpha &\to m^\alpha + bk^\alpha & \Psi_3 &\to \Psi_3 + b\Psi_4 \\ \bar{m}^\alpha &\to \bar{m}^\alpha + \bar{b}k^\alpha & \Psi_4 &\to \Psi_4 \end{aligned} \tag{2.86}$$

- **Class III:** Using the real scalars λ and θ, the frame is rotated such that the l^α and k^α directions and Ψ_2 remain intact:

$$\begin{aligned} l^\alpha &\to \lambda^{-1}l^\alpha & \Psi_0 &\to \lambda^2 e^{2i\theta}\Psi_0 \\ k^\alpha &\to \lambda k^\alpha & \Psi_1 &\to \lambda e^{i\theta}\Psi_1 \\ m^\alpha &\to e^{i\theta}m^\alpha & \Psi_2 &\to \Psi_2 \\ \bar{m}^\alpha &\to e^{-i\theta}\bar{m}^\alpha & \Psi_3 &\to \lambda^{-1}e^{i\theta}\Psi_3 \\ & & \Psi_4 &\to \lambda^{-2}e^{-2i\theta}\Psi_4 \end{aligned} \tag{2.87}$$

The class I and II rotations can easily be used to cancel certain Ψs, while the class III rotation does not give this possibility as clearly. For example, using a class I or II rotation where $\bar{a}$ or b is the root of the complex 4^{th} order polynomial

$$\begin{gathered} \Psi_4 + 4\bar{a}\Psi_3 + 6\bar{a}^2\Psi_2 + 4\bar{a}^3\Psi_1 + \bar{a}^4\Psi_0 = 0 \\ \text{or} \\ \Psi_0 + 4b\Psi_1 + 6b^2\Psi_2 + 4b^3\Psi_3 + b^4\Psi_4 = 0 \end{gathered} \tag{2.88}$$

gives the new $\hat{\Psi}$s that have $\hat{\Psi}_4 = 0$ or $\hat{\Psi}_0 = 0$ respectively. Then using class II or I where b or $\bar{a}$ is the root of the complex 2^{nd} order polynomial

$$\begin{gathered} \hat{\Psi}_1 + 3b\hat{\Psi}_2 + 3b^2\hat{\Psi}_3 = 0 \\ \text{or} \\ \hat{\Psi}_3 + 3\bar{a}\hat{\Psi}_2 + 3\bar{a}^2\hat{\Psi}_1 = 0 \end{gathered} \tag{2.89}$$

respectively gives the new $\tilde{\Psi}$s that have $\tilde{\Psi}_4 = \tilde{\Psi}_1 = 0$ such that only Ψ_0, Ψ_2 and Ψ_3 remains or $\tilde{\Psi}_0 = \tilde{\Psi}_3 = 0$ such that only Ψ_1, Ψ_2 and Ψ_4 remains. Either way, there is always a possibility to cancel out two of the Weyl scalars. Whether or not it is possible to cancel more can be deduced from the number of roots of Eq. (2.88), see Section 2.5.3.3, and this will establish if the spacetime is special as we shall see in Section 2.5.4.

2.5.3 Spacetime invariants

Spacetime invariants have been traditionally considered to address two main and related problems: *i)* to establish if two metrics, presented in seemingly different forms, e.g. in different coordinates, actually represent the same spacetime; this equivalence problem became an important one at the time when there was a proliferation of new exact solutions, and the development of the first computer algebra software was underway; *ii)* to classify exact solutions into Petrov types, which we describe in Section 2.5.4. The equivalence problem was originally formulated by Cartan (1946) and Brans (1965), then reconsidered and addressed, and related to the Petrov classification Petrov (2000), by D'Inverno and Russell-Clark (1971), see Karlhede (1980) for an early review. More general sets of invariants were then considered in Carminati and McLenaghan (1991) and Zakhary and McIntosh (1997). Recently, the specific equivalence problem for cosmological models has been addressed in Wylleman et al. (2019) ; in Bini, Geralico, and Jantzen (2023) a more refined classification for Petrov type I spacetimes has been proposed. For a classical and rather detailed account of invariants and the characterisation of spacetimes, we refer the reader to Stephani et al. (2003).

In the following, we are going to construct all the needed scalar invariants for spacetime comparison, as well as for the Petrov classification in Section 2.5.4, using $E^{\{v\}}_{\alpha\beta}$ and $B^{\{v\}}_{\alpha\beta}$ and the Ψs in an arbitrary frame. When a combination of frame-dependent quantities is frame-independent, this will be emphasised by dropping the index $\{v\}$.

To clarify the vocabulary used here, we use

- *coordinate variance or invariance* to identify whether a quantity is conserved under the coordinate transformation law given by Eq. (2.6) (as such all scalars are coordinate invariant (Wald, 1984; Stephani et al., 2003)),

- *coordinate dependent or independent* to identify whether a quantity retains its meaning in different coordinates, for example, whether a quantity calculated from two different spacetimes will be the same, and

- *frame-dependent or independent* to identify whether a quantity depends on a projection frame for its construction. An example of frame-dependant quantities is $E^{\{u\}}_{\alpha\beta}$ and $B^{\{u\}}_{\alpha\beta}$ that depend on the u^α frame, and the Ψs that depend on the chosen null tetrad.

All the spacetime invariants considered in this section are also coordinate independent, so for simplicity, here they are just referred to as invariants; the distinction between the two becomes more relevant in Section 4.2.6 where this discussion is continued in the context of cosmological perturbation theory.

2.5.3.1 Fundamental invariants

The two fundamental scalar invariants of the Weyl tensor are (Stephani et al., 2003)

$$I \equiv \frac{1}{2}\widetilde{C}_{\alpha\beta\mu\nu}\widetilde{C}^{\alpha\beta\mu\nu}, \qquad \text{and} \qquad J \equiv \frac{1}{6}\widetilde{C}_{\alpha\beta\lambda\sigma}\widetilde{C}^{\lambda\sigma}{}_{\mu\nu}\widetilde{C}^{\alpha\beta\mu\nu}, \tag{2.90}$$

where we use the complex self dual Weyl tensor $\widetilde{C}_{\alpha\beta\mu\nu} = \frac{1}{4}(C_{\alpha\beta\mu\nu} - iC^{*}_{\alpha\beta\mu\nu})$. By fundamental we identify invariants that can be used to express all others. Because these definitions are directly in terms of the Weyl tensor and do not use any projection, I and J are clearly frame-independent.

We can then express I and J in terms of $E_{\alpha\beta}$ and $B_{\alpha\beta}$ (McIntosh et al., 1995; Stephani et al., 2003; Alcubierre, 2008)[5] whatever the projection tensor used:

$$\begin{aligned} I &= \frac{1}{2}\overline{Q}_{\alpha\beta}\overline{Q}^{\alpha\beta} \\ &= \frac{1}{2}\left(E_{\alpha\beta}E^{\alpha\beta} - B_{\alpha\beta}B^{\alpha\beta}\right) - iE_{\alpha\beta}B^{\alpha\beta}, \end{aligned} \tag{2.91}$$

$$\begin{aligned} J &= \frac{-1}{6}\overline{Q}^{\alpha}{}_{\beta}\overline{Q}^{\beta}{}_{\mu}\overline{Q}^{\mu}{}_{\alpha} \\ &= \frac{-1}{6}\left[E^{\alpha}{}_{\beta}\left(E^{\beta}{}_{\mu}E^{\mu}{}_{\alpha} - 3B^{\beta}{}_{\mu}B^{\mu}{}_{\alpha}\right) + iB^{\mu}{}_{\alpha}\left(B^{\alpha}{}_{\beta}B^{\beta}{}_{\mu} - 3E^{\alpha}{}_{\beta}E^{\beta}{}_{\mu}\right)\right]. \end{aligned}$$

Then to express I and J in terms of the Weyl scalars, we expand the above explicitly using the inverse of the metric Eq. (2.79) to lower indices, e.g. $\bar{Q}^{\alpha}{}_{\beta} = g^{\alpha\mu}\bar{Q}_{\mu\beta}$, and using the definition Eq. (2.80) we obtain the well known expression:

$$I = \Psi_0\Psi_4 - 4\Psi_1\Psi_3 + 3\Psi_2^2, \qquad J = \begin{vmatrix} \Psi_4 & \Psi_3 & \Psi_2 \\ \Psi_3 & \Psi_2 & \Psi_1 \\ \Psi_2 & \Psi_1 & \Psi_0 \end{vmatrix}, \tag{2.92}$$

where J takes the determinant of the matrix.

2.5.3.2 Analogy to electromagnetism

We can construct invariants analogous to the fundamental invariants of electromagnetism (Landau and Lifshitz, 1975; Maartens, Gebbie, and Ellis, 1999). For $E_{\alpha\beta}$ and $B_{\alpha\beta}$ in any frame, these are (Matte, 1953; Bonnor, 1995),

$$\begin{aligned} L_B &\equiv \frac{1}{8}C_{\alpha\beta\mu\nu}C^{\alpha\beta\mu\nu} = E_{\alpha\beta}E^{\alpha\beta} - B_{\alpha\beta}B^{\alpha\beta} = 2\Re(I), \\ M &\equiv \frac{1}{4}C_{\alpha\beta\mu\nu}C^{*\alpha\beta\mu\nu} = E^{\alpha\beta}B_{\alpha\beta} = \Im(I). \end{aligned} \tag{2.93}$$

The equivalent of L_B in particular is the field energy density or Lagrange density. These correspond to the real and imaginary parts of I respectively so they are also frame-independent. In the case of a purely gravitational waves spacetime, i.e. Petrov type N, $L_B = M = 0$; these two conditions are also valid for Petrov type III (Bonnor, 1995).

[5] Note that various references use different normalisations of I and J.

2.5.3.3 Characterising spacetime

To characterise the spacetime with the Weyl tensor one considers the alignment possibilities, this is core to the Petrov classification, see Section 2.5.4. As we will see there are multiple approaches to finding this but given our introduction to the Weyl scalars and null tetrad frame rotations in Section 2.5.2 we will continue with the process of finding this alignment by finding the principal null directions. Core to this is the number of roots of Eq. (2.88), if all the roots are distinct, then there is no intrinsic alignment to the spacetime and it is general, otherwise it is special.

An invariant way to check this is with the speciality index (Baker and Campanelli, 2000),

$$\mathcal{S} = 27J^2/I^3, \tag{2.94}$$

or simply

$$\mathcal{D} = I^3 - 27J^2 \tag{2.95}$$

as in Coley, Peters, and Schnetter (2021). The spacetime is of a special Petrov type when $\mathcal{D} = 0$ and $\mathcal{S} = 1$ or $I = J = 0$ (Stephani et al., 2003). $\mathcal{S}$ and $\mathcal{D}$ are coordinate invariant and frame-independent scalars.

Then the different subcategories of the Petrov special types are distinguished based on the number of repeated roots. These can be determined based on the discriminants of Eq. (2.88), these are defined as[6] (Penrose, 1960; D'Inverno and Russell-Clark, 1971; Stephani et al., 2003):

$$K = \Psi_1\Psi_4^2 - 3\Psi_4\Psi_3\Psi_2 + 2\Psi_3^3, \quad L = \begin{vmatrix} \Psi_4 & \Psi_3 \\ \Psi_3 & \Psi_2 \end{vmatrix}, \quad N = 12L^2 - \Psi_4^2 I. \tag{2.96}$$

However, if $\Psi_4 = 0$ and $\Psi_0 \neq 0$ then Ψ_0 and Ψ_4 need to be interchanged as well as Ψ_1 and Ψ_3. K, L and N are coordinate invariant scalars but are also frame-dependent (Bini, Geralico, and Jantzen, 2023).

2.5.4 Petrov classification

Spacetimes can be classified according to their Weyl tensor, Ricci tensor, energy-momentum tensor, or some special vector fields and symmetries (Stephani et al., 2003). The Weyl tensor classification leads to the definition of the different Petrov types (Petrov, 2000) and because it can be obtained invariantly it has become more significant (Stephani et al., 2003). There are six different Petrov types going from the general one to the most special: I, II, D, III, N, and O. There are multiple interrelated methods to determine the classification, which we now briefly summarise; we refer the reader to Stephani et al. (2003), cf. Bini, Geralico, and Jantzen (2023) for a recent account.

- Via the **Q** matrix. This is the tensor $Q_{\alpha\beta}$, Eq. (2.71), expressed with respect to an arbitrary orthonormal basis. This matrix has 3 complex eigenvalues and whether or not they are distinct will establish the Petrov type (Stephani et al., 2003; Barnes, 2014; Bini, Geralico, and Jantzen, 2023).

- Via the principal spinors (or Debever spinors). The Weyl tensor can be expressed as a combination of these four spinors, and the Petrov type is related to whether or not these are independent or aligned (Plebański and Krasiński, 2006).

[6] K should not be confused with the trace of the extrinsic curvature Eq. (3.12) and Eq. (3.14).

- ❖ Via the principal null directions that can be found using the Weyl scalars (Newman and Penrose, 1962; Chandrasekhar, 1992; Stephani et al., 2003; Alcubierre, 2008; Owen, 2010; Shibata, 2015). Depending on the null tetrad base, certain Weyl scalars vanish[7]. In the frame that maximises the number of vanishing scalars, those scalars will determine the Petrov type. Starting from a generic null base, a frame rotation can be chosen such that the new Ψ_0 vanishes. This is done by solving the 4^{th} order complex polynomial Eq. (2.88) and the number of distinct roots, and whether or not they coincide, will determine the Petrov type and the principal null directions. Indeed, the more roots coincide, the more Weyl scalars can be made to vanish with further transformations.

- ❖ Via the I, J, K, L, and N invariants. Finding the roots of the polynomial Eq. (2.88) is not a trivial task. So, based on the discriminant of the polynomial, these invariants are constructed (D'Inverno and Russell-Clark, 1971) and whether or not they vanish will establish the number of distinct roots and therefore the Petrov type, see the flow diagram in Figure 9.1 of (Stephani et al., 2003) replicated in Fig. (6.13). For all special Petrov types $\mathcal{S} = 1$ (Baker and Campanelli, 2000), see Eq. (2.94), or $\mathcal{D} = I^3 - 27J^2 = 0$ (Coley, Peters, and Schnetter, 2021).

The six different Petrov types and their respective properties with regard to these different methods are presented in Fig. (2.1). Their physical interpretation has been described by Szekeres (1965) using a thought-device, the *gravitational compass*, measuring tidal effects, i.e. using the geodesic deviation equation. This physical interpretation is then based on looking at which of the Weyl scalars are non-zero in each case and on their specific distortion effects: Ψ_0 and Ψ_4 generate a transverse geodesic deviation, while Ψ_1 and Ψ_3 generate a longitudinal tidal distortion; the real part of Ψ_2 represents the tidal distortion associated with a Coulomb-type field originating from a central mass (the only one that would be present in a Newtonian gravitational field); its imaginary part, if present, is associated with frame dragging. If one thinks of the Weyl tensor as the combination of $E_{\alpha\beta}$ and $B_{\alpha\beta}$ in Eq. (2.72), with $E_{\alpha\beta}$ and $B_{\alpha\beta}$ expressed as in Eq. (2.84): they contain all of the effects mentioned above, notably $E_{\alpha\beta}$ contains the real part of Ψ_2, and $B_{\alpha\beta}$ its imaginary part. As can be seen in Section 4.2.4 for an FLRW spacetime linearly perturbed with only scalar perturbations, $B_{\alpha\beta}$ is zero and $E_{\alpha\beta}$ corresponds to the second derivatives of a linear combination of the Bardeen potentials called the Weyl potential (Lewis and Challinor, 2006). Then, with this physical description of the Weyl scalars, the physical interpretation of the different Petrov types, from most special to most general, is as follows.

- ❖ Type O is conformally flat, i.e. all Weyl scalars vanish and there are no tidal fields other than those associated with the Ricci curvature, e.g. like in FLRW spacetimes.

- ❖ The Petrov type N is associated with plane waves (Pirani, 1957), as the null tetrad can be chosen so that only Ψ_4 (or Ψ_0) is not zero; the tidal field associated with Ψ_4 (or Ψ_0) is purely transverse and, indeed, in the gauge-invariant perturbative formalism of Teukolsky (1973), cf. also (Stewart and Walker, 1974), gravitational wave perturbations of black holes are represented by Ψ_4 (or Ψ_0).

[7] The five complex Weyl scalars are just a different representation of the ten components of the Weyl tensor in 4-dimensional. Even in the general case, therefore, coordinates or frame transformations can be used to make four of these ten components vanish, or two complex Weyl scalars.

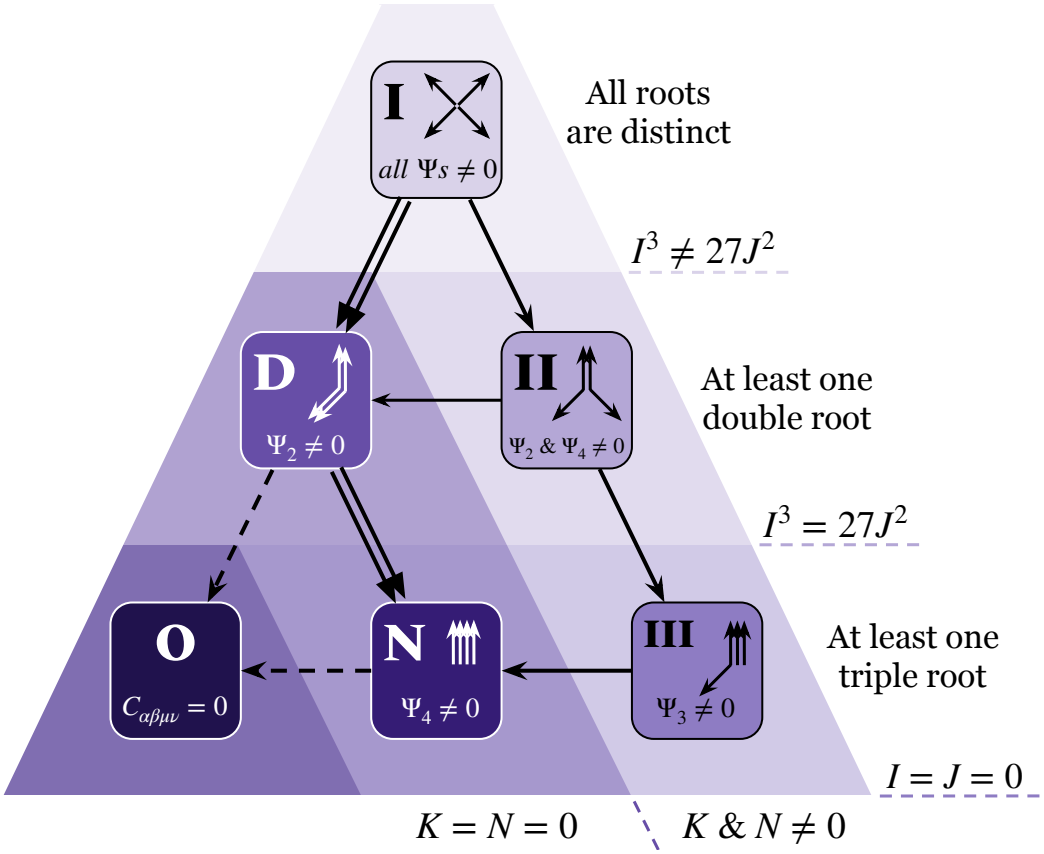

Figure 2.1: Penrose diagram of the different Petrov types, showing spinor alignments, non-vanishing Weyl scalars, number of roots of Eq. (2.88) and vanishing invariants

- In type III the null tetrad rotations allow us to make all Weyl scalars but Ψ_3 (or Ψ_1) zero: since Ψ_3 (or Ψ_1) gives rise to a longitudinal tidal effect, this is a strange case of spacetimes with pure longitudinal tidal fields. The sole perfect fluid solution known (Stephani et al., 2003) has been found in Allnutt (1981).

- In type D spacetimes, a null frame can be found such that only Ψ_2 is the non-zero Weyl scalar. This is the case of the Schwarzschild and Kerr spacetimes (Schwarzschild, 1916; Kerr, 1963; Szekeres, 1975), where the real part of Ψ_2 represents the Coulomb-type tidal field and the imaginary part (vanishing for Schwarzschild) is associated with frame-dragging. This is often referred to as the Kinnersley frame (Kinnersley, 1969; Teukolsky, 1973).

- In type II spacetimes the scalars Ψ_2 and Ψ_4 (or Ψ_0) can be made non-zero by appropriate rotations: these spacetimes can be seen as the superposition of an outgoing wave and a Coulomb-type field. A perfect fluid example of this Petrov type was found by Bonnor and Davidson (1985) as a special case of the Robinson–Trautman metrics (Robinson and Trautman, 1962).

- For Petrov type I, a standard choice is to have Ψ_1, Ψ_2 and Ψ_3 non-zero (Stephani et al., 2003; Bini, Geralico, and Jantzen, 2023), but the alternative choice Ψ_0,Ψ_2 and Ψ_4 non-zero is also possible. This latter choice of the NP null tetrad can be called transverse (Beetle and Burko, 2002; Berti, White, et al., 2005), then we can see from Eq. (2.84) that both $E^{\{v\}\alpha\beta}$ and $B^{\{v\}\alpha\beta}$ have a Coulombian component, plus one for each transverse “polarization". In the context of

black hole perturbation theory, this transverse tetrad can be called quasi-Kinnersley, as there are Ψ_0 and Ψ_4 perturbations on the Kinnersley background, as in Teukolsky (1973) and Stewart and Walker (1974). In NR applied to isolated sources of gravitational waves, the search for this quasi-Kinnersley frame is a non-trivial task associated with the goal of properly extracting gravitational waves, see Nerozzi, Beetle, et al. (2005) and Nerozzi, Bruni, et al. (2006) and Refs. therein. However, a type I spacetime doesn't necessarily contain gravitational waves; a noteworthy example is the spacetime of stationary rotating neutron stars. In this case, in the quasi-Kinnersley transverse frame, Ψ_0 and Ψ_4 can be interpreted as transverse (but stationary) tidal field deviation from the Kerr geometry, see Berti, White, et al. (2005).

In summary, the process of making some of the Weyl scalars vanish by rotations of the NP null tetrad can lead to ambiguities, as there is a certain set of degrees of freedom for each type leading to a set number of non-vanishing Weyl scalars, hence there is a certain freedom of choosing which scalar to cancel out. For instance, one may see that for type II it is also possible to have Ψ_2 and Ψ_3 instead of Ψ_2 and Ψ_4 non zero (Chandrasekhar, 1992). Nonetheless, each Weyl scalar has a precise interpretation as a specific type of tidal field on the basis of the geodesic deviation equation and the associated gravitational compass (Szekeres, 1965). In general, the geodesic deviation equation is linear in the Riemann tensor (and therefore in its Weyl plus Ricci decomposition), hence it allows a superposition of the tidal effects associated with each Weyl scalar. However, this decomposition is not unique, as it differs for different observers associated with the different possible tetrad bases. This just means that different observers would measure different tidal fields, even if the Petrov type - and the corresponding intrinsic nature of the tidal field - would be invariant.

3 - Numerical Relativity

As GR connects space, time and matter, this becomes a challenging ensemble to study; we then turn to numerical methods to solve these equations, namely Numerical Relativity (NR).

The field of NR became possible with the 3+1 splitting of the metric. This is based on choosing a timelike vector n^μ, defining its projection tensor γ_{ij} and using these to split all the relevant quantities into their temporal and spatial parts as discussed in Section 2.1.4. This was first initiated by Darmois (1927), where he referred to these coordinates as normalised or intrinsic coordinates, already using them to draw analogies to Maxwell's equations. However, it was truly popularised by Arnowitt, Deser, and Misner (1959) (ADM) as they pursued separating the metric's dynamical and coordinate components so that they could draw comparisons with electrodynamics and treat GR as an ordinary classical field. This 3+1 formalism, also called ADM, was later formally established by York (1973) where the spacetime, matter and evolution equations are foliated through time as described in Section 3.1, 3.2 and 3.3 respectively.

Before jumping to solving Einstein's field equations in the ADM+York form, studying them is crucial to know if they are well-posed (Rendall, 2008). Fourès-Bruhat (1952) was the first to address this Cauchy problem and proved this system to be unique using a harmonic formulation $\nabla_\mu \nabla^\mu v^\alpha = 0$. This system has further been proved to be well-posed using a number of different formulations, notably BSSNOK (Nakamura, Oohara, and Kojima, 1987; Shibata and Nakamura, 1995; Baumgarte and Shapiro, 1998) see Section 3.3.3.1, and even in modified theories of gravity (Torsello et al., 2020).

Within the coordinate freedom of GR, we shall discuss usual gauge choices in Section 3.4. Additionally, because gravito-electromagnetism is a key concept to this thesis, Section 3.5 shows the form the electric and magnetic parts of the Weyl tensor take in the 3+1 formalism, which is implemented in Section 5.1.2.

In order to run NR simulations, codes need to be developed using various numerical methods, these are discussed in Section 3.6.

3.1 Spacetime

The 3+1 or ADM formalism is based on splitting the spacetime into spatial hypersurfaces layered through time (Gourgoulhon, 2007; Alcubierre, 2008; Rendall, 2008; Baumgarte and Shapiro, 2010; Shibata, 2015). This is done with a timelike unit vector n^μ and its projection tensor $\gamma_{\mu\nu}$ that provides a spatial metric of the hypersurface

$$\gamma^{\mu\nu} = g^{\mu\nu} + n^\mu n^\nu, \qquad \gamma^\mu{}_\nu = \delta^\mu{}_\nu + n^\mu n_\nu, \qquad \gamma_{\mu\nu} = g_{\mu\nu} + n_\mu n_\nu. \tag{3.1}$$

Projecting along a given vector has been discussed in Section 2.1.4, keeping the notation general, but here in this chapter, the notation will be specific using only n^μ and $\gamma_{\mu\nu}$ as the timelike vector

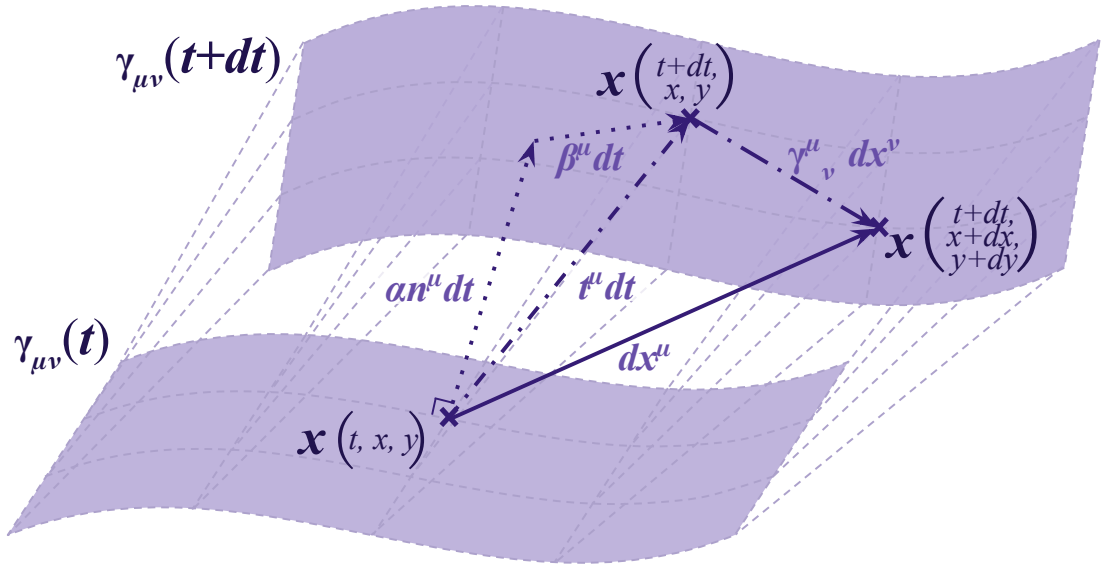

Figure 3.1: Schematic representation of spatial foliation with 2+1 dimensions and Cartesian coordinates showing how one event is connected to neighbouring events.

and projection tensor respectively. By definition $n^\mu n_\mu = -1$, $\gamma_{\mu\nu}$ is a spatial metric such that its determinant is positive $\gamma > 0$ and its trace is $\gamma^\mu{}_\mu = 3$. It is orthogonal to n^μ as $n^\mu \gamma_{\mu\nu} = 0$, and by construction $\nabla_{[\mu} n_{\nu]} = 0$.

In order for n^μ to exclusively capture the temporal information, it is chosen such that it is solely provided by the time components of the metric $n^\mu = n_0 g^{0\mu}$ with $n_i = 0$. This will ensure that the time coordinate t is constant on each $\gamma_{\mu\nu}$ hypersurfaces, which are mapped to each other with the normal to the hypersurface n^μ, the lapse α and the shift β^μ. The lapse function $\alpha(t,\ x^i)$ is defined such that $n_0 = -\alpha$ and with the timelike normalisation it is $\alpha^2 = -1/g^{00}$. The shift vector $\beta^\mu(t,\ x^i)$ with the components

$$\beta^\mu = \{0,\ \beta^i\} \qquad \text{and} \qquad \beta_\mu = \{\beta_k \beta^k,\ \beta_j\} \tag{3.2}$$

is defined such that it provides the remaining parts of $g^{0\mu}$ as $g^{0\mu} = |g^{00}|\{-1,\ \beta^i\}$. Because β^μ only has spatial components it is orthogonal to n_μ, $n_\mu \beta^\mu = n_0 \beta^0 = 0$, as such it lives on the $\gamma_{\alpha\beta}$ hypersurface and its indices are raised and lowered with $\gamma_{\alpha\beta}$: $\beta_\mu = \gamma_{\mu\nu}\beta^\nu$. These choices and the definitions of the lapse α and shift β^μ provide the normal to the hypersurface n^μ as

$$n^\mu = \{1/\alpha,\ -\beta^i/\alpha\}, \qquad\qquad n_\mu = \{-\alpha,\ 0,\ 0,\ 0\}. \tag{3.3}$$

where its acceleration is given by

$$\mathfrak{a}_\mu = \dot{n}_\mu = n^\nu \nabla_\nu n_\mu = \frac{D^{\{n\}}_\mu \alpha}{\alpha} = D^{\{n\}}_\mu \ln(\alpha). \tag{3.4}$$

Plugging Eq. (3.3) into Eq. (3.1), g^{ij} can easily be retrieved in terms of α and β^i providing $g^{\alpha\beta}$ expressed below. This can then be used to obtain $g_{\alpha\beta}$ using the system of equations provided by $g^{\alpha\mu} g_{\mu\beta} = \delta^\alpha{}_\beta$ such that

$$g^{\mu\nu} = \begin{pmatrix} -1/\alpha^2 & \beta^j/\alpha^2 \\ \beta^i/\alpha^2 & \gamma^{ij} - (\beta^i\beta^j/\alpha^2) \end{pmatrix}, \qquad g_{\mu\nu} = \begin{pmatrix} -\alpha^2 + \beta_k\beta^k & \beta_j \\ \beta_i & \gamma_{ij} \end{pmatrix}. \tag{3.5}$$

Then simply using this and Eq. (3.1), the spatial metric $\gamma_{\mu\nu}$ is

$$\gamma^{\mu\nu} = \begin{pmatrix} 0 & 0 \\ 0 & \gamma^{ij} \end{pmatrix}, \qquad \gamma_{\mu\nu} = \begin{pmatrix} \beta_k\beta^k & \beta_i \\ \beta_j & \gamma_{ij} \end{pmatrix}, \tag{3.6}$$

with its determinant γ related to the spacetime metric determinant as $g = -\alpha^2\gamma$.

Based on Eq. (3.5), the infinitesimal separation between two events is then expressed in this formalism as

$$\begin{aligned} ds^2 &= (-\alpha^2 + \beta_k\beta^k)dt^2 + 2\beta_i dt dx^i + \gamma_{ij}dx^i dx^j \\ &= -\alpha^2 dt^2 + \gamma_{ij}\left(dx^i + \beta^i dt\right)\left(dx^j + \beta^j dt\right). \end{aligned} \tag{3.7}$$

Two events are separated by a step in time dt and space dx^i that together are taken and combined with the Pythagorean theorem to provide this infinitesimal distance. This is essentially depicted in Fig. (3.1) with 2+1 dimensions and Cartesian coordinates. How these coordinates evolve in time is mapped out by α and β^μ. To see this, consider the vector tangent to the time axis (Baumgarte and Shapiro, 2010)

$$t^\mu = \{1,\ 0,\ 0,\ 0\} = \alpha n^\mu + \beta^\mu, \tag{3.8}$$

where the Lie derivative, Eq. (2.27), of some quantity ϕ along t^μ can be separated as

$$\mathcal{L}_t\phi = \partial_t\phi = \alpha\mathcal{L}_n\phi + \mathcal{L}_\beta\phi. \tag{3.9}$$

It is common practice to define $\frac{d}{dt}$ the coordinate time derivative exclusively along the normal to the hypersurface as

$$\frac{d\phi}{dt} = \alpha\mathcal{L}_n\phi = \partial_t\phi - \mathcal{L}_\beta\phi. \tag{3.10}$$

One position in time is brought from one hypersurface of time t, $\gamma_{\mu\nu}(t)$, to the next of time $t + dt$, $\gamma_{\mu\nu}(t + dt)$, along the direction normal to $\gamma_{\mu\nu}(t)$ provided by $n^\mu(t)$ and by taking a step of spacing $\alpha(t)dt$. Once on $\gamma_{\mu\nu}(t + dt)$ the spatial location is then adjusted by the shift $\beta^i(t)dt$. Therefore the step in time is provided by $t^\mu(t)dt$. Then to take a step in space, while on $\gamma_{\mu\nu}(t + dt)$, the location is moved by $\gamma^\mu{}_\nu(t)dx^\nu = \gamma^\mu{}_\nu(t + dt)dx^\nu = \{0,\ dx^1,\ dx^2,\ dx^3\}$. The combination of the time and space step is then $dx^\mu = t^\mu dt + \gamma^\mu{}_\nu dx^\nu$ which provides Eq. (3.7) as $ds^2 = g_{\mu\nu}dx^\mu dx^\nu$.

3.1.1 Curvature

What of the curvature? As described in Section 2.1.3 one can compute the curvature of spacetime $g_{\mu\nu}$ with the Riemann tensor $R^\alpha{}_{\sigma\mu\nu}$ with Eq. (2.18) and Eq. (2.19) using the Christoffel symbol $\Gamma^\alpha{}_{\mu\nu}$ Eq. (2.14). Now that we defined a spatial metric γ_{ij} one can use the same expressions to get the 3-dimensional Riemann tensor ${}^{(3)}R^k{}_{mij}$ with the 3-dimensional Christoffel symbol ${}^{(3)}\Gamma^k{}_{ij}$ by simply using γ_{ij} instead of $g_{\alpha\beta}$ in equations Eq. (2.19) and Eq. (2.14). In the definition provided by the Ricci identity Eq. (2.18) the spatial covariant derivative associated with γ_{ij}, $D^{\{n\}}_\alpha$, is used instead, see Eq. (2.32) providing the 3-dimensional Ricci identity

$$D^{\{n\}}_\mu D^{\{n\}}_\nu v^\alpha - D^{\{n\}}_\nu D^{\{n\}}_\mu v^\alpha = {}^{(3)}R^\alpha{}_{\sigma\mu\nu}v^\sigma. \tag{3.11}$$

However, γ_{ij} does not have any information on how time evolves, this is contained in n^μ. To quantify how curvature evolves with time, one uses the extrinsic curvature

$$\begin{aligned} K_{\mu\nu} &= -\frac{1}{2}\mathcal{L}_{\mathbf{n}}\gamma_{\mu\nu} = -\gamma^{\alpha}{}_{\mu}\gamma^{\beta}{}_{\nu}\nabla_{\alpha}n_{\beta} \\ &= -\frac{1}{2\alpha}\left(\partial_t\gamma_{\mu\nu} - \mathcal{L}_{\beta}\gamma_{\mu\nu}\right) = -\frac{1}{2\alpha}\frac{d\gamma_{\mu\nu}}{dt} \end{aligned} \tag{3.12}$$

i.e. the Lie derivative Eq. (2.27) of the spatial metric along the normal to the hypersurface. This quantity can be used to express how the coordinates expand/contract. Note that we do not use the spatial covariant derivative $D_\mu^{\{n\}}$, Eq. (2.32), instead of $\gamma_\mu{}^\sigma\nabla_\sigma$ because n_ν is orthogonal to $\gamma_{\mu\nu}$.

The extrinsic curvature is symmetric and covariantly purely spatial, i.e. it is orthogonal to n^α, $n_\alpha K^{\alpha\beta} = 0$. However, while $K^{00} = K^{0i} = 0$, K_{00} and K_{0i} are different from zero in general when the shift is not zero; we can write:

$$K^{\alpha\beta} = \begin{pmatrix} 0 & 0 \\ 0 & K^{ij} \end{pmatrix}, \qquad K_{\alpha\beta} = \begin{pmatrix} \beta_i\beta_j K^{ij} & \beta_i K^i{}_k \\ \beta_j K_l{}^j & K_{kl} \end{pmatrix}, \tag{3.13}$$

where its indices are raised and lowered with the spatial metric $K_i{}^j = \gamma_{ik}K^{kj}$ and $K_{ij} = \gamma_{ik}\gamma_{jl}K^{kl}$. It can be split into its trace $K = K^i{}_i$ and traceless part $A_{ij} = K_{\langle ij\rangle}$ as

$$K_{\mu\nu} = \frac{1}{3}\gamma_{\mu\nu}K + A_{\mu\nu}, \tag{3.14}$$

where the magnitude of the traceless part is

$$2A^2 = A_{\mu\nu}A^{\mu\nu} = K_{\alpha\beta}K^{\alpha\beta} - \frac{1}{3}K^2. \tag{3.15}$$

These two quantities will become useful when considering the evolution and constraint equations. How the extrinsic curvature $K_{\alpha\beta}$ and intrinsic curvature ${}^{(3)}R_{ij}$ relate to the 4-dimensional Riemann tensor is discussed in Section 3.3.2.

3.2 Matter

As NR is based on the foliation created along the n^μ vector, naturally, one would consider the decomposition of $T_{\mu\nu}$ as described in Section 2.3 using n^μ, this takes the form

$$T_{\mu\nu} = \rho^{\{n\}}n_\mu n_\nu + 2q^{\{n\}}_{(\mu}n_{\nu)} + S^{\{n\}}_{\mu\nu}. \tag{3.16}$$

The n^μ frame is commonly referred to as an Eulerian observer, while the observer moving with the fluid flow, the u^μ frame, is referred to as a Lagrangian observer. Here we will see how the hydrodynamical terms in the n^μ frame relate to those in the fluid frame u^μ ($q^{\{u\}} = 0$) should the fluid be described as a perfect fluid, then in its own frame

$$\begin{aligned} T_{\mu\nu} &= \varrho^{\{u\}}h^{\{u\}}u_\mu u_\nu + \left(p^{\{u\}} - \frac{\Lambda}{\kappa}\right)g_{\mu\nu} \\ &= \rho^{\{u\}}u_\mu u_\nu + p^{\{u\}}h_{\mu\nu} - \frac{\Lambda}{\kappa}g_{\mu\nu}. \end{aligned} \tag{3.17}$$

With the cosmological constant Λ introduced into the energy stress tensor rather than being its own term in Einstein's field equations as we follow from (Bentivegna, 2017) whose code we use during this thesis.

The timelike normalisation of the 4-velocity $u_\mu u^\mu = -1$ provides the temporal components as

$$u^0 = \frac{1}{\alpha}\sqrt{1+\gamma^{ij}u_i u_j}, \qquad u_0 = u_k\beta^k - \alpha^2 u^0. \tag{3.18}$$

We also use the 3-velocity of the fluid flow $v^i = u^i/u^0$. In literature, the 3-velocity is defined with different normalisations $v_i = u_i/\alpha u^0$ (Alcubierre, 2008) or $v^i = u^i/u^0$ but here we will use the latter to keep with the notation of Bentivegna (2017) (Anninos, 1998; Baumgarte and Shapiro, 2010; Shibata, 2015). While the indices of u^μ are raised and lowered with $g_{\mu\nu}$, those of v^i are raised and lowered with γ_{ij} providing

$$v^i = \frac{u^i}{u^0} = \frac{\gamma^{ij}u_j}{u^0} - \beta^i, \qquad v_i = \frac{u_i}{u^0} - \beta_i \tag{3.19}$$

For the same energy-stress tensor, $T_{\mu\nu}$, it is presented here in Eq. (3.16) and Eq. (3.17) using two different frames n^μ and u^μ. While we consider a perfect fluid, $T_{\mu\nu}$ only takes the simplified expression of Eq. (3.17) in the fluid frame, u^μ, otherwise for an arbitrary timeline vector n^μ it takes the more general form Eq. (3.16).

To go from one observer to the other, we need to see how they relate, so we consider their product, which is quantified by

$$\begin{aligned} W &= -u^\mu n_\mu = \alpha u^0 \\ &= \sqrt{1+\gamma^{ij}u_i u_j}. \end{aligned} \tag{3.20}$$

This corresponds to the Lorentz factor commonly used in special relativity to relate two observers moving at different speeds. Note that the product of two vectors is related to their tilt angle $\boldsymbol{\beta}$ as $u^\mu n_\mu = -\cosh\boldsymbol{\beta}$ (Bruni, 1991). Should u^μ and n^μ be in the same direction $u^\mu = n^\mu$, as is the case in comoving coordinates, then their respective timelike normalisation means $W = 1$ and so the terms expressed in the n^μ frame are the same as those in the u^μ frame.

Then using W, the fluid quantities measured in the Eulerian frame are expressed in terms of those in the Lagrangian frame as (Alcubierre, 2008)

$$\begin{aligned} \rho^{\{n\}} &= T^{\alpha\beta}n_\alpha n_\beta &&= \varrho^{\{u\}}h^{\{u\}}W^2 - \left(p^{\{u\}} - \frac{\Lambda}{\kappa}\right), \\ q_i^{\{n\}} &= -\gamma^\beta{}_i T_{\beta\alpha}n^\alpha &&= \varrho^{\{u\}}h^{\{u\}}W u_i, \\ S_{ij}^{\{n\}} &= \gamma^\mu{}_i\gamma^\nu{}_j T_{\mu\nu} &&= \varrho^{\{u\}}h^{\{u\}}u_i u_j + \gamma_{ij}\left(p^{\{u\}} - \frac{\Lambda}{\kappa}\right). \end{aligned} \tag{3.21}$$

Einstein's field equations Eq. (2.39) only require $T_{\mu\nu}$ which can be provided by either Eq. (3.16) or Eq. (3.17). However, the constraint and evolution equations derived from Eq. (2.39) are constructed by projecting a chosen timelike vector; this is shown in Eq. (2.60, 2.61, 2.62) with the fluid flow u^μ. However here, n^μ is going to be used instead in Section 3.3.3 which will require $\{\rho^{\{n\}},\ q^{\{n\}i},\ S^{\{n\}ij}\}$.

3.3 Constraint & evolution equations

3.3.1 Conservation equations

While in the Lagrangian frame (fluid frame), the fluid may be a perfect fluid of the form Eq. (3.17) whose evolution equations are provided by $\nabla_\mu T^{\mu\nu} = 0$ see Section 2.4.1, in the Eulerian frame (n^μ frame) the fluid may not appear as a perfect fluid, it instead takes the form Eq. (3.16), making the fluid equations more challenging. The state of the fluid can be established based on the primitive quantities $\{\varrho^{\{u\}},\ \varepsilon^{\{u\}},\ p^{\{u\}},\ v^i\}$, however, to express the evolution equations in a form analogous to the Eulerian equations in Newtonian theory, the Wilson scheme uses the conserved quantities $\{D,\ E,\ S_i\}$ instead (Wilson, 1972, 1979; Baumgarte and Shapiro, 2010). These are the rest mass-energy density, internal energy density and energy flux (or momentum density)

$$\begin{array}{rcccl} D & = & \sqrt{\gamma}\varrho^{\{n\}} & = & \mathcal{W}\varrho^{\{u\}} \\ E & = & \sqrt{\gamma}\epsilon^{\{n\}} & = & \mathcal{W}\varrho^{\{u\}}\epsilon^{\{u\}} \\ S^i & = & \sqrt{\gamma}q^{\{n\}i} & = & \mathcal{W}\varrho^{\{u\}}h^{\{u\}}u^i \end{array} \tag{3.22}$$

respectively, where

$$\mathcal{W} = W\sqrt{\gamma} = \alpha u^0\sqrt{\gamma}. \tag{3.23}$$

Usually, they are presented without $\mathcal{W}$, but this choice simplifies the expression of their evolution equations. The conservation equations, $\nabla_\mu T^{\mu\nu} = 0$ Eq. (2.40), in their various projections and the equation of state, $p^{\{u\}} = w\rho^{\{u\}}$ Eq. (2.48), provide the conservation of particles, energy[1] and momentum evolution equations (Anninos, 1998)

$$\begin{array}{rcl} \partial_t(D) + \partial_k\left(Dv^k\right) & = & 0, \\ \partial_t(E) + \partial_k\left(Ev^k\right) & = & -p^{\{u\}}\left(\partial_t\mathcal{W} + \partial_k\left(\mathcal{W}v^k\right)\right), \\ \partial_t(S_i) + \partial_k\left(S_iv^k\right) & = & \dfrac{S^\mu S^\nu}{2S^0}\partial_i g_{\mu\nu} - \alpha\sqrt{\gamma}\partial_i p^{\{u\}}, \end{array} \tag{3.24}$$

respectively[2]. This system is implemented in `CT_Dust` (Bentivegna, 2017), which was used for this thesis. Once $\{D,\ E,\ S_i\}$ are evolved $T_{\alpha\beta}$ is reconstructed via Eq. (3.16) and decomposed into $\{\rho^{\{n\}},\ q^{\{n\}i},\ S^{\{n\}ij}\}$ for Einstein's field equation, see Section 3.3.3.

3.3.2 Ricci identity

To algebraically relate the 4-dimensional Riemann tensor ${R^\alpha}_{\sigma\mu\nu}$ to the extrinsic curvature $K_{\alpha\beta}$ consider the Ricci identity Eq. (2.18) applied to n^μ. Projecting it and simplifying it corresponds to the Codazzi (or Codazzi-Mainardi) equation (Shibata, 2015)

$$D^{\{n\}}_\alpha K_{\beta\mu} - D^{\{n\}}_\beta K_{\alpha\mu} = -{\gamma^\nu}_\alpha{\gamma^\lambda}_\beta{\gamma^\sigma}_\mu R_{\nu\lambda\sigma\eta}n^\eta, \tag{3.25}$$

that relates the 4-dimensional curvature to the spatial covariant derivative $D^{\{n\}}_\alpha$, Eq. (2.32), of the extrinsic curvature.

[1] Because of the $\partial_t W$ term, the E quantity is often replaced by $\mathcal{E} = \sqrt{\gamma}\rho^{\{n\}} - D$ (Alcubierre, 2008; Baumgarte and Shapiro, 2010).

[2] Note that $S^\mu S^\nu\partial_i g_{\mu\nu} = -S_\mu S_\nu\partial_i g^{\mu\nu}$.

To then see how the intrinsic 3-dimensional Riemann curvature ${}^{(3)}R^{\alpha}{}_{\sigma\mu\nu}$ of the slices relates to $R^{\alpha}{}_{\sigma\mu\nu}$ and $K_{\alpha\beta}$ consider again the Ricci identity Eq. (2.18) but this time applied to an arbitrary vector $v^{\{n\}\mu}$ living on $\gamma_{\mu\nu}$ such that $v^{\{n\}\mu}n_{\mu} = 0$. With simplifications and using Eq. (3.11) this reduces to the Gauss equation (Shibata, 2015)

$$ {}^{(3)}R_{\alpha\beta\mu\nu} = \gamma^{\lambda}{}_{\alpha}\gamma^{\sigma}{}_{\beta}\gamma^{\omega}{}_{\mu}\gamma^{\eta}{}_{\nu}R_{\lambda\sigma\omega\eta} + K_{\alpha\nu}K_{\beta\mu} - K_{\alpha\mu}K_{\beta\nu}. \tag{3.26} $$

$R_{\alpha\beta\mu\nu}$ contains first and second order spatial and temporal derivatives of $g_{\alpha\beta}$. To separate these, the spatial derivatives ∂_i & $\partial_i\partial_j$ of $\gamma_{\alpha\beta}$ are all in ${}^{(3)}R_{\alpha\beta\mu\nu}$ given by Eq. (3.11) and Eq. (3.26). For temporal parts, at first order, ∂_t & ∂_i are in $K_{\alpha\beta}$ given by Eq. (3.12). Then, at second order, $\partial_i\partial_t$ & $\partial_i\partial_j$ are in $D^{\{n\}}_{\alpha}K_{\beta\mu}$ provided by Eq. (3.25), and the remaining derivatives $\partial_t\partial_t$ & $\partial_t\partial_j$ are in $\mathcal{L}_n K_{\alpha\beta}$ given by

$$ \mathcal{L}_n K_{\alpha\beta} = \gamma^{\lambda}{}_{\alpha}\gamma^{\omega}{}_{\beta}R_{\lambda\sigma\omega\eta}n^{\sigma}n^{\eta} - \frac{1}{\alpha}D^{\{n\}}_{\alpha}D^{\{n\}}_{\beta}\alpha - K^{\lambda}{}_{\beta}K_{\alpha\lambda} \tag{3.27} $$

This is obtained from expanding $\mathcal{L}_n K_{\alpha\beta} = n^{\mu}\nabla_{\mu}K_{\alpha\beta} + 2K_{\mu(\alpha}\nabla_{\beta)}n^{\mu}$, introducing the Ricci identity n^{μ}, $\nabla_{\mu}\nabla_{\alpha}n_{\beta} = R_{\beta\sigma\mu\alpha}n^{\sigma} + \nabla_{\alpha}\nabla_{\mu}n_{\beta}$, projecting with $\gamma^{\mu}{}_{\alpha}\gamma^{\nu}{}_{\beta}$ and simplifying based on the expressions

$$ \begin{aligned} K_{\alpha}{}^{\mu}K_{\mu\beta} + K_{\mu\beta}n_{\alpha}\mathfrak{a}^{\mu} &= \nabla_{\alpha}n^{\mu}\nabla_{\mu}n_{\beta} \\ D^{\{n\}}_{\mu}\mathfrak{a}_{\nu} + \mathfrak{a}_{\mu}\mathfrak{a}_{\nu} &= \tfrac{1}{\alpha}D^{\{n\}}_{\mu}D^{\{n\}}_{\nu}\alpha \end{aligned} \tag{3.28} $$

using Eq. (3.4), see Baumgarte and Shapiro (2010) for a step-by-step derivation of Eq. (3.27).

Since Eq. (3.25, 3.26, 3.27) contain all the derivatives that are in the 4-dimensional Ricci, these equations are essential to remove $R_{\alpha\beta}$ terms in Einstein's field equations.

3.3.3 Einstein's field equations

Just as in Section 2.4.3, Einstein's field equations $G_{\alpha\beta} - \kappa T_{\alpha\beta} = 0$ are projected along a chosen timelike normal vector. In Section 2.4.3, we projected them considering fluid flow; here, we project them with n^{μ} and $\gamma_{\alpha\beta}$. We omit the cosmological constant since the matter is treated as a source term to these evolution equations, Λ can be included in the energy stress tensor as $T_{\mu\nu} \to T_{\mu\nu} - \frac{\Lambda}{\kappa}g_{\mu\nu}$ as described in Eq. (3.17).

❖ $(G_{\alpha\beta} - \kappa T_{\alpha\beta})\, n^{\alpha}n^{\beta} = 0$ is the Hamiltonian constraint equation,

$$ \begin{aligned} {}^{(3)}R + \frac{2}{3}K^2 - 2A^2 &= 2\kappa\rho^{\{n\}} \\ \Leftrightarrow {}^{(3)}R + K^2 - 2K^{ij}K_{ij} &= 2\kappa\rho^{\{n\}} \end{aligned} \tag{3.29} $$

This is obtained using $G_{\alpha\beta}n^{\alpha}n^{\beta} = \frac{1}{2}\gamma^{\alpha\mu}\gamma^{\beta\nu}R_{\alpha\beta\mu\nu}$ where the 4-dimensional Riemann term can be replaced by the contraction of the Gauss equation Eq. (3.26) with $\gamma^{\alpha\mu}\gamma^{\beta\nu}$.

❖ $\gamma^{\beta}{}_{\alpha}\,(G_{\beta\mu} - \kappa T_{\beta\mu})\, n^{\mu} = 0$ are the Momentum constraint equations,

$$ D^{\{n\}}_{i}(K^{ij} - \gamma^{ij}K) = \kappa q^{\{n\}j} \tag{3.30} $$

This is obtained with $\gamma^{\beta}{}_{\alpha}G_{\beta\mu}n^{\mu} = \gamma^{\beta}{}_{\alpha}R_{\beta\mu}n^{\mu}$ where the 4-dimensional Ricci term is substituted with the Codazzi equation Eq. (3.25) contracted with $\gamma^{\beta\mu}$.

❖ and $\gamma^{\mu}{}_{\alpha}\gamma^{\nu}{}_{\beta}\left(G_{\mu\nu} - \kappa T_{\mu\nu}\right) = 0$ are the evolution equations of the extrinsic curvature (York, 1979)

$$\begin{aligned}\frac{dK_{ij}}{dt} =& - D_i^{\{n\}} D_j^{\{n\}} \alpha - \kappa\alpha \left[S_{ij}^{\{n\}} - \frac{1}{2}\gamma_{ij}(S^{\{n\}} - \rho^{\{n\}}) \right] \\ &+ \alpha \left[{}^{(3)}R_{ij} + K K_{ij} - 2K_{ik}K^{k}{}_{j} \right]\end{aligned} \tag{3.31}$$

where we use Eq. (3.10). This expression is essentially Eq. (3.27) where the Riemann term is substituted with the Gauss equation Eq. (3.26) and the Ricci term that would then appear is replaced with Einstein's field equation Eq. (2.39).

Evolving the extrinsic curvature with Eq. (3.31) would naturally provide the evolution equations of the spatial metric according to Eq. (3.12)

$$\frac{d\gamma_{ij}}{dt} = -2\alpha K_{ij} \tag{3.32}$$

Then the lapse α and shift β^i evolve according to the gauge choice, see Section 3.4.

The evolution equations Eq. (3.31, 3.32) provide a system of coupled quasilinear second-order partial differential equations (PDE). To numerically integrate this system, it needs to be well-posed, i.e. that a solution exists and is unique; this will ensure their stability such that if there is a small deviation, the system will remain close to the solution, and with increased resolution, it will converge to the true solution. To establish this, we consider the terms in the principal part of the PDE

$$\begin{aligned} D_i^{\{n\}} D_j^{\{n\}} \alpha &= \partial_i \partial_j \alpha + \ldots \\ {}^{(3)}R_{ij} &= -\frac{1}{2}\gamma^{mn}\left(\partial_m\partial_n\gamma_{ij} + \partial_i\partial_j\gamma_{mn} - \partial_i\partial_n\gamma_{mj} - \partial_m\partial_j\gamma_{in}\right) + \ldots \end{aligned} \tag{3.33}$$

PDEs are categorised, depending on the coefficients of the higher order terms, as either elliptic (Poisson's equation), parabolic (diffusion equation), or hyperbolic (wave equation) (Baumgarte and Shapiro, 2010). As they stand, the system's equations can not be classified amongst either group, but through coordinate choices, the constraint equations can be shown to be elliptic and the evolution equations to be hyperbolic (Rendall, 2008). Hyperbolic evolution equations can further be classified as either strongly or weakly hyperbolic, which identifies whether the solution can be bound by an arbitrary exponential function; if an equation is strongly hyperbolic, then its solution grows slower or equal to an exponential evolution, and this equation is therefore well-posed (Alcubierre, 2008). Such a reformulation was first provided by Fourès-Bruhat (1952) with harmonic coordinates that reduce the evolution equations to well-posed wave equations. Then amongst the formalisms that are now available, we shall describe BSSNOK.

3.3.3.1 BSSNOK

The BSSNOK formulation from (Nakamura, Oohara, and Kojima, 1987; Shibata and Nakamura, 1995; Baumgarte and Shapiro, 1998) express the ADM+York evolution equations, Eq. (3.32) and Eq. (3.31), in a well-posed form based on a conformal rescaling and the ${}^{(3)}\Gamma^k = \gamma^{ij\,(3)}\Gamma^k{}_{ij}$ connection function. The conformal mapping is applied to the spatial metric and the traceless part of the extrinsic curvature

$$\bar{\bar{\gamma}}_{ij} = \bar{\bar{\psi}}^{-4}\gamma_{ij}, \qquad \bar{\bar{A}}_{ij} = \bar{\bar{\psi}}^{-4}A_{ij} \tag{3.34}$$

such that the conformal spatial metric $\bar{\bar{\gamma}}_{ij}$ has unit determinant $\bar{\bar{\gamma}} = det\left(\bar{\bar{\gamma}}_{ij}\right) = 1$. This defines the conformal factor from the spatial determinant $\bar{\bar{\psi}} = e^{\bar{\bar{\phi}}} = \bar{\bar{\gamma}}^{1/12}$, where $\bar{\bar{\psi}}$ and $\bar{\bar{\phi}}$ can be used interchangeably depending on convenience. Naturally, the indices of $\bar{\bar{A}}_{ij}$ are raised and lowered with the conformal metric $\bar{\bar{A}}^{i}{}_{j} = \bar{\bar{\gamma}}^{ik}\bar{\bar{A}}_{kj}$. However, as indicated by the notation, with this rescaling $\bar{\bar{\gamma}}_{ij}$, $\bar{\bar{\psi}}$, $\bar{\bar{\phi}}$ and $\bar{\bar{A}}_{ij}$ are not tensors but tensor densities, they transform as Eq. (2.8) and their Lie derivative is Eq. (2.28) which is notable given d/dt defined in Eq. (3.10). $\bar{\bar{\psi}}$, $\bar{\bar{\phi}}$ have the same weight of $1/6$, then $\bar{\bar{\gamma}}_{ij}$ and $\bar{\bar{A}}_{ij}$ have a weight of $-2/3$ while in their contravariant form their weight is $2/3$.

Applying this decomposition to Eq. (3.32) provides evolution equations for the conformal factor $\bar{\bar{\phi}}$, and for the conformal spatial metric $\bar{\bar{\gamma}}_{ij}$

$$\frac{d\bar{\bar{\phi}}}{dt} = -\frac{1}{6}\alpha K, \qquad \frac{d\bar{\bar{\gamma}}_{ij}}{dt} = -2\alpha\bar{\bar{A}}_{ij}. \tag{3.35}$$

These are all stable first-order PDEs; indeed Eq. (3.32) is not posing stability concerns, Eq. (3.31) is the challenging equation. The evolution equation of the extrinsic curvature, Eq. (3.31), is split into its trace and traceless parts. The trace part provides the evolution equation of K, and although it depends on the trace of the 3-Ricci tensor, this is substituted with the Hamiltonian constraint Eq. (3.29) providing a stable evolution equation

$$\frac{dK}{dt} = -\gamma^{ij}D_i^{\{n\}}D_j^{\{n\}}\alpha + \alpha\left(2\bar{\bar{A}}^2 + \frac{1}{3}K^2\right) + \frac{\kappa}{2}\alpha\left(\rho^{\{n\}} + S^{\{n\}}\right). \tag{3.36}$$

The traceless part is expressed in terms of the conformal traceless part $\bar{\bar{A}}_{ij}$

$$\frac{d\bar{\bar{A}}_{ij}}{dt} = e^{-4\bar{\bar{\phi}}}\left(-D_{\langle i}^{\{n\}}D_{j\rangle}^{\{n\}}\alpha + \alpha^{(3)}R_{\langle ij\rangle} - \alpha\kappa S_{\langle ij\rangle}^{\{n\}}\right) + \alpha\left(K\bar{\bar{A}}_{ij} - 2\bar{\bar{A}}_{ik}\bar{\bar{A}}^{k}{}_{j}\right), \tag{3.37}$$

where $\langle ...\rangle$ is the traceless operator Eq. (2.26). This however still depends on the 3-Ricci tensor, ${}^{(3)}R_{ij}$, which is then calculated using the conformal 3-Ricci tensor ${}^{(3)}\bar{\bar{R}}_{ij}$ and additional terms that depend on $\bar{\bar{\phi}}$

$$\begin{aligned}
{}^{(3)}R_{ij} =& {}^{(3)}\bar{\bar{R}}_{ij} + {}^{(3)}R_{ij}^{\bar{\bar{\phi}}} \\
{}^{(3)}\bar{\bar{R}}_{ij} =& -\frac{1}{2}\bar{\bar{\gamma}}^{lm}\partial_l\partial_m\bar{\bar{\gamma}}_{ij} + \bar{\bar{\gamma}}_{k(i}\partial_{j)}{}^{(3)}\bar{\bar{\Gamma}}^{k} + {}^{(3)}\bar{\bar{\Gamma}}^{k}{}^{(3)}\bar{\bar{\Gamma}}_{(ij)k} \\
&+ \bar{\bar{\gamma}}^{lm}\left(2{}^{(3)}\bar{\bar{\Gamma}}^{k}{}_{l(i}{}^{(3)}\bar{\bar{\Gamma}}_{j)km} + {}^{(3)}\bar{\bar{\Gamma}}^{k}{}_{im}{}^{(3)}\bar{\bar{\Gamma}}_{klj}\right) \\
{}^{(3)}R_{ij}^{\bar{\bar{\phi}}} =& -2\bar{\bar{D}}_i\bar{\bar{D}}_j\bar{\bar{\phi}} - 2\bar{\bar{\gamma}}_{ij}\bar{\bar{D}}^k\bar{\bar{D}}_k\bar{\bar{\phi}} + 4\bar{\bar{D}}_i\bar{\bar{\phi}}\bar{\bar{D}}_j\bar{\bar{\phi}} - 4\bar{\bar{\gamma}}_{ij}\bar{\bar{D}}^k\bar{\bar{\phi}}\bar{\bar{D}}_k\bar{\bar{\phi}}
\end{aligned} \tag{3.38}$$

where $\bar{\bar{D}}$ is the covariant derivative of $\bar{\bar{\gamma}}_{ij}$. The mixed second-order derivatives in ${}^{(3)}\bar{\bar{R}}_{ij}$ are avoided as they are expressed using the conformal connection function

$${}^{(3)}\bar{\bar{\Gamma}}^{k} = \bar{\bar{\gamma}}^{ij}{}^{(3)}\bar{\bar{\Gamma}}^{k}{}_{ij} = -\partial_i\bar{\bar{\gamma}}^{ij} \tag{3.39}$$

which, instead of computing it from the metric, is considered a new variable with its own evolution equation

$$\begin{aligned}
\frac{d^{(3)}\bar{\bar{\Gamma}}^{i}}{dt} =& \bar{\bar{\gamma}}^{jk}\partial_j\partial_k\beta^i + \frac{1}{3}\bar{\bar{\gamma}}^{ij}\partial_j\partial_k\beta^k - 2\bar{\bar{A}}^{ij}\partial_j\alpha \\
&+ 2\alpha\left({}^{(3)}\bar{\bar{\Gamma}}^{i}{}_{jk}\bar{\bar{A}}^{jk} + 6\bar{\bar{A}}^{ij}\partial_j\phi - \frac{2}{3}\bar{\bar{\gamma}}^{ij}\partial_j K - \kappa\bar{\bar{\gamma}}^{ij}q_j^{\{n\}}\right)
\end{aligned} \tag{3.40}$$

that has been made more stable with the momentum constraint equation Eq. (3.30). ${}^{(3)}\bar{\bar{\Gamma}}^k$ is not actually a tensor density, but here it can be treated as a tensor density of weight $2/3$ in the Lie derivative of d/dt Eq. (3.10).

Thus this formalism provides a set of evolution equations for $\bar{\bar{\phi}}$, $\bar{\bar{\gamma}}_{ij}$, K, $\bar{\bar{A}}_{ij}$ and ${}^{(3)}\bar{\bar{\Gamma}}^k$, Eq. (3.35, 3.36, 3.37, 3.40), which are all well-posed. This has been demonstrated analytically (Nakamura, Oohara, and Kojima, 1987; Alcubierre, Allen, et al., 2000; Alcubierre, 2008) and numerically (Baumgarte and Shapiro, 1998).

3.4 Gauge choice

In NR the coordinate freedom of GR translates into initially defining α, β^i and γ_{ij} at the start of the simulation and making a choice as to how α and β^i evolve, while γ_{ij} evolves according to Einstein's field equations, see Section 3.3.3. Amongst these gauge options, a non-exhaustive list is presented below where a lapse condition is referred to as a type of slicing. See Section 4.2.3 for further discussion in the Cosmological context.

- ❖ **Synchronous gauge:** where coordinate time coincides with proper time $t = \tau$. This is provided by (Darmois, 1927)

$$\alpha = 1, \qquad \partial_t \alpha = \beta^i = \partial_t \beta^i = 0. \tag{3.41}$$

  In NR, this is commonly called the geodesic gauge because, as Eq. (3.4) and Eq. (2.17) show, if there is no lapse, these coordinates do not accelerate and thus follow geodesic curves, $\mathfrak{a}_\mu = n^\mu \nabla_\mu n^\alpha = 0$. Naturally, these geodesic observers will focus towards gravitational sources, and so simulations in this gauge are susceptible to creating coordinate singularities as the path of different observers cross each other, making $\gamma \to 0$.

- ❖ **Comoving gauge:** α and β^i are chosen such that there is no energy flux $q^{\{n\}i} = 0$; in this case the coordinates are those of a Lagrangian observer evolving with the fluid

$$n^\mu = u^\mu, \qquad K_{ij} = -\Theta_{ij} \tag{3.42}$$

  where the normal to the hypersurface is the fluid flow, and the extrinsic curvature is the fluid expansion. This is possible only for an irrotational fluid $\omega_{\alpha\beta} = 0$.

- ❖ **Maximal slicing:** Here, the volume element takes its maximal size and is constant. The volume being preserved along n^μ means that the extrinsic curvature and its time derivative are zero, (Smarr and York, 1978a; York, 1979)

$$\gamma = const, \qquad K = \partial_t K = 0, \tag{3.43}$$

  where the K evolution equation (trace of Eq. (3.31)) needs to be solved to provide α. This means that these coordinates do not expand or contract. Should there be a black hole, α freezes such that γ can remain constant and the singularity is avoided[3]. However, freezing a section of the grid while the rest continues to evolve can lead to issues with slice stretching. Additionally,

[3] Though not always (Eardley and Smarr, 1979).

this can only be used for asymptotically flat spacetimes, so for Cosmology, an alternative is to consider constant mean curvature where K is instead a homogeneous function (Barrera-Hinojosa and Li, 2020b).

❖ **Bona-Masso family:** In choosing an evolution equation for α, multiple slicing conditions can be summarised by (Bona et al., 1995)

$$\frac{d\alpha}{dt} = -f\alpha^n K \tag{3.44}$$

with $f \geqslant 0$ and n an integer. The BSSNOK formulation requires $f > 1$ to be well-posed, and if $n < 2$, this condition will present strong singularity avoidance, freezing the black hole region (Alcubierre, 2008). Two distinct cases are discussed below, but note that in cosmology, a common modification is subtracting a homogeneous function or scalar to K (Giblin, Mertens, Starkman, and Tian, 2019b).

✦ **Harmonic slicing:** Requiring the coordinates to satisfy Laplace's equation $\nabla_\mu \nabla^\mu x^\alpha = 0$ has the capacity to formulate Einstein's field equations into wave equations (Fourès-Bruhat, 1952). Considering only the temporal part, this provides a condition for the lapse

$$\nabla_\mu \nabla^\mu x^0 = 0 \quad \Rightarrow \quad g^{\mu\nu}\Gamma^0{}_{\mu\nu} = 0 \quad \Rightarrow \quad \frac{d\alpha}{dt} = -\alpha^2 K. \tag{3.45}$$

However, this does not satisfy the BSSNOK requirements to be well-posed.

✦ **1+log slicing:** An option that is well-posed for BSSNOK and avoids singularities, i.e. $f > 1$ and $n < 2$ in Eq. (3.44), is provided by (Bernstein, 1993; Anninos et al., 1995)

$$\frac{d\alpha}{dt} = -2\alpha K \quad \Rightarrow \quad \alpha = 1 + \ln(\gamma). \tag{3.46}$$

Which has become the preferred slicing condition for black hole simulations.

❖ **Harmonic shift condition:** Just like the harmonic slicing, coordinates satisfying the Laplace equation $\nabla_\mu \nabla^\mu x^\alpha = 0$, only considering the spatial part this time

$$\nabla_\mu \nabla^\mu x^i = 0 \quad \Rightarrow \quad g^{\mu\nu}\Gamma^i{}_{\mu\nu} = 0. \tag{3.47}$$

provides an evolution equation for β^i (Alcubierre, 2008). This can be used independently of the harmonic slicing condition.

❖ **Minimal strain/distortion shift condition:** Defining the coordinate strain and distortion along coordinate time as $\Theta_{ij} = \frac{1}{2}\mathcal{L}_t\gamma_{ij}$ and $\Sigma_{ij} = \Theta_{\langle ij\rangle}$ respectively, which are analogous to the expansion and shear tensors. The shift vector can be defined such that one or the other is minimised according to the minimal strain or minimal distortion conditions

$$D_i^{\{n\}}\Theta^{ij} = 0, \qquad D_i^{\{n\}}\Sigma_{ij} = 0 \tag{3.48}$$

respectively (Smarr and York, 1978a,b). While the minimal strain condition reduces variation in the size of the volume element, the minimal strain condition reduces its shape (or shear). The latter is then more appropriate for cosmological simulations and $D_i^{\{n\}}\Sigma_{ij} = 0$ is equivalent to $\partial_t{}^{(3)}\bar{\bar{\Gamma}}^i = 0$ known as the Gamma freezing gauge which simplifies the BSSNOK evolution equations. Furthermore, for a Minkowski spacetime $\eta_{\alpha\beta}$ with a small perturbation $h_{\alpha\beta}$, $g_{\alpha\beta} =$

$\eta_{\alpha\beta} + h_{\alpha\beta}$, in vacuum, the minimal distortion condition implies that the traceless part of $h_{\alpha\beta}$ is purely tensorial $h_{\langle\alpha\beta\rangle} = h^{TT}_{\alpha\beta}$ (Smarr and York, 1978a), which is the behaviour described in the transverse-traceless gauge. See Section 4.2.1 for scalar vector tensor decomposition.

- **Gamma driver shift condition:** Inspired by the Gamma freezing condition, it has been generalised to have

$$\partial_t^2 \beta^i = \alpha^2 \xi \partial_t {}^{(3)}\bar{\bar{\Gamma}}^i - \eta \partial_t \beta^i \tag{3.49}$$

where $\xi > 0$ is a function of α and x^i and controls the wave speed, while the second term on the right-hand side is a damping term adjusted with the $\eta > 0$ parameter. This also minimises the volume distortion, where it reduces slice stretching for rotating black hole simulations. The accuracy of binary black hole simulations if further improved with the inclusion of advection terms $\beta^i \partial_i$ with

$$\frac{d^2 \beta^i}{dt^2} = \alpha^2 \xi \frac{d {}^{(3)}\bar{\bar{\Gamma}}^i}{dt} - \eta \partial_t \beta^i \tag{3.50}$$

where $d/dt = \partial_t - \beta^i \partial_i$ (Alcubierre, 2008).

- **Puncture gauge:** The combination of the 1+log slicing and the Gamma driver conditions together are referred to as the puncture gauge; their combined properties make this the preferred gauge to simulate black holes (Baiotti and Rezzolla, 2006).

3.5 Gravito-electromagnetism

To express $E^{\{n\}}_{ij}$ and $B^{\{n\}}_{ij}$ with this formulation, the Weyl tensor in Eq. (2.68) needs to be replaced by 3+1 quantities. For $E^{\{n\}}_{ij}$ one starts with the Gauss equation Eq. (3.26), this is then contracted with $\gamma^{\beta\nu}$ and rearranged to find $n^\beta n^\nu R_{\alpha\beta\mu\nu}$. The resulting expression is introduced into Eq. (2.68), then the remaining 4-dimensional Ricci terms are substituted using Einstein's field equations Eq. (2.39) and its contraction, such that (Alcubierre, 2008)

$$E^{\{n\}ij} = {}^{(3)}R^{ij} + K^{ij}K - K^{ik}K^j_k - \frac{2}{3}\gamma^{ij}\left(\Lambda + \kappa\rho^{\{n\}}\right) - \frac{\kappa}{2}S^{\{n\}}_{\langle ij\rangle}. \tag{3.51}$$

Note that $E^{\{n\}\alpha\beta}$ is purely spatial, indeed from Eq. (2.68) $E^{\{n\}\alpha\mu} = \alpha^2 C^{\alpha 0 \mu 0}$, and the antisymmetric nature of the Weyl tensor implies that $E^{\{n\}\alpha\mu}$ can only have spatial components. One can then define $E^{\{n\}i}{}_j = E^{\{n\}ik}\gamma_{kj}$ and $E^{\{n\}}_{ij} = \gamma_{ik}\gamma_{jl}E^{\{n\}kl}$. In lowering the indices of $E^{\{n\}\alpha\beta}$ with $\gamma_{\alpha\beta}$, however, we see that the temporal components of $E^{\{n\}}_{\alpha\beta}$ do not vanish when the shift is non zero. $E^{\{n\}\alpha\beta}$ and $E^{\{n\}}_{\alpha\beta}$ can be written in terms of the shift and the space components, as in Eq. (3.13).

In Eq. (3.51), it is the Hamiltonian constraint Eq. (3.29) that ensures that $E^{\{n\}ij}$ remains traceless. However, in NR simulations, this constraint is used as a validity check, therefore, although small, it tends to be non-zero. This carries into $E^{\{n\}ij}$ when computed with Eq. (3.51), where the non-zero trace would correspond to the violation of the Hamiltonian constraint. Then, in order to avoid introducing errors in the calculation of $E^{\{n\}}_{ij}$, in particular a non-zero trace, we substitute in Eq. (3.51) the term $\Lambda + \kappa\rho^{\{n\}}$ from the Hamiltonian constraint, obtaining

$$E^{\{n\}}_{ij} = {}^{(3)}R_{\langle ij\rangle} + K_{\langle ij\rangle}K - K^k{}_{\langle i}K_{j\rangle k} - \frac{\kappa}{2}S^{\{n\}}_{\langle ij\rangle} \tag{3.52}$$

where the traceless operator Eq. (2.26) makes it explicit that this expression remains traceless up to numerical errors.

Similarly, $B^{\{n\}}_{ij}$ can be expressed using the Codazzi equation Eq. (3.25). This is contracted with $\gamma^{\alpha\mu}$ to provide $n^\beta R_{\nu\beta}$, and it is rearranged to have $n^\beta R_{\alpha\beta\mu\nu}$. These two terms can be introduced into the expression for $B^{\{n\}}_{ij}$, Eq. (2.68), so that

$$B^{\{n\}}_{ij} = \epsilon^{\{n\}kl}{}_j \left(D^{\{n\}}_k K_{li} + \frac{1}{2}\gamma_{ik}\left(D^{\{n\}}_l K - D^{\{n\}}_m K^m{}_l \right) \right). \tag{3.53}$$

At this point, the momentum constraint Eq. (3.30) is typically inserted (Alcubierre, 2008) to simplify the second term. Again, to avoid introducing errors in the numerical computation, we abstain from taking this last step. Here $B^{\{n\}}_{ij}$ can be seen to be trace-less because of the anti-symmetry of the Levi-Civita tensor. Finally, $B^{\{n\}}_{\alpha\beta}$ can be expressed in terms of the shift and its space components in the same way that $K_{\alpha\beta}$ and $E^{\{n\}}_{\alpha\beta}$ are, as in Eq. (3.13).

$E^{\{n\}}_{\alpha\beta}$ and $B^{\{n\}}_{\alpha\beta}$ calculated with Eq. (3.52) and Eq. (3.53), exclusively provide the electric and magnetic parts of the Weyl tensor projected orthogonally to n^μ, i.e. on γ_{ij}, as indicated with the $\{n\}$ superscript. If one were to prefer $E^{\{u\}}_{\alpha\beta}$ and $B^{\{u\}}_{\alpha\beta}$, where they are projected orthogonally to the fluid flow u^μ (since these have specific physical meaning as discussed in Section 2.5.1), then these can be obtained by constructing $C_{\alpha\beta\mu\nu}$ from $E^{\{n\}}_{\alpha\beta}$ and $B^{\{n\}}_{\alpha\beta}$ with Eq. (2.72), then projecting it with u^μ.

Note that $C_{\alpha\beta\mu\nu}$ is not gauge independent; the Weyl tensor computed with two different slicings will differ, and these can furthermore be projected on any arbitrary time-like vector. Here, we specifically discuss the Weyl tensor computed with the slicing of the simulation (along n^μ), and use the notation $\{n\}$ or $\{u\}$ to distinguish upon which vector it is further decomposed.

3.6 Numerical methods

Since the formalism of NR was created, there has been interest in running such simulations; with the advancement of numerical techniques, many codes are now available. A non-exhaustive list of named NR codes includes

- BAM (Brügmann, 1999; Thierfelder, Bernuzzi, and Brügmann, 2011; Chaurasia, Dietrich, and Rosswog, 2021)
- BAMPS (Hilditch, Weyhausen, and Brügmann, 2016)
- BHAC (Porth et al., 2017)
- CosmoGRaPH (Mertens, Giblin, and Starkman, 2016)
- DENDRO-GR (Fernando et al., 2019)
- *Einstein Toolkit* (n.d.) (Löffler et al., 2012; Brandt et al., 2020)
- HAD (Anderson et al., 2006)
- Hahndol (Imbiriba et al., 2004; Baker, Centrella, et al., 2006)
- KADATH (Grandclément, 2010)
- `GR-Athena++` (Daszuta et al., 2021)

- GRChombo (Clough, Figueras, et al., 2015; Andrade et al., 2021)
- Gmunu (Cheong et al., 2021)
- OllinSphere2 (Alcubierre and Mendez, 2011; Torres et al., 2014)
- SAGRA-MPI (Yamamoto, Shibata, and Taniguchi, 2008)
- Simflowny (Palenzuela et al., 2018)
- SFINGE (Meringolo and Servidio, 2021)
- SpEC (Kidder et al., 2000; Boyle, Lindblom, et al., 2007)
- `SPHINCS_BSSN_v1.0` (Rosswog, Torsello, and Diener, 2023)
- Whisky (Giacomazzo and Rezzolla, 2007)

but many more (Musco, Miller, and Rezzolla, 2005; East, Pretorius, and Stephens, 2012; Rekier, Cordero-Carrión, and Füzfa, 2015; Yoo, Harada, and Okawa, 2017; Escrivà, 2020) have been created with various motivations, each with its own strengths. While some may share parts of their infrastructure, these can be distinguished based on the NR formalism, fluid treatment, underlying grid, mesh refinement, parallelism, or evolution schemes. On this last point, evolution schemes can either be based on spectral methods, e.g. KADATH and SpEC, or based on finite difference (FD) methods. While results from spectral methods can be multiple orders of magnitude more accurate than FD methods, they are notoriously more challenging to implement, making FD schemes more popular. Therefore, some of the relevant FD schemes are presented in the following sections.

Based on their application, most were created for strong gravity simulations, while CosmoGRaPH has been exclusively created for cosmological simulations of LSS with the capacity to simulate either a fluid or particles, yet it is general enough to simulate a lattice of black holes (Giblin, Mertens, Starkman, and Tian, 2019a). This cosmological application has been explored in full NR with codes in spherical symmetry (Torres et al., 2014; Rekier, Cordero-Carrión, and Füzfa, 2015) and more in general without symmetry (Bentivegna and Bruni, 2016; East, Wojtak, and Pretorius, 2019; Macpherson and Heinesen, 2021). Yet because particle simulations are not the strong suit of NR codes, further relativistic codes have been created using different approaches

- gevolution (Adamek, Daverio, et al., 2013; Adamek, Durrer, and Kunz, 2014; Adamek, Daverio, et al., 2016b) N-body code in the Poisson gauge in the weak field limit
- GRAMSES (Barrera-Hinojosa and Li, 2020a,b) N-body code extended to include all scalar and vector terms of GR in the constant mean curvature and minimal distortion gauge
- simsilun (Bolejko, 2018) fluid NR code exclusively for an irrotational silent universe

Within this wealth of options, this thesis uses the Einstein Toolkit code following (Bentivegna and Bruni, 2016), whose structure and implementation are described in Section 6.2. See Section 4.3.5 for further discussion about cosmological simulations.

3.6.1 Differentiating

To differentiate a quantity, the FD schemes are based on the Taylor series where an infinitely differentiable function $f(x)$ is expressed in terms of a power series of its derivatives at x_0 as (Landau, Páez, and Bordeianu, 2007; Shibata, 2015)

$$\begin{aligned} f(x) =& \sum_{n=0}^{\infty} \frac{f^{(n)}(x_0)}{n!} (x - x_0)^n \\ =& f(x_0) + f^{(1)}(x_0)\,(x - x_0) + \frac{f^{(2)}(x_0)}{2} (x - x_0)^2 + \frac{f^{(3)}(x_0)}{6} (x - x_0)^3 \\ &+ \frac{f^{(4)}(x_0)}{24} (x - x_0)^4 + \frac{f^{(5)}(x_0)}{120} (x - x_0)^5 + \frac{f^{(6)}(x_0)}{720} (x - x_0)^6 + \ldots \end{aligned} \tag{3.54}$$

While we know the value of $f(x)$ we seek $f^{(1)}(x_0)$. The x parameter in Eq. (3.54) can be chosen at any location; therefore, we can create a system of equations to isolate $f^{(1)}(x_0)$. Consider the location $x_0 + \Delta x$ where

$$f(x_0 + \Delta x) = f(x_0) + f^{(1)}(x_0)\Delta x + \mathcal{O}(\Delta x^2) \tag{3.55}$$

rearranging this for $f^{(1)}(x_0)$ provides

$$\begin{aligned} f^{(1)}(x_0) &= \frac{f(x_0 + \Delta x) - f(x_0)}{\Delta x} + \mathcal{O}(\Delta x) \\ &= \lim_{\Delta x \to 0} \frac{f(x_0 + \Delta x) - f(x_0)}{\Delta x} \end{aligned} \tag{3.56}$$

where all terms with Δx or higher are not included in the equation. This will lead to a truncation error $\mathcal{O}(\Delta x)$; however, as $\Delta x \to 0$, this expression will converge to the true value. This expression will have a first-order convergence. To increase the order, additional locations are considered, say the locations before x_0 for a backward mask, the locations around x_0 for a centred mask, or the locations after x_0 for a forward mask (as is the case with Eq. (3.56)). If two locations are provided for each scheme, each system is rearranged to provide the following backward, centred, and forward second-order schemes

$$\begin{aligned} f^{(1)}(x_0) &= \frac{1}{\Delta x}\left(\frac{1}{2} f(x_0 - 2\Delta x) - 2f(x_0 - \Delta x) + \frac{3}{2} f(x_0)\right) + \mathcal{O}(\Delta x^2) \\ f^{(1)}(x_0) &= \frac{1}{\Delta x}\left(-\frac{1}{2} f(x_0 - \Delta x) + \frac{1}{2} f(x_0 + \Delta x)\right) + \mathcal{O}(\Delta x^2) \\ f^{(1)}(x) &= \frac{1}{\Delta x}\left(-\frac{3}{2} f(x_0) + 2f(x_0 + \Delta x) - \frac{1}{2} f(x_0 + 2\Delta x)\right) + \mathcal{O}(\Delta x^2) \end{aligned} \tag{3.57}$$

respectively. Providing more locations will further increase the convergence scheme. The weights of each location in the various schemes are summarised in Table (3.1) where Eq. (3.56) and Eq. (3.57) can be recognised. These schemes were implemented in the codes described in Chapter 5, which were applied in Chapter 6. See Appendix C on how to compute errors and convergence, and Appendix A where we show the centred schemes to outperform the backward and forward ones.

Order	-6	-5	-4	-3	-2	-1	0	1	2	3	4	5	6
	Backwards												
1						-1	1						
2					$\frac{1}{2}$	-2	$\frac{3}{2}$						
4			$\frac{1}{4}$	$-\frac{4}{3}$	3	-4	$\frac{25}{12}$						
6	$\frac{1}{6}$	$-\frac{6}{5}$	$\frac{15}{4}$	$-\frac{20}{3}$	$\frac{15}{2}$	-6	$\frac{49}{20}$						
	Centred												
2						$-\frac{1}{2}$	0	$\frac{1}{2}$					
4					$\frac{1}{12}$	$-\frac{2}{3}$	0	$\frac{2}{3}$	$-\frac{1}{12}$				
6				$-\frac{1}{60}$	$\frac{3}{20}$	$-\frac{3}{4}$	0	$\frac{3}{4}$	$-\frac{3}{20}$	$\frac{1}{60}$			
	Forwards												
1							-1	1					
2							$-\frac{3}{2}$	2	$-\frac{1}{2}$				
4							$-\frac{25}{12}$	4	-3	$\frac{4}{3}$	$-\frac{1}{4}$		
6							$-\frac{49}{20}$	6	$-\frac{15}{2}$	$\frac{20}{3}$	$-\frac{15}{4}$	$\frac{6}{5}$	$-\frac{1}{6}$

Table 3.1: Coefficients of backward, centred and forward finite differencing schemes at second, fourth and sixth order (Fornberg, 1988).

3.6.2 Integrating

PDEs have multiple independent variables, time t and space x^i, which are separated to be integrated. This is key to the method of lines technique (Schiesser, 1991) where the spatial derivatives are replaced by their numerical approximations, given the schemes described in Section 3.6.1, and treated as source terms such that the PDE can be treated as an ordinary differential equation with only time derivatives. In this case, the initial value problem (or Cauchy problem) is provided by a set of evolution equations and initial conditions

$$\partial_t f = S\left(f,\ t\right) \qquad f\left(t_{IN}\right) = f_{IN} \tag{3.58}$$

where $S\left(f,t\right)$ corresponds to the source terms of the evolution equation. This is typically studied for well-posedness; however, now we seek to evolve this system.

One way to integrate this is by using Taylor's expansion Eq. (3.56) (with t instead of x) where $f\left(t+\Delta t\right)$ is isolated and $f^{(1)}\left(x_0\right)$ (or $\partial_t f$ here) is replaced by the source terms from Eq. (3.58) providing

$$f\left(t+\Delta t\right) = f\left(t\right) + \Delta t S\left(f,\ t\right) + \mathcal{O}\left(\Delta t^2\right) \tag{3.59}$$

which simply corresponds to Euler's first-order forward-stepping rule (Landau, Páez, and Bordeianu, 2007). The initial conditions provide the right-hand side of the first step, and the left-hand side can then be used for the next step and so on. This is an explicit iterative method where the system at the current time is used to calculate the system's state at a later time.

Next, we shall consider the more robust Runge-Kutta method. To start, we Taylor expand the source function around the point in time $t_n + \frac{\Delta t}{2}$, i.e. the time at the n^{th} iteration with half a time step Δt. To simplify notation we use $t_{n+\frac{1}{2}} = t_n + \frac{\Delta t}{2}$ and $f_{n+\frac{1}{2}} = f\left(t_{n+\frac{1}{2}}\right)$, such that $S\left(f,\ t\right)$ around $t_{n+\frac{1}{2}}$ is

$$\begin{aligned} S\left(f,\ t\right) =& S\left(f_{n+\frac{1}{2}},\ t_{n+\frac{1}{2}}\right) \\ &+ \left(t - t_{n+\frac{1}{2}}\right) \frac{\partial S\left(f_{n+\frac{1}{2}},\ t_{n+\frac{1}{2}}\right)}{\partial t} + \mathcal{O}\left(\left(t - t_{n+\frac{1}{2}}\right)^2\right). \end{aligned} \tag{3.60}$$

Integrating this from t_n to $t_{n+1} = t_n + \Delta t$, where all except the t terms are constant provides

$$\begin{aligned} \int_{t_n}^{t_{n+1}} S\left(f,\ t\right) dt &= \Delta t S\left(f_{n+\frac{1}{2}},\ t_{n+\frac{1}{2}}\right) + \mathcal{O}\left(\Delta t^3\right) \\ \Rightarrow f_{n+1} - f_n &= \Delta t S\left(f_{n+\frac{1}{2}},\ t_{n+\frac{1}{2}}\right) + \mathcal{O}\left(\Delta t^3\right) \\ \Rightarrow f_{n+1} &= f_n + \Delta t S\left(f_{n+\frac{1}{2}},\ t_{n+\frac{1}{2}}\right) + \mathcal{O}\left(\Delta t^3\right) \end{aligned} \tag{3.61}$$

where the integrated second-order term of Eq. (3.60) cancels out when t_{n+1} and $t_{n+\frac{1}{2}}$ are expanded, and the left-hand side term is replaced by its integral provided by Eq. (3.58). The remaining issue with this expression is that $f_{n+\frac{1}{2}}$ is unknown; trying to find it with the same methodology will require $f_{n+\frac{1}{4}}$ and so on, therefore an other scheme needs to be used, notably Euler's method Eq. (3.59), the expression then becomes second-order Runge-Kutta evolution scheme

$$f_{n+1} = f_n + \Delta t S\left(f_n + \frac{\Delta t}{2} S\left(f_n,\ t_n\right),\ t_{n+\frac{1}{2}}\right) + \mathcal{O}\left(\Delta t^2\right) \tag{3.62}$$

where $f_n = f\left(t_n\right)$ and t_n are the input information to determine the values at the next step.

Using the same methodology, the fourth-order Runge-Kutta evolution scheme is

$$\begin{aligned} f_{n+1} &= f_n + \frac{\Delta t}{6}\left(k_1 + 2k_2 + 2k_3 + k_4\right) + \mathcal{O}\left(\Delta t^4\right) \\ &\begin{cases} k_1 = S\left(f_n, t_n\right) \\ k_2 = S\left(f_n + k_1 \frac{\Delta t}{2},\ t_n + \frac{\Delta t}{2}\right) \\ k_3 = S\left(f_n + k_2 \frac{\Delta t}{2},\ t_n + \frac{\Delta t}{2}\right) \\ k_4 = S\left(f_n + k_3 \Delta t,\ t_n + \Delta t\right) \end{cases} \end{aligned} \tag{3.63}$$

where the source terms need to be calculated four times, and interpolated between time steps for $t_n + \frac{\Delta t}{2}$, to advance one step, yet f_n is the only information needed.

Note that neither Euler nor Runge-Kutta methods presented here are symplectic. This means that when applying these schemes to a system of equations with conserved quantities (such as the Hamiltonian and momentum constraint here), the truncation error may accumulate over time, causing the solution to drift and violate the conservation properties of the system. Hence the importance of monitoring the constraint violations.

4 - Cosmology

Cosmology is the field of study of the universe as a whole. As we look out into the starry night, we see stars in all directions as far as the eye can see, and with binoculars, even more of them. These stars have differing luminosity, and the further they are, the dimmer they appear. What we can see has led to the cosmological principle (Peacock, 1999): the universe is homogeneous and isotropic. Yet this is challenged by Olber's paradox or dark night sky paradox: if the universe is infinite static, and eternal, then the light from an infinity of stars would accumulate to completely fill the sky such that there would be no darkness. As this is not what we see, there must be something wrong with these assumptions, so further observations are needed.

Some of these stars appear grouped, forming clusters, and some luminous regions do not look like point sources; these were then called nebulae. Placing ourselves in the universe, (Hubble, 1929) has shown that most of these astronomical objects are relatively close, contained in our galaxy, the Milky Way. Yet some of the nebulae are actually other galaxies extremely far away populating the universe, and they are moving away from us as their electromagnetic light is redshifted; the further away, the larger the redshift, meaning that each galaxy is expanding away from the other. The distance between us and these galaxies and their redshift is related by the current expansion rate of the universe, also known as Hubble's constant H_0.

Another pivotal discovery is the detection of the same faint electromagnetic signal from every direction in the universe that follows a perfect black body curve (Penzias and Wilson, 1965). This Cosmic Microwave Background (CMB) proves that in the past, the universe had a radiation-dominated era where there was only plasma and that the universe has expanded out of this state such that the photons are free to travel and be redshifted with the expansion of the universe. This CMB is the furthest possible electromagnetic observation we can measure, prior to this all emitted photons were absorbed straight away.

These two observational facts have confirmed the Big Bang theory (Friedmann, 1922, 1924; Lemaître, 1931, 1933) of the evolution of the universe: which was hot and dense at early times and has expanded out of that state and continues to expand today. This expansion with an initially dense state answers Olber's paradox leaving the cosmological principle intact; we, therefore, discuss a homogeneous isotropic and expanding universe in Section 4.1.

These measurements have since been improved with more astronomical objects and increasingly accurate observational tools. To measure short distances, one can use parallax, then further out, one needs to know the absolute magnitude of an astronomical object and compare it to the apparent magnitude measured (Schneider, 2015). Such objects are referred to as standard candles, they include cepheids and type Ia supernovae. Probing large distances has shown that the universe is not only expanding, but expanding at an accelerated rate (Riess, Filippenko, et al., 1998). This new force

driving this acceleration is called dark energy; it can be accounted for in Einstein's field equations, Eq. (2.39), by a positive constant, the cosmological constant Λ (Einstein, 1917).

Additionally, it was discovered that the radial velocity of stars within galaxies differs from that expected according to the observed mass of the galaxy (Rubin and Ford, 1970). So there must be more matter that does not emit any electromagnetic signal and only interacts gravitationally, i.e. Cold Dark Matter (CDM) (Peebles, 1982).

Current measurements of the CMB confirm the ΛCDM model (Planck Collaboration, 2020), finding that the universe content is composed of 5% of normal visible matter, 27% of dark matter, and 68% of dark energy, although the inferred value of H_0 differs from that measured using type Ia supernovae (Riess, Yuan, et al., 2022). The mystery around this dark content and measurement discrepancies lead us to continually question our understanding of the universe (Di Valentino et al., 2021; Abdalla et al., 2022).

While the assumptions of the cosmological principle have held on average and at large scales, there are small fluctuations in the CMB temperature (Planck Collaboration, 2020) meaning that the CMB is neither isotropic nor homogeneous. These inhomogeneities can be described with cosmological perturbation theory, where they are depicted as small perturbations to the homogeneous universe, as discussed in Section 4.2. Indeed reflecting on our position in the universe, our presence proves that the universe is not perfectly homogeneous, it can only be treated as statistically homogeneous. As observed, the universe is filled with stars populating clusters and galaxies which have grouped together, forming galaxy clusters that create the large-scale structures (LSS) that fill our universe with a cosmic web whose notable elements are: haloes, filaments, sheets and voids (Peebles, 1980; Springel, Frenk, and White, 2006). How these structures form is key to this thesis. Mapping the CMB fluctuations to the present-day universe, over-dense (OD) and under-dense (UD) regions are identified, and during the matter-dominated era, the sufficiently OD regions have grown to accumulate enough matter to locally counter the universe's expansion and be gravitationally bound allowing them to create the relevant astronomical objects (Mo, Bosch, and White, 2010), some models depicting this behaviour are discussed in Section 4.3.

4.1 Homogeneous & isotropic universe

Assuming a homogeneous and isotropic universe, we discuss its spacetime, matter, constraint and evolution equations with their solutions below. Since the terms introduced here are relevant in the next sections and referred to as the background quantities, we define these with an overhead bar to clearly identify them.

4.1.1 Spacetime

The FLRW metric, named after Friedmann (1922, 1924), Lemaître (1931, 1933), Robertson (1935, 1936a,b), and Walker (1937), provides a homogeneous and isotropic spacetime. It is given below in comoving spherical coordinates using the 4-dimensional and 3-dimensional metric $\bar{g}_{\alpha\beta}$ and $\bar{\gamma}_{ij}$

respectively (Vittorio, 2018)

$$\begin{aligned} ds^2 &= \bar{g}_{\alpha\beta} dx^\alpha dx^\beta \\ &= -d\tau^2 + \bar{\gamma}_{ij} dx^i dx^j \\ &= -d\tau^2 + a^2(\tau) \left(\frac{dr^2}{1-kr^2} + r^2 d\Omega^2 \right) \\ &= a^2(\eta) \left(-d\eta^2 + \frac{dr^2}{1-kr^2} + r^2 d\Omega^2 \right) \end{aligned} \tag{4.1}$$

with r the comoving radial coordinate, $d\Omega^2 = d\theta^2 + \sin^2(\theta) d\phi^2$ the metric of a two-sphere with θ and ϕ the polar and azimuthal angles, and τ and η are respectively the proper and conformal time. The time derivatives are denoted with an overhead dot and a superscript dash as

$$\begin{gathered} d\tau = a(\eta) d\eta, \\ \frac{df}{d\tau} = \dot{f}, \qquad \frac{df}{d\eta} = f'. \end{gathered} \tag{4.2}$$

$a(\tau)$ is the scale factor to be determined in Section 4.1.4, it quantifies the scale over which a distance has grown from the reference point in time τ_R where it is normalised $a(\tau_R) = 1$. This means that a proper physical distance d_{phy} that evolves over time is related to the constant comoving distance d_{com} as $d_{phy}(\tau) = a(\tau) d_{com}$, then given the normalisation of the scale factor, the comoving distance corresponds to the physical distance at the reference time $d_{phy}(\tau_R) = d_{com}$. A typical choice for τ_R is today, while in cosmological NR simulations, it is common to see it chosen as the initial simulation time.

k is the curvature constant, which can be set to $+1$, 0, or -1 for closed, flat or open curvatures with the units of r accordingly defined. With this spacetime metric, the corresponding Weyl tensor and 4-dimensional and 3-dimensional Ricci tensor and scalar are

$$\begin{gathered} \bar{C}_{\alpha\beta\mu\nu} = 0, \\ \bar{R}_{00} = -3\frac{\ddot{a}}{a}, \qquad \bar{R}_{ij} = \frac{\bar{\gamma}_{ij}}{a^2} \left(a\ddot{a} + 2\dot{a}^2 \right) + {}^{(3)}\bar{R}_{ij}, \qquad \bar{R} = \frac{6}{a^2} \left(a\ddot{a} + \dot{a}^2 \right) + {}^{(3)}\bar{R}, \\ {}^{(3)}\bar{R}_{ij} = \frac{2k}{a^2} \bar{\gamma}_{ij}, \qquad {}^{(3)}\bar{R} = \frac{6k}{a^2}, \end{gathered} \tag{4.3}$$

where $\bar{R}_{\alpha\beta}$ and ${}^{(3)}\bar{R}_{ij}$ have no off-diagonal terms and ${}^{(3)}\bar{R}$ emphasises the role that k has. The Weyl tensor is zero indicating that the FLRW spacetime is conformally flat, i.e. of Petrov type O, see Section 2.5.4 about different Petrov types. Note that should the spacetime be flat $k = 0$, the metric, its inverse and determinant can be expressed with Cartesian coordinates as

$$\bar{\gamma}_{ij} = a^2(\tau) \delta_{ij} \qquad \bar{\gamma}^{ij} = a^{-2}(\tau) \delta^{ij} \qquad \bar{\gamma} = a^6(\tau) \tag{4.4}$$

and clearly given Eq. (4.3), ${}^{(3)}\bar{R}_{ij} = {}^{(3)}\bar{R} = 0$.

4.1.1.1 Hubble expansion

The universe's expansion can be measured with standard candles (Schneider, 2015) whose relation between the redshift z or recession velocity v and its physical distance d_{phy} is such that (Hubble, 1929)

$$v(\tau) = z(\tau) = H(\tau)d_{phy}(\tau). \tag{4.5}$$

The units are accordingly v length/time, d_{phy} length, and H 1/time. The recession velocity is simply the time derivative of the physical distance $v = d(d_{phy})/d\tau = \dot{d}_{phy}$. Then, using the scale factor where $d_{phy}(\tau) = a(\tau)d_{com}$, the Hubble scalar is recognisable as

$$H(\tau) = \frac{\dot{d}_{phy}(\tau)}{d_{phy}(\tau)} = \frac{\dot{a}(\tau)}{a(\tau)} = \frac{1}{a(\tau)}\frac{da(\tau)}{d\tau}. \tag{4.6}$$

The Hubble scalar H, the rate of change of distances, is shown to quantify the universe's expansion. Its inverse provides the Hubble time, $\tau_H = H^{-1}$, that corresponds to the age of the universe only if a evolves linearly in time, however amongst the models discussed in Section 4.1.4 this is only relevant for the Milne model, see Section 4.1.4.1 which despite this still provides the order of magnitude. Note that for the conformal time η, the derivation of the scale factor with respect to η provides the conformal Hubble scalar

$$\mathcal{H}(\eta) = \frac{a'(\eta)}{a(\eta)} = \frac{1}{a(\eta)}\frac{da(\eta)}{d\eta}. \tag{4.7}$$

The redshift z, due to the Doppler effect, quantifies the wavelength shift between the electromagnetic light observed today τ_0 where $z(\tau_0) = 0$ and $a(\tau_0) = a_0$ and when it was emitted τ. This corresponds to the ratio of physical distances between these two times

$$\frac{d_{phy}(\tau)}{d_{phy}(\tau_0)} = \frac{a(\tau)}{a_0} = \frac{1}{1+z(\tau)}, \qquad \frac{d_{phy}(\tau_1)}{d_{phy}(\tau_2)} = \frac{a(\tau_1)}{a(\tau_2)} = \frac{1+z(\tau_2)}{1+z(\tau_1)}. \tag{4.8}$$

The cumulative effect in Eq. (4.5) with an expanding universe $H > 0$ shows that the larger the distance d_{phy}, the larger the recession velocity v to the point where it is larger than the speed of light $v > c$, this identifies the Hubble distance or radius $R_H = cH^{-1}$ within which spacetime is causally connected, which is called the *Hubble horizon* or Hubble sphere. This differs from other types of observational boundaries (Davis and Lineweaver, 2004) such as the *past light cone* which encompasses all past events whose information is able to reach us. This will include events that have receded out of the light cone, yet we can still detect their past light, measuring their recession velocity to be larger than the speed of light. Then, the expansion of the universe implies that we can only observe as far as information has had the time to travel, which is delimited by the *particle horizon*. Or equivalently, the future light cone determined at our position when the CMB was emitted. The overlap between the past light cone and the particle horizon identifies the *observable universe*.

The value of H measured today H_0, the current expansion rate of the universe, is called Hubble's constant and its measurement is a pivotal topic in current cosmological discussions (Di Valentino et al., 2021; Abdalla et al., 2022), it is parametrised with the dimensionless Hubble parameter

$$h = H_0/100 \text{ km s}^{-1} \text{ Mpc}^{-1}. \tag{4.9}$$

From this, one quantifies Hubble's time and Hubble's radius today as (Peebles, 1980)

$$\begin{aligned} t_{H0} &= H_0^{-1} \simeq 9.78\ h^{-1} \text{ Gyr}, \\ R_{H0} &= cH_0^{-1} \simeq 2997.9\ h^{-1} \text{ Mpc}. \end{aligned} \tag{4.10}$$

4.1.2 Matter

The properties of matter have evolved throughout the universe's history. Considering it to be a homogeneous perfect fluid the energy density takes the form (Ellis, Maartens, and MacCallum, 2012)

$$T_{\alpha\beta} = \bar{\rho} u_\alpha u_\beta + \bar{p} h_{\alpha\beta} \tag{4.11}$$

where the fluid energy density $\bar{\rho} = T^{\mu\nu} u_\mu u_\nu$ and pressure $\bar{p} = \frac{1}{3} T^{\mu\nu} h_{\mu\nu}$ are in the frame of the fluid 4-velocity u^μ and its orthogonal projection tensor $h_{\mu\nu}$ Eq. (2.49). For a homogeneous fluid, these are all constant in space and only a function of time. Note that the curvature terms Eq. (4.3) are purely diagonal therefore via Einstein's field equations Eq. (2.39) we can see that the energy stress tensor is also diagonal.

The specific type of perfect fluid at hand is approximated to be the most dominant type during different eras of the universe's evolution. Based on the equation of state Eq. (2.48) $\bar{p} = w\bar{\rho}$, it is w that is given different values based on the era.

- ❖ At early times $z > 3600$ during the **radiation-dominated era**, the matter in the universe takes a radiative plasma form as seen with the CMB so $w = 1/3$.
- ❖ Then during the **matter-dominated era**, there is enough distance between particles to assume that they are non-relativistic and only interact gravitationally so it is considered pressureless, $w = 0$, and called dust. Since CDM identifies matter that only interacts gravitationally, this is also represented as dust $w = 0$ and appears as the dominant contribution during this era.
- ❖ At late times $0.4 > z$ during the **dark energy-dominated era**, vacuum energy $w = -1$ is dominant. A vacuum energy density, however, is to be used as an alternative to having a cosmological constant Λ based on preference.

Typically, depending on the case considered, one of these fluids is considered exclusively. Alternatively, these fluids can be combined by adding their respective energy density,

$$T^{\mu\nu} = T^{\mu\nu}_{rad} + T^{\mu\nu}_{dust} + T^{\mu\nu}_{vac}. \tag{4.12}$$

4.1.2.1 Kinematics

The energy rest frame is given by the frame where there is no energy flux (Bruni, 1991), which is identically zero for the energy-stress tensor in Eq. (4.11) as $q^\alpha = -(g^{\beta\alpha} + u^\beta u^\alpha) T_{\beta\mu} u^\mu = 0$. Using the metric Eq. (4.1) with proper time, $q^i = 0$ is simply satisfied by $u^i = 0$, and the timelike normalisation $u^\alpha u_\alpha = -1$ provides the other components

$$u^\mu = \{1,\ 0,\ 0,\ 0\} \quad \text{and} \quad u_\mu = \{-1,\ 0,\ 0,\ 0\}. \tag{4.13}$$

With the synchronous spacetime at hand Eq. (4.1) we see that with the ADM decomposition, the normal to the hypersurface $n^\mu = u^\mu$ thus the spacetime is also comoving and the orthogonal hypersurfaces are the same $\bar{\gamma}_{\alpha\beta} = h_{\alpha\beta}$.

Because the fluid 4-velocity is constant in time and in space, its gradients are zero (no acceleration) leaving only the second term in its covariant derivative $\nabla_\nu u_\mu = -\bar{\Gamma}^0_{\nu\mu} u_0 = \frac{1}{2} \dot{\bar{g}}_{\nu\mu}$ which is symmetric (no vorticity), traceless (no shear), and only has spatial components. Therefore from

Eq. (2.50) $\nabla_i u_j$ is entirely given by the expansion tensor and scalar (Ellis, Maartens, and MacCallum, 2012)

$$\nabla_i u_j = \bar{\Theta}_{ij} = \frac{1}{2}\dot{\bar{\gamma}}_{ij} = \frac{1}{3}\bar{\gamma}_{ij}\bar{\Theta}. \tag{4.14}$$

The expansion scalar is further expressed with the scale factor and Hubble function as

$$\bar{\Theta} = \frac{1}{2}\bar{\gamma}^{ij}\dot{\bar{\gamma}}_{ij} = 3\frac{\dot{a}}{a} = 3H. \tag{4.15}$$

The absence of 4-acceleration can be understood physically from the pressure. Since this is a homogeneous fluid there is no vorticity, shear or spatial pressure gradient, thus no acceleration see Eq. (2.56).

4.1.3 Evolution Equations

The general spacetime and fluid evolution and constraint equations were discussed in Section 2.4, as we consider the FLRW spacetime from Section 4.1.1 with a homogeneous perfect fluid from Section 4.1.2, these are simplified and we list them below.

4.1.3.1 Conservation equations

Of the conservation equations, $u_\beta \nabla_\alpha T^{\alpha\beta} = 0$, Section 2.4.1, since there is no acceleration only the energy conservation equation Eq. (2.55) remains non-trivial, it is also called the continuity equation (Vittorio, 2018)

$$\dot{\bar{\rho}} = -3H\left(\bar{\rho} + \bar{p}\right). \tag{4.16}$$

Integrating with the equation of state Eq. (2.48) provides

$$\frac{\bar{\rho}}{\bar{\rho}_0} = \left(\frac{a}{a_0}\right)^{-3(1+w)} = s^{-3(1+w)} \tag{4.17}$$

where the integration constants $\bar{\rho}_0$ and a_0 are the values of the energy density and scale factor measured today. As a/a_0 is a recurring ratio a common normalisation is $a_0 = 1$ but for clarity here, we will use the variable $s = a/a_0$. For radiation $\bar{\rho} \propto a^{-4}$ and for dust $\bar{\rho} \propto a^{-3}$ which for a flat spacetime Eq. (4.4) shows that the energy density simply grows with the volume element $\bar{\rho} \propto \sqrt{\bar{\gamma}}$.

4.1.3.2 Einstein's field equations

Projecting Einstein's field equations, Section 2.4.3, with this homogeneous fluid flow $\left(G_{\alpha\beta} + \Lambda g_{\alpha\beta} - \kappa T_{\alpha\beta}\right) u^\alpha u^\beta = 0$, only the Hamiltonian constraint Eq. (2.60), remains non-trivial which for this particular spacetime corresponds to the first Friedmann equation (Friedmann, 1922)

$$H^2 = \frac{\dot{a}^2}{a^2} = -\frac{k}{a^2} + \frac{\kappa\bar{\rho}}{3} + \frac{\Lambda}{3}. \tag{4.18}$$

The other field equations rely on spatial gradients that are obviously not present in this homogeneous solution. The first Friedmann equation is rewritten in terms of the dimensionless curvature, matter and dark energy density parameters:

$$\begin{gathered} \Omega_k + \Omega_m + \Omega_\Lambda = 1 \\ \Omega_k = -\frac{k}{a^2H^2}, \qquad \Omega_m = \frac{\kappa\bar{\rho}}{3H^2}, \qquad \Omega_\Lambda = \frac{\Lambda}{3H^2}. \end{gathered} \tag{4.19}$$

These quantify the content of the universe by conservation of matter and energy; the sum will always be one though the individual terms may vary. Rescaling this with the values measured today shows how each of these grow with the expansion of the universe (Vittorio, 2018)

$$\begin{aligned}\frac{H^2}{H_0^2} &= \Omega_{k0}s^{-2} + \Omega_{m0}s^{-3(1+w)} + \Omega_{\Lambda 0} \\ &= \Omega_{k0}s^{-2} + \Omega_{m0,\,dust}s^{-3} + \Omega_{m0,\,rad}s^{-4} + \Omega_{\Lambda 0}\end{aligned} \tag{4.20}$$

where the matter parameter is split into its radiation and dust parts. Therefore at early times, depending on the values of these parameters, when s is small, $\Omega_{m0,\,rad}$ dominates H, then as s grows, this transitions to $\Omega_{m0,\,dust}$, then Ω_{k0}, then finally at late times $\Omega_{\Lambda 0}$ dominates.

4.1.3.3 Ricci identity

From the Ricci identity applied to the fluid flow u^α, $\nabla_\mu\nabla_\nu u^\alpha - \nabla_\nu\nabla_\mu u^\alpha = R^\alpha{}_{\sigma\mu\nu}u^\sigma$, see Section 2.4.2, the only non-trivial equation is the Raychaudhuri equation Eq. (2.57) (Raychaudhuri, 1955) that becomes

$$\dot{H} + H^2 = \frac{\ddot{a}}{a} = -\frac{\kappa}{6}\left(\bar{\rho} + 3\bar{p}\right) + \frac{\Lambda}{3} \tag{4.21}$$

which is the second Friedmann equation (Friedmann, 1922). It can also be retrieved from the contraction of Einstein's field equations $G^\alpha{}_\alpha + 4\Lambda = \kappa T^\alpha{}_\alpha$ and substituting with the first Friedmann equation Eq. (4.18). Expressing this with the dimensionless density parameters measuremed today, this becomes

$$\begin{aligned}\frac{\ddot{a}}{aH_0^2} &= -\frac{1}{2}\Omega_{m0}s^{-3(1+w)}(1+3w) + \Omega_{\Lambda 0} \\ &= -\frac{1}{2}\Omega_{m0,\,dust}s^{-3} - \Omega_{m0,\,rad}s^{-4} + \Omega_{\Lambda 0}\end{aligned} \tag{4.22}$$

where we see here and in Eq. (4.21) that the presence of radiation and matter decelerates the expansion of the universe, whereas depending on the sign of Λ, it accelerates $\Lambda > 0$ or decelerates $\Lambda < 0$ the expansion of the universe.

4.1.4 Solutions

The Friedmann equations Eq. (4.18) and Eq. (4.21) provide the first and second-order evolution equation of the scale factor a; finding the solution to these will provide cosmological solutions to the expansion of the universe. From simplest to most complex we present some of those solutions below.

4.1.4.1 Milne

Considering an empty universe with no cosmological constant, the dimensionless density parameters are $\Omega_m = \Omega_\Lambda = 0$ leaving $\Omega_k = 1$. The Friedmann equations reduce to $\dot{a}^2 = -k$ and $\ddot{a} = 0$, this is not possible for $k = +1$ or 0, and for $k = -1$ the solution is given by the Milne (1935) model (Vittorio, 2018)

$$s = \sqrt{-k}\left(\frac{\tau}{\tau_0}\right), \qquad H = \frac{1}{\tau}, \tag{4.23}$$

which is an expanding universe $H > 0$. Here we use the variable $s = a/a_0$ with a_0 and τ_0 the scale factor and proper time today.

4.1.4.2 Einstein's closed static universe

Assuming the universe is static $\dot{a} = \ddot{a} = 0$ with positive curvature, dust and the cosmological constant (Einstein, 1917), Eq. (4.20) and Eq. (4.22) become (Vittorio, 2018)

$$\begin{gathered}\Omega_{k0}s^{-2} + \Omega_{m0,\,dust}s^{-3} + \Omega_{\Lambda 0} = 0, \qquad -\tfrac{1}{2}\Omega_{m0,\,dust}s^{-3} + \Omega_{\Lambda 0} = 0 \\ \Rightarrow \quad \Omega_{m0,\,dust} = -\tfrac{2}{3}\Omega_{k0}s = 2\Omega_{\Lambda 0}s^3\end{gathered} \tag{4.24}$$

meaning that k and Λ are both positive. Indeed considering Eq. (4.21) the matter decelerates the universe's expansion, this is made static with a precise value of the cosmological constant Λ.

4.1.4.3 de Sitter

Considering two non-zero components while having an empty universe, the dimensionless density parameters are $\Omega_m = 0$ leaving $\Omega_k + \Omega_\Lambda = 1$. The solution to the Friedman equations are given by the de Sitter (1917) model

$$s = \begin{cases} \cosh(H\tau) & \text{if } \ k > 0 \\ \exp(H\tau) & \text{if } \ k = 0 \\ \sinh(H\tau) & \text{if } \ k < 0 \end{cases} \qquad\qquad H = \sqrt{\frac{\Lambda}{3}}. \tag{4.25}$$

In the dark energy-dominated era of the ΛCDM model, where $\Omega_k = 0$ and $\Omega_m \to 0$ such that Ω_Λ dominates, the ΛCDM scale factor will tend towards that provided by the $k = 0$ de Sitter solution.

4.1.4.4 Einstein-de Sitter

Considering a universe with zero cosmological constant, the dimensionless density parameters are $\Omega_\Lambda = 0$ leaving $\Omega_k + \Omega_m = 1$. While k and Λ are constants, that is not the case for $\bar{\rho}$ so to solve the Friedmann equations, assuming a perfect fluid, it needs to be substituted with the scale factor using Eq. (4.17). Assuming only radiation and dust, there are six solutions to the Friedmann equations based on curvature and matter, these are listed in Table (4.1) (Vittorio, 2018), where ς is used as a dimensionless parameter (see Eq. (4.66) in Section 4.3.2) as well as proper time τ.

		open $k < 0$	flat $k = 0$	closed $k > 0$
radiation	$w = 1/3$	$a \propto \sinh(\varsigma)$ $\tau \propto (\cosh(\varsigma) - 1)$	$a \propto \tau^{1/2}$	$a \propto \sin(\varsigma)$ $\tau \propto (1 - \cos(\varsigma))$
dust	$w = 0$	$a \propto (\cosh(\varsigma) - 1)$ $\tau \propto (\sinh(\varsigma) - \varsigma)$	$a \propto \tau^{2/3}$	$a \propto (1 - \cos(\varsigma))$ $\tau \propto (\varsigma - \sin(\varsigma))$

Table 4.1: Solutions to the Friedmann equations for $\Lambda = 0$ considering radiation and dust matter and open flat or closed curvature.

Both closed models collapse, we shall discuss the dust case in more detail in Section 4.3.2.3, the flat cases show monotonic growth and the dust open case tends towards the Milne model.

For the flat dust case in particular, the first Friedmann equation Eq. (4.18) is trivial and the second Friedmann equation Eq. (4.21) is

$$\ddot{a} + \frac{\dot{a}^2}{2a} = 0, \quad \Rightarrow \quad \dot{H} + \frac{3}{2}H^2 = 0 \tag{4.26}$$

whose solution is known as the Einstein and de Sitter (1932) solution

$$s = \left(\frac{\tau}{\tau_0}\right)^{2/3}, \qquad H = \frac{2}{3\tau}. \tag{4.27}$$

This is often considered when Λ is negligible in the ΛCDM solution; during the matter-dominated era, the scale factor tends towards the flat dust solution, and likewise the flat radiation solution during the radiation-dominated era.

4.1.4.5 ΛCDM

Lastly but most importantly, considering a flat universe with Λ and matter, the dimensionless density parameters are $\Omega_k = 0$ leaving $\Omega_m + \Omega_\Lambda = 1$. Choosing only to consider dust $w = 0$, which accounts for both baryons and CDM, Eq. (4.20) can be expressed as

$$H = H_0\sqrt{\Omega_{m0}s^{-3} + \Omega_{\Lambda 0}}, \qquad \Omega_m = \frac{\Omega_{m0}}{\Omega_{m0} + \Omega_{\Lambda 0}s^3}, \tag{4.28}$$

where Ω_m comes from its definition Eq. (4.19) with the energy density substituted with the scale factor with Eq. (4.17). With these choices, the solution to the Friedmann equation is the ΛCDM model

$$s = \left(\frac{\Omega_{m0}}{\Omega_{\Lambda 0}}\right)^{1/3} \sinh^{2/3}\left(\frac{3\tau H_0}{2}\sqrt{\Omega_{\Lambda 0}}\right). \tag{4.29}$$

This provides the best current model describing the universe. Based on CMB data the Planck Collaboration (2020) has found that the values today are $\Omega_{m0} = 0.3147 \pm 0.0074$ and $h = 0.6737 \pm 0.0054$, see Eq. (4.9).

4.2 Perturbation theory

While the universe models described in Section 4.1 perfectly satisfy the cosmological principle, in order to account for anisotropy and inhomogeneity perturbations are introduced (Kodama and Sasaki, 1984; Bruni, 1991; Ma and Bertschinger, 1995; Bertschinger, 2000; Malik and Wands, 2009), such that, on average, the universe is still isotropic and homogeneous. With this approach, the universe is composed of a background, Section 4.1, upon which are added scalar, vector, or tensor perturbations of small amplitude.

4.2.1 Spacetime

First of all, perturbing a flat spacetime $k = 0$, in the most general form with all types of perturbations, the metric takes the form (Bruni, Hidalgo, Meures, et al., 2014)

$$\begin{aligned} ds^2 &= a^2\left[-(1+2\phi)d\eta^2 + 2\omega_i d\eta dx^i\right] + \gamma_{ij}dx^i dx^j, \\ \gamma_{ij} &= a^2\left[(1-2\psi)\delta_{ij} + \chi_{ij}\right]. \end{aligned} \tag{4.30}$$

The perturbations are the scalar ϕ and ψ, vector ω_i, and tensor χ_{ij} quantities. While scalars can be used to construct vectors or tensors by using the scalar's gradient, those will be curl-free, see Section 2.1.4.2. So a vector perturbation can be decomposed into its purely scalar (curl-free part) and purely vectorial parts as (Bertschinger, 2000; Malik and Wands, 2009)

$$\omega_i = \partial_i \omega + \omega_i^S \tag{4.31}$$

with S standing for a solenoidal vector that is divergence-free and can not be constructed from a scalar. This constitutes the longitudinal (curl-free) and transverse (divergence-free) parts of the Helmholtz decomposition (Bertschinger, 2000).

In the perturbations to the spatial metric γ_{ij}, ψ is the perturbation to the trace, and so χ_{ij} is a traceless tensor containing all the other types of perturbations. It is itself decomposed as

$$\chi_{ij} = \Box_{ij}\chi + D^{\{n\}}_{(j}\chi^S_{i)} + \chi^{TT}_{ij} \tag{4.32}$$

with $\Box_{ij} = \partial_i\partial_j - \frac{1}{3}\delta_{ij}\delta^{kl}\partial_k\partial_l$ a traceless operator, $D^{\{n\}}_i$ the covariant derivative from γ_{ij} and TT stands for transverse traceless. Here all three terms are traceless; only one index at a time of the solenoidal term is transverse, hence the symmetrisation, while both indices of the tensor term are transverse, making it doubly transverse. While χ^S_i is divergence-free, that is not the case of $D_{(j}\chi^S_{i)}$, while it is the case for χ^{TT}_{ij}. A doubly transverse traceless tensor can not be constructed from a vector.

Therefore we identify the scalar perturbations ϕ, ω, ψ, and χ, vector perturbations ω^S_i, and χ^S_i, and tensor perturbations χ^{TT}_{ij}. This full decomposition has the advantage of being decoupled in the evolution equations allowing perturbations to be solved separately at linear order. During the matter-dominated era, the vector and tensor perturbations are neglected at first order (Lu et al., 2009) as scalar perturbation are the main contributors to structure formation, see Section 4.3.1.

Furthermore, this decomposition makes gauge choices a simple modification to the metric. Each scalar perturbation provides one degree of freedom, and the solenoidal vector and transverse traceless tensor perturbations each provide two. Therefore the perturbed metric possesses 10 degrees of freedom, allowing a large range of gauge choices, see Section 4.2.3.

4.2.2 Matter

Just as what was done for spacetime, all the fluid terms are perturbed while still assuming a perfect fluid description. To simplify the task, we shall only consider irrotational dust, so there is no vorticity, pressure or acceleration. Therefore the full energy density is

$$\rho^{\{u\}} = \bar{\rho}(1+\delta) \tag{4.33}$$

where δ is a new scalar perturbation corresponding to the density contrast $\delta = \rho^{\{u\}}/\bar{\rho} - 1$ that quantifies the inhomogeneity of the fluid.

The new fluid 4-velocity will differ from the homogeneous one but because of its normalisation, its components will depend on the choice of coordinates see Section 4.2.3. Should we work with synchronous comoving coordinates, then even with inhomogeneities the fluid velocity will be provided by Eq. (4.13).

For this irrotational dust, the covariant derivative of the fluid is provided by the expansion tensor $\nabla_\nu u_\mu = \Theta_{\mu\nu}$ which is the homogeneous background expansion tensor $\bar{\Theta}_{ij}$ plus the deformation tensor ϑ_{ij} (Bruni, Hidalgo, Meures, et al., 2014)

$$\Theta_{ij} = \bar{\Theta}_{ij} + \vartheta_{ij} = \frac{1}{3}\bar{\gamma}_{ij}\bar{\Theta} + \frac{1}{3}\gamma_{ij}\vartheta + \sigma_{ij} \tag{4.34}$$

with the deformation scalar ϑ and shear σ_{ij} which, like χ_{ij}, is composed of scalar vector and tensor terms.

4.2.3 Gauge choice

Some of the degrees of freedom provided by the perturbations to spacetime and matter are redundant, these are then reduced by making gauge choices. This consists of cancelling certain terms such that the coordinate observers can not "see" those perturbations according to the direction of the gauge, see Malik and Wands (2009).

- **Synchronous**: $\phi = \omega = \omega_i^S = 0$ such that with these coordinates, each observer evolves according to the cosmic proper time.
- **Comoving**: $u^\mu = n^\mu$ this is a Lagrangian observer, meaning that the coordinates follow the fluid, the normal to the hypersurface is the same as the fluid flow, so the expansion of the coordinates provided by the extrinsic curvature Eq. (3.12) corresponds to the fluid expansion Eq. (2.50) $K_{ij} = -\Theta_{ij}$. Because the fluid flow is orthogonal to the spatial hypersurface, this is sometimes called the comoving orthogonal gauge. Note that a smooth spatial hypersurface requires the fluid to have no vorticity and that the comoving curvature perturbation is defined as $\mathcal{R}_c$, see Eq. (4.40, 4.45, 4.54) in Section 4.2.6.1.
- **Newtonian**: $\omega = \omega_i^S = \chi = \chi_i^S = \chi_{ij}^{TT} = 0$ as indicated by the name, the evolution equations in this gauge resemble the most the Newtonian ones (see the Poisson equation Eq. (4.55)) therefore this is often considered the most physically intuitive gauge. When proper time τ is used, this gauge is referred to as the Newtonian gauge; when conformal time η is used, this gauge is called the conformal Newtonian or longitudinal gauge (Ma and Bertschinger, 1995). Note that the conformal Newtonian curvature perturbation is defined as Ψ, see Section 4.2.6.3.
- **Poisson**: $\omega = \omega_i^S = \chi = 0$ this generalises the Newtonian gauge where the spatial vector and tensor modes remain.
- **Spatially flat or uniform curvature**: $\psi = \chi = \chi_i^S = \chi_{ij}^{TT} = 0$ such that $\gamma_{ij} = \bar{\gamma}_{ij}$ where the curvature terms then match with the homogeneous background hence the name uniform curvature. It is common to work with a flat background; therefore, the spatially flat name also works.
- **Uniform density**: $\delta = 0$, none of the spacetime perturbation terms are set to zero but are instead accordingly defined such that $\delta = 0$. This is a practical gauge choice for inflation and is reversed to the uniform curvature gauge. Note that the uniform density curvature perturbation is defined as ζ.

Also see Section 3.4 for a gauge discussion from the point of view of NR, although in both cases, this can be reduced to a choice of slicing.

4.2.4 First order scalar constraint & evolution equations

Here we consider the constraint and evolution equations of an irrotational dust perfect fluid from Section 2.4.4 where we introduce the perturbations in the spacetime from Section 4.2.1 and matter from Section 4.2.2. Since scalar perturbations are the main contributors in structure formation in the matter-dominated era, we omit the vector and tensor terms $\omega_i^S = \chi_i^S = \chi_{ij}^{TT} = 0$. Additionally, we choose to work with synchronous and comoving coordinates $\phi = \omega = 0$ and NR $\alpha = 1$ and $\beta^i = 0$. These choices mean that the metric and stress-energy tensor we work with are (Bruni, Hidalgo, Meures, et al., 2014)

$$\begin{aligned} ds^2 &= -d\tau^2 + \gamma_{ij}dx^i dx^j, \\ \gamma_{ij} &= a^2\left[(1-2\psi)\delta_{ij} + \Box_{ij}\chi\right], \end{aligned} \qquad T^{\mu\nu} = \bar{\rho}(1+\delta)u^\mu u^\nu. \tag{4.35}$$

The deviations from the FLRW background spacetime are ψ and the trace-less $\Box_{ij}\chi$, corresponding to the volume perturbation and anisotropic distortion respectively (Kodama and Sasaki, 1984). Then, ψ is the only perturbation in the determinant of the spatial metric up to first order

$$\gamma \simeq \bar{\gamma}(1-6\psi^{(1)}), \qquad \text{with} \qquad \bar{\gamma} = a^6. \tag{4.36}$$

Additionally, these comoving coordinates mean that the normal to the hypersurface and the fluid flow are the same

$$u^\mu = n^\mu = \{1,\ 0,\ 0,\ 0\}, \tag{4.37}$$

and so the coordinated expansion K_{ij} corresponds to the fluid expansion Θ_{ij} with a sign difference

$$K_{ij} = -\frac{1}{2}\dot{\gamma}_{ij} = -\Theta_{ij} \quad \Rightarrow \quad \begin{cases} K = -\Theta, \\ A_{ij} = -\sigma_{ij}. \end{cases} \tag{4.38}$$

Θ and σ_{ij} can then be expressed in terms of the metric perturbations ψ and χ as

$$\vartheta^{(1)} = -3\dot{\psi}^{(1)} \qquad \sigma_{ij}^{(1)} = \frac{a^2}{2}\Box_{ij}\dot{\chi}^{(1)} \tag{4.39}$$

where ϑ is the deformation scalar Eq. (4.34). Due to the complexity of this calculation, we will only work with first-order perturbations, denoted with the (1) superscript.

Furthermore, for the spacetime metric Eq. (4.35), the first-order curvature quantities are

$$\begin{aligned} {}^{(3)}R^{(1)} &= 4\nabla^2\mathcal{R}_c = 4\nabla^2\left(\psi^{(1)} + \frac{a^2}{6}\nabla^2\chi^{(1)}\right), \\ E_{ij}^{\{u\}(1)} &= \frac{1}{2}\Box_{ij}\left(\psi^{(1)} - \frac{a^2}{2}\left(H\dot{\chi}^{(1)} + \ddot{\chi}^{(1)} - \frac{1}{3}\nabla^2\chi^{(1)}\right)\right), \qquad B_{ij}^{\{u\}(1)} = 0, \end{aligned} \tag{4.40}$$

where the Laplacian $\nabla^2 = \gamma^{ij}\nabla_i\nabla_j$ is such that for first-order scalar perturbations, it takes the form $a^{-2}\delta^{ij}\partial_i\partial_j$. We preemptively express $\mathcal{R}_c$, the comoving curvature perturbation, see Section 4.2.6, as this is a key quantity in Section 6.1. The magnetic part of the Weyl tensor $B_{ij}^{\{u\}(1)}$ is zero since we only consider scalar perturbations and no curl can be constructed from them at first-order; however, at second and higher order, their coupling no longer vanishes $B_{ij}^{\{u\}(2)} \neq 0$. The traceless operator $\Box_{ij} = \partial_i\partial_j - \frac{1}{3}\delta_{ij}\delta^{kl}\partial_k\partial_l$ emphasises the traceless nature of the electric part of the Weyl tensor

$E_{ij}^{\{u\}}$. While the above is for the synchronous gauge, only considering scalar perturbations, note that for the Newtonian gauge $E_{ij}^{\{u\}}$ is

$$E_{ij}^{\{u\}(1)} = \frac{1}{2}\Box_{ij}\left(\Phi^{(1)} - \Psi^{(1)}\right), \tag{4.41}$$

where $\frac{1}{2}(\Phi - \Psi)$ is called the Weyl potential (Lewis and Challinor, 2006) which emphasises that at first-order $E_{ij}^{\{u\}}$ can be perceived as the tidal gravitational force.

Now as we go back to the constraint and evolution equations of Section 2.4.4, these are expressed for the above-perturbed spacetime with the background part from Section 4.1.3 removed, leaving only first-order scalar expressions. Firstly from the conservation equations Eq. (2.40) we have the continuity equation Eq. (2.63) which becomes

$$\dot{\delta}^{(1)} = -\vartheta^{(1)}. \tag{4.42}$$

Then from the Ricci identity applied to the fluid flow, Eq. (2.18), we have the Raychaudhuri equation Eq. (2.65) (second Friedmann equation in the background Eq. (4.21)) that provides the evolution equation of the deformation scalar

$$\dot{\vartheta}^{(1)} + 2H\vartheta^{(1)} = -\frac{3}{2}H^2\Omega_m\delta^{(1)} \tag{4.43}$$

where Eq. (4.19) was used. The projected Ricci identity also gives the shear evolution equation, Eq. (2.66), that provides a second-order evolution equation for $\chi^{(1)}$ which we omit here. Then from Einstein's field equations Eq. (2.39) we have the Hamiltonian constraint Eq. (2.60) (first Friedmann equation in the background Eq. (4.18))

$${}^{(3)}R^{(1)} + 4H\vartheta^{(1)} = 6H^2\Omega_m\delta^{(1)} \tag{4.44}$$

and the momentum constraint Eq. (2.61)

$$\partial_i\dot{\mathcal{R}}_c = 0 \tag{4.45}$$

essentially saying that $\mathcal{R}_c$ is constant in time, so from Eq. (4.40) the conformal 3-Ricci, $a^{2(3)}R^{(1)}$, is also constant in time. We again omit the evolution equations in Einstein's field equations for simplicity.

How these equations are used to determine how $\delta^{(1)}$ evolves is addressed in Section 4.3.1 where we talk about structure formation.

4.2.5 Backreaction

It is clear that the universe is not exactly homogeneous, hence the inhomogeneous perturbations, however it is assumed that on average and on large scales it can be considered as such. The evolution equations are local evolution equations satisfied everywhere, but that may not necessarily be the case should their terms be individually averaged (Buchert and Räsänen, 2012). To express this, consider the first and second Friedmann equations Eq. (4.18) and Eq. (4.21) whose general form are the Hamiltonian constraint Eq. (2.60) and Raychaudhuri equation Eq. (2.57) which for an irrotational

dust with no cosmological constant respectively take the form

$$\begin{aligned} \frac{1}{3}\Theta^2 &= 3\frac{\dot{a}}{a} &&= -\frac{{}^{(3)}R}{2} + \kappa\rho^{\{u\}} + \sigma^2, \\ \dot{\Theta} + \frac{1}{3}\Theta^2 &= 3\frac{\ddot{a}}{a} &&= -\frac{\kappa}{2}\rho^{\{u\}} - 2\sigma^2. \end{aligned} \tag{4.46}$$

This is expressed in terms of the hypersurface orthogonal to the fluid flow, and so this is averaged on this same hypersurface. The spatial metric is given by the projection tensor $h_{\alpha\beta}$ Eq. (2.49) where its square root determinant $\sqrt{h}$ gives the local fluid volume element on this hypersurface. We then define the domain-averaging operator $\langle ... \rangle_{\mathcal{D}\{u\}}$ and the domain averaged scale factor $a_{\mathcal{D}\{u\}}$ as

$$\begin{aligned} \langle\phi\rangle_{\mathcal{D}\{u\}}(\tau) &= \frac{\Delta x^3 \sum_{\mathcal{D}\{u\}} \phi(\tau, x^i)\sqrt{h(\tau, x^i)}}{\Delta x^3 \sum_{\mathcal{D}\{u\}} \sqrt{h(\tau, x^i)}}, \\ a_{\mathcal{D}\{u\}}(\tau) &= \left(\frac{\Delta x^3 \sum_{\mathcal{D}\{u\}} \sqrt{h(\tau, x^i)}}{\Delta x^3 \sum_{\mathcal{D}\{u\}} \sqrt{h\left(\tau_R, x^i\right)}} \right)^{\frac{1}{3}}. \end{aligned} \tag{4.47}$$

where $\mathcal{D}^{\{u\}}$ is the domain on the hypersurface $h_{\alpha\beta}$ which is averaged upon, Δx is the spacing between the integrated measurements, and τ_R is the reference proper time chosen to normalise the scale factor. More on numerically integrating in Appendix D.

Taking the domain average of the terms in Eq. (4.46) and expanding according to the domain averaging's algebraic properties provides

$$\begin{aligned} 3\frac{\dot{a}^2_{\mathcal{D}\{u\}}}{a^2_{\mathcal{D}\{u\}}} &= -\frac{\langle {}^{(3)}R\rangle_{\mathcal{D}\{u\}}}{2} + \kappa\langle\rho^{\{u\}}\rangle_{\mathcal{D}\{u\}} - \frac{1}{2}\mathcal{Q}_{\mathcal{D}\{u\}} \\ 3\frac{\ddot{a}_{\mathcal{D}\{u\}}}{a_{\mathcal{D}\{u\}}} &= -\frac{\kappa}{2}\langle\rho^{\{u\}}\rangle_{\mathcal{D}\{u\}} + \mathcal{Q}_{\mathcal{D}\{u\}} \end{aligned} \tag{4.48}$$

with $\mathcal{Q}_{\mathcal{D}\{u\}}$ the kinematical backreaction variable defined as

$$\mathcal{Q}_{\mathcal{D}\{u\}} = \frac{2}{3}\left(\langle\Theta^2\rangle_{\mathcal{D}\{u\}} - \langle\Theta\rangle^2_{\mathcal{D}\{u\}}\right) - 2\langle\sigma^2\rangle_{\mathcal{D}\{u\}}. \tag{4.49}$$

The first term in particular is essentially the variance of the expansion. If the universe were homogeneous this would vanish, otherwise, this quantifies the dispersion of expansion rates. This comes from expanding $\langle\Theta^2\rangle_{\mathcal{D}\{u\}}$ in terms of the domain averaged scale factor, providing the left-hand side terms of Eq. (4.48).

Comparing Eq. (4.48) to the Friedmann equations Eq. (4.46) we can see that $\mathcal{Q}_{\mathcal{D}\{u\}}$ substitutes the cosmological constant term. In particular, if the expansion variance is larger than the domain average shear and energy density terms, i.e. $\mathcal{Q}_{\mathcal{D}\{u\}} > 0$ and $\mathcal{Q}_{\mathcal{D}\{u\}} > \frac{\kappa}{2}\langle\rho^{\{u\}}\rangle_{\mathcal{D}\{u\}}$, then the universe expansion is accelerated $\ddot{a}_{\mathcal{D}\{u\}} > 0$. This behaviour has therefore been suggested as an explanation for dark energy (Buchert and Räsänen, 2012).

To verify this, various groups have set out to quantify this effect using NR (Adamek, Clarkson, Durrer, et al., 2015; Bentivegna and Bruni, 2016; Macpherson, 2019; Macpherson, Price, and Lasky, 2019), however, measurements tend to disagree and be generally small. This can be amplified by considering highly non-linear simulations yet the inconsistency between different simulations is due to the lack of gauge invariance of this quantity. Indeed $\mathcal{Q}_{\mathcal{D}\{u\}}$ has been defined covariantly using fluid

quantities so it is in the fluid frame u^μ, but more importantly, it depends on the averaged hypersurface. Naturally, quantities averaged on different hypersurfaces will have different values (Adamek, Clarkson, Daverio, et al., 2018; Giblin, Mertens, Starkman, and Tian, 2019b). So the domain on the hypersurface orthogonal to the fluid flow $\mathcal{D}^{\{u\}}$, is different to the domain on the hypersurface orthogonal to n^μ $\mathcal{D}^{\{n\}}$, so $\mathcal{Q}_{\mathcal{D}^{\{u\}}} \neq \mathcal{Q}_{\mathcal{D}^{\{n\}}}$ (if not comoving). Furthermore, these would also differ from the domain measured by an observer looking into their past light cone. One ought to then consider gauge invariant quantities and observables.

4.2.6 Covariant & gauge invariants

We first discussed invariants in Section 2.5.3 where we identified valuable quantities that are coordinate invariant, coordinate independent and frame-independent, these are I and J, thus subsequently that is also the case for L_B, M, $\mathcal{S}$ and $\mathcal{D}$. Then we also defined coordinate invariant, coordinate independent and frame-dependent quantities K, L and N (Bini, Geralico, and Jantzen, 2023).

In the context of cosmological perturbation theory, we deal with two spacetimes: the realistic one Eq. (4.30), which we wish to describe as a small deviation from an idealised background Eq. (4.4), and the fictitious background spacetime itself whose form is unknown. Furthermore, the realistic spacetime Eq. (4.30) is expressed with different gauges obtained by reducing the degrees of freedom according to Section 4.2.3, providing different sets of coordinates or slicings.

Continuing with the vocabulary of Section 2.5.3, we use

- ❖ *gauge variance or invariance* to identify whether a quantity is conserved under gauge transformation,
- ❖ *gauge dependent or independent* to identify whether a quantity retains its meaning in different gauges.

The gauge-variance of perturbations is due to the fact that a gauge choice in this context is a choice of mapping between points of the realistic spacetime and points of the background, so that a passive change of coordinates in the first (a change of labels for a given point) produces a change of points in the background. Since the background points also have their own coordinates, the change of points in the background results in what is sometimes referred to as an active coordinate transformation (or point transformation) of the perturbation fields on the background. The latter is the point of view in Weinberg (1972), and also affects scalar quantities in general. Based on this spacetime mapping, there are two ways to create gauge invariants, based on coordinate transformation rules and the Stewart-Walker lemma.

4.2.6.1 Stewart-Walker invariants

This gauge-variance can be formalised (at first order) with the Stewart-Walker lemma (Stewart and Walker, 1974), the essence of which is that for a tensorial quantity T the relation between its perturbations in two different gauges is given by $\delta\tilde{T} = \delta T + \mathcal{L}_\xi \bar{T}$, where ξ is the vector field generating the said mapping of points in the background at first order and $\mathcal{L}_\xi \bar{T}$ is the Lie derivative along ξ of $\bar{T}$, the tensor T evaluated in the background. It then immediately follows that a tensorial quantity is gauge-invariant at first order if the background value is either zero $\bar{T} = 0$, a constant

scalar, or a constant linear combination of Kronecker deltas. Gauge transformations and conditions for gauge invariance of perturbations generalising the Stewart-Walker lemma to an arbitrary higher order were derived (Bruni, Matarrese, Mollerach, et al., 1997; Sonego and Bruni, 1998; Bruni and Sonego, 1999), soon leading to applications in cosmology (Mollerach and Matarrese, 1997; Matarrese, Mollerach, and Bruni, 1998; Maartens, Gebbie, and Ellis, 1999; Bartolo et al., 2004; Clarkson, 2004; Noh and Hwang, 2004; Lyth, Malik, and Sasaki, 2005; Nakamura, 2007; Osano et al., 2007; Pettinari et al., 2013; Bruni, Hidalgo, Meures, et al., 2014; Villa and Rampf, 2016; Gressel and Bruni, 2018) and the theory of black holes perturbations (Campanelli and Lousto, 1999; Garat and Price, 2000; Gleiser et al., 2000; Loutrel et al., 2021; Ripley et al., 2021; Cheung et al., 2023; Mitman et al., 2023), that have been summarised in various reviews (Kokkotas and Schmidt, 1999; Malik and Matravers, 2008; Tsagas, Challinor, and Maartens, 2008; Berti, Cardoso, and Starinets, 2009; Malik and Wands, 2009; Berti, Yagi, et al., 2018; Pound and Wardell, 2020). The theory of gauge variance of relativistic perturbations was then extended to higher order with two and more parameters in Bruni, Gualtieri, and Sopuerta (2003) and Sopuerta, Bruni, and Gualtieri (2004), again with applications in cosmology (Pitrou, Pereira, and Uzan, 2015; Goldberg, Clifton, and Malik, 2017; Talebian-Ashkezari, Ahmadi, and Abolhasani, 2018) and sources of gravitational waves (Passamonti, Bruni, Gualtieri, and Sopuerta, 2005; Passamonti, Bruni, Gualtieri, Nagar, et al., 2006; Passamonti, Stergioulas, and Nagar, 2007; Sopuerta and Yunes, 2009; Lenzi and Sopuerta, 2021), cf. also (Pani, 2013) and references therein.

Applying the Stewart-Walker lemma to cosmology, we then consider the vanishing terms in the FLRW background. For a flat background spacetime ${}^{(3)}\bar{R}$ is zero so ${}^{(3)}R^{(1)}$ is gauge invariant, and if the background is curved, it is the conformal curvature $a^{2}{}^{(3)}\bar{R}$ that is constant so $a^{2}{}^{(3)}R^{(1)}$ is gauge invariant. Indeed taking the ${}^{(3)}R^{(1)}$ calculated from a spatial hypersurface A so ${}^{(3)}R^{(1)}_{A}$, and coordinate transforming it to another gauge, that describes the spatial hypersurface B, will show that the first order part is unchanged, making ${}^{(3)}R^{(1)}_{A}$ gauge invariant. However, while ${}^{(3)}R^{(1)}_{A}$ has a clear spatial curvature meaning to hypersurface A, that is not the case for hypersurface B which has its own spatial curvature ${}^{(3)}R^{(1)}_{B}$. Therefore, ${}^{(3)}R^{(1)}_{A} \neq {}^{(3)}R^{(1)}_{B}$, while they are both gauge invariant, they are gauge-dependent (Malik and Wands, 2009).

Thus, the first order 3-Ricci is commonly expressed in terms of various gauge invariant terms: the comoving curvature perturbation $\mathcal{R}_c$, the uniform density curvature perturbation $\zeta^{(1)}$, and the conformal Newtonian curvature perturbation Ψ. In the synchronous-comoving gauge ${}^{(3)}R^{(1)}$ is related to $\mathcal{R}_c$ as (Lyth, 1985)

$$ {}^{(3)}R^{(1)} = 4\nabla^2\mathcal{R}_c, \qquad \text{with} \qquad \mathcal{R}_c = \psi^{(1)} + \frac{a^2}{6}\nabla^2\chi^{(1)} = \frac{1}{3}\delta^{(1)} - \zeta^{(1)}. \tag{4.50} $$

Considering the metric perturbations that are naturally zero in the background, at first order, the scalar, vector and tensor perturbations are decoupled but since there are multiple scalar and vector terms only the tensor perturbation $\chi^{TT(1)}_{ij}$ is separate from the other terms. Therefore, $\chi^{TT(1)}_{ij}$ is gauge invariant and gauge independent at first order, since it is invariant under gauge transformations and has the same physical meaning in all gauges (Malik and Wands, 2009; Ota, Macpherson, and Coulton, 2022).

The Weyl tensor itself is zero in the background, whether it is curved or flat. Therefore all first-order terms constructed from $C_{\alpha\beta\mu\nu}$ are gauge invariant at first order. Cosmology aside, both

Teukolsky (1973) for the Kerr black hole and Stewart and Walker (1974) for any type D spacetime based their studies of first-order perturbations on Weyl scalars in the principal null direction (creating frame-dependent quantities). If the background is of type D, only Ψ_2 is non-zero, so all other Weyl scalars are gauge invariant at first-order[1], including Ψ_4 which is then commonly used to extract first-order gauge invariant gravitational wave information. However, the discussion that follows the decomposition of the Weyl tensor is usually frame-dependent, the principal null direction is preferred for the Weyl scalars, and an arbitrary frame can be chosen for the gravito-electromagnetic decomposition. This frame needs to be chosen in a physically meaningful way.

4.2.6.2 Covariant invariants

In cosmology, a physically meaningful unique frame that is always present is the fluid rest frame. This is key to the covariant approach to cosmological perturbation theory where first order gauge-invariant quantities explicitly depending on the fluid frame are considered (Ellis and Bruni, 1989). Hawking (1966) first used this as the shear and vorticity of the matter 4-velocity vanish in an FLRW background, together with the electric and magnetic parts of the Weyl tensor in the fluid frame $E^{\{u\}}_{\alpha\beta}$ and $B^{\{u\}}_{\alpha\beta}$ from Eq. (2.73), where their first order quantities are gauge invariant (Bruni, Dunsby, and Ellis, 1992). If we define $E^{\{n\}}_{\alpha\beta}$ and $B^{\{n\}}_{\alpha\beta}$ with respect to a frame $n^\mu = u^\mu + V^\mu$, where V^μ is a first order deviation from the background u^μ. Contracting $C_{\alpha\beta\mu\nu}$ with n^μ gives, at first order, the same result as contracting with u^μ, i.e. $E^{\{n\}\mu\nu} = E^{\{u\}\mu\nu} + \mathcal{O}(2)$ and $B^{\{n\}\mu\nu} = B^{\{u\}\mu\nu} + \mathcal{O}(2)$. Should there be only scalar perturbations, then the first order magnetic term is zero $B^{\{u\}(1)}_{\alpha\beta} = 0$, so the second order term $B^{\{u\}(2)}_{\alpha\beta}$ is gauge invariant.

This covariant approach was then extended in Ellis and Bruni (1989) by defining fully nonlinear variables characterising inhomogeneities. While most of the background terms do not vanish or are not constant, they are homogeneous, that is the case of the energy density $\bar{\rho}$, expansion scalar $\bar{\Theta}$ and 3-Ricci ${}^{(3)}\bar{R}$. They evolve in time but are constant in space, so their spatial derivative vanishes which will then be gauge invariant at first-order. Here again, the frame chosen to define these spatial derivatives is that of the fluid frame, so we use the covariant derivative of the spatial hypersurface orthogonal to the fluid flow $D^{\{u\}}_i$. We then consider (Bruni, Ellis, and Dunsby, 1992)

$$\mathcal{D}_i = \frac{a}{\rho^{\{u\}}} D^{\{u\}}_i \rho^{\{u\}}, \qquad \mathcal{Z}_i = a D^{\{u\}}_i \Theta \qquad \text{and} \qquad \mathcal{C}_i = a^3 D^{\{u\}}_i {}^{(3)}R \tag{4.51}$$

that correspond to the comoving fractional density, expansion, and curvature gradients respectively. Due to the nature of these variables, their first-order evolution equations show strong similarities to those of $\delta^{(1)}$, $\vartheta^{(1)}$ and ${}^{(3)}R^{(1)}$ respectively. The continuity equation Eq. (4.42) and the momentum constraint Eq. (4.45) provide

$$h^j{}_i \dot{\mathcal{D}}_j{}^{(1)} = -\mathcal{Z}^{(1)}_i \qquad \text{and} \qquad h^j{}_i \dot{\mathcal{C}}^{(1)}_j = 0. \tag{4.52}$$

While $\mathcal{D}_i$, $\mathcal{Z}_i$ and $\mathcal{C}_i$ by definition live in the hypersurface orthogonal to the fluid flow, given by the spatial metric h_{ij}, that is not the case for their time derivative. That is why the quantity $h^j{}_i$ appears, as it projects these terms back onto the spatial hypersurface. Then the first and second order evolution

[1] Things are more complicated for more general black holes (Pani, 2013).

equations of $\delta^{(1)}$ Eq. (4.56), see Section 4.3.1 for their derivation and solution, provide the first and second order evolution equations of $\mathcal{D}_i^{(1)}$

$$\begin{aligned} h^j{}_i \ddot{\mathcal{D}}_j{}^{(1)} + 2H h^j{}_i \dot{\mathcal{D}}_j{}^{(1)} - \frac{3}{2} H^2 \Omega_m \mathcal{D}_i^{(1)} = 0, \\ 4H h^j{}_i \dot{\mathcal{D}}_j{}^{(1)} + 6H^2 \Omega_m \mathcal{D}_i^{(1)} - \frac{\mathcal{C}_i^{(1)}}{a^2} = 0. \end{aligned} \tag{4.53}$$

Showing that $\mathcal{D}_i^{(1)}$, $\mathcal{Z}_i^{(1)}$ and $\mathcal{C}_i^{(1)}$ are the covariant first-order gauge invariant equivalent of $\delta^{(1)}$, $\vartheta^{(1)}$ and ${}^{(3)}R^{(1)}$ in the fluid rest frame.

4.2.6.3 Invariant by coordinate transformation

Clearly, not all perturbations of interest can be directly characterised by a tensor field that vanishes in the background, notably perturbations of the metric (other than the tensor perturbation). Nonetheless, first-order gauge-invariant variables can be constructed as linear combinations of gauge-variant quantities, such as the metric components and velocity perturbations, as first proposed by Gerlach and Sengupta (1978), then fully developed for perturbations of an FLRW background by Bardeen (1980) and extended by Kodama and Sasaki (1984) to the multi-fluid and scalar field cases. This way of creating invariants is done by considering coordinate transformation rules and creating quantities where the transformation terms cancel out such that they are invariant at first order under gauge transformation. Most notably, amongst the quantities created this way, there are the Barden potentials

$$\Phi = \phi + \left(\omega' + \mathcal{H}\omega\right) - \frac{1}{2}\left(\chi'' + \mathcal{H}\chi'\right), \qquad \Psi = -\psi - \nabla^2\chi + \mathcal{H}\left(\omega - \frac{1}{2}\chi'\right). \tag{4.54}$$

Bardeen's approach is such that gauge-invariant variables only acquire a physical meaning in a specific gauge. Note that in the Newtonian gauge $\Phi = \phi$ and $\Psi = -\psi$, where Φ is referred to as the Newtonian potential and Ψ as the conformal Newtonian curvature perturbation and it satisfies the Poisson equation

$$\nabla^2\Psi = \frac{3}{2} H^2 \Omega_m \delta, \tag{4.55}$$

where it takes the role of the gravitational potential. The sign of Φ and Ψ differs within the literature as this is an arbitrary choice but the difference between the two $|\Phi|/|\Psi|$ or $\Phi - \Psi$ is the anisotropic slip commonly used to quantify higher order effects (Macpherson, Lasky, and Price, 2017; Sobral-Blanco and Bonvin, 2021).

It is clear, however, that physical results can't depend on the mathematical approach used, and the two approaches are equivalent[2], as shown in (Goode, 1989; Bruni, Dunsby, and Ellis, 1992; Dunsby, Bruni, and Ellis, 1992), indeed the physical meaning of Bardeen-like variables is elucidated through the use of the covariant variables, e.g. Bardeen's potentials appear in the expansion of the electric Weyl tensor Eq. (4.41); Bardeen's evolution equations for the gauge-invariant variable are also recovered in the same process, see Bruni, Dunsby, and Ellis (1992) section 5.

[2] More precisely, a full equivalence with Bardeen's original variables is obtained under minimal and reasonable assumptions, in essence, those required for a harmonic expansion on the homogeneous and isotropic 3-space of the FLRW background, see also (Stewart, 1990).

4.2.6.4 Observables

Measurable quantities in relativity (Rovelli, 1991), commonly referred to as observables, should be gauge-invariant, and the invariant scalars discussed in Section 2.5.3 are gauge-invariant observables in that sense, i.e. they are coordinate independent.

How about observables as usually intended by cosmologists? Both the scalar invariants of the previous section and the gauge-invariant perturbations discussed above are local quantities, but in cosmology, observers can't go in a galaxy far far away and measure $E^{\{u\}\mu\nu}$ and $B^{\{u\}\mu\nu}$ there: rather we have to link points (spacetime events) on the past light-cone of the observer, points where local observables are defined, with the point of the observers themselves, i.e. ray tracing is key, see Adamek, Barrera-Hinojosa, et al. (2020) for a concrete example in NR cosmology and an application to simulation comparisons and Grasso and Villa (2021), Grasso, Villa, et al. (2021), Buchert, Elst, and Heinesen (2023), and Macpherson (2023) and references therein for a general discussion. Nonetheless, although the issue of defining observables is simple for first-order perturbations but more involved at second and higher-order, first-order gauge invariance, i.e. the vanishing in the background of the value of the observable tensorial quantity, plays a crucial role, see Bruni and Sonego (1999) and Yoo and Durrer (2017) for a recent and extended discussion.

4.3 Structure formation

As small fluctuations in an otherwise homogeneous universe grow, they become the LSS we observe today (Peacock, 1999; Mo, Bosch, and White, 2010; Vittorio, 2018). These fluctuations initially grow according to the overall global evolution of the universe, but gradually they decouple to create an independent bound system. During this transition, they experience an expansion, turn-around (TA), contraction and virilisation phase. To describe this evolution non-linearly, multiple approaches have been created (Sahni and Coles, 1995; Monaco, 1997; Peacock, 1999; Mo, Bosch, and White, 2010; Vittorio, 2018), starting with the simple Top-Hat spherical and homogeneous collapse model (Gunn and Gott, 1972), see Section 4.3.2, to then gradually consider more elaborated models (Mo, Bosch, and White, 2010), see Section 4.3.4, to finally work with numerical simulations when the system becomes too complex see Section 4.3.5.

4.3.1 From perturbation theory

The first-order scalar constraint and evolution equations for an irrotational dust perfect fluid have been expressed in Section 4.2.4, upon these, we will determine how δ evolves. The continuity, Raychaudhuri and Hamiltonian equations Eq. (4.42), Eq. (4.43) and Eq. (4.44) provide the first and second order evolution equations of $\delta^{(1)}$ as (Bruni, Hidalgo, Meures, et al., 2014)

$$\begin{aligned} H\dot{\delta}^{(1)} + \frac{3}{2}H^2\Omega_m\delta^{(1)} &= \frac{1}{4}{}^{(3)}R^{(1)}, \\ \ddot{\delta}^{(1)} + 2H\dot{\delta}^{(1)} - \frac{3}{2}H^2\Omega_m\delta^{(1)} &= 0. \end{aligned} \tag{4.56}$$

These are ordinary differential equations, so the solution to the first order equation is composed of a homogeneous solution δ_- (no source term) and a particular solution δ_+ which is sourced by the

curvature ${}^{(3)}R^{(1)}$. To find these solutions, in the matter-dominated era, we shall set the background to be EdS from Section 4.1.4.4 with $\Omega_m = 1$.

Firstly, the homogeneous solution, setting $\delta_- \propto H$, we see that the first-order equation corresponds with the second Friedmann equation Eq. (4.26) they then have the same solution and so $\delta_- \propto 1/\tau$. This means that as $\tau \to +\infty$ then $\delta_- \to 0$, so this is commonly called the decaying solution or mode.

Secondly, considering the particular solution, setting $\delta_+ \propto a$, we see that the second order differential equation corresponds to the second Friedmann equation Eq. (4.26), so they have the same solution $\delta_+ \propto \tau^{2/3}$. δ_+ then grows over time; it is called the growing solution or mode.

Combining the two solutions together, with constant factors of the same order of magnitude, as time evolves, the growing mode dominates the evolution, as $\tau \to +\infty$ then $\delta \to \delta_+$, such that in the matter-dominated era, δ_- is negligible, and only δ_+ is considered.

Yet the best current model of the universe is the ΛCDM solution, see Section 4.1.4.5, which differs from the EdS solution, see Section 4.1.4.4 as the former has the cosmological constant Λ. This is quantified with the difference between the growth of δ and that of the scale factor a known as the growth factor (Peebles, 1980; Wang and Steinhardt, 1998; Bernardeau et al., 2002; Linder and Cahn, 2007)

$$f_1 = \frac{d\ln\delta}{d\ln a} = \frac{a\dot{\delta}}{\dot{a}\delta} = \frac{\dot{\delta}}{H\delta} \simeq \Omega_m^{6/11}, \tag{4.57}$$

where if Λ were absent, $f_1 = 1$.

4.3.2 Top-Hat spherical collapse model

To describe the density contrast's nonlinear growth, the Top-Hat spherical collapse model was created by Gunn and Gott (1972). It describes a homogeneous spherically symmetric OD in the matter-dominated era, with a dust fluid in an otherwise flat FLRW universe. The density profile of such a distribution resembles a Top-Hat, hence the name of the model. This OD sphere is modelled by a closed (positive spatial curvature) FLRW "separate universe" within an external FLRW background universe, usually spatially flat (zero curvature). The radius of the Top-Hat OD expands at a slower rate than the background, gradually slowing down, as it is bound by its positive curvature (equivalent to the conserved and negative mechanical energy in the Newtonian description of the Top-Hat). It eventually reaches its maximal size, turns around (TA), and then contracts into itself to collapse. The dynamics of this OD are highly nonlinear due to decoupling with the expanding universe, so three methods beyond linear perturbation theory are considered here. Firstly, with Newtonian mechanics in Section 4.3.2.1 considering kinetic and potential energy (Sahni and Coles, 1995; Mo, Bosch, and White, 2010; Vittorio, 2018), then with the Schwarzschild and closed FLRW spacetimes in Section 4.3.2.2 and Section 4.3.2.3 respectively to describe the evolution of this sphere while "patching" those spacetimes with the otherwise flat FLRW universe.

4.3.2.1 Newtonian

❖ **Radius**

With basic mechanics, one splits the total energy of the sphere's outer shell into kinetic and potential energy

$$E_{Tot} = E_{Kin} + E_{Pot}, \tag{4.58}$$

which naturally remains constant by the conservation of energy. The two contributing terms that do vary are the kinetic energy E_{Kin}, due to the size variation, and the potential energy E_{Pot} simply corresponding to that obtained by Newtonian gravitational theory (Newton, 1687). These are expressed per unit mass with $G = 1$ as

$$E_{Kin} = \frac{1}{2}\dot{R}^2, \qquad E_{Pot} = -\frac{M}{R}, \tag{4.59}$$

where R is the radius of the outer shell, and M is the mass contained within, that can be identified with its energy density ρ and density contrast δ

$$\rho = \frac{3M}{4\pi R^3} = \bar{\rho}(1+\delta), \tag{4.60}$$

and since mass is conserved, one can identify it with the corresponding initial values. At an early initial time, the sphere expands according to the expansion of the universe, so the kinetic energy is solely sourced by the Hubble expansion at that initial time (Vittorio, 2018)

$$E_{Kin,\,IN} = \frac{1}{2}H_{IN}^2 R_{IN}^2, \qquad E_{Pot,\,IN} = -\frac{M}{R_{IN}} = -E_{Kin,\,IN}\,\Omega_{m,\,IN}(1+\delta_{IN}), \tag{4.61}$$

where M in $E_{Pot,\,IN}$ is substituted with Eq. (4.60) and $\bar{\rho}$ with Eq. (4.19).

In order for collapse to occur $E_{Tot} < 0$ therefore the initial density contrast is given the requirement (Sahni and Coles, 1995)

$$1 + \delta_{IN} > \Omega_{m,\,IN}^{-1}. \tag{4.62}$$

Should this be satisfied then the sphere transitions from expanding to infalling, at turn-around (TA), where R reaches its maximal size R_{TA} and $\dot{R}$ changes sign such that there is no kinetic energy, leaving only the potential energy non-zero

$$E_{Kin,\,TA} = 0, \qquad E_{Pot,\,TA} = -\frac{M}{R_{TA}}, \tag{4.63}$$

and so $E_{Tot} = E_{Pot,\,TA}$. By conservation of energy, the evolution equation of R is then retrieved as

$$\frac{1}{2}\dot{R}^2 - \frac{M}{R} = -\frac{M}{R_{TA}}, \tag{4.64}$$

and R_{TA} is expressed as a function of the initial values as

$$R_{TA} = \frac{R_{IN}(1+\delta_{IN})}{1+\delta_{IN}-\Omega_{m,\,IN}^{-1}}, \tag{4.65}$$

where M and H_{IN} in $E_{Tot,\,IN} = E_{Tot,\,TA}$ were substituted with Eq. (4.60) and Eq. (4.19). The solution to the evolution equation, Eq. (4.64), is found with the new variable ς such that

$$\begin{aligned} R &= \frac{R_{TA}}{2}(1-\cos(\varsigma)), \\ \tau &= \frac{\tau_{TA}}{\pi}(\varsigma - \sin(\varsigma)), \end{aligned} \qquad \text{with} \qquad \left(\frac{R_{TA}}{2}\right)^3 = \left(\frac{\tau_{TA}}{\pi}\right)^2 M. \tag{4.66}$$

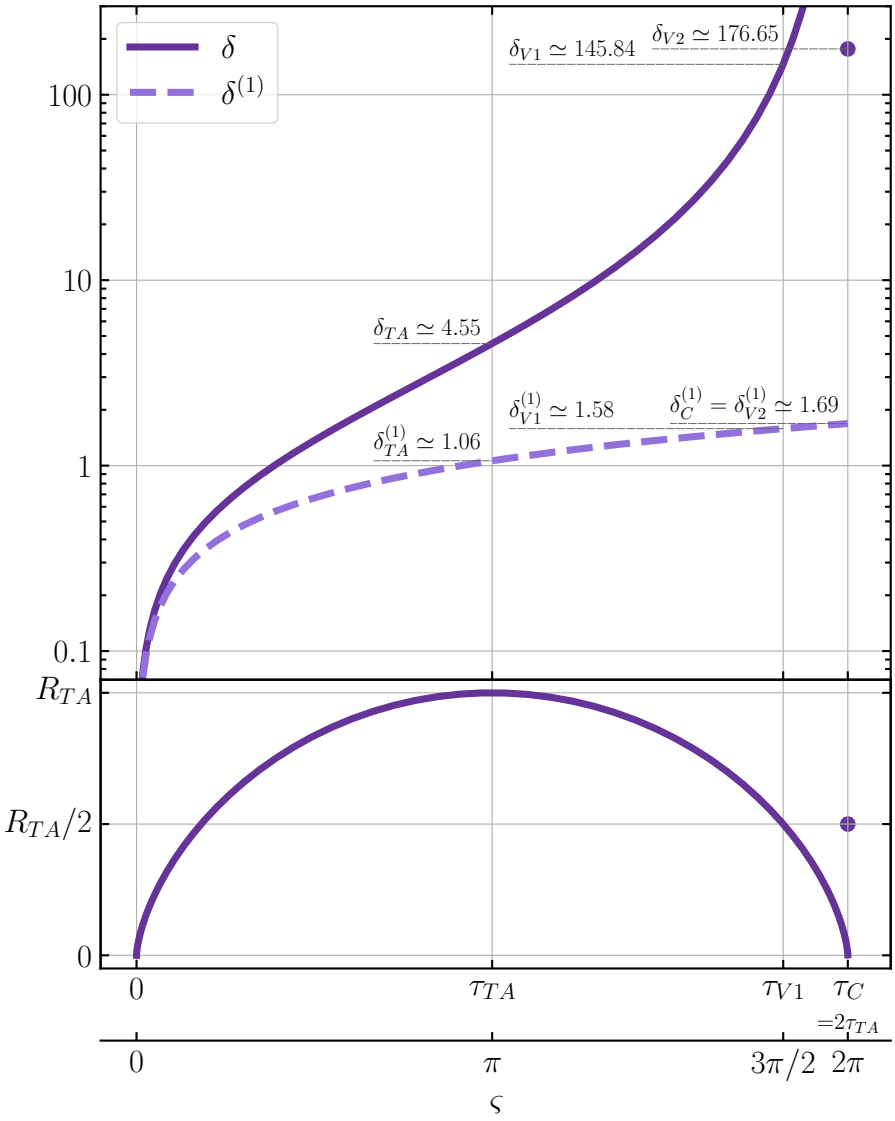

Figure 4.1: Top-Hat spherical collapse model: radius R Eq. (4.66), nonlinear and linear density contrast δ Eq. (4.60) and $\delta^{(1)}$ Eq. (4.74) of a homogeneous spherical over-density in an otherwise flat EdS universe as a function of proper time τ whose corresponding ς Eq. (4.66) is presented below with its own axis. The moments of turn-around (TA), virialisation (V) and collapse (C) are emphasised with vertical lines with their density contrast constants listed in the top panel. Virialisation according to the first definition $V1$ is on the Eq. (4.66) curve, but since the virialisation, according to the second definition $V2$, is not on this curve (requiring extra relaxation mechanisms) it is marked on each plot with a dot.

τ_{TA} can then also be expressed as a function of the initial conditions with Eq. (4.65)

$$\tau_{TA} = \frac{\pi(1+\delta_{IN})}{2H_{IN}\Omega_{m,\,IN}^{1/2}(1+\delta_{IN}-\Omega_{m,\,IN}^{-1})^{3/2}}. \tag{4.67}$$

The practical parametrisation of ς allows us to see that R reaches its maximal size R_{TA} at $\varsigma_{TA} = \pi$ or τ_{TA} and is zero at $\varsigma_C = 2\pi$ or $\tau_C = 2\tau_{TA}$ which identifies TA and collapse, see Fig. (4.1) whose bottom plot presents Eq. (4.66).

According to the virial theorem (Clausius, 1870), virialisation happens when the potential energy is double the kinetic energy, with a sign change, $E_{Pot,\,V} = -2E_{Kin,\,V}$ such that the total energy is

$E_{Tot,\,V} = E_{Pot,\,V}/2$. As energy is conserved, this means that the potential energy at virialisation can be related to the potential energy at TA, $E_{Pot,\,V}/2 = E_{Pot,\,TA}$, therefore at virialisation the radius becomes $R_V = R_{TA}/2$, which according to Eq. (4.66) is when $\varsigma_V = 3\pi/2$. In literature, different authors identify virialisation following different definitions (Sahni and Coles, 1995; Peacock, 1999; Mo, Bosch, and White, 2010; Vittorio, 2018). The first choice, simply following Eq. (4.66) identifies it as above at $\varsigma_{V1} = 3\pi/2$, while the second choice is based on additional relaxation mechanisms that are not present in this simplistic description. In practice, particles would start interacting with each other, slowing down the collapse such that it reaches its virialised state $R_V = R_{TA}/2$ at a later time, notably when it would otherwise collapse $\varsigma_{V2} = \varsigma_C = 2\pi$. This requires a discontinuity with the Eq. (4.66) curve, see the bottom plot of Fig. (4.1) where this theoretical point in time is marked at $R_{TA}/2$ and τ_C.

❖ Nonlinear density contrast

The energy density can be retrieved with Eq. (4.60), keeping M constant, and substituting R and R_{TA} with Eq. (4.66) such that

$$\rho = \frac{3\pi}{4\tau_{TA}^2(1-\cos(\varsigma))^3}. \tag{4.68}$$

At the key instances of the evolution $\varsigma_{TA} = \pi$, $\varsigma_{V1} = 3\pi/2$, and $\varsigma_C = 2\pi$, the energy density is then

$$\rho_{TA} = \frac{3\pi}{32\tau_{TA}^2}, \qquad \rho_{V1} = \frac{3\pi}{4\tau_{TA}^2}, \qquad \rho_C = +\infty. \tag{4.69}$$

To further quantify the density contrast $\delta = \rho/\bar{\rho} - 1$, one needs to make a choice as to the model considered to express $\bar{\rho}$. The usual choice is with EdS, see Section 4.1.4.4, where $\bar{\rho} = 1/6\pi\tau^2$ such that substituting τ with Eq. (4.66) provides δ as (Sahni and Coles, 1995)

$$\delta = \frac{9(\varsigma - \sin(\varsigma))^2}{2(1-\cos(\varsigma))^3} - 1, \tag{4.70}$$

which is plotted in the top panel of Fig. (4.1). At the relevant events, with Eq. (4.69), δ is

$$\delta_{TA} = \left(\frac{3\pi}{4}\right)^2 - 1 \simeq 4.55, \qquad \delta_V = 2\left(\frac{3\pi\tau_V}{2\tau_{TA}}\right)^2 - 1, \qquad \delta_C = +\infty. \tag{4.71}$$

where τ_V is chosen according to the corresponding virialisation definition

$$\delta_{V1} = 2\left(\frac{3(3\pi+2)}{4}\right)^2 - 1 \simeq 145.84, \qquad \delta_{V2} = 2\,(3\pi)^2 - 1 \simeq 176.65. \tag{4.72}$$

All of these constants are identified in the top panel of Fig. (4.1).

❖ Linear density contrast

Taking the limit of Eq. (4.70) as ς tends towards zero, where the evolution of δ would be accurately portrayed by its linear value, provides

$$\lim_{\varsigma\to 0}\delta \simeq \delta^{(1)} = \frac{3}{5}\delta_{IN}\left(\frac{\tau}{\tau_{IN}}\right)^{2/3}, \tag{4.73}$$

which is proportional to the scale factor, as shown in Section 4.3.1 for a growing mode. The extra factor means that only $3/5$ of the initial amplitude contributes to the growing mode (Sahni and

Coles, 1995). Then substituting τ with Eq. (4.66) and τ_{TA}, Eq. (4.67), expressed at first order in EdS $\tau_{TA}^{(1)} = \frac{3\pi}{4}\tau_{IN}\delta_{IN}^{-3/2}$, then provides

$$\delta^{(1)} = \frac{3}{5}\left(\frac{3}{4}\right)^{2/3}(\varsigma - \sin(\varsigma))^{2/3}, \tag{4.74}$$

$$\begin{aligned} \delta_{TA}^{(1)} &= \frac{3(6\pi)^{2/3}}{20} \simeq 1.06, \\ \delta_{V1}^{(1)} = \frac{3(9\pi+6)^{2/3}}{20} \simeq 1.58, &\qquad \delta_{C}^{(1)} = \delta_{V2}^{(1)} = 2^{2/3}\delta_{TA}^{(1)} \simeq 1.69. \end{aligned} \tag{4.75}$$

Again these constants are identified in the top panel of Fig. (4.1). $\delta_C^{(1)}$, in particular, is a crucial constant present in the Press-Schechter mass function (Press and Schechter, 1974), see Section 4.3.3.

4.3.2.2 Schwarzschild

The Schwarzschild (1916) metric for a static spherically symmetric star of mass M is

$$ds^2 = -F(r)dt^2 + F^{-1}(r)dr^2 + r^2 d\Omega^2 \qquad \text{with} \qquad F(r) = 1 - \frac{2M}{r}. \tag{4.76}$$

The Schwarzschild radius $2M$ corresponds to an event horizon, if the radius of the star's surface is larger than the Schwarzschild radius then it is a normal star, otherwise, it is a black hole.

We shall now consider the 4-velocity of a sphere of particles around this star such that θ and ϕ are constant. Following from Section 2.1.2.2 this vector is along a geodesic and takes the form $v^\alpha = \left(\dot{t},\ \dot{r},\ 0,\ 0\right)$, and its timelike normalisation provides (Chandrasekhar, 1992)

$$v^\alpha v_\alpha = g_{\alpha\beta}v^\alpha v^\beta = -F(r)\dot{t}^2 + F^{-1}(r)\dot{r}^2 = -1. \tag{4.77}$$

Because the metric does not depend on t or ϕ, then this spacetime has the two Killing fields $\xi_t^\alpha = \{1,\ 0,\ 0,\ 0\}$ and $\xi_\phi^\alpha = \{0,\ 0,\ 0,\ 1\}$, see Section 2.1.4.1. ξ_t^α indicates that the spacetime is static and the contraction with our vector along the geodesic curve identifies the particle's total energy $g_{\alpha\beta}\xi_t^\alpha v^\beta = F(r)\dot{t} = E_{Tot}$ (Wald, 1984). Likewise, $\xi_{\phi\alpha}v^\alpha$ provides the angular momentum which is zero for our sphere of particles. Simply introducing E_{Tot} into Eq. (4.77) provides the equation of motion $\dot{r}^2 = E_{Tot}^2 - F(r)$. Should $\dot{r} = 0$, as it is the case at TA, then E_{Tot} is identified as $E_{Tot}^2 = F(r_{TA})$ meaning that

$$\dot{r}^2 = -\frac{2M}{r_{TA}} + \frac{2M}{r} \tag{4.78}$$

which is identical to Eq. (4.64), therefore having the same solution Eq. (4.66) plotted in the bottom panel of Fig. (4.1). Typically for a black hole or star the expanding phase of this sphere is omitted, using r_{TA} as the initial size of the sphere, and no virialisation is considered as the particles are all absorbed by the black hole or star.

4.3.2.3 Closed FLRW

The first Friedmann equation Eq. (4.18) of a dust filled closed universe, $k = 1$, with no cosmological constant using Eq. (4.17), takes the form

$$\dot{a}^2 = -1 + \frac{a_{TA}}{a} \qquad \text{with} \qquad a_{TA} = \frac{\kappa\bar{\rho}_0 a_0^3}{3} \tag{4.79}$$

where a_{TA} is taken when $\dot{a}$ is at rest, marking a transition between expansion and contraction. The Friedmann equation in this form has taken the same expression as Eq. (4.66) whose solution is

$$a = \frac{a_{TA}}{2}(1 - \cos(\varsigma)), \qquad \tau = \frac{\tau_{TA}}{\pi}(\varsigma - \sin(\varsigma)), \tag{4.80}$$

as seen in Table (4.1). This solution can again be found should we consider the Lemaître (1933), Tolman (1934), and Bondi (1947) (LTB) metric (Vittorio, 2018).

These methods of finding Eq. (4.66) show that this model is valid no matter the gravitational attractor, as long as the matter is spherically distributed. Even though in the Newtonian description, there is no curvature, the GR picture provided here shows that indeed this sphere is positively curved. Fitting this into the universe, one can think of a Swiss-cheese universe, it is a flat FLRW universe with OD holes which contain a positively curved FLRW or LTB solution (Marra et al., 2007) but also UD holes of a negative curvature FLRW solution.

4.3.3 Mass function

However simple the Top-Hat model seems, this provides a critical value that is essential for the Press-Schechter mass function and the Sheth-Tormen extension (Press and Schechter, 1974; Sheth and Tormen, 1999). The mass function is a crucial estimator providing the number of virialised objects of mass M at a given time (Monaco, 1997; White, 2002; Mo, Bosch, and White, 2010). This comes from the probability that the density contrast is greater than $\delta_C^{(1)}$.

Consider the initial δ_{IN} distribution, linearly extrapolated to the redshift of interest $\delta^{(1)}$ and smoothed over to the relevant scale R, providing $\delta_M^{(1)}$, where R is the radius of a sphere encompassing the chosen mass M in the background $\frac{4\pi}{3}R^3 = \frac{M}{\bar{\rho}}$. The spherical smoothing is key to the Press-Schechter mass function; it is improved with Sheth-Tormen using an ellipsoid window function. The $\delta_M^{(1)}$ distribution will then have the corresponding variance σ_M (filtered with the same spherical window function) and a mean of zero (in accordance with the cosmological background). Assuming this is a Gaussian distribution, the cumulative probability density function is

$$\begin{aligned} P\left(\delta_M^{(1)} > \delta_C^{(1)}\right) &= \frac{1}{\sigma_M\sqrt{2\pi}} \int_{\delta_C^{(1)}}^{\infty} \exp\left(-\frac{\delta_M^{(1)2}}{2\sigma_M^2}\right) d\delta_M^{(1)} \\ &= \frac{1}{2}\mathrm{erfc}\left(\frac{\delta_C^{(1)}}{\sigma_M\sqrt{2}}\right) \end{aligned} \tag{4.81}$$

where erfc() is the error function.

The probability $P(\delta_M^{(1)} > \delta_C^{(1)})$ provides the mass fraction of collapsed objects; when differentiated, this gives the number density of collapsed objects known as the mass function. Using $\delta_C^{(1)}$ as a virialisation identifier is key to this method and so it is worthwhile to check this constant.

4.3.4 More complicated analytical models

More complex models have since been created with either inhomogeneity, a non-spherical shape, or with angular momentum (Mo, Bosch, and White, 2010; Giusti and Faraoni, 2021), most notably the Zel'dovich approximation, in the context of Newtonian structure formation, informs us on how pancakes are formed (Zel'dovich, 1970) and how they represent the attractors for the dynamics (Bruni,

Maartens, and Tsagas, 2003). Yet, all these models lack relaxation mechanisms that would bring the structure to its final virialised stable state. The first attempt to describe this was with statistical mechanics (Lynden-Bell, 1967), however, analytical limitations have led many researchers to work with numerical simulations instead. With these tools, an inhomogeneous universe is either modelled with a fluid or particle description of matter.

4.3.5 Simulations

N-body simulations have the advantage of going beyond shell crossing and inform us on the virialisation process and the shape of LSS (White and Rees, 1978; Navarro, Frenk, and White, 1996; Gosenca et al., 2017; Pace et al., 2019; Angulo and Hahn, 2022; Saga, Taruya, and Colombi, 2022). With some caveat, it has been shown that in the Newtonian case the simulations accurately portray structure formation when compared with GR simulations, except when the weak gravity regime doesn't hold (East, Wojtak, and Abel, 2018). To make the description of gravity in N-body simulations somehow more accurate, multiple approaches have been attempted (Fidler et al., 2016). A simple approximation has been used in Rácz, Dobos, et al. (2017), where matter is coupled to the expansion of distances with the average expansion-rate approximation. A fully relativistic approach neglecting only tensor modes has been used in Barrera-Hinojosa and Li (2020a,b) and Barrera-Hinojosa, Li, Bruni, et al. (2021), based on the constant mean curvature and minimal distortion gauge. In Adamek, Daverio, et al. (2016a,b) and Lepori et al. (2023) a weak field expansion has been used, based on the Poisson gauge with six degrees of freedom in the metric, see also Adamek, Barrera-Hinojosa, et al. (2020). Alternatively, a relativistic post-processing treatment of Newtonian simulations can measure vector modes (Bruni, Thomas, and Wands, 2014; Thomas, Bruni, and Wands, 2015; Barrera-Hinojosa, Li, and Cai, 2021), even for $f(R)$ gravity (Thomas, Bruni, Koyama, et al., 2015). Finally, some relativistic effects can be extracted from Newtonian simulations with ray-tracing, see e.g. (Barreira et al., 2016; Rasera et al., 2022; Tian, Carney, et al., 2022; Macpherson, 2023). To make the gravitational description fully relativistic, one may instead simplify the matter description and consider collisionless particles that evolve according to the global distribution (Yoo, Harada, and Okawa, 2017; East, Wojtak, and Pretorius, 2019; Giblin, Mertens, Starkman, and Tian, 2019b) or using smooth particle hydrodynamics (Magnall et al., 2023; Rosswog, Torsello, and Diener, 2023).

The fluid description of matter lends itself more conveniently to the 3+1 formalism of NR (East, Pretorius, and Stephens, 2012; Torres et al., 2014; Rekier, Cordero-Carrión, and Füzfa, 2015; Bentivegna and Bruni, 2016; Giblin, Mertens, and Starkman, 2016; Mertens, Giblin, and Starkman, 2016; Macpherson, Lasky, and Price, 2017, 2018; Adamek, Barrera-Hinojosa, et al., 2020; Staelens, Rekier, and Füzfa, 2021). While convenient for early times cosmology, together with scalar fields (Kurki-Suonio et al., 1987; Goldwirth and Piran, 1990; Musco, Miller, and Polnarev, 2009; Alcubierre, Macorra, et al., 2015; Clough and Lim, 2016; Braden et al., 2017; Clough, Lim, et al., 2017; Yoo, Ikeda, and Okawa, 2019; Aurrekoetxea, Clough, Flauger, et al., 2020; Andrade et al., 2021; Kou et al., 2022), it finds its limitations at the first shell crossing. As structures decouple from the background and subsequently virialise, particles should go into a multi-stream regime, while in a fluid description, shell crossing crashes simulations with comoving coordinates.

Both methods have their advantages and disadvantages, and it is important to keep those in mind depending on the simulated scenario.

5 - EBWeyl

NR simulations are based on the 3+1 formalism (Alcubierre, 2008; Arnowitt, Deser, and Misner, 2008; Shibata, 2015), see Chapter 3, where obtained results depend on the gauge choice in general, which in the 3+1 context corresponds to a choice of lapse and shift, i.e. a choice of mapping between a time-slicing and the next one, see Section 3.4 cf. (Giblin, Mertens, Starkman, and Tian, 2019b; Tian, Anselmi, et al., 2020) for a discussion in the cosmological context. In practice, this gauge choice is equivalent to fixing coordinates, therefore, the raw results of simulations are gauge/-coordinate dependent. Physical interpretations and simulation comparisons then need to be done in a gauge-independent manner based on invariants (East, Wojtak, and Abel, 2018; East, Wojtak, and Pretorius, 2019; Adamek, Barrera-Hinojosa, et al., 2020), see Section 2.5.3, these are quantities that characterise the spacetime (D'Inverno and Russell-Clark, 1971; Karlhede, 1980; Carminati and McLenaghan, 1991; Bonnor, 1995; McIntosh et al., 1995; Zakhary and McIntosh, 1997; Stephani et al., 2003; Alcubierre, 2008; Wylleman et al., 2019; Bini, Geralico, and Jantzen, 2023) and should be, at least in principle, observable, i.e. measurable quantities (Rovelli, 1991). The invariant characterisation of spacetimes obtained in NR, specifically in cosmological simulations, is our main motivation, together with the presentation of `EBWeyl`, a publicly available Python post-processing code built for this purpose (Munoz, 2022). An application of `EBWeyl` to the computation of the various invariants discussed here is presented in Munoz and Bruni (2023b) see Chapter 6, where we analyse the evolution of cosmic structures and a quasi-spherical collapse from initial curvature perturbations.

Within cosmological perturbation theory, according to the Stewart-Walker lemma (Stewart and Walker, 1974), the electric and magnetic parts of the Weyl tensor, $E^{\{u\}}_{\alpha\beta}$ and $B^{\{u\}}_{\alpha\beta}$ (Matte, 1953; Jordan et al., 1964; Hawking, 1966) see Section 2.5.1, are gauge-independent at first order because they vanish in the background, see Section 4.2.6.2. Therefore, if we consider linear perturbations of an FLRW spacetime, $E^{\{u\}}_{\alpha\beta}$ and $B^{\{u\}}_{\alpha\beta}$ are first-order gauge-invariant variables (Hawking, 1966; Ellis and Bruni, 1989; Bruni, Dunsby, and Ellis, 1992); they are related to the Bardeen potentials (Bardeen, 1980; Bruni, Dunsby, and Ellis, 1992; Lewis and Challinor, 2006), and so are scalars constructed from them, see Eq. (4.41) in Section 4.2.4.

$E^{\{u\}}_{\alpha\beta}$ and $B^{\{u\}}_{\alpha\beta}$ are of specific interest for their physical meaning: they describe the non-local tidal gravitational fields (overall represented by the Weyl curvature) and they are related to the shear and vorticity of matter (Maartens and Bassett, 1998; Ellis, 2009; Ellis, Maartens, and MacCallum, 2012) see Section 2.5.1. They can be computed from simulations in NR, and because of their physical meaning, and since they are gauge invariant at first order, they are a clear asset in describing the simulated scenario and comparing with different codes and with perturbation theory (Wylleman et al., 2019). Additionally, they can be used to build a full set of coordinate independent and invariant scalars that characterises the spacetime see Section 2.5.3, some frame-dependent and some frame-independent, and these scalars can be used for the Petrov classification described in Section 2.5.4.

Describing the spacetime of an NR simulation using $E^{\{u\}}_{\alpha\beta}$ and $B^{\{u\}}_{\alpha\beta}$ was first considered for colliding black holes (Owen et al., 2011). A cosmological application has been studied for universe models containing lattice of masses where a significant magnetic part can arise (Korzyński, Hinder, and Bentivegna, 2015; Clifton, Gregoris, and Rosquist, 2017). Furthermore, an approximation where the magnetic part has no divergence has been found to be valid on large scales in simulations of a non-linear matter-dominated spacetime (Heinesen and Macpherson, 2022). Indeed gravitomagnetic effects have been gaining interest for their possible implications in cosmology (Bruni, Thomas, and Wands, 2014; Milillo et al., 2015; Thomas, Bruni, Koyama, et al., 2015; Thomas, Bruni, and Wands, 2015; Barrera-Hinojosa, Li, Bruni, et al., 2021; Barrera-Hinojosa, Li, and Cai, 2021).

In this chapter, based on Munoz and Bruni (2023a), we present two methods to compute $E^{\{u\}}_{\alpha\beta}$ and $B^{\{u\}}_{\alpha\beta}$, with the goal of computing them numerically: we call the first “geometrical" as the computation only requires the spacetime metric, while we call the second “slicing" (Munoz, 2022), as the required variables are those of the 3+1 decomposition of spacetime. The defining difference between the two methods is in how the time derivatives of the spacetime metric are computed; for the former, this is done numerically, while for the latter this is obtained from the extrinsic curvature. For each of these two methods, a code was created and tested on five example spacetimes, four of which are known exact solutions of GR; these tests demonstrate the reliability of our codes. These spacetimes were specifically chosen because they provide examples from cosmology. One of the examples we consider is inhomogeneous, it is a generalisation of the dust-only Szekeres models (Szekeres, 1975) that includes the cosmological constant Λ (Barrow and Stein-Schabes, 1984), which we call Λ-Szekeres. Since it doesn't have a magnetic Weyl part, in order to test the codes on an inhomogeneous spacetime with a non-zero $B^{\{u\}}_{\alpha\beta}$ we have also introduced a conveniently made-up metric. Our tests and results show that the code based on the slicing method outperforms the other: on this basis, we have made the slicing code, which we dub `EBWeyl`, publicly available at (Munoz, 2022).

This chapter is structured as follows. Section 5.1 presents our two Python post-processing codes: the geometrical and slicing codes. In Section 5.1.1 we describe how the electric and magnetic parts of the Weyl tensor, $E_{\alpha\beta}$ and $B_{\alpha\beta}$, are derived from the Riemann tensor; this establishes the geometrical method used in our first code, see Section 2.5.1. Then, in Section 5.1.2, we present an alternative computational method to obtain $E_{\alpha\beta}$ and $B_{\alpha\beta}$ directly based on the 3+1 slicing formulation; this establishes the slicing method used in our second code (Munoz, 2022), see Section 3.5. Invariants needed for the Petrov classification that can be computed from $E_{\alpha\beta}$ and $B_{\alpha\beta}$ are now described in Section 2.5.3, where we also introduce the Weyl scalars. Our codes are tested on five spacetimes, these are each presented in Section 5.2. The usefulness of these codes is demonstrated using the Λ-Szekeres metric (Barrow and Stein-Schabes, 1984) in Section 5.3.1, where for this spacetime we compute $E_{\alpha\beta}$ and $B_{\alpha\beta}$, the 3-dimensional and 4-dimensional Ricci scalars, the invariants of Section 2.5.3 and the Petrov type. Finally, the performance and computing errors are discussed in Section 5.3.2. In Section 5.4 we draw our conclusions. In two appendices we demonstrate finite difference limitations (Appendix A) and list the analytical expressions we computed with Maple (Maplesoft, 2019) and used in this chapter (Appendix B).

5.1 Codes

In this section, we present the two codes, the theoretical methods and numerical implementations to compute $E^{\{n\}2} = E^{\{n\}}_{\mu\nu} E^{\{n\}\mu\nu}$, and $B^{\{n\}2} = B^{\{n\}}_{\mu\nu} B^{\{n\}\mu\nu}$. These are both Python post-processing codes, one referred to as the geometrical code and the other which is based on the slicing method that we call `EBWeyl` (Munoz, 2022). These are applied in Section 5.3 to the test-bed metrics reviewed in Section 5.2. The theoretical framework section has been shortened and merged with the code description section compared to Munoz and Bruni (2023a) since the relevant information can now be found in the background chapters Chapter 2, Chapter 3, and Chapter 4.

5.1.1 Geometrical code

In the code using the geometrical approach, the 4-dimensional Riemann tensor is calculated from its definition in terms of the derivatives of the metric $g_{\alpha\beta}$. From the 4-dimensional metric $g_{\alpha\beta}$, its derivatives are computed numerically and these are then used to compute the Christoffel symbols Eq. (2.14) and its derivatives to then calculate the 4-dimensional Riemann tensor $R_{\alpha\beta\mu\nu}$ with Eq. (2.19). Because of the added complexity in computing time derivatives, this code has been developed only for the synchronous gauge, $g_{0\alpha} = \{-1,\ 0,\ 0,\ 0\}$. In practice, assuming that this post-processing code is applied to data produced by a numerical simulation in this gauge, then the metric is directly given by γ_{ij}.

The first spatial derivatives of the metric are computed with a centred finite difference (FD) scheme where the boundary points are obtained using a periodic boundary condition when applicable (here only for the test metric case Section 5.2.2), otherwise a combination of forward and backward schemes are used, see Section 3.6.1. As the centred scheme has lower relative error than either the forward or backward scheme, the points along the edges affected by this boundary choice are cut off, see Appendix A. These considerations are of no concern when applying these codes to cosmological simulation results, as in this case the boundary conditions commonly used are periodic.

The first time derivative of the metric in the synchronous gauge coincides with the extrinsic curvature, $K_{ij} = -\frac{1}{2}\partial_t \gamma_{ij}$, and therefore can directly be retrieved from the data of the underlying simulation.

Finally, to compute second derivatives of the metric, spatial derivatives of all of the above are computed with the same scheme applied for the first spatial derivatives, and time derivatives are computed with a backward scheme. The FD schemes are all of 4^{th} order, then to increase accuracy we also implement the option to use 6^{th} order schemes (Fornberg, 1988), and to have Riemann symmetries enforced with $R_{\alpha\beta\mu\nu} = -R_{\beta\alpha\mu\nu} = -R_{\alpha\beta\nu\mu} = R_{\mu\nu\alpha\beta}$.

Once the 4-dimensional Riemann tensor $R_{\alpha\beta\mu\nu}$ is obtained, its trace is taken to compute the Ricci tensor $R_{\alpha\beta}$ and scalar R, Eq. (2.22, 2.23), which are removed from the Riemann tensor providing the Weyl tensor $C_{\alpha\beta\mu\nu}$ with Eq. (2.24). From these, the Weyl tensor is simply projected along the chosen timelike unit vector, say n^μ, to provide the electric and magnetic parts of the Weyl tensor according to Eq. (2.68) (Matte, 1953; Jordan et al., 1964; Hawking, 1966):

$$E^{\{n\}}_{\alpha\mu} = n^\beta n^\nu C_{\alpha\beta\mu\nu}, \qquad B^{\{n\}}_{\alpha\mu} = n^\beta n^\nu C^*_{\alpha\beta\mu\nu}, \tag{5.1}$$

where $C^*_{\alpha\beta\mu\nu} = \frac{1}{2}C_{\alpha\beta\lambda\sigma}\epsilon^{\lambda\sigma}{}_{\mu\nu}$ is the dual of the Weyl tensor and $\epsilon_{\alpha\beta\mu\nu}$ is the Levi-Civita completely antisymmetric tensor Eq. (2.12). See Section 2.5.1 for an in-depth description of their properties where their magnitudes are taken as $E^{\{n\}2} = E^{\{n\}\alpha\beta}E^{\{n\}}_{\alpha\beta}$ and $B^{\{n\}2} = B^{\{n\}\alpha\beta}B^{\{n\}}_{\alpha\beta}$.

The outputs of this code are the 4-dimensional Ricci scalar R (also written as ${}^{(4)}R$), and the magnitudes of the electric and magnetic parts of the Weyl tensor $E^{\{n\}2}$, and $B^{\{n\}2}$; these are used in the examples in Section 5.3.

5.1.2 Slicing code: `EBWeyl`

We now consider the method applied in our second code: this consists of calculating $E^{\{n\}}_{\alpha\beta}$ and $B^{\{n\}}_{\alpha\beta}$ by using the 3+1 formalism, see Chapter 3 and more in particular Section 3.5 (Wald, 1984; Gunnarsen, Hisa-Aki, and Kei-Ichi, 1995; Alcubierre, 2008; Arnowitt, Deser, and Misner, 2008; Choquet-Bruhat, 2015; Shibata, 2015) that explains how the 4-dimensional Riemann and 4-dimensional Ricci tensors are substituted out of Eq. (5.1) to provide the following expressions Eq. (3.52) and Eq. (3.53)

$$\begin{aligned} E^{\{n\}}_{ij} &= {}^{(3)}R_{\langle ij\rangle} + K_{\langle ij\rangle}K - K^k{}_{\langle i}K_{j\rangle k} - \frac{\kappa}{2}S^{\{n\}}_{\langle ij\rangle} \\ B^{\{n\}}_{ij} &= \epsilon^{\{n\}kl}{}_j\left(D^{\{n\}}_k K_{li} + \frac{1}{2}\gamma_{ik}\left(D^{\{n\}}_l K - D^{\{n\}}_m K^m{}_l\right)\right), \end{aligned} \tag{5.2}$$

where $\langle..\rangle$ is a spatial traceless operator, Eq. (2.26).

As we use the 3+1 decomposition, $E^{\{n\}}_{ij}$ and $B^{\{n\}}_{ij}$ are only projected orthogonally to the normal to the slicing, whereas it is when they are projected orthogonally to the fluid flow that they take specific physical meaning for cosmologists. While one can use a slicing such that $n^\mu = u^\mu$, in general the two do not coincide, as the slicing/gauge is chosen in order to optimise numerical computations, or one wishes to consider a fluid with vorticity. For these reasons, we are now going to construct $E^{\{u\}2}$ and $B^{\{u\}2}$ by projecting along the fluid flow u^μ, c.f. (King and Ellis, 1973; Bruni, Dunsby, and Ellis, 1992; Bini, Carini, and Jantzen, 1995). Changing the projection vector in the geometrical method is straightforward but the slicing method is built on n^μ and the resulting 3-metric and extrinsic curvature. Hence we need to construct the Weyl tensor from $E^{\{n\}}_{\alpha\beta}$ and $B^{\{n\}}_{\alpha\beta}$. Assuming that these have been computed from Eq. (5.2), we can construct $C_{\alpha\beta\mu\nu}$ using Eq. (2.72) then it is projected along the fluid flow in the same method as the geometrical code to get $E^{\{u\}}_{\alpha\mu}$ and $B^{\{u\}}_{\alpha\mu}$ following Eq. (2.73).

This is implemented in `EBWeyl` (Munoz, 2022), where the metric $g_{\alpha\beta}$ provides the 3+1 variables needed to compute ${}^{(3)}R_{ij}$ and the spatial covariant derivative $D^{\{n\}}$. Then with $K_{\alpha\beta}$ and $T_{\alpha\beta}$, $E^{\{n\}}_{\alpha\beta}$ and $B^{\{n\}}_{\alpha\beta}$ are computed with Eq. (5.2)). No time derivatives are needed and the spatial derivatives are obtained with the same scheme used in the geometrical code.

This is implemented in `EBWeyl` (Munoz, 2022) which is essentially a post-processing Python module with functions and classes providing FD tools and computations of tensorial expressions. In the `github` repository there is an example Jupyter Notebook demonstrating how to use it for the Bianchi IV vacuum plane wave spacetime in Section 5.2.5. The user first needs to provide the data box grid spacing, the number of data points per direction, the boundary conditions and the FD order to a `FiniteDifference` class. This class provides FD tools to apply backward, centered, and forward FD schemes of 4^{th} and 6^{th} order using either periodic boundary conditions (as it is relevant for cosmological simulations) or a combination of the three different types of schemes as an alternative to boundary conditions, as explained above in Section 5.1.1.

Next, the user needs to provide the defined `FiniteDifference` class along with $g_{\alpha\beta}$, and K_{ij} as numerical `numpy` arrays to the class called `Weyl`, this will automatically define the terms $g^{\alpha\beta}$, γ_{ij}, γ^{ij}, β_i, β^i, α, n_α, and n^α, then the class's functions can be used to compute the 3-dimensional Christoffel symbols ${}^{(3)}\Gamma^i{}_{jk}$ and the 3-dimensional Ricci tensor ${}^{(3)}R_{ij}$ and scalar ${}^{(3)}R$. The spatial derivatives of the spatial metric and the 3-dimensional Christoffel symbols are computed numerically using the `FiniteDifference` class. Further functions are then available to compute $E^{\{n\}}_{ij}$ and $B^{\{n\}}_{ij}$ according to Eq. (5.2), note that for $B^{\{n\}}_{ij}$ the covariant derivative is computed by again using `FiniteDifference`, and that for $E^{\{n\}}_{ij}$ the energy-momentum tensor $T_{\alpha\beta}$ needs to be provided[1]. Another function is then available to compute $E^{\{n\}2}$ and $B^{\{n\}2}$. These two terms along with ${}^{(3)}R$ are those whose numerical error is considered in Section 5.3.2.

Furthermore, the equations described in Section 2.5.3 are also provided by `EBWeyl`, as demonstrated in the Jupyter Notebook (Munoz, 2022). With $E^{\{n\}}_{ij}$ and $B^{\{n\}}_{ij}$ there is a function available to compute $C_{\alpha\beta\mu\nu}$ following Eq. (2.72), then another function to project it along any chosen timelike unit vector, say u^α to have $E^{\{u\}}_{ij}$ and $B^{\{u\}}_{ij}$ with Eq. (2.73). Additionally, using $C_{\alpha\beta\mu\nu}$ there is a function available to compute the Weyl scalars, the Ψs, for an arbitrary null tetrad starting from a user-provided timelike unit vector according to Eq. (2.76, 2.77, 2.78, 2.80) where the Gram-Schmidt process has been implemented in order to ensure that the $\mathbf{e}_{(\alpha)}$ tetrad is orthonormal (-1 for timelike leg) no matter the numerical metric. These scalars can then be passed to another function that provides all the invariants needed for the Petrov classification of spacetime I, J, K, L and N according to Eq. (2.92, 2.96). An application of their usefulness is given in Section 5.3.1 and 6.3.6.

Finally, we emphasise that although the examples of this chapter are all cosmological and we always use the synchronous gauge, `EBWeyl` is general enough to be applied to any spacetime in any gauge.

5.2 Test-bed spacetimes

In this section, we summarise the spacetimes that we use to test our two codes. These are all exact solutions of GR, except for the test metric of Section 5.2.2. Since our codes are motivated by cosmological applications, most of the solutions are homogeneous but we also consider one inhomogeneous solution, a Λ-Szekeres spacetime in Section 5.2.1; and because it has no magnetic part of the Weyl tensor, we have created a test metric that presents an inhomogeneous spacetime with an electric and magnetic part of the Weyl tensor. These metrics were chosen for their potential challenge to the codes, indeed by order of presentation, two of these spacetimes have a sinusoidal dependence on the space coordinates, the next is polynomial, and the last two are exponential. They are all provided to the two codes which then compute ${}^{(3)}R$ or ${}^{(4)}R$, E^2, and B^2 that we compare to the analytical solutions to establish code performance, see Section 5.3.2. Then for the Λ-Szekeres spacetime, in particular, we show what those variables and the scalar invariants look like, and we verify the resulting Petrov classification Section 5.3.1.

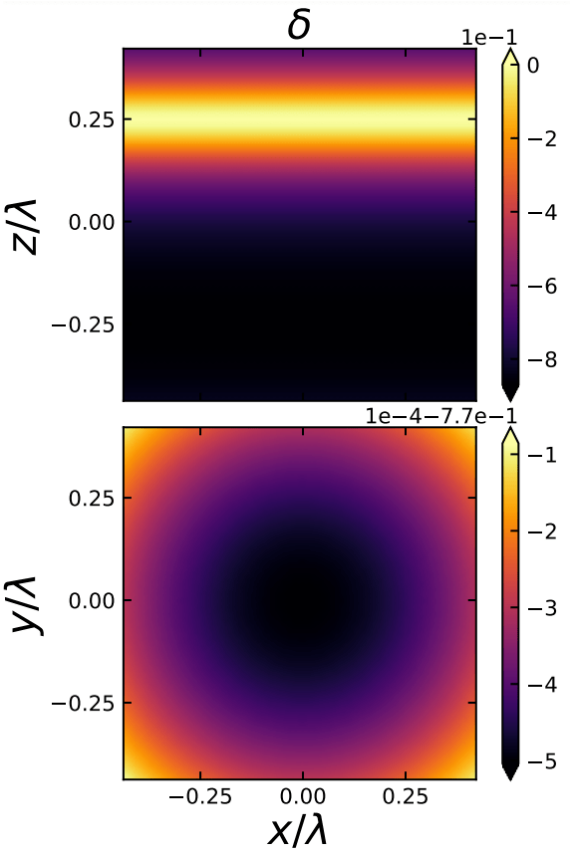

Figure 5.1: Space distribution of the density contrast δ in Eq. (5.4) indicated by colour coding (the top plot ranges from -0.8 to 0 and the bottom plot ranges from -0.7705 to -0.7701) for the Λ-Szekeres spacetime on the z-x and y-x planes (with $y/\lambda = 0$ and $z/\lambda = 0$ respectively) of a data box of size $\lambda = 20$Mpc with 64^3 grid points, at redshift 230.

5.2.1 The Λ-Szekeres models of Barrow and Stein-Schabes

The first spacetime we consider is a cosmological solution generalising the FLRW metric to include a nonlinear inhomogeneity, it is the Λ-Szekeres (Szekeres, 1975; Goode and Wainwright, 1982) model with dust and cosmological constant Λ first considered by Barrow and Stein-Schabes (1984). Following the representation of Szekeres models introduced in Goode and Wainwright (1982), this model can be presented as a nonlinear exact perturbation of a flat (zero curvature) ΛCDM background (Meures and Bruni, 2011, 2012) where the dust fluid represents CDM. In Cartesian-like coordinates the line element is:

$$ds^2 = -d\tau^2 + a^2(\tau)(dx^2 + dy^2 + Z^2(t, x, y, z)dz^2). \tag{5.3}$$

This model is well known to be Petrov type D and has no magnetic part of the Weyl tensor. It is a well-understood exact inhomogeneous cosmological solution, making it an interesting example for code testing, cf. (Grasso and Villa, 2021).

It turns out (Goode and Wainwright, 1982; Meures and Bruni, 2011, 2012) that the scale factor $a(\tau)$ in Eq. (5.3) satisfies the Friedmann equations for the flat ΛCDM model, see Section 4.1.4.5, so $a(\tau)$ is provided by Eq. (4.29), with background matter density $\bar{\rho}(\tau)$ from Eq. (4.19).

[1] For example, in vacuum, as in Section 5.2.5, this simply means that $T_{\alpha\beta}$ should be provided as an array of zeros.

The inhomogeneous matter density is $\rho^{\{u\}} = \bar{\rho}(1+\delta)$, where the density contrast δ can be written as:

$$\delta(\tau, x, y, z) = -F(\tau, z)/Z(\tau, x, y, z). \tag{5.4}$$

The function $Z(\tau, x, y, z)$ represents inhomogeneity in the metric Eq. (5.3) and can be written as:

$$Z(\tau, x, y, z) = 1 + F(\tau, z) + \beta_+(z)(x^2 + y^2)\frac{3}{4}H_0^2\Omega_{\Lambda 0}^{1/3}\Omega_{m0}^{2/3}. \tag{5.5}$$

Remarkably, as far as its time-dependence is concerned, the nonlinear perturbation $F(\tau, z)$ satisfies exactly the same linear second order differential equation satisfied by δ in linear perturbation theory Eq. (4.56) (Goode and Wainwright, 1982; Meures and Bruni, 2011, 2012), cf. (Bruni, Hidalgo, Meures, et al., 2014). Because of this, F is in general composed of a growing and decaying mode. The latter is usually neglected in cosmological structure formation theory, while the former is sourced by the curvature perturbations related to ${}^{(3)}R$ (Bruni, Hidalgo, Meures, et al., 2014), cf. also (Bruni, Hidalgo, and Wands, 2014) for a different approximation leading to the same equations. Therefore for our test, we only consider the growing mode:

$$F(t, z) = \beta_+(z)\frac{3}{5}\cosh(t)\sinh(t)^{2/3}{}_2F_1\left(\frac{5}{6}, \frac{3}{2}; \frac{11}{6}; -\sinh(t)^2\right), \tag{5.6}$$

where $t = \tau\sqrt{\frac{3\Lambda}{4}}$, and ${}_2F_1$ is a hypergeometric function, see Appendix B.1. Then we chose the spatial perturbation to be $\beta_+(z) = 10^3(1 - \sin(2\pi z/\lambda))$, λ being the data box size. Given these choices, the density contrast δ in Eq. (5.4) is negative and it is illustrated in Fig. (5.1), where we can see the influence of the sinusoidal distribution on the $x - z$ plane, and the paraboloid structure on the $x - y$ plane. This spacetime's invariants and its Petrov type will be discussed in Section 5.3.1.

5.2.2 A non-diagonal inhomogeneous test metric

In order to have an inhomogeneous example with a non-vanishing magnetic part of the Weyl tensor, we introduce a spacetime with the following line element:

$$ds^2 = -d\tau^2 + \tau A(z)\delta_{ij}dx^i dx^j + 2dx(dy + dz), \tag{5.7}$$

where $A(z)$ is an arbitrary function, that for practical purposes we assume to be positive. This can be found as a solution to Einstein's equations by the method of reverse engineering the metric, where one starts with the metric, and then finds the corresponding energy-momentum tensor with Einstein's field equations. In the analytical computations of this spacetime, we find it to be of Petrov type I, see Appendix B.2.

However, since the determinant of this metric is $g = A(z)\tau[2 - A(z)^2\tau^2]$, one can see that this spacetime is only valid for a certain domain in time, when $g < 0$, also depending on $A(z)$. Additionally, the resulting energy-momentum tensor doesn't have any particular physical meaning, so we are not referring to this spacetime as a GR solution. All we need to test our code is a specific form of the metric. In this light, although $A(z)$ is an arbitrary function, we define it for the purpose of the test as $A(z) = 2.3 + 0.2\sin(2\pi z/\lambda)$ so we can use periodic boundary conditions, with λ the box size. Then, in the frame associated with n^μ, we obtain the (rather fictitious) non-perfect fluid energy-momentum tensor $T_{\alpha\beta}$ from Einstein's equations, see Appendix B.2.

5.2.3 Bianchi II Collins-Stewart

The Collins and Stewart Bianchi II $\tilde{\gamma}$-law perfect fluid homogeneous solution (Collins and Stewart, 1971; Wainwright and Ellis, 1997) has the spatial metric

$$\gamma_{ij} = \begin{pmatrix} \tau^{(2-\tilde{\gamma})/\tilde{\gamma}} & \tau^{(2-\tilde{\gamma})/\tilde{\gamma}}(sz/2\tilde{\gamma}) & 0 \\ \tau^{(2-\tilde{\gamma})/\tilde{\gamma}}(sz/2\tilde{\gamma}) & \tau^{(2+\tilde{\gamma})/2\tilde{\gamma}} + \tau^{(2-\tilde{\gamma})/\tilde{\gamma}}\left(sz/2\tilde{\gamma}\right)^2 & 0 \\ 0 & 0 & \tau^{(2+\tilde{\gamma})/2\tilde{\gamma}} \end{pmatrix}, \tag{5.8}$$

with the constant $s^2 = (2-\tilde{\gamma})(3\tilde{\gamma}-2)$. This is with the synchronous comoving gauge and Cartesian-like coordinates. The perfect fluid has energy density $\rho^{\{u\}} = (6-\tilde{\gamma})/4\kappa\tau^2\tilde{\gamma}^2$, and pressure following the $\tilde{\gamma}$-law: $p^{\{u\}} = (\tilde{\gamma}-1)\rho^{\{u\}}$, so $\tilde{\gamma} = 1$ for dust and $\tilde{\gamma} = 4/3$ for radiation. In the latter case ${}^{(4)}R = 0$, in both cases this spacetime is of Petrov type D, see Appendix B.3. This is our sole example showing the spatial metric having a polynomial dependence on the space coordinates.

5.2.4 Bianchi VI tilted model

Assuming the synchronous gauge and Cartesian-like coordinates, the Rosquist and Jantzen Bianchi VI tilted $\tilde{\gamma}$-law perfect fluid homogeneous solution with vorticity (Rosquist and Jantzen, 1985; Stephani et al., 2003), has the spatial metric:

$$\gamma_{ij} = \begin{pmatrix} (1+m^2)(k\tau)^2 & mk\tau^{1+s-q}e^x & 0 \\ mk\tau^{1+s-q}e^x & \tau^{2(s-q)}e^{2x} & 0 \\ 0 & 0 & \tau^{2(s+q)}e^{-2x} \end{pmatrix}, \tag{5.9}$$

with the constants:

$$\begin{gathered} s = (2-\tilde{\gamma})/(2\tilde{\gamma}), \\ m^2 = -32q^2 s/(s-q-1)^2(3s+3q-1), \\ q = (6-5\tilde{\gamma})(2-\tilde{\gamma}+2\sqrt{(9\tilde{\gamma}-1)(\tilde{\gamma}-1)})/2\tilde{\gamma}(35\tilde{\gamma}-36), \\ k^2 = -(3s+3q-1)/(s+3q-1)(3s^2+(6q-1)s-q^2-q). \end{gathered} \tag{5.10}$$

With this definition of q, $\tilde{\gamma}$ is limited to the domain $6/5 < \tilde{\gamma} < 1.7169...$ (Stephani et al., 2003). For our test, we use $\tilde{\gamma} = 1.22$ and although this solution is described by a perfect fluid following the $\tilde{\gamma}$-law in a tilted frame, $T_{\alpha\beta}$ used in `EBWeyl` was computed from Einstein's equations in the n^α frame using Eq. (3.16). Another relevant note for the code testing, is that the space dependence of the metric is exponential. Using Maple (Maplesoft, 2019), we find that this spacetime is of Petrov type I, see Appendix B.4.

5.2.5 Bianchi IV vacuum plane wave

The final spacetime we consider is the Harvey and Tsoubelis Bianchi IV vacuum plane wave homogeneous solution (Harvey and Tsoubelis, 1977; Harvey, Tsoubelis, and Wilsker, 1979; Wainwright and Ellis, 1997) with spatial metric:

$$\gamma_{ij} = \begin{pmatrix} \tau^2 & 0 & 0 \\ 0 & \tau e^x & \tau e^x(x+\log(\tau)) \\ 0 & \tau e^x(x+\log(\tau)) & \tau e^x((x+\log(\tau))^2+1) \end{pmatrix}. \tag{5.11}$$

Again, this is for the synchronous comoving gauge and Cartesian-like coordinates. This is in vacuum so ${}^{(4)}R = 0$, and the plane wave represented by this model makes it a very interesting example: it is easy to check with Maple (Maplesoft, 2019), see Appendix B.5, that $E^{\{u\}2} = B^{2\{u\}} = 1/2\tau^4$ and that the Petrov type is N (Bonnor, 1995). This gives an additional point of comparison for $E^{\{u\}2}$ and $B^{\{u\}2}$.

5.3 Results

Here we present two forms of tests. Firstly, we demonstrate applications of these codes to the Λ-Szekeres spacetime in Section 5.2.1 (Szekeres, 1975; Barrow and Stein-Schabes, 1984; Meures and Bruni, 2011, 2012). We compute ${}^{(4)}R$ with the geometrical code and we compute ${}^{(3)}R$, B^2, E^2 and the invariants of Section 2.5.3 with `EBWeyl`. With the invariants, we then check that this spacetime is of Petrov type D. This process is then applicable to any numerical spacetime where the Petrov type is not known, see Section 6.3.6.

Secondly, we show the numerical error, and convergence, on computing ${}^{(4)}R$, ${}^{(3)}R$, E^2, and B^2 for each code on each example spacetime of Section 5.2. As we identify different types of numerical errors, each is addressed individually showing how reliable these codes are.

To do these tests using the metrics of Section 5.2 we generate 3-dimensional data boxes of N^3 points where the x, y, and z coordinates vary, such that each data point is associated with a numerical metric tensor computed from the analytical metric. We additionally associate a numerical extrinsic curvature and stress tensor with each of these points. The provided data has been generated exactly at a single arbitrary time for `EBWeyl`, and multiple times, with a small time step, for the geometrical code. These numerical arrays are provided to the two codes where the outputs can be plotted, as in Section 5.3.1, or compared to the expected solution as in Section 5.3.2. This comparison is done by computing the average relative difference between the code outputs, say v, and the analytical solution, v_{th}: $\mathbb{E}\left(|v/v_{th} - 1|\right)$. These solutions are derived analytically using Maple, see Appendix B, and provided as numerical arrays for comparison.

5.3.1 Invariants for the Λ-Szekeres spacetime

The 4-dimensional and 3-dimensional Ricci scalars and the invariants from Section 2.5.3 of the Λ-Szekeres spacetime have been computed and are presented in Fig. (5.2). This is organised in three main rows, with panels depicting the spatial distribution of the various quantities, with each main row divided into two sub-rows showing the distribution in the $x-z$ and $x-y$ planes. We present all quantities in homogeneous (first) powers of the Weyl tensor, e.g. $I^{1/2}$, and make them dimensionless by dividing by the Hubble scalar $H = \dot{a}/a$, cf. (Wainwright and Ellis, 1997), e.g. $I^{1/2}/H^2$. For complex scalars, only the real part is shown; for the imaginary part, which is zero analytically, we only get numerical noise. The geometrical code was used for ${}^{(4)}R$, and then `EBWeyl` otherwise.

In Fig. (5.2) the behaviour of the various quantities seem to differ according to two regions, where $\delta \to 0^-$ towards the $z/\lambda = 0.25$ plane and the rest where $\delta < 0$, see Fig. (5.1). These region-dependent properties are summarized in Table (5.1).

The Szekeres spacetime and the Barrow and Stein-Schabes model with Λ is well known to be of Petrov type D (Barnes and Rowlingson, 1989; Stephani et al., 2003; Meures and Bruni, 2011),

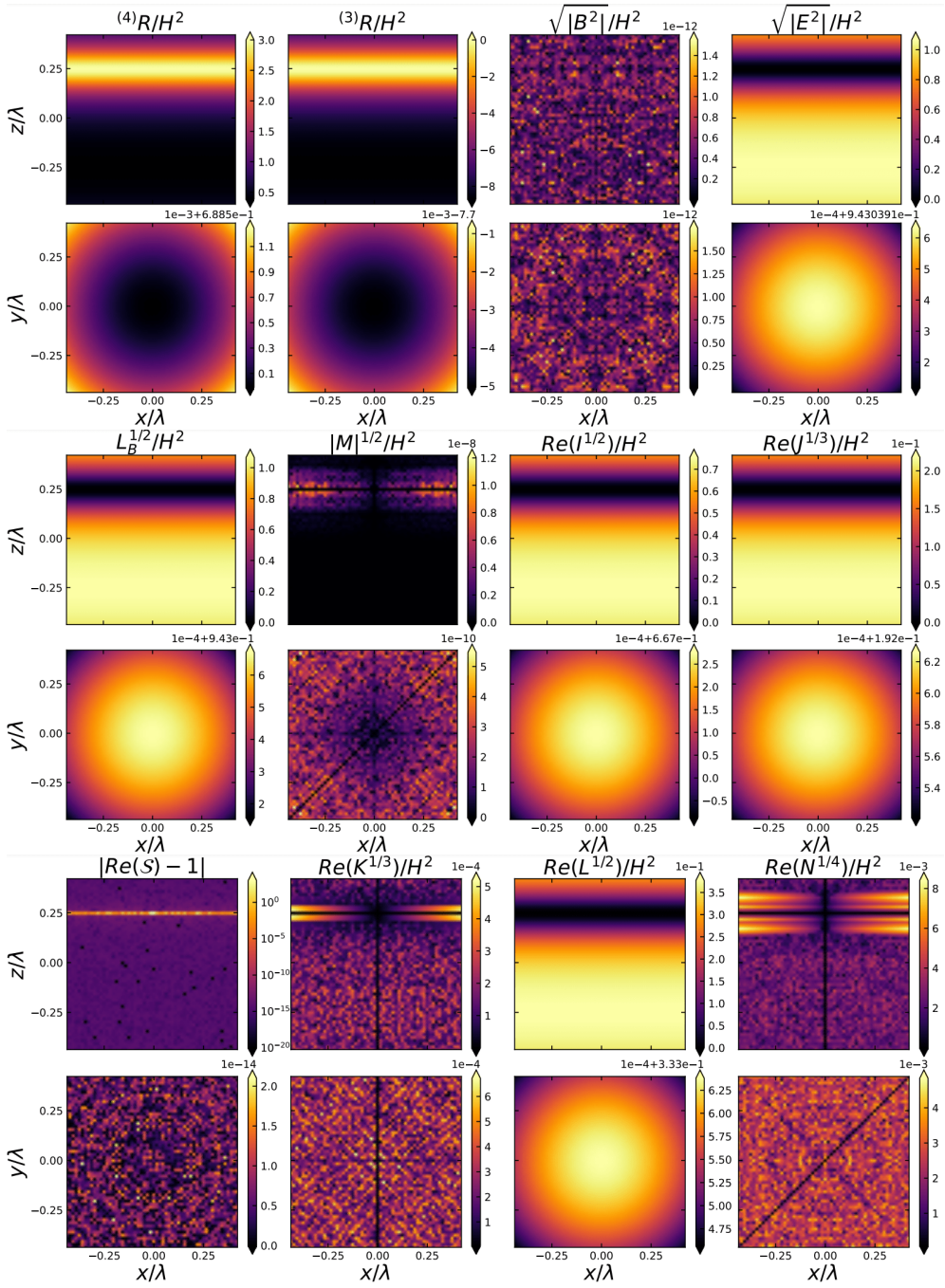

Figure 5.2: For the Λ-Szekeres spacetime we show the spatial distribution of the 4-dimensional and 3-dimensional Ricci scalar ${}^{(4)}R$ and ${}^{(3)}R$, the magnitude of the magnetic and electric parts of the Weyl tensor $\sqrt{|B^2|}$ and $\sqrt{|E^2|}$ and the invariant scalars along the z-x and y-x planes (with $y/\lambda = 0$ and $z/\lambda = 0$ respectively) of a data box with 64^3 grid points. These quantities are made dimensionless by dividing by the square of the Hubble scalar H. Only the real part of the complex invariants are shown, as the imaginary parts are zero, up to numerical noise.

	${}^{(4)}R$	${}^{(3)}R$	B^2	E^2
$\delta \to 0^-$	$\in \mathbb{R}^+$ larger	$\to 0^-$	$= 0$	$\to 0^+$
$\delta \in \mathbb{R}^-$	$\in \mathbb{R}^+$ smaller	$\in \mathbb{R}^-$	$= 0$	$\in \mathbb{R}^+$

	L_B	M	$Re(I^{1/2})$	$Re(J^{1/3})$
$\delta \to 0^-$	$\to 0^+$	$= 0$	$\to 0^+$	$\to 0^+$
$\delta \in \mathbb{R}^-$	$\in \mathbb{R}^+$	$= 0$	$\in \mathbb{R}^+$	$\in \mathbb{R}^+$

	$Re(\mathcal{S})$	$Re(K^{1/3})$	$Re(L^{1/2})$	$Re(N^{1/4})$
$\delta \to 0^-$	$+\infty$ at $z = 0.25\lambda$	$= 0$	$\to 0^+$	$= 0$
$\delta \in \mathbb{R}^-$	$= 1$	$= 0$	$\in \mathbb{R}^+$	$= 0$

Table 5.1: Summary of the quantities presented in Fig. (5.2) based on the spatial distribution of δ as presented in Fig. (5.1).

meaning that $I \neq 0$, $J \neq 0$, $\mathcal{S} = 1$, and $K = N = 0$ see Figure 9.1 of (Baker and Campanelli, 2000; Stephani et al., 2003) and Fig. (2.1). We can check this here, indeed in the second rows of each main row of Table (5.1) (for $\delta \in \mathbb{R}^-$) we can see that all of these properties are fulfilled such that we can identify this spacetime to be of type D. Additionally, we see that $B^2 = 0$, it just corresponds to numerical noise, meaning that for the invariants, based on equations Eq. (2.93, 2.94, 2.91): $M = 0$ (also numerical noise) and L_B, I, and J are all some type of combination of $E_{\alpha\beta}$, explaining the similarities in their spatial distributions in Fig. (5.2).

On the $z/\lambda = 0.25$ plane, corresponding to the $z/\lambda = 0.25$ horizontal line in the $z - x$ panels of Fig. (5.2), $\delta \to 0^-$ as it approaches this plane, and the Λ-Szekeres spacetime tends towards a flat FLRW spacetime which is of Petrov type O. This type of spacetime has the properties $B^2 = E^2 = L_B = M = I = J = K = L = N = 0$ as the Weyl tensor itself is zero, it is conformally flat, and we indeed observe this behaviour in the first rows of Table (5.1) (for $\delta \to 0^-$), and we also see that the spatial curvature ${}^{(3)}R$ also tends towards flatness as $z/\lambda = 0.25$ is approached. In particular, on this plane we do not have I exactly zero, but a small value, as there is always numerical noise. Consequently, on this plane $\mathcal{S} = 27J^2/I^3$ from Eq. (2.94) is numerically extremely large, see the yellow line in the first column and fifth row of Fig. (5.2). This is expected, since $\mathcal{S}$ is ill-defined for spacetimes other than I, II, and D.

We can then numerically confirm that this Λ-Szekeres metric is of Petrov type D, except on the $z/\lambda = 0.25$ plane where it is of Petrov type O. In summary, we have shown the potential of this code in deriving various invariants of an analytic spacetime. The same type of analysis can be done on any spacetime generated numerically as seen in Section 6.3.6. We next look into the accuracy of these measurements.

5.3.2 Code tests

To test our codes, we run them on all the example spacetimes listed in Section 5.2 and compare the results to the expected analytical expressions of Appendix B. Fig. (5.3) shows the resulting numerical error when computing ${}^{(3)}R$ or ${}^{(4)}R$, E^2, B^2, E^T and B^T (their trace, which should be zero). If the analytical solution is different from zero, the relative error is shown, otherwise, the value itself is

presented. The scalars that are absent from the plot, are omitted because the error is too small to fit in, and so is of lesser interest. All these plots display multiple types of numerical errors so we will address these individually. To complete this analysis, we show again in Fig. (5.4) the numerical error for the Bianchi VI and the plane wave cases, this time using the 6^{th} order FD and Riemann symmetry enforcement options. Additionally, the plane wave case has $E^2 = B^2$, so Fig. (5.5) shows how accurately each code can reproduce this.

5.3.2.1 Truncation error

The derivatives are computed with FD schemes, this introduces truncation errors that decrease as resolution increases. This follows the power law N^{-o}, with N^3 the number of grid points, and o the order of the FD scheme. In Figs. (5.3, 5.4, 5.5, A.1) this power law is shown with dashed green lines. The codes' capacity to numerically compute derivatives will be determined by the dependence of the metric on the time and space coordinates (time coordinate only for the geometrical method).

- The Bianchi II metric in Eq. (5.8) has a polynomial dependence on z and τ. The top plots of Fig. (5.3) show that the spatial dependence is not an issue as the slicing method is not limited by the truncation error, however, the additional FD for the time derivatives is the limiting factor in the geometrical method. Even the change in the temporal powers of Eq. (5.8) that results from changing the $\tilde{\gamma}$-law index from 1 to $4/3$ has changed the B^2 error to being truncation dominated.

- The test metric in Eq. (5.7) has a sinusoidal dependence on z and linear dependence on τ. The middle right plots in Fig. (5.3) shows that the truncation error is the limiting factor here, the error decreases following 4^{th} order convergence, as predicted by the FD order used in Fig. (5.3).

- The Λ-Szekeres metric in Eq. (5.3) is sinusoidal along z and paraboloidal in the orthogonal direction and its time dependence follows hyperbolic functions. The middle left plots in Fig. (5.3) show that the truncation error is a limiting factor, it indeed follows the expected power law, occasionally with an even steeper slope (showing better convergence). More on the middle left plots of Fig. (5.3) in the floating point error section.

- Both Bianchi VI and Bianchi IV plane wave metrics in Eq. (5.9) and Eq. (5.11) have an exponential spatial distribution. The bottom row plots of Fig. (5.3) are similar as they both decrease with 4^{th} order convergence. For these cases, a Christoffel component of interest, and its derivative, are also displayed to demonstrate the errors introduced by the FD scheme. Being inhomogeneous and zero in certain locations there are bumps in these curves. These Christoffel components are limited by the FD order, so they benefit from the 6^{th} order scheme as seen in the top row of Fig. (5.4). In this case, we can see that the error in the Christoffel components manages to reach lower values, therefore decreasing the errors in the other terms as they all have 6^{th} order convergence. This behaviour is also visible in Fig. (5.5). More on this in the cancellation error section.

Whether the spacetime is inhomogeneous (Λ-Szekeres and test metric) or homogeneous (other spacetimes) does not seem to make much of a difference on the truncation error, only extra bumps

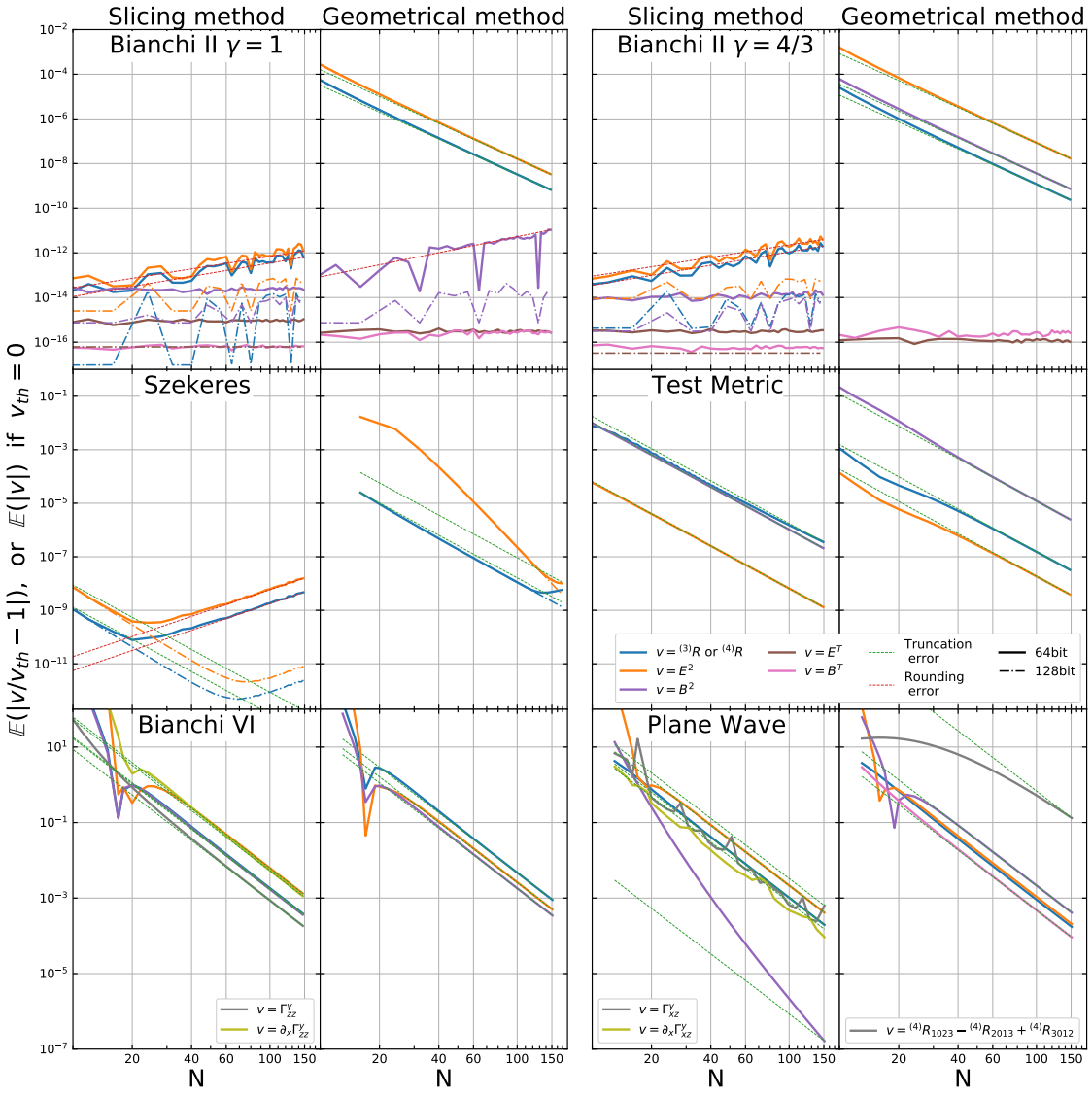

Figure 5.3: Six panels showing, respectively, the average relative error of the slicing method with `EBWeyl`, left side, and geometrical code, right side, of the Bianchi II (with $\gamma = 1$ and $\gamma = 4/3$), Λ-Szekeres, test metric, Bianchi VI, and Bianchi IV plane wave spacetimes, applied to data boxes of N^3 grid points, using a 4^{th} order FD scheme. Predicted numerical errors are plotted as dotted lines, green and decreasing corresponds to truncation error, red and increasing corresponds to rounding error (or floating point error). As truncation error is the dominating type of numerical error, the theoretical prediction often overlaps with the computational results. The Λ-Szekeres case with the slicing code (first panel in the middle row) in particular shows the results transition from truncation error dominated to rounding error dominated. This error is identified as a rounding error since the error is reduced by increasing the computational precision from 64bit to 128bit.

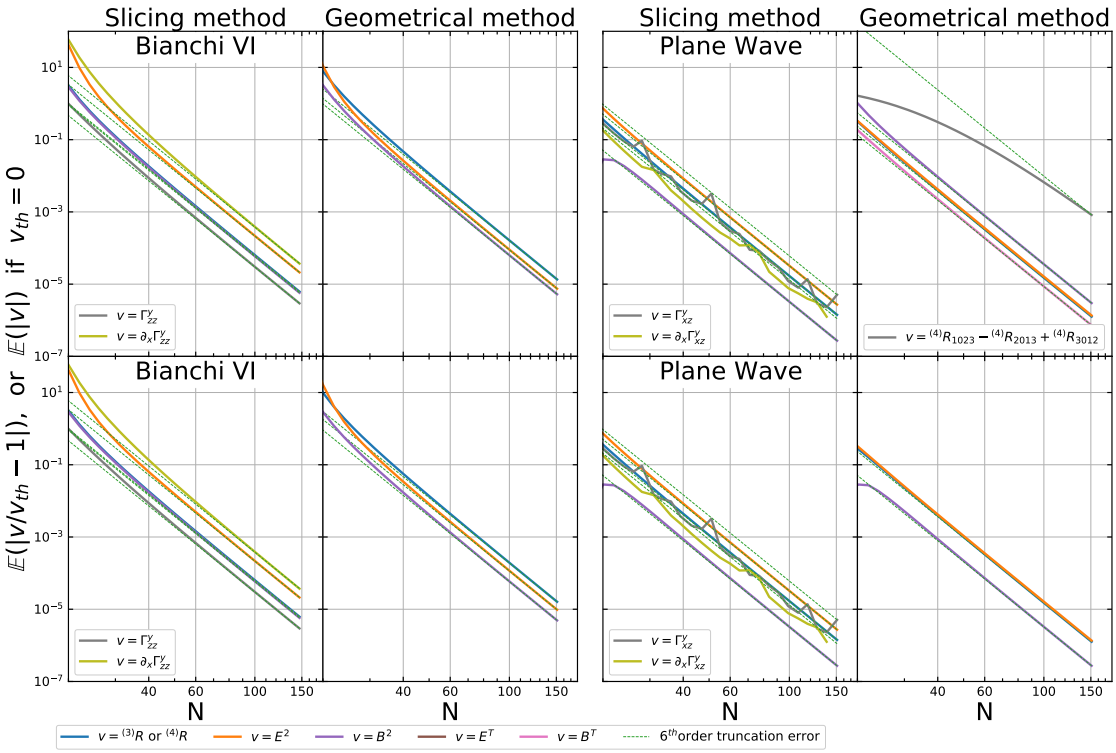

Figure 5.4: Top row: Two panels showing, respectively, the average relative error of the slicing, left side, and geometrical code, right side, of the Bianchi VI and Bianchi IV plane wave spacetimes with data boxes of N^3 grid points, using a 6^{th} order FD scheme. Bottom row: the same with Riemann symmetries enforced. For the plane wave geometrical case, B^T and the Bianchi identity vanish. Using a 6th order scheme has reduced numerical error with respect to Fig. (5.3), and enforcing Riemann symmetries has improved results for the Plane Wave Geometrical case, removing cancellation error.

along the curves. However, awareness of the metric spatial and temporal dependence is needed to understand the impact of the truncation error. If the space dependence is simple, as is the case of the Bianchi II metric, then the slicing method is preferred. Otherwise, if the space dependence is challenging, as is the case for the Bianchi VI and plane wave cases, the higher order FD method ought to be used for more accurate results, more on this in Appendix A.

5.3.2.2 Floating point error

Floating point error or round-off error comes from the limited number of digits stored in the computer memory. It accumulates as the amount of handled numbers and computational steps increases. Consequently, this type of error grows with the resolution, as it is visible in the top plots and middle left plot of Fig. (5.3), the increasing slopes follow power laws between N^0 and $N^{2.5}$. To ensure this is a floating point error and not a coding error we change the computational precision from 64bit continuous lines to 128bit (dash-dotted lines in Fig. (5.3)). In all cases the amplitude of these dash-dotted lines is smaller, confirming the origin of this error. `EBWeyl` applied to the Λ-Szekeres case, middle left-most plot of Fig. (5.3), is an interesting example where the transition from truncation error to floating point error is visible. The precision change decreases the amount of floating point error, therefore, pushing the error transition to happen at a higher resolution. This type of error displays computational limitations, however in all cases, it remains very small, so this does not pose much

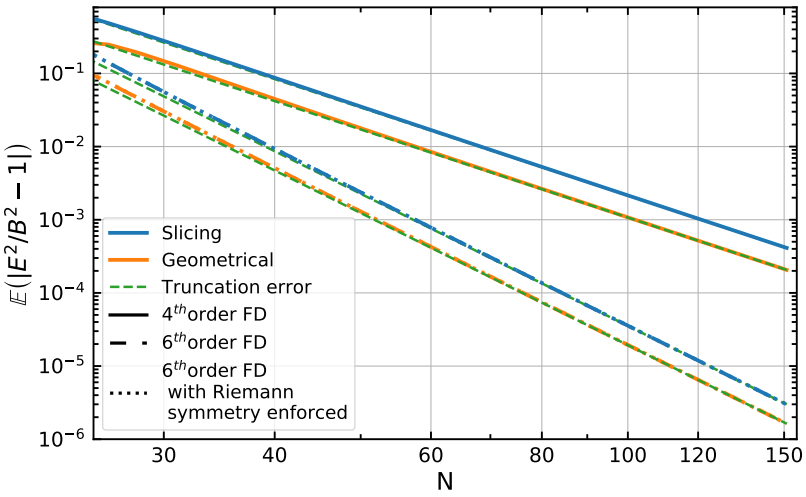

Figure 5.5: Average relative difference between B^2 and E^2 for both the slicing and geometrical codes applied to the Bianchi IV plane wave spacetime, where $B^2 = E^2$, with data boxes of N^3 grid points. Both 4^{th} and 6^{th} order FD schemes were used, and Riemann symmetries were enforced for the 6^{th} order scheme.

concern to results obtained with our codes.

5.3.2.3 Cancellation error

When comparing large numbers to small ones the relative error may mislead the result if the error on the large number is of the same order of magnitude as the small number. Large numbers cancelling each other out will then introduce significant errors in the rest of the computation. A good example of this type of error arises in the computation of the Bianchi identity Eq. (2.70). In the Bianchi IV plane wave case, see bottom right in Fig. (5.3) and right side of Fig. (5.4), each of the Riemann components in Eq. (2.70) are $\sim 10^3$, say the relative error is 10^{-3} from truncation error, then the introduced cancellation error is of $\sim 10^0$. It is then multiplied with smaller numbers and gives the error in the trace B^T (this should be zero and is indeed negligible in all other cases). This error can be related to the truncation error so the cancellation error here decreases as the former gets corrected. This can then be improved by increasing the FD order, as seen from 4^{th} order FD Fig. (5.3) to 6^{th} order Fig. (5.4) (top row) where the error in the Bianchi identity and other quantities in the plot significantly decrease. Additionally, this can also be improved by enforcing the symmetries of the Riemann tensor, see bottom row of Fig. (5.4), where the Bianchi identity is enforced and B^T vanishes and the B^2 error decreases. This additional step does not make a difference in the slicing method or the Bianchi VI case, i.e. symmetries of the Riemann or Ricci tensors are not limiting issues in `EBWeyl` or when the magnetic part is small with respect to the electric part.

5.3.2.4 Performance comparison

The results of the two methods are comparable in the test metric, Bianchi VI and Bianchi IV plane wave cases in Fig. (5.3, 5.4, 5.5). In some of the tests, as can be seen in the test metric case, middle right plots of Fig. (5.3), the geometric code computes ${}^{(4)}R$ more accurately than `EBWeyl` computes

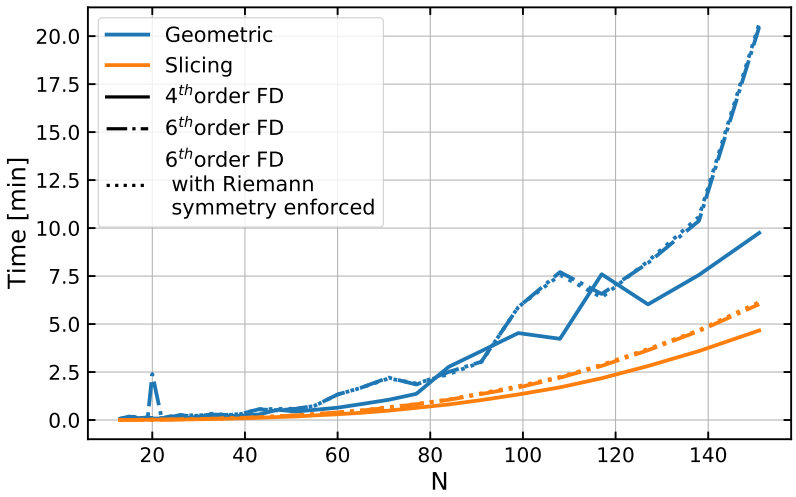

Figure 5.6: Computing time of both codes applied to data boxes of N^3 grid points at a given time, with both 4^{th} and 6^{th} order FD and Riemann symmetry enforcing.

${}^{(3)}R$. However, in other tests `EBWeyl` is more accurate, as can be seen in E^2 and B^2 of the same spacetime. Fig. (5.5), where B^2 and E^2 results are compared, as they should be equal for the plane wave case, shows that the geometrical code is more accurate. To understand this, see bottom right plots of Fig. (5.3) where the slicing error in E^2 is larger than the geometrical errors in E^2 and B^2, making the geometrical code more accurate with the E^2 and B^2 comparison in Fig. (5.5). While the geometrical code may occasionally be more accurate than `EBWeyl`, the latter is never an order of magnitude worse than the geometrical one. A clear preference can not be established by just using these more complicated scenarios.

The Bianchi II and Λ-Szekeres cases in Fig. (5.3) clearly show that the slicing method is more accurate than the geometrical one. The geometrical code can be found to be more than one order of magnitude worse than the slicing one on a number of occasions. This is because the latter requires temporal FD which introduces more truncation errors. Those additional computational steps also significantly increase the computing time of the geometrical method as seen in Fig. (5.6). To manage time derivatives over the entire data box, data files are appropriately written and read making the computing time curve bumpy. Additionally, the higher order FD needs more time steps, this then significantly increases computing time for the geometrical code, but not for `EBWeyl`. For consistent accuracy, computational cost and ease of independently treating simulation time steps, the slicing method is therefore preferred here (Munoz, 2022).

5.4 Summary

Motivated by the need to characterise NR results of cosmological simulations in a gauge-invariant fashion, here we have presented two codes to compute $E_{\alpha\beta}$ and $B_{\alpha\beta}$ and the Ricci scalars ${}^{(4)}R$ and ${}^{(3)}R$, along with further scalar invariants that can be used to invariantly characterise any spacetime and to classify it according to the Petrov type, see Section 2.5.3. The first method is geometrical as it computes these quantities in full from the metric, and the second, which we dub slicing, uses

the 3+1 decomposition of the metric. Special care has been taken to not introduce the constraint equations into the expressions in the slicing method, see Section 3.5. However, for the electric part of the Weyl tensor, Einstein's equations were necessary, therefore, this could potentially be a caveat when applying this method to simulation results, possibly introducing extra numerical error.

A post-processing Python code has been developed for each method, they have been applied to the Λ-Szekeres spacetime in Section 5.3.1. We have shown that where β_+ is strongest we find negative curvature and a strong electric part, then when it is small the curvature tends to flatness and $E_{\alpha\beta}$ is weak. As is well known, the magnetic part vanishes and the spacetime is of Petrov type D, everywhere but when $\beta_+ = 0$ where it is of Petrov type O (Meures and Bruni, 2011). We have verified this with our codes to demonstrate their applicability.

We have tested our two codes on the five different spacetimes introduced in Section 5.2. The results, in Section 5.3.2, show the presence of truncation, floating point and cancellation error depending on the spatial and temporal distribution of the metric. In the most challenging cases, we make higher-order FD schemes and Riemann symmetry enforcing available. With all best efforts introduced, in the most difficult case, we can report a relative error of 10^{-4} for a box with 100^3 points, and the relative error continues to decrease for higher resolution. But one should keep in mind that the numerical error we find depends on the considered case, in less challenging scenarios we find smaller errors. Then, when applying these codes to simulation results, one would also need to consider the accuracy of the simulation results. Should a 4^{th} order Runge Kutta scheme be used to evolve a simulation, then one could not expect better than 4^{th} order convergence on variables computed with these post-processing codes (even if the 6^{th} order FD scheme is used).

For three of the spacetimes we considered, our tests show that both methods have comparable performance, however in the two other ones, the slicing method outperforms the geometrical one. Then when considering the computing time, the slicing method drastically outperforms the geometrical one. This is because of the additional FD scheme required by the geometrical method. On the basis of its capacities demonstrated here, we have made the slicing post-processing code `EBWeyl` available in `github` (Munoz, 2022); it can be used on any spacetime in any gauge.

While these methods and codes were developed for post-processing NR simulations, in this chapter they were solely tested on exact solutions. The applicability and usefulness of our `EBWeyl` code (Munoz, 2022) in the context of cosmological simulations is shown in detail in Munoz and Bruni (2023b), see Section 6.3.5 and Section 6.3.6, where we have used it to characterise the evolution of cosmic structures and a quasi-spherical collapse, also introducing a novel effective Petrov classification of different regions at different times. Finally, we remark that the use of `EBWeyl` is not limited to NR simulations, as it can be applied to any spacetime obtained numerically where the spacetime metric and extrinsic curvature are available.

6 - Quasi-spherical collapse

The goal of this chapter is to study the nonlinear evolution of the basic elements of the cosmic web, namely over-densities, filaments and voids, extending the analysis in Bentivegna and Bruni (2016), where a 3-dimensional sinusoidal inhomogeneity in the matter density was evolved with varying amplitudes, and backreaction was found to be measurable, but extremely small. This 3-dimensional structure effectively represents a basic cosmic web, a lattice of over-densities (OD) periodically connected through the boundary conditions by filaments and separated by under-dense (UD) voids; also used in Bentivegna and Bruni (2016), Macpherson, Lasky, and Price (2017), East, Wojtak, and Abel (2018), Aurrekoetxea, Clough, Flauger, et al. (2020), Saga, Taruya, and Colombi (2022), and Magnall et al. (2023) This is referred to as quasi-spherical since it approximates spherical symmetry close to the peak of the OD; meaning its evolution can reliably be compared to the Top-Hat model (Gunn and Gott, 1972; Sahni and Coles, 1995; Monaco, 1997; Peacock, 1999; Mo, Bosch, and White, 2010; Vittorio, 2018).

Here we evolve this 3-dimensional structure in full GR, describing CDM as a pressureless fluid with the same evolution codes in Einstein Toolkit (Löffler et al., 2012; Bentivegna, 2017; Brandt et al., 2020) as Bentivegna and Bruni (2016). However, we take a different approach to set the initial conditions, implementing the 3-dimensional sinusoidal structure in the comoving curvature perturbation $\mathcal{R}_c$, originally introduced in Lyth (1985). This is convenient because $\mathcal{R}_c$ is gauge-invariant and time-independent at first order in perturbation theory and in the long wavelength approximation (Bruni, Hidalgo, and Wands, 2014), and it is commonly used to model inhomogeneities in the early universe, e.g. in inflationary models, see Malik and Wands (2009) and Refs. therein. Starting from the scalar potential $\mathcal{R}_c$, following the method described in Bruni, Hidalgo, Meures, et al. (2014) we the synchronous comoving gauge and set the initial spatial metric γ_{ij} and the extrinsic curvature K_{ij} as if these were only perturbed with first-order scalars, but then we treat them exactly, with no approximations, and use γ_{ij} to compute the 3-Ricci scalar ${}^{(3)}R$ in full nonlinearity, and this ${}^{(3)}R$ and K_{ij} are used in the Hamiltonian constraint to construct the matter density distribution $\rho^{\{u\}}$, so that the Hamiltonian constraint is automatically satisfied on the initial slice. By the same token, the momentum constraint is satisfied at first-perturbative order (Bruni, Hidalgo, Meures, et al., 2014).

This novel method to set up initial conditions for NR cosmological simulations has two advantages: *i)* it directly implements a purely growing mode, the only one that should exist in the matter-dominated era and *ii)* it can be used to directly implement initial curvature perturbations predicted by inflationary models (Malik and Wands, 2009; Bruni, Hidalgo, Meures, et al., 2014; Bruni, Hidalgo, and Wands, 2014). After summarising the necessary ΛCDM perturbations results (Bruni, Hidalgo, Meures, et al., 2014) in Section 6.1.2 our method of setting up nonlinear initial conditions and how they are implemented is described in Section 6.1.3. These depend on three parameters, namely

the amplitude, wavelength, and initial redshift, whose impact on the initial inhomogeneities is explored in Section 6.1.3.2. The Fortran thorn `ICPertFLRW` (Munoz, 2023a) adapted to the Cactus code (Goodale et al., 2003) was developed to implement these initial conditions in Einstein Toolkit (Brandt et al., 2020); it is described in Section 6.2.

We describe the evolution at the centre of the OD and UD in Section 6.3.1 and, to explain this evolution, we consider the contributions to the Raychaudhuri equation in Section 6.3.2. We also look at how the turn-around (TA) boundary evolves, describing the infalling domain, in Section 6.3.3, and we consider the evolution of a domain contained within a comoving sphere of various comoving radii in Section 6.3.4.

Furthermore, our simulations are in full GR, hence we also consider the gravitational description of our 3-dimensional structure using the Weyl tensor. The electric and magnetic parts of the Weyl tensor (Matte, 1953; Hawking, 1966; Maartens and Bassett, 1998; Ellis, 2009; Owen et al., 2011; Ellis, Maartens, and MacCallum, 2012; Bentivegna, Clifton, et al., 2018; Heinesen and Macpherson, 2022) are computed in post-processing with `EBWeyl`, the code presented in Chapter 5 (Munoz, 2022; Munoz and Bruni, 2023a), we then characterise the gravito-electromagnetic evolution of the 3-dimensional structure in Section 6.3.5. Additionally, the same code can be used to compute the invariants needed to classify the spacetime according to the Petrov types (Jordan et al., 1964; Stephani et al., 2003). The 3-dimensional structure in our fully nonlinear simulations is general enough to find in Section 6.3.6 that the spacetime is of Petrov type I, as expected. We then introduce a novel method for the dynamical Petrov classification of different regions in space by using thresholds: this enables us to define a leading-order Petrov type in each region and at different times. This invariant-based method contrasts the null vector approach (Owen, 2010), and has similarities with (Campanelli, Lousto, and Zlochower, 2009) that are both applied to spacetimes with black holes. In addition, we also show how this Petrov type depends on the shape of the inhomogeneity.

6.1 Initial conditions

We will be using NR for cosmological simulations of the evolution of inhomogeneities, where the matter consists of CDM represented as irrotational dust and is evolved in the matter-dominated era in the synchronous comoving gauge. With these choices, the lapse $\alpha = 1$, the shift $\beta^i = 0$, the fluid 4-velocity u^μ is the same as the normal to the hypersurface $u^\mu = n^\mu = \{1,\ 0,\ 0,\ 0\}$ and the expansion tensor Θ_{ij} is the same as the extrinsic curvature $\Theta_{ij} = -K_{ij} = \frac{1}{2}\dot{\gamma}_{ij}$ (with a sign change) and is purely spatial. The evolution equations of such a set-up are described in Section 2.4.4, in this section we describe their starting point.

To implement the initial conditions of these simulations we start with cosmological perturbation theory where the background is perturbed at first order with the comoving curvature perturbation $\mathcal{R}_c$ in Section 6.1.2. Background quantities[1] are indicated with an overhead bar and can either be based on the EdS model see Section 4.1.4.4 or the ΛCDM model see Section 4.1.4.5. First-order perturbations are indicated with a (1) superscript and during the matter-dominated era only scalar perturbations are relevant for structure formation, which are expressed in terms of $\mathcal{R}_c$ in Section 6.1.2.

[1]We emphasise that our simulations do not assume an overall ΛCDM or EdS expansion of the box domain, as in Newtonian N-body simulations, rather we use these models for the initial conditions' background and for comparison.

Introducing inhomogeneities with $\mathcal{R}_c$ comes from inflationary motivations that are described in Section 6.1.1.

With those initial conditions, Einstein's field equations are satisfied at first order but in Section 6.1.3 we shall satisfy them in full nonlinearity, defining $\mathcal{R}_c$ and discussing how the initial amplitude and redshift of the inhomogeneities, together with the ratio of their length-scale to that of the Hubble scale, determine the change from linearity to non-linearity of the initial conditions, and the long-wavelength regime dominated by the spatial curvature perturbations.

6.1.1 Motivations

In the standard scenario for the generation of structure formation in cosmology, the seeds are produced at large scales, inside the horizon during inflation, then exit; these scales then re-enter the horizon after the accelerated phase ceases and the seeds can grow. More precisely, inflation produces an almost scale-invariant spectrum of fluctuations. Starting from Bardeen, Steinhardt, and Turner (1983), it is then customary to introduce a variable that has the advantage of remaining constant while the perturbation scale is much larger than the Hubble scale, so that one can easily relate perturbations produced during inflation to when the same perturbations evolve in the radiation and matter eras, eventually re-entering the Hubble horizon. One such variable is the so-called curvature perturbation on uniform density hypersurfaces ζ (Malik and Wands, 2009). This is a metric variable, with the line element written as

$$ds^2 = -d\tau^2 + a^2(\tau)e^{2\zeta(\tau,\, x^i)}\widetilde{\gamma}_{ij}dx^i dx^j, \tag{6.1}$$

where $\det(\widetilde{\gamma}_{ij}) = 1$, see Malik and Wands (2009), Langlois and Vernizzi (2010), Bruni, Hidalgo, Meures, et al. (2014), and Bruni, Hidalgo, and Wands (2014) and Refs. therein. This nonlinear ζ is also used to model the birth of primordial black holes, see Shibata and Sasaki (1999) and Musco (2019) and Refs. therein, c.f. (Clough, Lim, et al., 2017; Aurrekoetxea, Clough, and Lim, 2022; Corman and East, 2022) for different approaches in NR. In single-field slow-roll inflation, the primordial ζ is an almost Gaussian random field (Acquaviva et al., 2003; Maldacena, 2003). In practice, therefore, non-Gaussianities are commonly modelled with an expansion of ζ in terms of its first perturbative order $\zeta^{(1)}$, parameterised by f_{NL} and higher order parameters, $\zeta = \zeta^{(1)} + f_{NL}\zeta^{(1)2} + \cdots$. For reviews see Malik and Wands (2009) and Langlois and Vernizzi (2010), where a fully nonlinear conserved quantity related to $\zeta^{(1)}$ and $\mathcal{R}_c$ is also introduced.

At large scales (in the long-wavelength approximation) and at leading order ζ is constant and $\widetilde{\gamma}_{kj} \simeq \delta_{kj}$, so that in this approximation the spatial metric in Eq. (6.1) is conformally flat, and the 3-Ricci scalar ${}^{(3)}R$ is then given by a beautifully simple expression in terms of ζ and its gradients (Bruni, Hidalgo, and Wands, 2014). We remark that ${}^{(3)}R$ vanishes in any flat FLRW background, therefore according to the Stewart-Walker lemma (Stewart and Walker, 1974) cf. (Ellis and Bruni, 1989; Bruni, Dunsby, and Ellis, 1992; Dunsby, Bruni, and Ellis, 1992), its first perturbative order ${}^{(3)}R^{(1)}$ as well as $\zeta^{(1)}$ are gauge-invariant, see Section 4.2.6.1 for a general discussion on invariant quantities in cosmology. It actually turns out (Bruni, Hidalgo, and Wands, 2014) that at leading order in this large-scales approximation, the equations for the inhomogeneities are formally exactly the same as those for first-order perturbations (Bruni, Hidalgo, Meures, et al., 2014). Relating this to comoving coordinates, at first perturbative order ${}^{(3)}R^{(1)}$ simplifies to Eq. (4.50) above, and $\zeta^{(1)} = \mathcal{R}_c$ at large

scales, where $\delta^{(1)}$ is suppressed, otherwise when $\delta^{(1)}$ is non-negligible

$$\zeta^{(1)} = \frac{1}{3}\delta^{(1)} - \mathcal{R}_c. \tag{6.2}$$

$\delta^{(1)}$ represents the gauge-invariant first-order density perturbation on comoving hypersurfaces, therefore automatically coinciding with the density contrast $\delta = \rho^{\{u\}}/\bar{\rho} - 1$ in the synchronous-comoving gauge we use here, and $\mathcal{R}_c$ known as the comoving curvature perturbation (Lyth, 1985) is the first-order gauge-invariant scalar perturbation potential for ${}^{(3)}R^{(1)}$, the first-order perturbation of the 3-Ricci scalar.

Motivated by this standard modelling of primordial inhomogeneities, we now set up fully nonlinear initial conditions using the scalar curvature variable $\mathcal{R}_c$. The advantage of using $\mathcal{R}_c$ as a starting point is twofold: *i)* it is directly related to $\zeta^{(1)}$ by Eq. (6.2), and it coincides with it at large scales, where $\delta^{(1)}$ is suppressed with respect to $\mathcal{R}_c$, see Eq. (6.4) below; hence our set up for initial condition can be used to directly implement perturbation predictions from inflationary models; *ii)* for dust, $\mathcal{R}_c$ is a conserved quantity at all times and for all scales, which can be used to implement all first-order scalar perturbations variables for the growing mode.

6.1.2 ΛCDM first-order perturbations

In the following, we shall summarise the approach to perturbations in the synchronous-comoving gauge used in Bruni, Hidalgo, Meures, et al. (2014), based on $\mathcal{R}_c$, to use this as a starting point for our nonlinear initial condition set-up. A parallel nonlinear long-wavelength approximation for inhomogeneities on large scales is used in Bruni, Hidalgo, and Wands (2014). With only scalar perturbations in the synchronous-comoving gauge, the corresponding spacetime, curvature, matter and evolution equations are presented in Section 4.2.4 with the specific evolution equations for $\delta^{(1)}$ discussed in Section 4.3.1. Here we shall express the first-order scalar perturbations $\delta^{(1)}$, $\psi^{(1)}$ and $\chi^{(1)}$ as a function of $\mathcal{R}_c$.

Then, the starting point (Bruni, Hidalgo, Meures, et al., 2014) is to consider the first order evolution equation of the density contrast Eq. (4.56) where the curvature term is provided by $\mathcal{R}_c$ Eq. (4.50)

$$4H\dot{\delta}^{(1)} + 6H^2\Omega_m\delta^{(1)} = 4\nabla^2\mathcal{R}_c. \tag{6.3}$$

Only considering the particular solution, the so-called growing mode sourced by the curvature, Eq. (6.3) can be rearranged by introducing the growth factor $f_1 = d\ln\delta/d\ln a \simeq \Omega_m^{6/11}$ (Peebles, 1980; Wang and Steinhardt, 1998), to express $\delta^{(1)}$ as a function of $\mathcal{R}_c$

$$\delta^{(1)} = \frac{\nabla^2\mathcal{R}_c}{FH^2}, \tag{6.4}$$

with $F = f_1 + \frac{3}{2}\Omega_m$; in the early-matter era, when the EdS model is a good approximation with $\Omega_m = 1$ and $f_1 = 1$ then $\delta^{(1)} \propto a$. With Eq. (6.4), $\psi^{(1)}$ and $\chi^{(1)}$ can be expressed by using the deformation $\vartheta^{(1)}$. In the synchronous comoving gauge $\vartheta^{(1)}$ is expressed with metric perturbations as $\vartheta^{(1)} = -3\dot{\psi}^{(1)}$ Eq. (4.39). Likewise, the first order continuity equation is $\dot{\delta}^{(1)} = -\vartheta^{(1)}$ Eq. (4.42). Then, putting these two expressions together $\dot{\delta}^{(1)} = 3\dot{\psi}^{(1)}$, and so $\psi^{(1)}$ can be expressed as a function of $\mathcal{R}_c$ using Eq. (6.4), where the integration constant is identified to be $\mathcal{R}_c$ from Eq. (4.50). Furthermore, $\psi^{(1)}$ can be introduced into Eq. (4.50) to provide $\chi^{(1)}$, such that

$$\psi^{(1)} = \frac{1}{3}\delta^{(1)} + \mathcal{R}_c, \qquad \text{and} \qquad \chi^{(1)} = -\frac{2\mathcal{R}_c}{a^2FH^2}. \tag{6.5}$$

Therefore, introducing these into Eq. (4.35), the spatial metric perturbed with a purely growing mode expressed up to first order as a function of $\mathcal{R}_c$ is

$$\gamma_{ij} = \bar{\gamma}_{ij} + \gamma^{(1)}_{ij} = a^2(1-2\mathcal{R}_c)\delta_{ij} - \frac{2}{FH^2}\partial_i\partial_j\mathcal{R}_c. \tag{6.6}$$

Introducing Eq. (6.4) into Eq. (6.3) shows that $\frac{d}{d\tau}(1/FH^2) = (2+f_1)/FH$ and $\mathcal{R}_c$ is constant in time (Bruni, Hidalgo, Meures, et al., 2014), so that ${}^{(3)}R^{(1)} \propto a^{-2}$, therefore the extrinsic curvature $K_{ij} = -\Theta_{ij} = -\frac{1}{2}\dot{\gamma}_{ij}$ is

$$K_{ij} = \bar{K}_{ij} + K^{(1)}_{ij} = -a^2H(1-2\mathcal{R}_c)\delta_{ij} + \frac{(2+f_1)}{FH}\partial_i\partial_j\mathcal{R}_c. \tag{6.7}$$

K_{ij} can be separated into its trace K and traceless A_{ij} part Eq. (3.14) such that in this gauge both are related to the fluid kinematical quantities. A_{ij} is associated with the shear tensor of the matter flow σ_{ij}, $A_{ij} = -\sigma_{ij}$, at first order

$$A^{(1)}_{ij} = -\sigma^{(1)}_{ij} = \frac{f_1}{FH}\left(\partial_i\partial_j - \frac{1}{3}\delta_{ij}\delta^{kl}\partial_k\partial_l\right)\mathcal{R}_c. \tag{6.8}$$

We remark that in the background $\bar{\sigma}_{ij} = 0$, hence the shear is a first-order gauge invariant quantity, following Section 4.2.6.2 (Hawking, 1966), however it is frame-dependent so this is specific to the fluid frame. Then, K is associated with the expansion scalar Θ:

$$K = -\Theta = \bar{K} - \vartheta, \qquad \text{with} \qquad \bar{K} = -3H, \qquad \text{and} \qquad K^{(1)} = -\vartheta^{(1)} = f_1 H\delta^{(1)}. \tag{6.9}$$

In this gauge the momentum density $q^{\{u\}i} = 0$, this means that the momentum constraint Eq. (3.30) takes the form $D^{\{u\}}_i(K^i_j) - D^{\{u\}}_j(K) = 0$. It was shown in Section 4.2.4 (Bruni, Hidalgo, Meures, et al., 2014) that at first order this expression reduces to $\partial_j(\dot{\mathcal{R}}_c) = 0$, and for dust $\dot{\mathcal{R}}_c = 0$ at all times at all scales at first order, then at this order the momentum constraint is automatically satisfied.

As $\delta \equiv \rho^{\{u\}}/\bar{\rho} - 1$ is the density contrast for the matter field, we can define similar quantities for the contrast of the volume element γ and expansion K:

$$\delta\gamma \equiv \gamma/\bar{\gamma} - 1, \qquad \text{and} \qquad \delta K \equiv K/\bar{K} - 1. \tag{6.10}$$

Given Eq. (4.36), Eq. (6.5), and Eq. (6.9) these can be expressed at first order as:

$$\delta\gamma^{(1)} = -6\left(\frac{1}{3}\delta^{(1)} + \mathcal{R}_c\right) \qquad \text{and} \qquad \delta K^{(1)} = -\frac{f_1\delta^{(1)}}{3}. \tag{6.11}$$

6.1.3 Fully nonlinear initial conditions

6.1.3.1 Ansatz & implementation

To set up initial conditions, we have developed a new thorn `ICPertFLRW` (Munoz, 2023a). The starting ansatz is that the metric and the extrinsic curvature are precisely given by their expressions Eq. (6.6) and Eq. (6.7), but should otherwise be thought of as quantities to be used in full non-linearity, generated by the scalar potential $\mathcal{R}_c$. From γ_{ij} and K_{ij}, we then compute the 3-Ricci scalar ${}^{(3)}R$, the trace K, and the magnitude $K^{ij}K_{ij}$. Given our ansatz, based on $\mathcal{R}_c$ and its derivatives, these quantities are computed analytically by `ICPertFLRW` (Munoz, 2023a). We can then use the Hamiltonian constraint to compute the initial matter density

$$\rho^{\{u\}} = \frac{1}{2\kappa}\left({}^{(3)}R + K^2 - K^{ij}K_{ji} - 2\Lambda\right) = \frac{1}{2\kappa}\left({}^{(3)}R + \frac{2}{3}K^2 - 2A^2 - 2\Lambda\right), \tag{6.12}$$

with $A^2 = A^{ij}A_{ji}/2$. We emphasise that in setting up initial conditions in full non-linearity, we introduce vector and tensor modes, in particular in the shear $\sigma_{ij} = -A_{ij}$ that sources the magnetic part of the Weyl tensor $B^{\{u\}}_{ij}$: this is non-zero, as it will be shown in Section 6.3.5, while at first order $B^{\{u\}(1)}_{ij} = 0$ (in all gauges) for the purely scalar perturbation of the previous section.

The main advantage of using the Hamiltonian constraint to set up the matter density $\rho^{\{u\}}$ initial distribution in Eq. (6.12) is twofold: *i)* its algebraic use makes the constraint automatically satisfied in the initial time step, *ii)* in order to set up the initial conditions we don't need to solve an elliptic equation, as is the case if the starting point is $\rho^{\{u\}}$, as in Bentivegna and Bruni (2016). The Hamiltonian constraint was also used to non-linearly provide $\rho^{\{u\}}$ in Giblin, Mertens, and Starkman (2016), although not using $\mathcal{R}_c$. Note that we could have set up initial conditions exclusively using first-order quantities: we emphasise the benefit of our fully nonlinear method in Appendix C, where we show that even starting from small initial perturbations nonlinear effects are important in GR.

All that remains is to define the comoving curvature perturbation $\mathcal{R}_c$. A fully realistic initial set-up should consist of generating a spatial realisation of $\mathcal{R}_c$ starting from a Gaussian (or quasi-Gaussian) scale-invariant spectrum, but this is beyond our current scope. Instead, we chose a single 3-dimensional sinusoidal mode:

$$\mathcal{R}_c = A_{pert}\Big(\sin\left(xk_{pert}\right) + \sin\left(yk_{pert}\right) + \sin\left(zk_{pert}\right) \Big), \tag{6.13}$$

with $k_{pert} = 2\pi/\lambda_{pert}$ and the simulation box spanning $x,\ y,\ z \in [-\lambda_{pert}/2,\ \lambda_{pert}/2]$. λ_{pert} is the comoving wavelength at the reference redshift $a(z_R) = 1$, such that the physical wavelength is retrieved as $\lambda_{phy} = a\lambda_{pert}$. We work with $a(z_R = 0) = 1$ so that the comoving wavelength corresponds to a physical wavelength today, as defined in a reference ΛCDM FLRW spacetime, which would be the background in a perturbative setting. The impact of λ_{pert} on the initial inhomogeneity is discussed in Section 6.1.3.2 and in the simulations of this chapter λ_{pert} is chosen such that the initial physical scale is super-horizon $\lambda_{phy,\,IN} = 4/H_{IN}$, as we are interested in large-scale relativistic effects and we would like to compare to the simulations of (Bentivegna and Bruni, 2016). Furthermore, if a spatial region of a given comoving scale contains an OD that grows non-linearly, then its physical size today[2] will eventually be much smaller than the corresponding FLRW physical scale.

We then have a simulation box containing a "compensated inhomogeneity", i.e. one as that in Eq. (6.13), such that its linear average vanishes, while its nonlinear average does not. Note that averages discussed here are proper domain averages obtained by integrating with the determinant of the spatial metric, see Appendix D. We emphasise that in general with our setup, averaged quantities do not exactly coincide with those of the FLRW model: even in the initial conditions, the non-linearity of GR implies that the nonlinear average of Eq. (6.13) is non-zero. This can be intuitively seen for the initial nonlinear density contrast in Fig. (6.2) where $\delta_{OD} \neq -\delta_{UD}$ and other quantities as seen in Fig. (6.5).

The spatial distribution Eq. (6.13) allows us to focus on some specific relativistic features that emerge clearly in this simple set-up, features that would probably be harder to characterise in a more realistic scenario. Specifically, it will enable us to study the growth of an OD whose centre is at $x = y = z = -\lambda_{pert}/4$ and an UD whose centre is at $x = y = z = \lambda_{pert}/4$. It produces the initial δ presented in Fig. (6.1, 6.2, 6.3). Fig. (6.1) shows the initial δ distribution in the simulation box with

[2]The size agreed by a network of comoving observers with synchronised clocks.

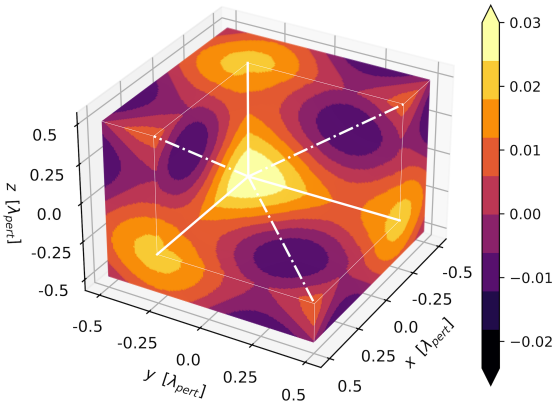

Figure 6.1: Initial distribution at $z_{IN} = 302.5$ of the density contrast δ in the simulation box, for a ΛCDM universe. The x, y, and $z > -0.25\lambda_{pert}$ region is removed exposing the centre of the over-density at $x = y = z = -0.25\lambda_{pert}$, where $\delta_{IN,\,OD} = 0.03$. The full lines go through the vertices and dash-dotted lines through the centre of the edges of an octahedron centred at the over-density.

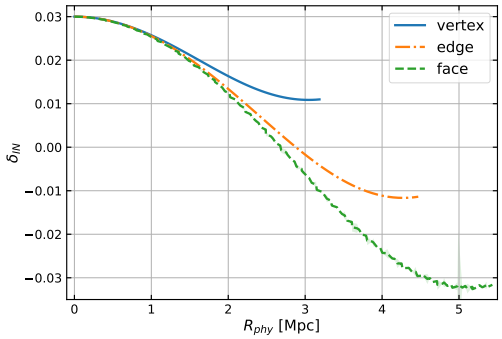

Figure 6.2: Initial radial profile at $z_{IN} = 302.5$ of the initial density contrast δ starting from the centre of the over-density to its minimum in three different directions, towards the vertices, edges, and faces of the octahedral distribution in Eq. (6.13) plotted against the proper radius from the over-dense peak. Error bars, when visible, are indicated as shaded regions.

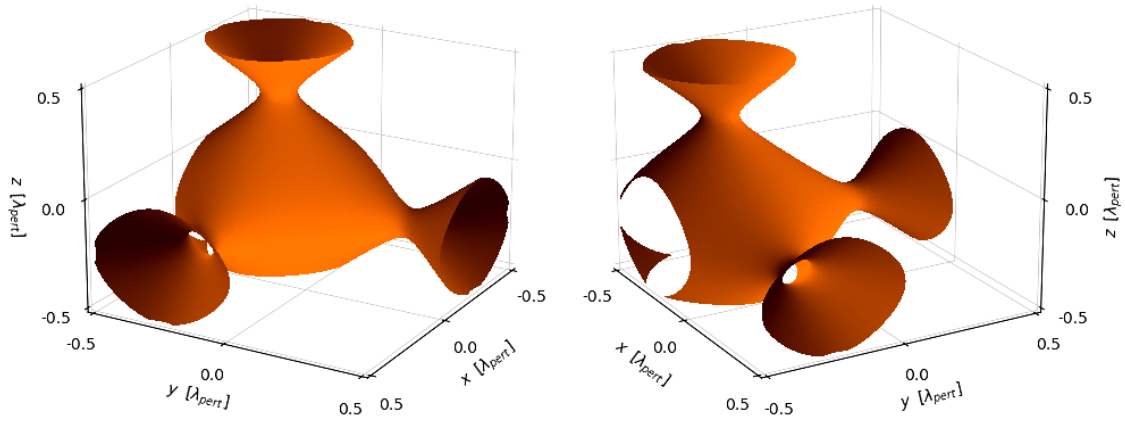

Figure 6.3: Isosurface for $\delta = 0.01$ in the initial distribution of the matter density contrast at $z_{IN} = 302.5$. The two different panels show different points of view. The periodic boundary conditions insure that this distribution is a lattice of over-densities connected by filaments and separated by voids.

the centre of the OD exposed, while Fig. (6.3) shows the isosurface where $\delta = 0.01$. These figures emphasise the non-spherical shape of this distribution. Indeed, the equation $\sum_{i=1}^{3} \sin(x^i k_{pert}) = 1$ parameterises an octahedron, so when close to the peak of the OD, spherical symmetry is approximated, further out an octahedron geometry creates filamentary-like structures periodically connecting each OD peak. We satisfy the boundary conditions by using periodic boundaries. However, we emphasise that the non-spherical nature of the distribution is not due to the boundary conditions in the simulation (Rácz, Szapudi, et al., 2021), but due to the choice of the initial distribution.

Centring an octahedron around the OD we identify three main directions of interest from the centre of the OD: along the vertices, the centre of the edges and the centre of the faces. A half period

of δ along each direction is presented in Fig. (6.2). Close to the peak of the OD, the three directions overlap, highlighting the proximity to spherical symmetry. Beyond that, we see the axis going through the vertices never goes through an UD region, since this direction goes through the filaments (full white lines in Fig. (6.1), and full blue lines in Fig. (6.2)), and the axis going through the centre of the faces goes through the centre of the UD (not in Fig. (6.1), and green dashed lines in Fig. (6.2)). Although the spatial distribution that we derive from Eq. (6.13) is unrealistic, it contains the three basic elements of the cosmic web, namely ODs, filaments, and voids and as such, can be viewed as a skeleton description of large-scale structures and it is more realistic than the spherical Top-Hat model.

6.1.3.2 Nonlinear & long-wavelength regimes

The above initial distribution lets us freely choose the amplitude and wavelength of the inhomogeneity, A_{pert} and λ_{pert}, as well as the initial redshift z_{IN}. The impact of these parameters on the initial amplitude of $\delta\gamma$, δK, δ and ${}^{(3)}R$ at the peak of the OD is presented in Fig. (6.4). The thin lines are the first-order quantities from Eq. (4.50, 6.4, 6.11) whereas the thick lines are the fully nonlinear quantities obtained from Eq. (6.6, 6.7, 6.10, 6.12). Each panel shows their dependencies on A_{pert}, z_{IN} and λ_{pert} while keeping the other two parameters constant (with their values listed in the box).

In the left panel, we consider inhomogeneities on a scale well inside the Hubble horizon at that time. This shows that the inhomogeneities are proportional to A_{pert} when it is small enough. However, when A_{pert} is large, there is a separation between the thick and thin lines: this identifies the emergence of the nonlinear regime. This is also visible in the other panels for low redshift and small scales, domains where local dynamics become dominant. Otherwise, inhomogeneities in the linear regime are given by the Laplacian of $\mathcal{R}_c$, Eq. (6.4), and as such, they are proportional to λ_{pert}^{-2} for the right panel and proportional to $a(\tau)$ in the middle panel, except ${}^{(3)}R \propto a^{-2}(\tau)$. In the middle panel, at low redshift, linear curves are no longer straight because in ΛCDM we depart from the δ-dominated era.

We emphasise that the inhomogeneity in the proper volume at the OD $\delta\gamma_{IN,\,OD}$ has a peculiar dependence on A_{pert}, z_{IN} and λ_{pert} even in the linear regime, as clearly visible in the middle and right panels in Fig. (6.4). To understand this, consider Eq. (6.11), which shows that $\delta\gamma^{(1)}$ is composed of two terms: $\mathcal{R}_c$ and $\delta^{(1)}$. Given the $\mathcal{R}_c$ sinusoidal distribution Eq. (6.13), the Laplacian in $\delta^{(1)}$, Eq. (6.4), creates a sign difference between these two terms. $\delta\gamma$ then has $\mathcal{R}_c$-dominated and δ-dominated regimes, and the transition is highlighted by a sign change (the downward spike in the log-plot Fig. (6.4)). $\mathcal{R}_c$ and $\delta^{(1)}$ are both proportional to A_{pert}, so that their relative weight in the left panel is constant; in practice, for the given z_{IN} and λ_{pert} in this panel (which is sub-horizon), $\delta\gamma_{IN,\,OD}$ is δ-dominated. Considering now the middle and right panel in Fig. (6.4), z_{IN} and λ_{pert} impact the amplitude of $\delta^{(1)}$, while A_{pert}, the amplitude of $\mathcal{R}_c$, is constant in these panels. Then, when $|\mathcal{R}_{c,\,OD}| > |\delta^{(1)}_{OD}|$, in the $\mathcal{R}_c$-dominated regime (at large z_{IN} and λ_{pert}) $\delta\gamma_{IN,\,OD}$ shows a plateau, while $\delta\gamma_{IN,\,OD} \propto a(\tau)\lambda_{pert}^{-2}$ in the δ-dominated regime, when $|\mathcal{R}_{c,\,OD}| < |\delta^{(1)}_{OD}|$.

Intuitively, in an OD region ($\delta > 0$ and $\mathcal{R}_c < 0$), you would expect the volume to be smaller than the background average, meaning that $\delta\gamma$ is negative, as that region of space is more compact. However, in the $\mathcal{R}_c$-dominated regime, $|\mathcal{R}_{c,\,OD}| > |\delta_{OD}|$, the volume element is larger than that of

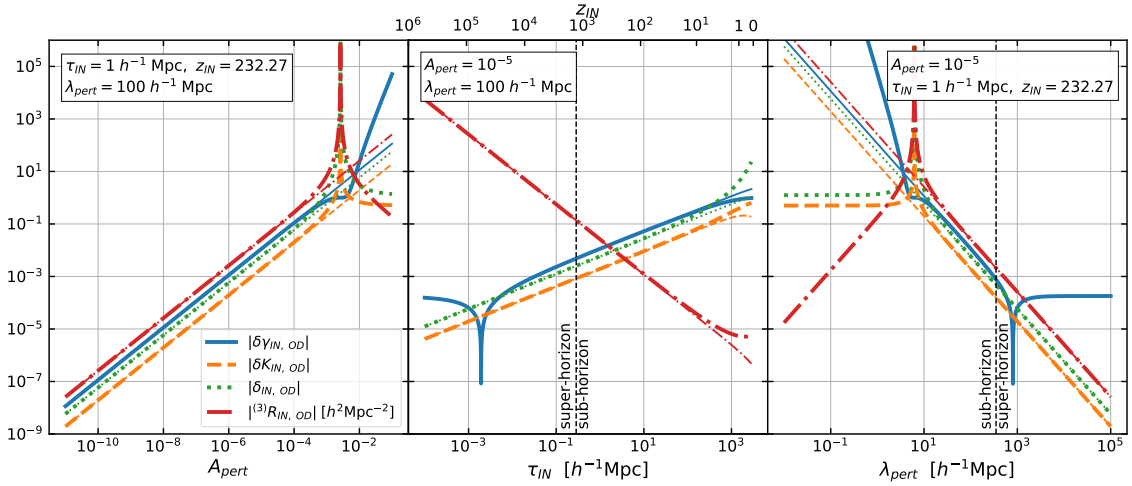

Figure 6.4: Amplitude of initial (IN) $\delta\gamma$, δK, δ and ${}^{(3)}R$ in the centre of the over-density (OD) as a function of A_{pert}, z_{IN} and λ_{pert} presented in each panel left to right. While each is varied the other parameters are kept constant as presented in the top box. The thinner lines correspond to the first-order expressions of these quantities, while the thicker lines correspond to their nonlinear expressions, thus the separation of these two lines emphasises non-linearity. The vertical dashed black lines indicate the instance where the physical wavelength corresponds to the Hubble distance $\lambda_{phy} = c/H$ hence separating sub and super Hubble horizon regimes. *Left panel:* for the given initial redshift z_{IN} and perturbation wavelength λ_{pert}, non-linearities start to be relevant when $A_{pert} > 10^{-4}$. *Middle panel:* for the given A_{pert} and λ_{pert} non-linearities would only be relevant for $z_{IN} \lesssim 50$. The first-order thin lines become curved when Λ becomes relevant. The proper volume perturbation $\delta\gamma_{IN,\,OD}$ shows a plateau during the $\mathcal{R}_c$-dominated regime, see Eq. (6.11) and Eq. (6.14), when $\delta\gamma_{IN,\,OD} > 0$, and its sign changes in the transition to the δ-dominated regime $\delta\gamma_{IN,\,OD} < 0$. *Right panel:* for the given A_{pert} and z_{IN} non-linearities are only relevant on scales smaller than $\lambda_{pert} \lesssim$ few $\times$ 10h^{-1}Mpc. The $\mathcal{R}_c$-dominated regime is again identifiable with the plateau in $\delta\gamma_{IN,\,OD}$ on large scales.

the background in the OD, $\delta\gamma_{OD} > 0$. This counter-intuitive behaviour is observed when:

$$\lambda_{phy} > \frac{2\pi}{H\sqrt{3F}}. \tag{6.14}$$

This $\mathcal{R}_c$-dominated regime then occurs when the wavelength is much bigger than the Hubble horizon ($> c/H$), so we also call it the long-wavelength regime. This phenomenon has previously been discussed (Abramo, Brandenberger, and Mukhanov, 1997; Mukhanov, Abramo, and Brandenberger, 1997; Brandenberger, 2002; Geshnizjani and Brandenberger, 2002), where long wavelength modes were proposed to act as a form of cosmological constant.

6.2 Code description and Numerical implementation

In NR (Gourgoulhon, 2007; Alcubierre, 2008; Baumgarte and Shapiro, 2010; Shibata, 2015), Einstein's field equations are separated into constraint equations Eq. (3.29, 3.30) and evolution equations Eq. (3.32, 3.31). So to run simulations, an initial spacetime and matter distribution satisfying the constraints is set, then evolved according to the evolution equations, and the constraint equations are used to monitor accuracy throughout the evolution. While the initial quantities can be set using the

ADM formalism (York, 1979; Arnowitt, Deser, and Misner, 2008), the evolution equations take a form that is not well-posed; this will then cause stability issues in the simulation. These quantities need to be transformed to a formulation with well-posed evolution equations, such as BSSNOK (Nakamura, Oohara, and Kojima, 1987; Shibata and Nakamura, 1995; Baumgarte and Shapiro, 1998) see Section 3.3.3.1. The quantities associated with the fluid that are sourcing Einstein's evolution equations are called the primitive hydrodynamics variables; these are evolved with the conservation equations $\nabla_\mu T^{\mu\nu} = 0$. Typically these variables are also transformed, in this case, to the corresponding conserved quantities see e.g.(Font, 2003; Alcubierre, 2008; Bentivegna, 2017) and Section 3.3.1, such that high-resolution shock-capturing numerical schemes can be applied to the evolution equations. This is particularly relevant to turbulent scenarios, and so are not applied here.

We use the open-source code *Einstein Toolkit* (n.d.) (Löffler et al., 2012; Brandt et al., 2020) for our simulations. This code is a compilation of multiple modules, named thorns, that communicate within the Cactus framework (Goodale et al., 2003). These thorns have different tasks and capacities and may be written in C++ or Fortran adapted to Cactus code or in Mathematica or Python to then be converted to C++ Cactus code by Kranc (Husa, Hinder, and Lechner, 2006) or NRPy+ (Ruchlin, Etienne, and Baumgarte, 2018). To manage this infrastructure, the simfactory job manager (Thomas and Schnetter, 2010) is used for compilation and running jobs.

The initial distributions for our simulations are calculated by our new thorn `ICPertFLRW` (Munoz, 2023a), developed in Fortran and adapted to Cactus code for this project. It defines the initial ADM variables: γ_{ij} Eq. (6.6), K_{ij} Eq. (6.7), with $\alpha = 1$, $\beta^i = 0$ and $\rho^{\{u\}}$ given by Eq. (6.12). As explained in Section 6.1.3, defining $\rho^{\{u\}}$ using the Hamiltonian constraint implies that this is initially automatically satisfied, while the momentum constraint is initially satisfied at first-order, see Appendix C showing that while initial conditions remain linear his is not an issue. `ICPertFLRW` then provides the ADM quantities to the `ADMBase` (Löffler et al., 2012) and `CT_Dust` thorns (Bentivegna, 2017). The variables are provided on a Cartesian grid, supported by `Carpet` (Schnetter, Hawley, and Hawke, 2004); this has mesh refinement capacities, although we have not used these in this chapter.

To evolve the geometrical variables, they are transformed into the BSSNOK formalism (Nakamura, Oohara, and Kojima, 1987; Shibata and Nakamura, 1995; Baumgarte and Shapiro, 1998) and the subsequent variables are evolved by the `ML_BSSN` thorn (Brown et al., 2009). The primitive hydrodynamics variables are transformed to their conserved form and evolved by `CT_Dust` (Bentivegna, 2017) without shock-capturing schemes, which differs from the usual thorn `GRHydro` (Mösta et al., 2013) since here we exclusively use dust. This system of equations is integrated with the 4^{th} order Runge-Kutta scheme provided by the `MoL` thorn (Löffler et al., 2012) and described in Section 3.6.2. The coupling between the metric and the matter field is ensured by the `TmunuBase` thorn (Löffler et al., 2012).

The simulations were run on the Sciama HPC Cluster (*SCIAMA* n.d.) with box sizes of 32^3, 64^3 and 128^3 data points. Sciama's job manager Slurm (*Slurm* n.d.) was made to communicate with simfactory (Thomas and Schnetter, 2010).

The simulation outputs are τ, γ_{ij}, K_{ij} and $\rho^{\{u\}}$ these have been analysed with data processing codes developed exclusively for this project, notably `EBWeyl` see Chapter 5 (Munoz, 2022) and `sphereint` see Appendix D (Munoz, 2023b).

6.3 Simulation results

In this section, we describe two simulations with the initial conditions of Section 6.1.3, one with Λ and one without. Both are compared to the spherical collapse model in Section 6.3.1, and the simulation with Λ is then described more in the following subsections. We fix some of the parameters as in Bentivegna and Bruni (2016), namely $\lambda_{phy,\,IN} = 4/H_{IN} = 6$Mpc and $\delta_{IN,\,OD} = 3 \times 10^{-2}$, where we assume $H_0 = ch/2997.9$ Mpc^{-1}, with $c = 1$ and $h = 0.6737$ (Planck Collaboration, 2020). As such the simulation without Λ starts at $z_{IN} = 205.4$ with $\lambda_{pert} = 1206$Mpc and the simulation with Λ at $z_{IN} = 302.5$ with $\lambda_{pert} = 1821$Mpc. The initial δ_{OD} is chosen in order for the OD to collapse at $2 < z < 5$.

These initial conditions evolve until the OD collapses on itself; in practice, the simulation 'crashes' as NaN (not a number) values appear. This is due to our fluid description of matter and use of synchronous-comoving coordinates, while such a structure would otherwise be expected to relax into a virialised dark matter halo. To go beyond the limitations of the synchronous gauge, with other gauge choices, such as the 1+log or harmonic gauges, the lapse would decrease during the contraction, gradually slowing down the evolution of the centre of the OD, freezing it such that it would not collapse while the rest of the cosmic web would freely evolve. Therefore those gauges, particularly the harmonic gauge, are common choices for cosmological simulations in NR (East, Wojtak, and Abel, 2018; Giblin, Mertens, Starkman, and Tian, 2019b; Macpherson, 2019), and will be considered for future work. One may also consider gauge choices such that the shift is no longer zero. However, whatever the gauge, so long as one uses the fluid description, the virialisation process can't be described; one would need to consider a different method of implementing matter (East, Wojtak, and Pretorius, 2019; Magnall et al., 2023). Here it is precisely the collapse of the structure in the fluid frame that is of interest, hence the use of the synchronous-comoving gauge (Bentivegna and Bruni, 2016), which helps in the comparison with the Top-Hat model.

6.3.1 Over-density peak evolution & Top-Hat model

The evolution of the inhomogeneities at the OD peak and at the UD's bottom is presented in Fig. (6.5) for the ΛCDM case. For the top row, from left to right, we show the density, volume, and expansion contrasts δ, $\delta\gamma$, and δK in Eq. (6.10). The dashed lines are the first-order expectations from Eq. (6.4), Eq. (6.11) and Eq. (4.50) while the full lines are the results of the simulation. The separation between those lines shows a departure from linearity, which happens early on in the simulation. The unphysical regions ($\rho^{\{u\}}$ and γ need to be positive) and Milne model limit, see Section 4.1.4.1, in the plots show that these departures from linearity are indeed necessary for this system to remain physical.

In the centre of the OD, still on the top row from left to right: δ_{OD} becomes very large, the volume element tends towards zero, so that $\delta\gamma_{OD} \to -1$, the initial expansion is more and more decelerated until it turns around (TA) and contraction begins, when $K_{OD} = 0$ and $\delta K_{OD} = -1$. The reverse is observed in the centre of the UD: the density tends to zero $\delta_{UD} \to -1$, the volume element becomes much larger than the reference FLRW and the expansion is faster. In the centre of the simulation box, where initially $\mathcal{R}_c = 0$, the first-order quantities all remain zero, but the non-linearity introduced by ${}^{(3)}R$ in the initial conditions makes all quantities in the figure measurably non-zero (beyond numerical error) although they remain very small.

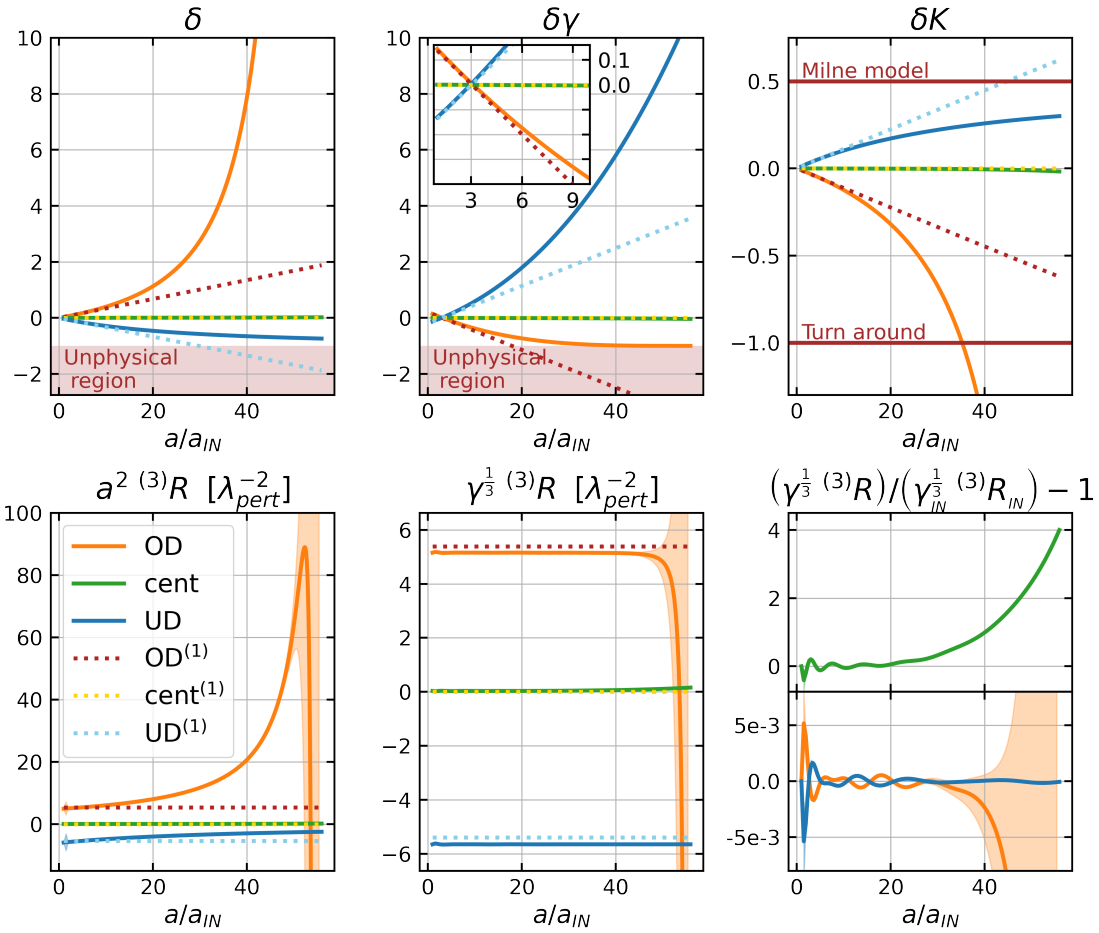

Figure 6.5: Evolution of various quantities at the peak of the over and under-density (OD in orange and UD in blue) as well as the central location of the simulation box (in green). *Top:* the matter density, volume, and expansion contrasts δ, $\delta\gamma$ and δK. *Bottom:* the conformal 3-Ricci scalar defined with the ΛCDM FLRW scale factor $a^{2}{}^{(3)}R$; conformal 3-Ricci scalar defined with the nonlinear scale factor $\gamma^{\frac{1}{3}\,(3)}R$; the same quantity normalised with its initial value $\left(\gamma^{1/3\,(3)}R\right) / \left(\gamma_{IN}^{1/3\,(3)}R_{IN}\right) - 1$. The dashed lines are the first-order projections from Eq. (6.4), Eq. (6.11) and Eq. (4.50), and the full lines are the simulation results. Initial conditions are $\delta_{IN,\,OD} = 3 \times 10^{-2}$, $z_{IN} = 302.5$ and $\lambda_{pert} = 1821$Mpc, and Λ is present. Error bars, when visible, are indicated as shaded regions.

Notice the sign change in the volume contrast $\delta\gamma$ at $a/a_{IN} \simeq 3.1$. This behaviour is representative of the transition experienced by long wavelength perturbations as they evolve from the $\mathcal{R}_c$-dominated to δ-dominated regime, according to Eq. (6.14) (Abramo, Brandenberger, and Mukhanov, 1997; Mukhanov, Abramo, and Brandenberger, 1997; Brandenberger, 2002; Geshnizjani and Brandenberger, 2002).

Then the second row of panels in Fig. (6.5) show, first on the left, the conformal 3-Ricci scalar defined with respect to the ΛCDM FLRW scale factor, $a^{2}{}^{(3)}R$ (Bruni, Hidalgo, Meures, et al., 2014; Bruni, Hidalgo, and Wands, 2014). At first order, this quantity is conserved at all scales for dust, as shown by the dashed lines, however in the OD the curvature is positive and grows larger and larger up until the crash (where there are large error bars), while in the UD it is initially negative and tends towards zero. The middle panel, on the other hand, shows the conformal 3-Ricci scalar defined with respect to the nonlinear scale factor from the simulation, $\gamma^{\frac{1}{3}\,(3)}R$: for the OD, essentially this is

conserved throughout the evolution up until just before the crash. Indeed, when normalised with its initial value, as can be seen in the rightmost panel, only sub-percent fluctuations are observed in the UD and OD (when error bars are reasonable), but a more notable deviation can be seen in the central location. This shows that the locations at the top/bottom of the inhomogeneity conserve their local nonlinear conformal curvature, which is essentially consistent with the closed FLRW description of the Top-Hat model, see Section 4.3.2.3. As the volume element in the OD shrinks, the curvature grows, therefore the two effects evolve together such that nonlinear conformal curvature is constant, conversely in the UD the volume element grows and the curvature tends towards zero such that the conformal curvature is also constant. In the central region, although too small to be seen in Fig. (6.5), the volume element shrinks and the curvature grows like in the centre of the OD; however, in this location the nonlinear conformal curvature is not conserved. This may be due to this location having a much greater density gradient $\partial_i \mathcal{R}_c = A_{pert} k_{pert}$ than the OD and UD centre $\partial_i \mathcal{R}_c = 0$.

To compare with the Top-Hat model as described in Section 4.3.2, the exact values of various quantities at TA, at times corresponding to virialisation according to two different definitions (Gunn and Gott, 1972; Peacock, 1999; Mo, Bosch, and White, 2010; Vittorio, 2018), and at the collapse/crash time are listed in Table (6.1). Defining R as the radius of the Top-Hat sphere, in this model R increases to reach its maximal size at TA, R_{TA}, when K_{OD} changes sign, from expansion to contraction, so TA measurements are taken when $K_{OD} = 0$. After that, R shrinks and collapses to $R = 0$. While the Top-Hat model does not have the mechanisms to enable virialisation, there are two different definitions typically used to approximate it. The first definition of virialisation is when R, evolving according to the Top-Hat model, reaches $R_{TA}/2$ (Peacock, 1999).
The second definition also works with $R_V = R_{TA}/2$ but assumes that relaxation mechanisms are present, and so establishes that R would reach this value at the time of collapse τ_C (Peacock, 1999; Vittorio, 2018). This means that this second definition has a discontinuity in the R evolution, which is assumed to be filled with relaxation mechanisms. Either way, these two definitions predict specific nonlinear δ_{OD}, so here we record a/a_{IN} when δ_{OD} reaches those values, see Section 4.3.2.1 for more details.

Recording the values reported in Table (6.1) was done in multiple ways. The proper times when $K_{OD} = 0$, $\delta_{OD} = 145.84$ or $\delta_{OD} = 176.65$ occur between recorded iterations, so they were obtained with a linear interpolation and then passed to Eq. (4.27), Eq. (4.29) or Eq. (6.4) to obtain a/a_{IN}, z or $\delta^{(1)}$. The nonlinear values $\gamma_{OD}^{1/6}/\gamma_{IN,\,OD}^{1/6}$, $\langle\gamma^{1/6}\rangle_{\mathcal{D}\{u\}}/\langle\gamma^{1/6}\rangle_{\mathcal{D}\{u\},\,IN}$ and δ_{OD} were obtained by linear interpolation to the previously determined time. Then, for the collapse/crash, the last valid values are recorded giving the nonlinear terms and a last proper time that was used to compute the corresponding a/a_{IN}, z or $\delta^{(1)}$. For each case ($\Lambda = 0$ or $\Lambda \neq 0$) this process was repeated for the three simulations of varying resolution, the high-resolution result is reported in Table (6.1) and the two lower resolution results are used to compute the corresponding error bars according to Eq. (C.4).

In our simulations, the TA and collapse/crash, with and without Λ, occur at an earlier time than the time in Bentivegna and Bruni (2016). This shows that the presence of the decaying mode in their case has significantly slowed down the evolution, as was also shown by (East, Wojtak, and Abel, 2018). Correspondingly, they also have a bigger[3] $\delta_{OD}^{(1)}$ at those moments, this is simply due to the

[3]That is, for the linearly extrapolated density contrast we have $\delta_{TA,\,OD}^{(1)} = 1.8$ for a TA at $a/a_{IN} = 60$ as in

		Top-Hat, $\Lambda = 0$	Here, $\Lambda = 0$	Here, $\Lambda \neq 0$	(Bentivegna and Bruni, 2016)
Initially	z_{IN}		205.4	302.5	205.4
Turn Around (TA) $K_{OD} = 0$	a/a_{IN}	35.4137	35.24467 ± 7e-5	35.195 ± 3e-3	60
	z		4.85620 ± 1e-5	7.6234 ± 7e-4	2.44
	$\frac{\gamma_{OD}^{1/6}}{\gamma_{IN,\,OD}^{1/6}}$		20.10169 ± 3e-5	20.0600 ± 1e-4	
	$\frac{\langle\gamma^{1/6}\rangle_{\mathcal{D}\{u\}}}{\langle\gamma^{1/6}\rangle_{\mathcal{D}\{u\},\,IN}}$		35.2064 ± 1e-4	35.154 ± 3e-3	
	$\delta_{OD}^{(1)}$	1.06241	1.05734 ± 2e-6	1.05584 ± 8e-5	1.8*
	δ_{OD}	4.55165	4.55164 ± 1e-5	4.5626 ± 5e-4	
Collapse /Crash	a/a_{IN}	56.22	55.9 ± 1e-1	55.87 ± 8e-2	96
	z		2.692 ± 7e-3	4.432 ± 8e-3	1.15
	$\frac{\gamma_{OD}^{1/6}}{\gamma_{IN,\,OD}^{1/6}}$		0.4 ± 6e-1	0.8 ± 2e-1	
	$\frac{\langle\gamma^{1/6}\rangle_{\mathcal{D}\{u\}}}{\langle\gamma^{1/6}\rangle_{\mathcal{D}\{u\},\,IN}}$		55.8 ± 1e-1	55.77 ± 2e-2	
	$\delta_{OD}^{(1)}$	1.686	1.678 ± 3e-3	1.676 ± 2e-3	2.88
	δ_{OD}	$+\infty$	2e+6 ± 2e+6	4e+5 ± 4e+5	
Virialisation $R = R_{TA}/2$	a/a_{IN}	52.64	52.5055 ± 9e-4	52.469 ± 2e-3	
	δ_{OD}	145.84	145.84	145.84	
Virialisation $R = R_{TA}/2$ & $\tau = \tau_C$	a/a_{IN}	56.22	52.83625 ± 7e-5	52.801 ± 2e-3	
	δ_{OD}	176.65	176.65	176.65	

Table 6.1: Various variables during the evolution of an over-density (OD) whose initial (IN) density contrast is $\delta_{IN,\,OD} = 0.03$ and physical size $\lambda_{phy,\,IN} = 4/H_{IN}$. These variables are recorded for four scenarios at different *stages of the evolution*: the turn around (TA), the collapse/crash of the OD, and its virialisation according to two different definitions, when the radius of the Top-Hat sphere is half its radius at TA, and when that property happens at the time of the collapse. *The four scenarios* are the theoretical Top-Hat spherical and homogeneous collapse model (first column (Gunn and Gott, 1972; Peacock, 1999; Mo, Bosch, and White, 2010; Vittorio, 2018) see Section 4.3.2.1) and three numerical relativity simulations of a 3-dimensional sinusoidal peak. These are: our simulations with a purely growing mode with $\Lambda = 0$ (second column), and with $\Lambda \neq 0$ (third column); from (Bentivegna and Bruni, 2016), with a growing and decaying mode with $\Lambda = 0$ (fourth column). *The variables* are: the normalised background scale factor a/a_{IN}, with its corresponding redshift z and linear density contrast $\delta_{OD}^{(1)}$ ($\delta_{OD}^{(1)} = \delta_{IN,\,OD}\ a/a_{IN}$ for EdS), this is to be compared to the local scale factor $\gamma_{OD}^{1/6}/\gamma_{IN,\,OD}^{1/6}$, the domain average scale factor $\langle\gamma^{1/6}\rangle_{\mathcal{D}\{u\}}/\langle\gamma^{1/6}\rangle_{\mathcal{D}\{u\},\,IN}$ (averaged over the whole simulation box), and the nonlinear density contrast δ_{OD}. For the two definitions of virialisation a/a_{IN} is recorded at the given δ_{OD}. The asterisk indicates a factor of three correction to the value reported in Bentivegna and Bruni (2016).

Bentivegna and Bruni (2016), thus correcting the value for $\delta^{(1)}$ at TA reported in Bentivegna and Bruni (2016), $\delta_T^{(1)} = 0.6$. Similarly, given that the collapse in Bentivegna and Bruni (2016) is at $a/a_{IN} \simeq 96$, $\delta^{(1)} \simeq 0.96$ under the same assumptions, while the correct value is $\delta^{(1)} \simeq 2.8$, as we report in Table (6.1). The presence of the decaying mode in Bentivegna and Bruni (2016) implied that a direct match with the prediction of the Top Hat model was not expected and somehow confused the interpretation of the results. This was based on assuming that the initial density contrast was $\delta_{IN,\,OD} = \delta_i = 10^{-2}$, as reported in the text around Eq. (9) in Bentivegna and Bruni (2016), while the correct value of

longer evolution since $\delta^{(1)}_{OD} = \delta^{(1)}_{IN,\,OD}\, a/a_{IN}$ in EdS.

Otherwise, we see that at the peak of the OD we reach TA and collapse/crash precisely when the Top-Hat model predicts it, with the expected a/a_{IN}, $\delta^{(1)}_{OD}$ and δ_{OD} values in agreement with East, Wojtak, and Abel (2018). With the conservation of the local conformal curvature, this shows that the Top-Hat model provides excellent predictions for the centre of the OD. Furthermore, the domain averaged scale factor, $\langle\gamma^{1/6}\rangle_{\mathcal{D}\{u\}}/\langle\gamma^{1/6}\rangle_{\mathcal{D}\{u\},\,IN}$, is also close to the Top-Hat model prediction for a/a_{IN}. This is not the case for the local measurement, $\gamma^{1/6}_{OD}/\gamma^{1/6}_{IN,\,OD}$, which instead shows the compactness of the region.

For virialisation, we recover the expected a/a_{IN} for the first definition of $R = R_{TA}/2$, but not for the second $R = R_{TA}/2$ and $\tau = \tau_C$. The first definition is based on the exact evolution of R for the Top-Hat model, while the second provides an approximation by making the assumption that, relaxation mechanisms are present. The matter in these simulations is described as a pressureless perfect fluid, it therefore does not have any relaxation mechanism, so instead, as we observe in the centre of the OD, the evolution of the density contrast is well predicted by the Top-Hat model.

We see a slight difference depending on the presence of Λ in the simulation. However, the error estimates overlap in many cases and we measure up to a maximum $\simeq 0.57\%$ difference between the $\Lambda = 0$ and the $\Lambda \neq 0$ simulations.

6.3.2 Raychaudhuri equation: local evolution & Top-Hat approximation

Our results, in either case, show that at the peak of the OD the Top-Hat model is an excellent approximation. To understand this, consider the Raychaudhuri equation Eq. (2.65)

$$\dot{\Theta} + \frac{1}{3}\Theta^2 + 2\sigma^2 + \frac{\kappa}{2}\rho^{\{u\}} - \Lambda = 0, \tag{6.15}$$

describing the local evolution of the fluid expansion scalar. Each term contributing to $\dot{\Theta}$ is plotted along the $x = y = z$ diagonal, in Fig. (6.6). This direction goes from the centre of the OD through the centre of the face of the octahedron such that it also goes through the centre of the UD (this is the dashed green line in Fig. (6.2)).

The matter density $\rho^{\{u\}}$ curve, i.e. the dot-dot-dashed red line in Fig. (6.6), clearly shows the OD and UD regions located at $\pm 0.25\lambda_{pert}$. The shear contribution, σ^2, shown with the dashed green line, is subdominant everywhere; it does grow around the OD but it is always essentially zero at the peak of the OD and at the centre of the UD. The reason that σ^2 is negligible in these specific locations is because of the triaxial symmetry, so that around these two points the distribution is almost spherical. The fact that the shear gives a negligible contribution to the Raychaudhuri equation implies that at the OD and the UD locations the evolution is in essence independent of the environment. Mathematically, neglecting the shear implies that the Raychaudhuri equation is only coupled to the continuity equation Eq. (4.16): then at the OD these two equations are formally identical to those in FLRW with positive 3-curvature, as implied by the Hamiltonian constraint Eq. (6.12). Therefore, at the peak, the Top-Hat model is a very good approximation.

the initial δ was $\delta_{IN,\,OD} = 3\delta_i = 3 \times 10^{-2}$, as it is clearly visible in the leftmost panel of Fig. 1 and their Eq. (9).

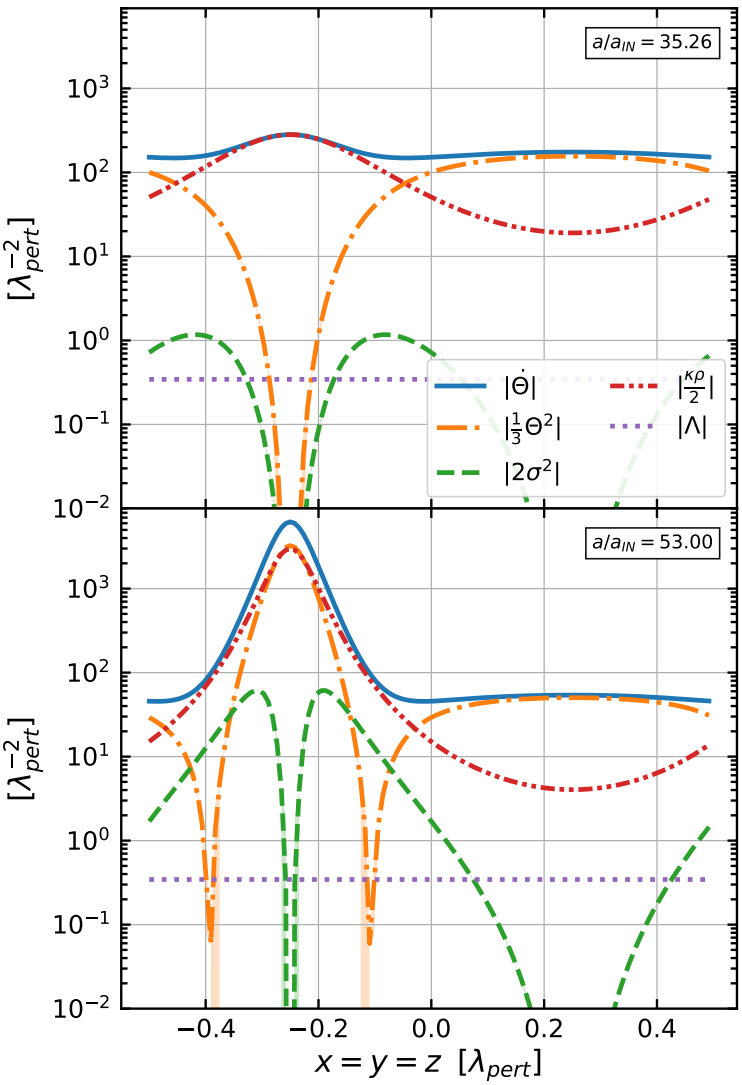

Figure 6.6: Contributions to the Raychaudhuri equation just after the turn-around of the peak (top panel) and just before the crash (bottom panel): since $c = G = 1$ all these terms have units of length^{-2}, therefore we measure them in λ_{pert}^{-2} units. Each term is presented along the $x = y = z$ diagonal of the data box, the peak of the over-density is at $x = -0.25\lambda_{pert}$ and the bottom of the under-density is at $x = 0.25\lambda_{pert}$. Error bars, when visible, are indicated as shaded regions.

Then the expansion, Θ, shown with the dot-dashed orange line, peaks downwards, $\Theta = -K = 0$, in locations experiencing TA. The peak of the OD experiences TA first, then its surrounding region. This identifies the infalling domain discussed in the next Section 6.3.3.

6.3.3 Expansion of the infalling domain

Throughout the evolution of the collapsing region, the expansion $\Theta = -K$ of the OD is positive but more decelerated than the reference ΛCDM, until it reaches TA at $\Theta = 0$ and then contracts inwards $\Theta < 0$. The peak of the OD is the first to reach TA, followed by its surrounding region, where points at a larger distance from the peak reach TA at later times.

The infalling region, identified using the TA boundary $\Theta = 0$, is shown in Fig. (6.7) at two differ-

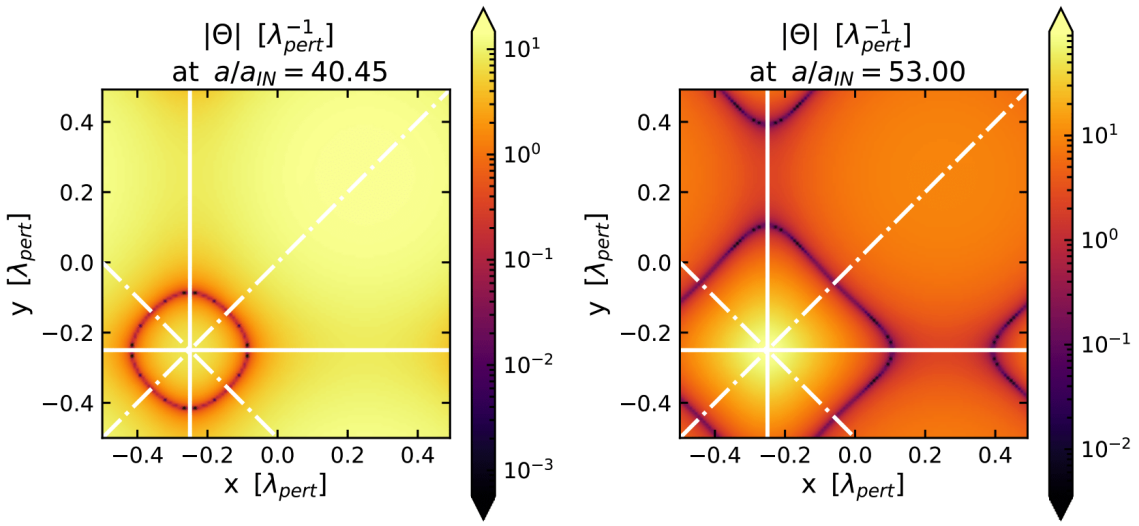

Figure 6.7: Absolute expansion scalar Θ in units λ_{pert}^{-1} in the x-y plane passing by the peak of the over-density ($z = -0.25\lambda_{pert}$) at $a/a_{IN} = 40.45$ and 53.00. The full lines indicate directions along the vertices and the dash-dotted lines are the directions along the centre of the edges.

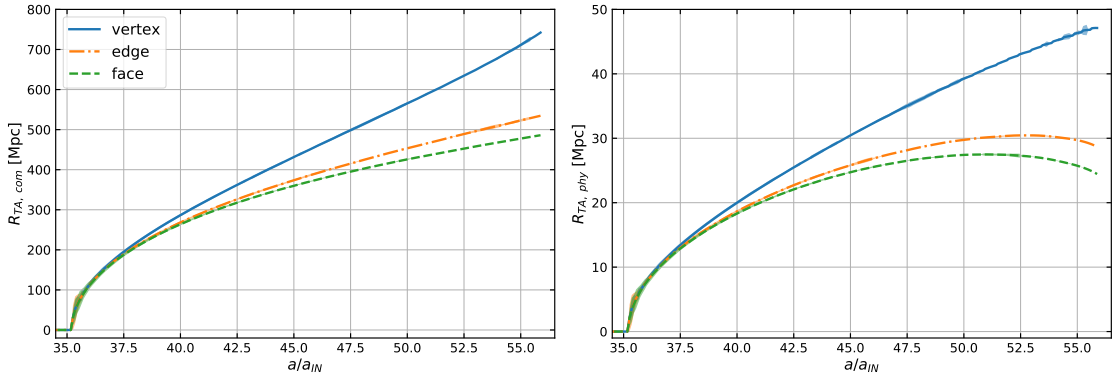

Figure 6.8: Evolution of the turn around radius R_{TA} - distance from the peak of the over-density to $\Theta = 0$ in three directions. On the left, R_{TA} measured in terms of the comoving length today; on the right the corresponding proper length; we emphasise that the physical length is an order of magnitude smaller than the comoving length. Error bars, when visible, are indicated as shaded regions.

ent times. Initially, the boundary surface is close to spherical symmetry, but later, as it encompasses a greater comoving volume and therefore a larger mass, the non-spherical shape becomes apparent. As the TA boundary expands outward it tends towards an octahedron, this appears as an almost square boundary in the 2-dimensional slicing through the box in the right panel of Fig. (6.7), extending beyond the box sides with the periodic boundary condition.

With octahedrons, there are three directions of interest: from the centre to the vertices, to the centre of the edges, and to the centre of the faces. The plane in Fig. (6.7) shows the vertex and the centre of the edge directions (full and dash-dotted lines). As the TA boundary $\Theta = 0$ expands outward, we measure the distance between the peak of the OD and the TA point in each direction, which we call the TA radius R_{TA}. The evolution along the three different directions is presented in Fig. (6.8), where we depict the comoving coordinate TA radius $R_{TA,\,com}$ in the left panel, and the physical TA

radius $R_{TA,\,phy}$ in the right panel, see Appendix D.

In the left panel, the TA boundaries grow in the same way in the three directions, so long as they stay in the region that is almost spherically symmetric around the peak, and then they split out according to the direction-dependent distribution. In the directions with the biggest δ, the TA radius grows the fastest.

This is also true when we consider the proper distances $R_{TA,\,phy}$, by integrating with the local scale factor, see Appendix D, which are shown in the right panel of Fig. (6.8). Notably, we see that in the two directions that go through an UD region, edges and faces, $R_{TA,\,phy}$ stops growing and starts decreasing. So in these two directions, the region of infalling material reaches a maximal size and then starts shrinking, while in the direction where δ is always positive, the infalling region continues to grow.

6.3.4 Evolution of a comoving sphere

We can draw another comparison to the Top-Hat model by considering the evolution of a comoving sphere, a region with constant mass, centred on the peak of the OD and compare its evolution with that of a homogeneous spherical Top-Hat with $\delta = \langle\delta\rangle_{\mathcal{D}\{u\}}$. For a given comoving radius, we integrate to measure the proper physical radius and present it in the left panels of Fig. (6.9). Two comoving radii are considered, one small $0.02\lambda_{pert}$, where we see that all three directions behave in the same way, and one big $0.33\lambda_{pert}$, with a direction-dependent evolution such that the bigger the δ, the sooner the collapse. In the latter case, we see how a spherical comoving region gradually gets distorted in physical space.

The Top-Hat models from Section 4.3.2.1, grey dotted lines in the left panels of Fig. (6.9), were computed with the domain average δ within the given comoving sphere, $\langle\delta\rangle_{\mathcal{D}\{u\}}$, see Munoz (2023b) and Appendix D. The small comoving radius case closely follows the Top-Hat model but falls just short of reaching collapse as the peak had already reached that point, stopping the simulation. In the large comoving radius case, there is a clear departure from the Top-Hat model, the region would collapse sooner than what the Top-Hat model would have predicted. Indeed for such an inhomogeneity, it is unfair to compare it to a homogeneous sphere.

The average relative difference between the physical radius and the Top-Hat model prediction is measured for a range of comoving radii and presented in the top right panel of Fig. (6.9). The grey dot-dot dashed vertical lines identify the two cases on the left panels. This indeed shows that as the radius of the comoving sphere is increased, the bigger the difference between the results and the corresponding Top-Hat model. This indicates the limit with which inhomogeneous structures can be predicted with homogeneous models.

In Section 6.3.2 we identified the sub-dominance of shear in the proximity of the peak to be the main reason why the evolution of this region closely follows the Top-Hat model prediction described in Section 6.3.1. Then, in the bottom right panel of Fig. (6.9) we also show the shear as a function of the comoving radius R_{com}. Indeed, further out from the peak of the OD, the shear is no longer negligible, even if it is still subdominant at this radius as a contribution to the Raychaudhuri equation in Fig. (6.6).

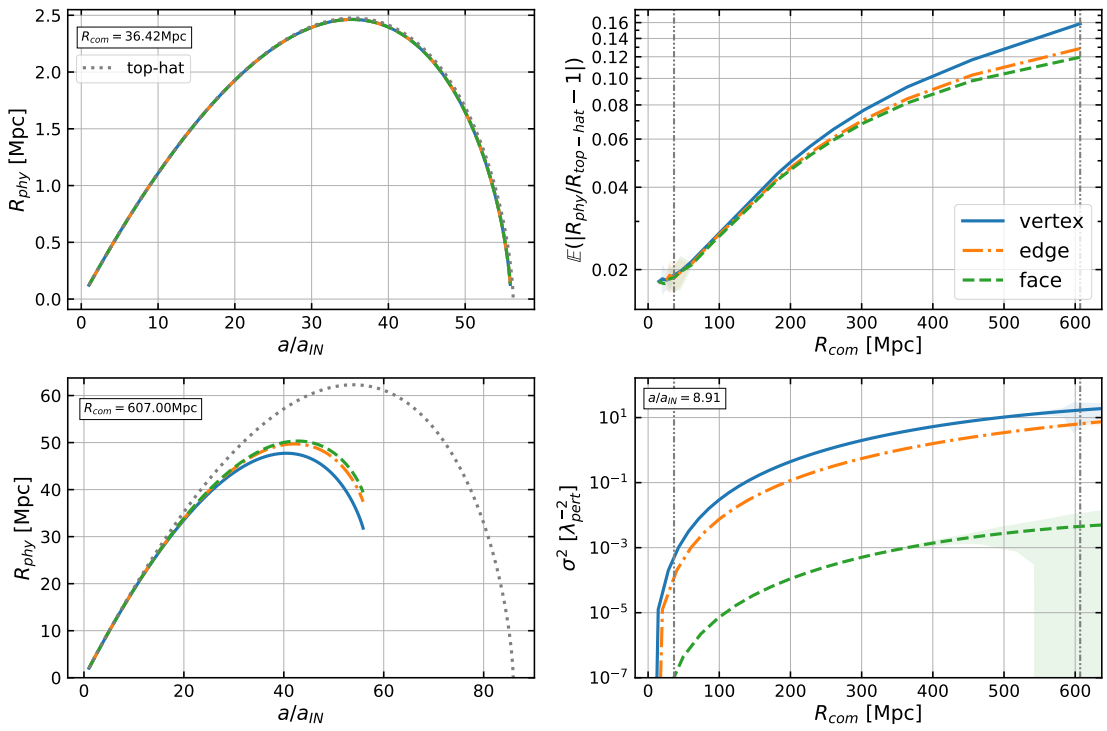

Figure 6.9: *Left panels:* evolution of proper physical radius of two comoving spheres, one small (top panel) and one large (bottom panel), centred on the peak of the over-density, in all three directions, compared to the Top-Hat spherical and homogeneous collapse model. The comoving radii are listed as text in the plots. The Top-Hat models were computed using the domain average δ within the two spheres, $\langle\delta\rangle_{\mathcal{D}\{u\}}$ see Appendix D. *Top right panel:* average relative difference between the simulation results and the Top-Hat model prediction for a range of comoving radii. The two cases on the left are identified with grey dot-dot-dashed lines. *Bottom right panel:* shear in the three directions from the peak of the over-density. Error bars, when visible, are indicated as shaded regions.

6.3.5 Gravito-electromagnetism

The electric and magnetic parts of the Weyl tensor defined with respect to the fluid flow, u^α, are given by $E^{\{u\}}_{\alpha\beta}$ and $B^{\{u\}}_{\alpha\beta}$ Eq. (2.73), see Section 2.5.1 (Matte, 1953; Hawking, 1966; Maartens and Bassett, 1998; Ellis and Elst, 1999; Ellis, 2009; Ellis, Maartens, and MacCallum, 2012) where they are shown to describe the non-local gravitational field. In general, in 3+1 they are computed with respect to a unit timelike hypersurface-orthogonal vector field n^α providing $E^{\{n\}}_{\alpha\beta}$ and $B^{\{n\}}_{\alpha\beta}$.

We compute $E^{\{n\}}_{\alpha\beta}$ and $B^{\{n\}}_{\alpha\beta}$ with `EBWeyl`, the code presented and tested in Chapter 5 (Munoz, 2022; Munoz and Bruni, 2023a), together with their divergence $D^{\{n\}\nu}E^{\{n\}}_{\nu\mu}$ and curl $\left(D^{\{n\}}\times E^{\{n\}}\right)_{\alpha\beta}$ (Ellis, Maartens, and MacCallum, 2012), see Section 2.1.4.2 defined in the hypersurface with metric γ_{ij}, see Chapter 5 (Munoz and Bruni, 2023a):

$$D^{\{n\}i}E^{\{n\}}_{i\mu}, \quad \text{and} \quad \left(D^{\{n\}}\times E^{\{n\}}\right)_{\mu\nu} = -\epsilon^{\alpha\beta\sigma}{}_{(\mu}n_\alpha D^{\{n\}}_\beta E^{\{n\}}_{\nu)\sigma} = \alpha\epsilon^{0ij}{}_{(\mu}D^{\{n\}}_i E^{\{n\}}_{\nu)j}, \quad (6.16)$$

where $D^{\{n\}}_i$ is the covariant derivative with respect to γ_{ij}. In this chapter we use the synchronous-comoving gauge, so the normal to the γ_{ij} hypersurface is the fluid 4-velocity $n_\mu = u_\mu$, so $E^{\{u\}}_{\alpha\beta}$ and $B^{\{u\}}_{\alpha\beta}$, their divergence and curl Eq. (6.16) are computed with respect to the fluid flow. Additionally, because of the nature of the Levi-Civita tensor and the symmetrisation applied to the curl,

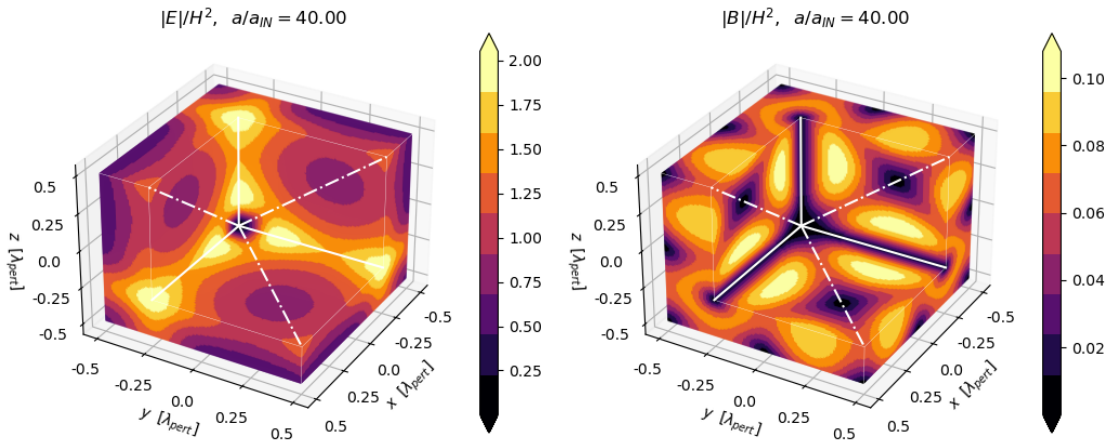

Figure 6.10: Distribution of the electric and magnetic parts of the Weyl tensor (left and right) in the simulation box, made dimensionless with the Hubble scalar H. The x, y, and $z > -0.25\lambda_{pert}$ region is removed exposing the centre of the over-density. The full white lines go through the vertices and dash-dotted lines through the centre of the edges of an octahedron centred at the over-density.

$\left(D^{\{u\}} \times E^{\{u\}}\right)_{\mu\nu}$ only has spatial components. We compute the magnitude of these tensors following: $|T| = \sqrt{g^{\alpha\mu}T_{\alpha}T_{\mu}}$ or $|T| = \sqrt{g^{\alpha\mu}g^{\beta\nu}T_{\alpha\beta}T_{\mu\nu}}$, where we drop the frame-dependent notation for simplicity presenting the magnitude of the variable, of its divergence and of its curl as $|E|$, $|\nabla \cdot E|$ and $|\nabla \times E|$ respectively.

Fig. (6.10) shows the $|E|$ and $|B|$ distribution in 3-dimensions. These are made dimensionless by dividing by H^2. The electric part is strongest along the vertices of the OD gradually moving towards the peak of the OD. To some extent, the electric part is analogous to the Newtonian description of gravity as it embodies tidal gravitational pull. The regions experiencing this the strongest are along the vertices as the matter is being pulled along the filaments towards the centre of the OD. At the peak, where the curvature is strongest, $|E|$ is small as the matter is already at the bottom of the potential well.

Conversely, the magnetic part is strongest around the vertices. The filaments along the vertex direction, connecting the ODs periodically present, can be perceived, by analogy to electromagnetism, to be carrying a gravitational current, with $|E|$ strong along it, and $|B|$ strong around it. In perturbation theory, at first order the magnetic part is only constructed from vector and tensor modes and embodies relativistic effects. When we set the initial conditions, as explained in Section 6.1.3, the density is defined non-linearly from the Hamiltonian constraint and the simulation freely evolves in full GR. At nonlinear order the scalar, vector and tensor perturbations couple, explaining the non-zero magnetic part. Connecting this to the fluid flow, the magnetic part in general is sourced by shear, vorticity and acceleration (Ellis, Maartens, and MacCallum, 2012). Yet, in the synchronous-comoving gauge and with pressureless dust there is no vorticity or acceleration. Therefore, in this case, the magnetic part embodies the curl of the shear Eq. (2.74)

$$B^{\{u\}}_{\alpha\beta} = \left(D^{\{u\}} \times \sigma\right)_{\alpha\beta}, \tag{6.17}$$

and we have shown the shear to be present in Fig. (6.6) and Fig. (6.9).

On the leftmost panels of Fig. (6.11) the dimensionless $|E|$ and $|B|$ distributions are shown on a 2-dimensional plane, where the notable axes of symmetry are marked in the top panel. These are

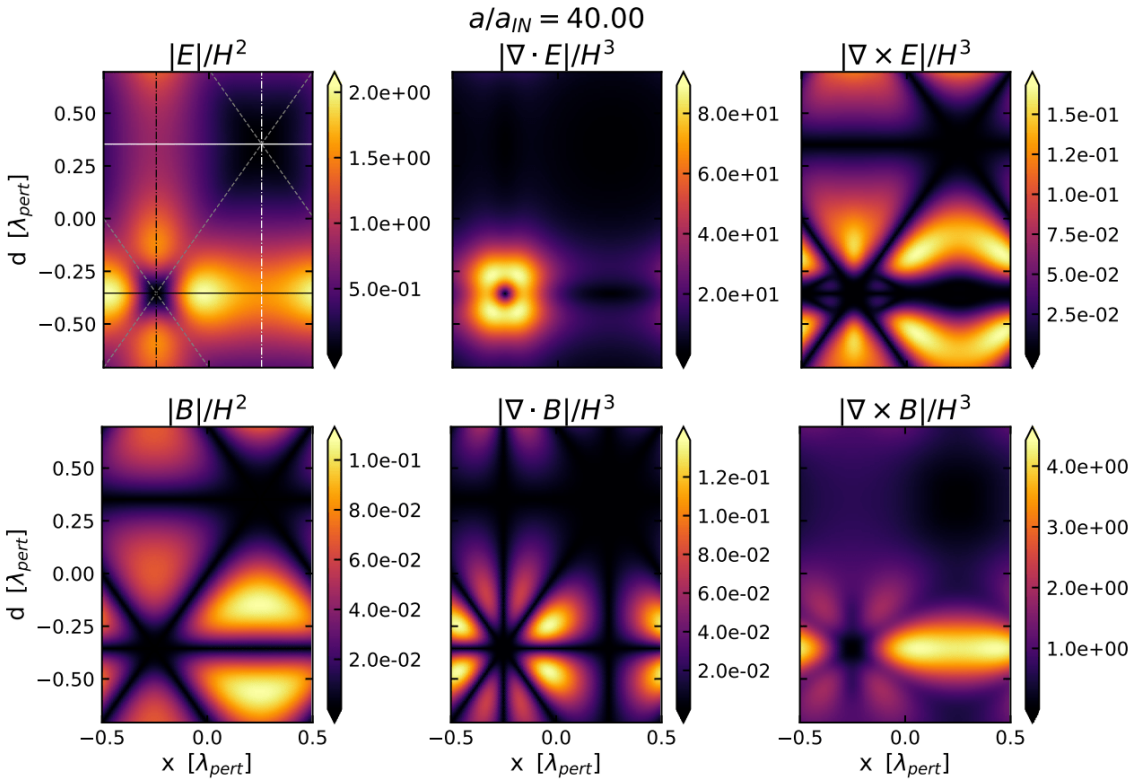

Figure 6.11: Magnitude of the electric and magnetic parts of the Weyl tensor, and their divergences and curls along the x and $y = z$ plane of the simulation box (with $d^2 = y^2 + z^2$) at $a/a_{IN} = 40.0$, and made dimensionless with the Hubble scalar H. The relevant axes of symmetry are marked on the top left panel. The directions going from the centre of the octahedrons to the vertices are marked with full lines, to the centre edges with dash-dotted, and to the centre of the faces with dashed lines. Directions going from the centre of the over-density are marked with black lines, and from the under-density with white lines, the directions going along the faces are valid for both the over-density and the under-density and so are in grey.

to be compared with Fig. (6.10) to grasp these distributions. $|E|$ is indeed strongest along the OD vertex, black full line, and $|B|$ wraps around it. However we also see that they become negligible in the UD, and along the faces directions, dashed grey lines, and $|B|$ also disappears in the UD vertex direction, white full line. These axes of symmetry are notable features in the divergence and curl distributions, middle and right panels. The divergence is strongest close to the peak of the OD, and to the other OD present through periodic boundaries. Then the curl of $|B|$ is strongest along the vertex and the curl of $|E|$ is strongest around the vertex axis.

The presence of $|B|$ in itself is not proof of the benefit we get from having a fully relativistic simulation, as frame-dragging can be measured from Newtonian simulations (Bruni, Thomas, and Wands, 2014; Milillo et al., 2015; Thomas, Bruni, and Wands, 2015; Rampf et al., 2016) as well as in relativistic simulations (Adamek, Daverio, et al., 2016a; Barrera-Hinojosa, Li, Bruni, et al., 2021; Barrera-Hinojosa, Li, and Cai, 2021). However, when only gravitational waves are present $|E| = |B|$ (Bonnor, 1995), the divergences vanish and the curls are present (Hogan and Ellis, 1997). We look at Fig. (6.12) to see that here the domain average divergence does not vanish, and looking at the ratios, $|B|$ is smaller than $|E|$ but still has a per cent level presence. We also find that for the electric part, the domain average of the divergence is stronger than that of the curl, $\langle|\nabla \cdot E|\rangle_{\mathcal{D}\{u\}} > \langle|\nabla \times E|\rangle_{\mathcal{D}\{u\}}$,

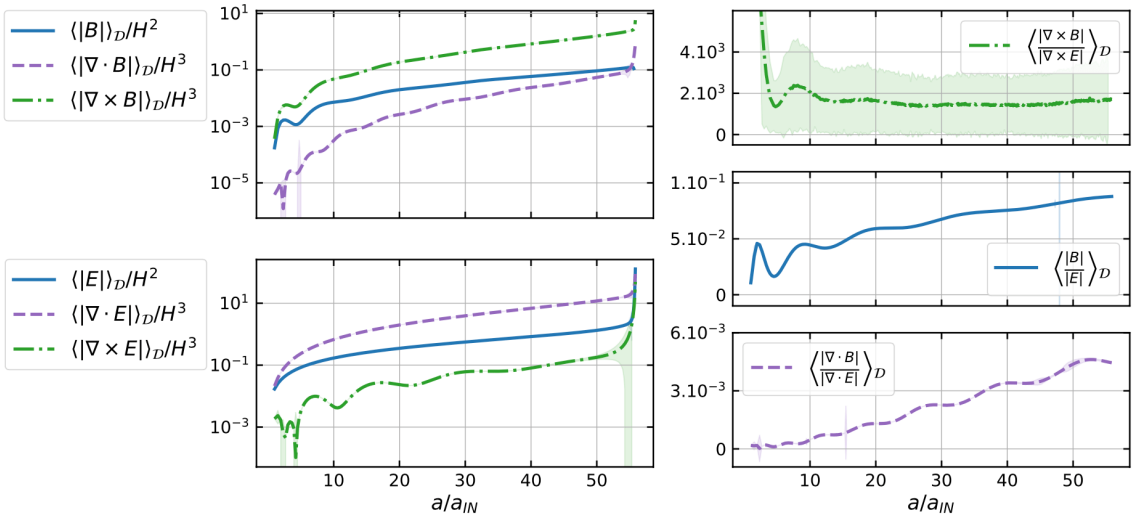

Figure 6.12: *Top left:* comoving domain average magnitude of the magnetic part of the Weyl tensor, of its divergence and curl throughout the simulation, made dimensionless with the Hubble scalar H. *Bottom left:* same as above but with the electric part of the Weyl tensor. *Right:* ratios between the magnetic and electric terms. Error bars, when visible, are indicated as shaded regions.

and the reverse is true for the magnetic part, $\langle|\nabla\cdot B|\rangle_{\mathcal{D}\{u\}} < \langle|\nabla\times B|\rangle_{\mathcal{D}\{u\}}$.

The electric and magnetic parts of the Weyl tensor have previously been measured in NR cosmological simulations: *i)* for a lattice of black holes, where the potential bias that is introduced by the magnetic part in optical measurements is quantified (Korzyński, Hinder, and Bentivegna, 2015; Bentivegna, Clifton, et al., 2018); *ii)* in more realistic cosmological simulations, where models with vanishing divergence of the magnetic part are found to be a valid approximation on large scales (Heinesen and Macpherson, 2022). This differs from what we find as $\langle|\nabla\cdot B|\rangle_{\mathcal{D}\{u\}}$ is initially present and grows throughout the simulation, even though it has the smallest amplitude in Fig. (6.12). These results do not contradict each other since we are considering very different spatial distributions, and here the simulation evolves into a highly nonlinear regime.

6.3.6 Effective Petrov classification

The Weyl tensor is the traceless part of the Riemann curvature tensor and describes, in essence, the tidal gravitational fields, far richer in a metric theory of gravity than in the Newtonian case. It is classified according to the Petrov classification (Petrov, 2000) see Section 2.5.4, with complex scalar invariants I, J, K, L, and N that we compute with `EBWeyl` from $E^{\{u\}}_{\alpha\beta}$ and $B^{\{u\}}_{\alpha\beta}$, following the equations provided in Section 2.5.2 and Section 2.5.3 (Munoz, 2022; Munoz and Bruni, 2023a). These invariants can then be used to classify different regions of the spacetime as Petrov type I, II, D, III, N, or O according to the scheme presented in Fig. (6.13), where we apply the theory of classification of exact solutions in Stephani et al. (2003). Each Petrov type has a specific physical interpretation, e.g. type D is characteristic of the Schwarzschild and Kerr black holes, as well as of the tidal field outside a spherically symmetric gravitational field, while type N is characteristic of plane gravitational waves; we refer the reader to Section 2.5.4 (Munoz, 2022; Munoz and Bruni, 2023a) and Refs. therein for more details.

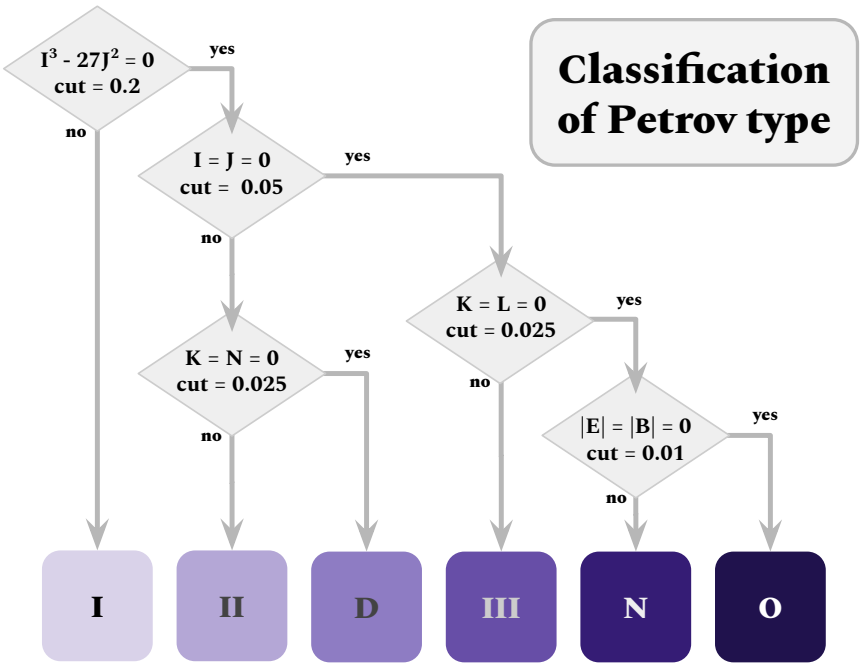

Figure 6.13: Flow diagram of Petrov classification, with a couple of modifications this is an adapation of Fig. (9.1) in Stephani et al. (2003). Cutoff values used in our analysis are listed here.

Numerically we hardly reach exact numbers; additionally, our simulation can be thought of as containing all types of perturbations at all orders, so our spacetime is of Petrov type I, the most general type. However, we consider the leading order type by introducing thresholds; then, because the background FLRW is of Petrov type O, that of conformally flat spacetimes, initially, this is the leading order Petrov type, as the perturbations are initially small. As non-linearities grow, the spacetime becomes more general. To see this transition, we adapt the IF statements described in Fig. (6.13) by considering the real and imaginary parts of each quantity separately, normalising them, making them dimensionless, and comparing them to a chosen cutoff value. This is done by making these invariants have the same power as the Weyl tensor and dividing by H^2. For example for the real part of I, we then have the value: $V = |Re(I^{1/6})|/H^2$, that we compare to a cutoff $V < cut$. We also consider the numerical error V_{error} obtained with the lower resolution simulations; see Appendix C. So we adapt the statement to $V < cut$ AND $(V > V_{error}$ OR $cut > V_{error})$ where the part in parenthesis establishes how reliable the variable is, if it isn't reliable, we keep the classification general.

The cutoff value c is an arbitrary choice; if it is too small, the whole spacetime is of type I; if it is large then it is of type O. No matter the cutoff value the order of transition between the Petrov types remains the same; we then choose the cutoff values as presented in Fig. (6.13) to emphasise this behaviour. The cutoff values are different at all stages as we disentangle leading order contributions.

Following this process, Fig. (6.14) shows the leading order spacetime on the x and $y = z$ plane throughout the simulation. Overall the simulation starts as an effective type O spacetime, that of FLRW, as all the inhomogeneities embodied in the invariant scalars are below the cutoff values; then the spacetime gradually transitions towards type I. This sort of peeling-off (D'Inverno, 1992; Alcubierre, 2008) goes as O $\rightarrow$ N $\rightarrow$ D $\rightarrow$ II $\rightarrow$ I, from most special to least special. In this transition, we pass through all these spacetime types, with notable features related to the OD structure.

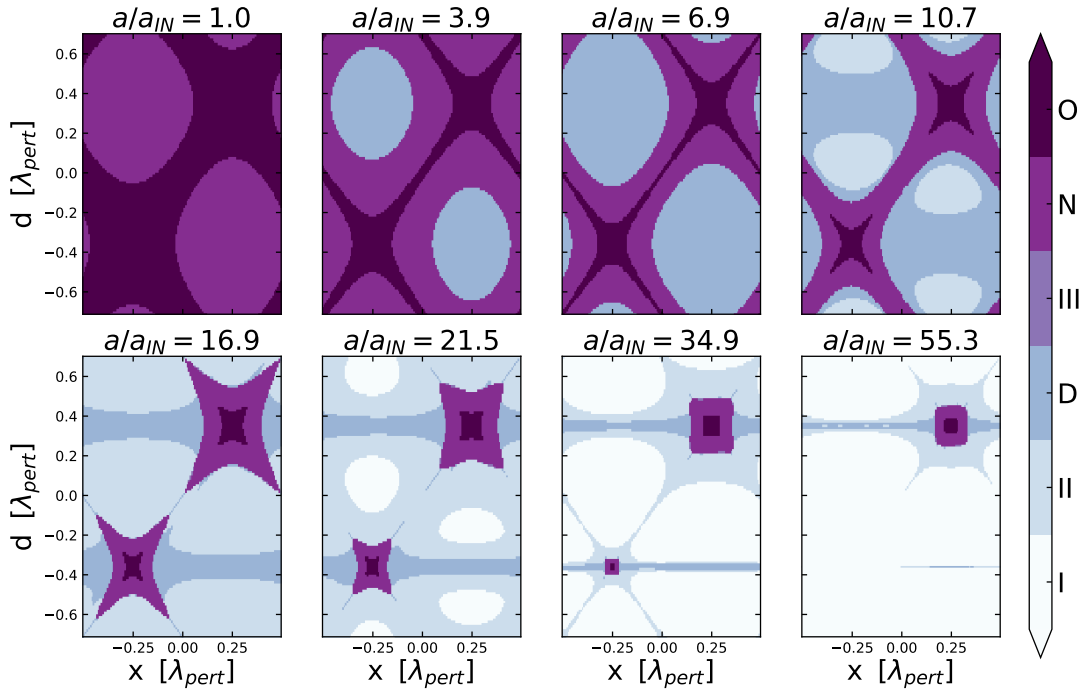

Figure 6.14: Classification of the spacetime regions according to the leading order Petrov type as defined in Fig. (6.13), along the x and $y = z$ plane of the simulation box (with $d^2 = y^2 + z^2$). Eight points in time in the simulation are presented, and the corresponding normalised scale factor is on top of each panel. The peak of the over-density is in the bottom left quadrant, at $x = -0.25\lambda_{pert}$ and $d \simeq -0.35\lambda_{pert}$, it is periodically connected to other over-densities with a filament along the $d \simeq -0.35\lambda_{pert}$ direction, and the bottom of the under-density is in the top right quadrant at $x = 0.25\lambda_{pert}$ and $d \simeq 0.35\lambda_{pert}$.

Throughout this evolution, the OD's peak and the UD's bottom are type O. These regions are conformally flat, which is not what we expected *a priori* from the peak of the OD. However, as we saw previously, in this location $|E| = |B| = 0$, therefore the spacetime is type O and the conformal curvature is constant like a local closed FLRW. Thus, this is another reason why the Top-Hat model describes the evolution of the peak of the OD very well.

Along the vertex direction, the transition goes as O $\rightarrow$ N $\rightarrow$ D. The focus of a D spacetime along the filament is interesting as this group includes the Schwarzschild, Kerr, and Szekeres metrics. The Weyl tensor of type D spacetimes has been described (Szekeres, 1965; D'Inverno, 1992) as a Coulomb-like tidal field, where the matter gets elongated in a given direction towards a gravitational source, see Section 2.5.4 for more details. Indeed, we find that along the filaments matter is being pulled towards the two OD peaks they connect.

Then, remarkably, we note the strong presence of type N, the spacetime of gravitational waves. A non-spherically symmetric collapse is naturally expected to generate gravitational waves; here, tensor modes have a temporary leading order presence. We leave the study of the generation of gravitational waves in nonlinear structure formation in full NR to future work.

6.4 Summary

This work presents NR simulations of a simple nonlinear inhomogeneous structure growing in a ΛCDM universe. The simulations are run with Einstein Toolkit (Löffler et al., 2012; Brandt et al., 2020) using the new publicly available `ICPertFLRW` thorn (Munoz, 2023a), then post-processed with our `EBWeyl` code (Munoz, 2022) described in Chapter 5 (Munoz and Bruni, 2023a). We have used the synchronous-comoving gauge, i.e. the rest frame of CDM, represented as a pressureless and irrotational perfect fluid.

Inhomogeneities are introduced with the comoving curvature perturbation $\mathcal{R}_c$, defined as a 3-dimensional sinusoidal. This creates a periodic lattice of over-densities (OD) connected by filaments and surrounded by under-dense (UD) voids. Near the peak of the OD, the matter distribution and other fields are close to spherical symmetry, but this is no longer the case further out, as the structure tends towards an octahedron-like symmetry, with OD filaments along the vertices.

We obtain three main results: *i)* using $\mathcal{R}_c$, a gauge-invariant curvature perturbation typically used in early universe perturbation theory (Malik and Wands, 2009), we successfully implement a purely growing mode in our initial conditions, following (Bruni, Hidalgo, Meures, et al., 2014; Bruni, Hidalgo, and Wands, 2014); in particular, we use $\mathcal{R}_c$ to set up our initial metric and extrinsic curvature inhomogeneity, the fully nonlinear 3-Ricci curvature ${}^{(3)}R$, then defining the fully nonlinear matter density field from the Hamiltonian constraint, which is then automatically satisfied; *ii)* we study the evolution of the peaks through turn-around and collapse, finding that it is very well described by the Top-Hat model, to a level better than 1%, see Table (6.1); *iii)* we study the Weyl tensor, both from the perspective of the electric and magnetic parts $E_{\alpha\beta}$ and $B_{\alpha\beta}$ and through a novel dynamical Petrov classification, finding that the gravito-magnetic effects are stronger around the filaments, and Petrov type N, the signature of gravitational waves, emerges in the directions connecting the OD peaks with the UD.

More in detail, the main points are the following.

- The configuration described above leaves us free to choose the initial amplitude and wavelength of the inhomogeneities, as well as the initial redshift. These are chosen such that initially, we are in the linear regime, and the simulation remains within the matter-dominated era (i.e. Λ is negligible), even if our treatment is fully nonlinear. Additionally, we identify the curvature-dominated regime, when the physical wavelength is larger than the Hubble scale, see Eq. (6.14). In this regime, the volume element is larger than the background in the OD region.

- Monitoring the peak of the OD we find that, in this specific location, the turn-around (TA) and collapse are reached when the linearly extrapolated density contrast $\delta^{(1)}$ has values $\delta^{(1)}_{TA} = 1.05584 \pm 8 \times 10^{-5}$ and $\delta^{(1)}_{C} = 1.676 \pm 2 \times 10^{-3}$ in the ΛCDM case, within 1% of the theoretically predicted values in the Top-Hat spherical and homogeneous collapse model (Sahni and Coles, 1995; Monaco, 1997; Peacock, 1999; Mo, Bosch, and White, 2010; Vittorio, 2018) see Section 4.3.2. We explain this by looking at the contribution of the different terms in the Raychaudhuri equation, finding that the shear is, in general, subdominant around the peak and totally negligible at the peak, so that in this location, the evolution is independent of its environment and in essence described by the Friedmann equations of a closed (positively curved)

model. Indeed, our analysis also shows that at the peak location $\gamma^{1/3(3)}R$ is constant in time, generalising into the fully nonlinear regime the conformal-curvature variable $\mathcal{R}_c$. However, when considering a comoving sphere with a large comoving radius, containing a more significant inhomogeneity, its evolution can no longer be well described with the Top-Hat model.

- The peak of the OD is the first location to reach TA when the expansion scalar reaches $\Theta = 0$, then the surface $\Theta = 0$ expands outward in the neighbouring region. This TA boundary distinguishes an infalling and an expanding region. The infalling region encompasses more and more material, eventually taking the shape of the entire OD region. In the direction where δ is the biggest, the TA radius increases the most, and in directions going through an UD region, the TA radius eventually stops growing and shrinks instead. These features are due to the inhomogeneous non-spherical shape we are working with.

- Filaments are a fundamental part of the cosmic web structure due to tidal fields (Bond, Kofman, and Pogosyan, 1996). In computing the electric and magnetic parts $E_{\alpha\beta}$ and $B_{\alpha\beta}$ of the Weyl tensor with `EBWeyl` (Munoz, 2022; Munoz and Bruni, 2023a), we find that $E_{\alpha\beta}$ is strongest along the filaments periodically connecting the ODs, stretching matter towards the OD centres, while $B_{\alpha\beta}$ wraps around the filaments. On average, the magnetic part is smaller than the electric part, changing the ratio from $< 10^{-2}$ to almost 10% during the evolution. The divergence of $E_{\alpha\beta}$ is stronger than $E_{\alpha\beta}$ itself, while the curl of $B_{\alpha\beta}$ is stronger than $B_{\alpha\beta}$. For both, the divergence is strongest towards the OD, and the curl of $E_{\alpha\beta}$ is strongest on the filaments while the curl of $B_{\alpha\beta}$ is strongest around them.

- We also use `EBWeyl` (Munoz, 2022; Munoz and Bruni, 2023a) to classify the spacetime as Petrov type I. However, introducing a novel dynamical Petrov classification using thresholds that define leading order contributions, we find that the centres of the OD and UD are of type O, i.e. conformally flat as an FLRW model at leading order. At the same time, the spacetime is type D along the filaments, representing a tidal stretching along these directions, and transition as O $\to$ N $\to$ III $\to$ II $\to$ I elsewhere, with a notable presence of type N, typical of gravitational waves.

7 - Future prospects

This work has brought about the creation of an initial conditions code for cosmological simulations in numerical relativity `ICPertFLRW`, and a post-processing code to invariantly characterise numerical spacetimes using the Weyl tensor `EBWeyl`. These tools allowed for creating and analysing numerical relativity simulations of a quasi-spherical cosmological collapse. Results showed that the Top-Hat spherical and homogeneous collapse model could be perceived as a robust approximation, that gravitational waves are generated in this process and that by gravito-electromagnetic analogy, filaments can be perceived as carrying a gravitational current. For further details on the conclusion, see Section 6.4. Going forward, we believe several interesting questions should be investigated as a follow-up to this work.

❖ **Collapsing structures:** We have confirmed that the Top-Hat collapse description is valid at the OD's peak, finding only a 1% difference. We believe this result is robust for profiles around the peak that tend to be spherically symmetric. Still, the analysis here should be extended in two directions: to model the effects of different quasi-spherical profiles on virialisation and to understand the effects of introducing some anisotropy at the peak, in particular, to measure how large the change of collapse time due to shear and vorticity would be, cf. (Lucie-Smith et al., n.d.).

✦ **Anisotropy:** Considering that close to the OD peaks and around UD voids, the spacetime is close to spherical symmetry, extending our work to look for self-similar behaviour (Bertschinger, 1985a,b; Jain and Bertschinger, 1996) would be interesting. Here, we have considered an over-simplified structure based on a single initial wavelength, going further with this or starting from a more complex structure, the effects of different wavelengths, mode-coupling during nonlinear evolution (Jain and Bertschinger, 1993) and the effects of very large-scale tidal fields (Schmidt et al., 2018) should be explored.

This study of collapsing structures in full GR could be further developed by considering the impact of the cosmological horizon, the cosmological constant, and mode coupling. To do this, the sinusoidal wavelength and initial redshift would be chosen accordingly, and multiple sinusoidal distributions would be added. These considerations have never been studied with full GR simulations when the gravitational collapse has to decouple from the otherwise expanding universe to collapse into forming a dark matter halo.

Related to this, we are also considering a structure that breaks the triaxial symmetry of the 3-dimensional sinusoidal, by changing the sinusoidal wavelength in one direction and two, with the goal of investigating the shear evolution at and around the peak of the OD. It is possible that the shear would be non-negligible in the central region and thus impact the formation of the pancakes

expected from the Newtonian generic tri-axial collapse. This is of particular interest as shear significantly contributes to gravito-magnetic effects. It is possible that the gravitational waves generated may backreact into bringing the structure around the peak to a more spherical distribution, therein partially changing the standard Newtonian picture of first shell crossing and pancakes.

Here we have neglected vorticity for the good reason that it vanishes for purely scalar first-order perturbations while it is typically sourced in the multi-stream regime following the first shell crossing (Pueblas and Scoccimarro, 2009), and it is a subdominant source for gravito-magnetic effects in N-body simulations (Bruni, Thomas, and Wands, 2014; Thomas, Bruni, and Wands, 2015; Barrera-Hinojosa, Li, Bruni, et al., 2021). A rough test-field estimate suggests that even if vorticity were initially present at the peak of the OD, its value at the last reliable step of our simulations would only be about twice its initial value. However, it would be interesting to study the effect of vorticity in detail using a more general gauge, cf. (Ellis, Bruni, and Hwang, 1990).

✦ **Virialisation:** While the central region of the OD in the simulation is well described by the top-hat spherical collapse model, such a structure would otherwise be expected to virialise. Yet the particle dynamics that should be present for the relaxation mechanism can't be described within the fluid approximation used in the Einstein Toolkit simulations, this needs to be extended (Magnall et al., 2023). Recently a relativistic particle code, GRAMSES, has been created (Barrera-Hinojosa and Li, 2020a), and it can address the shortcomings of the simulation run with Einstein Toolkit. It would then be worthwhile to run twin simulations, up to the first shell crossing, one with Einstein Toolkit and one with GRAMSES. Eventually, GRAMSES will be able to evolve simulations into the fully nonlinear multi-stream regime, describing the virialisation of the proto-halo. Additionally, while transverse deformations were identified to have a transitory but leading order role in the collapse evolution, Petrov type **N** in Fig. (6.14), GRAMSES does not evolve tensorial perturbations. Therefore, this would be a point of comparison to establish the presence of gravitational waves.

❖ **Initial conditions and approximations:** A modern concern in the era of precision cosmology is the issue of how best to set up initial conditions for large-scale structure simulations to optimise computational efficiency while maintaining the required modelling accuracy. Historically many approximations have been introduced to model quasi-linear stages (Sahni and Coles, 1995; Monaco, 1997), and more recently to consider relativistic effects (Fidler et al., 2016, 2017). Various quasi-linear relativistic approximations have been considered in the past (Matarrese, Pantano, and Saez, 1993, 1994b,a; Bruni, Matarrese, and Pantano, 1995a,b; Kofman and Pogosian, 1995; Hui and Bertschinger, 1996; Maartens, Ellis, and Siklos, 1997; Sopuerta, Maartens, et al., 1999) and more recently (Pareja and MacCallum, 2006; Ip and Schmidt, 2017; Heinesen and Macpherson, 2022); we believe that these should be further investigated to understand how to improve the setting up of initial conditions for the modelling of relativistic effects in nonlinear stages of structure formation, cf. (Quintana-Miranda, Monaco, and Tornatore, 2023).

❖ **Primordial Black Holes and Gravitational Waves:** A natural extension of my work so far will be to consider primordial black hole (PBH) formation during the radiation-dominated era, beyond spherical symmetry. Indeed, PBHs have been experiencing a renaissance in the last few years (Shibata and Sasaki, 1999; Hawke and Stewart, 2002; Yoo, Harada, and Okawa, 2020; de Jong, Aurrekoetxea, and Lim, 2022; Musco and Papanikolaou, 2022; de Jong, Aurrekoetxea, Lim, and França,

2023; Escrivà and Yoo, 2023). We could use Einstein Toolkit in tandem with the hydrodynamical and horizon-finder thorns as well as the inflation-inspired initial conditions of Section 6.1 based on the 3-curvature variable $\mathcal{R}_c$. Simulations of this kind would have two main goals: firstly, studying how breaking spherical symmetry changes the critical-density threshold for the formation of PBHs and their masses; secondly, invariantly studying the gravitation radiation that will necessarily be emitted in the non-spherical collapse, where `EBWeyl` would be relevant. This would be a worthwhile contribution to constraints on PBHs and gravitational wave predictions.

❖ **Gravito-electromagnetism:** `EBWeyl` could be applied to other cosmological simulations. We have demonstrated in Section 6.3.5 and Section 6.3.6 the wealth of information that this can provide and its potential contributions to the understanding of structure formation. We could apply this methodology to all future simulations described above, but eventually, `EBWeyl` could be applied to other more realistic simulations starting from a typical power spectrum, for instance, publicly available simulation data, since it is a post-processing code. Each simulation's properties may impact how the Weyl tensor evolves; despite this, the invariant nature of the decomposition will give a fair characterisation of the spacetime. Additionally, applying `EBWeyl` to simulations with a realistic distribution of large-scale structures would take this gravitational description one step forward from the idealistic lattice distribution of the universe used so far. This process of exploring spacetime would be further developed by considering the eigenvectors and eigenvalues of the electric and magnetic part of the Weyl tensor, which would complete the gravitational description of spacetime (Nichols et al., 2011). We also emphasise that the application of this code is not limited to simulations in full GR; it is also possible to extract gravito-magnetic information from simulations evolved with Newtonian gravity (Thomas, Bruni, and Wands, 2015; Barrera-Hinojosa, Li, Bruni, et al., 2021; Barrera-Hinojosa, Li, and Cai, 2021).

A - Finite Differencing test

To understand the limitations of the FD schemes, described in Section 3.6.1, we test them in 3 simple cases: a polynomial, a sinusoidal and an exponential, with both the 4^{th} and 6^{th} order schemes.

As seen in Fig. (A.1), the polynomial case is no challenge to the scheme, having a relative error of 10^{-14} and a rounding error increasing with a N^1 slope. This error does not originate from the FD approximation but from computing limitations, so the higher-order FD has a slightly higher error due to the additional operations. This error is reduced by increasing computing precision, as seen from 64bit to 128bit.

The sinusoidal case shows convergence according to the expected truncation error, so this benefits from increasing the FD order.

The same could be said of the exponential; however, the boundary points must be considered. Unless periodic boundary conditions can be applied, a combination of forward and backward FD schemes were used. Fig. (A.2) shows that the relative error of these different schemes can significantly differ for an exponential distribution. Indeed the left-most points (calculated with a forward scheme) and right-most points (backward scheme) have larger errors than the central ones computed with the centred scheme. The forward and backward schemes are of the same convergence order as the centred scheme but start with a higher relative error. In the right panel of Fig. (A.1), we then consider the case where these edge points are included (full lines) and when they are cut off (dash-dotted lines). In the first case, the order of convergence is higher at low resolution and tends towards the expected value at high resolution. This is because, as the resolution is increased, more points are computed with the centred scheme, whereas the same number of points are computed with the forward and backward scheme throughout. Then, excluding the boundary points reduces the initial relative error and allows it to follow the expected convergence explicitly. For the examples considered in Section 5.3.2, the edge points have then been excluded.

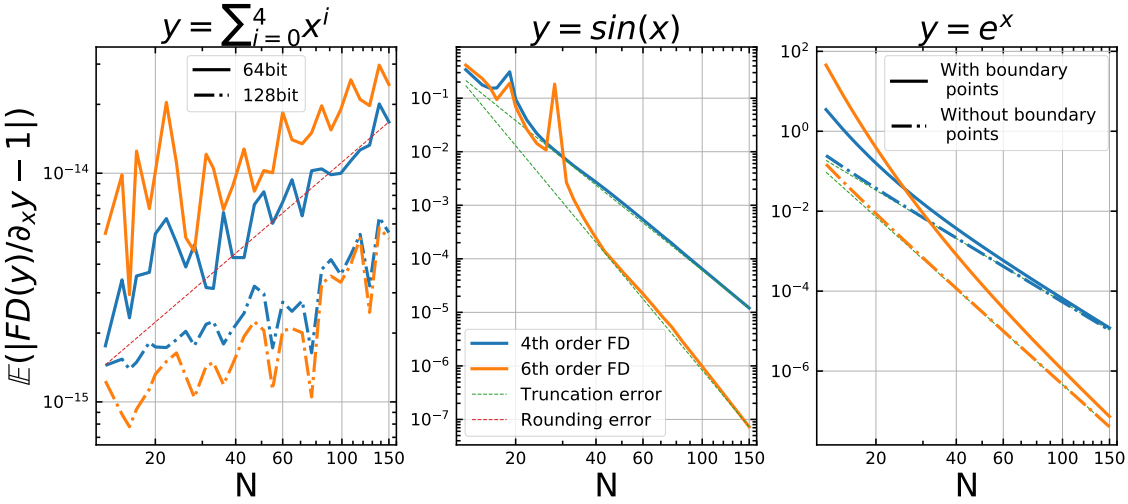

Figure A.1: Average relative error of the FD scheme applied to a polynomial, sinusoidal and exponential as a function of the N points in the data arrays. The FD uses a 4^{th} (blue) or 6^{th} (orange) order scheme. The dash-dotted lines on the left plot distinguish floating point precision, and on the right, they distinguish cases where the edge points calculated with forward and backward FD schemes are included or cut out.

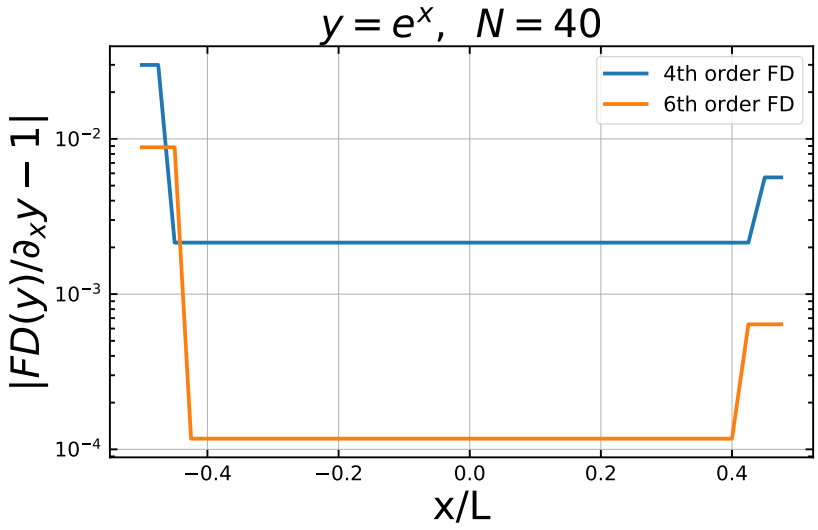

Figure A.2: Relative error of the FD scheme applied to an exponential distribution, for 4^{th} and 6^{th} order schemes and applied to a data array of 40 points.

B - Analytic expressions

The metric $g_{\alpha\beta}$, the extrinsic curvature $K_{\alpha\beta}$ and the energy-momentum tensor $T_{\alpha\beta}$ are passed to our codes in Chapter 5 in order to retrieve ${}^{(4)}R$, ${}^{(3)}R$, E^2, and B^2. The analytic expressions of $g_{\alpha\beta}$ have been presented in Section 5.2, then $K_{\alpha\beta}$ can easily be obtained from its time derivative $K_{\alpha\beta} = -\frac{1}{2}\partial_t g_{\alpha\beta}$ in the synchronous gauge, and we will present below the analytical expressions of $T_{\alpha\beta}$ for the different metrics. For the Λ-Szekeres, Bianchi II Collins-Stewart, and Bianchi IV Harvey and Tsoubelis metrics, the coordinates are comoving with the fluid, so the fluid velocity is $u^\alpha = \{1,\ 0,\ 0,\ 0\}$, and because this matches the normal to the hypersurfaces, we will drop the frame specific notation $\rho^{\{n\}} = \rho^{\{u\}} = \rho$. For the test-metric, $T_{\alpha\beta}$ is built from Einstein's equations; here, for simplicity, we choose to express this $T_{\alpha\beta}$ in the normal frame n^α. Finally, for the Bianchi VI Rosquist and Jantzen metric, although it describes a tilted perfect fluid, the different terms of $T_{\alpha\beta}$ are again expressed in the frame n^α: then, in this frame, the fluid no longer appears as that of a perfect fluid.

Then with Maple (Maplesoft, 2019), we have derived the expressions of ${}^{(4)}R$, ${}^{(3)}R$, E^2, and B^2 listed below. Here, an overhead dot, e.g. $\dot{v}$ means the proper time derivative of said variable v.

B.1 The Λ-Szekeres models of Barrow and Stein-Schabes

To help compute time derivatives of the metric in Section 5.2.1, we provide here the Hubble scalar

$$H = \frac{\dot{a}}{a} = H_0\sqrt{\Omega_{m0}a^{-3} + \Omega_{\Lambda 0}}. \tag{B.1}$$

The hypergeometric function in Eq. (5.6) is the result of the following integral

$$\int \frac{\sinh(\tau)}{\cosh(\tau)}d\tau = \frac{3}{5}\cosh(\tau)\frac{\sinh(\tau)^{5/3}}{\cosh(\tau)}{}_2F_1\left(\frac{5}{6},\ \frac{3}{2};\ \frac{11}{6};\ -\sinh(\tau)^2\right). \tag{B.2}$$

The Λ-Szekeres metric is a solution of Einstein's equations with dust and Λ: the energy-momentum tensor takes the form $T_{\alpha\beta} = \rho u_\alpha u_\beta$, with the energy density provided by Eq. (4.19) and Eq. (5.4). Then the Maplesoft (2019) results for this spacetime are:

$$\begin{aligned}
{}^{(3)}R &= -\frac{4v_1}{a^2 Z},\\
{}^{(4)}R &= {}^{(3)}R + 6\left(H^2 + \frac{\ddot{a}}{a}\right) + \frac{2}{Z}\left(4H\dot{Z} + \ddot{Z}\right),\\
E^2 &= \frac{(v_1+v_2)^2}{6a^4Z^2},\\
B^2 &= 0,
\end{aligned} \tag{B.3}$$

with $v_1 = \partial_x\partial_x Z = \partial_y\partial_y Z$, and $v_2 = a\dot{a}\dot{Z} + a^2\ddot{Z}$, and we use the property $\partial_x\partial_y Z = \partial_y\partial_x Z = 0$. In particular, here, the magnetic part of the Weyl tensor is null, $B_{\alpha\beta} = 0$, because $\partial_x\dot{Z} = \partial_y\dot{Z} = 0$.

Then we also have the invariants $I = E^2/2$ and $J = (E^2/6)^{3/2}$, confirming that $I^3 = 3^3J^2$: therefore this is a spacetime of special type. With the null vector base obtained by following the methodology of Section 2.5.2, we find the Weyl scalars

$$\Psi_\alpha = \{3\Psi_2,\ 0,\ \Psi_2,\ 0,\ 3\Psi_2\}, \tag{B.4}$$

with $\Psi_2^2 = E^2/24$. These are not built with the principal null direction, and, given their expressions, one can see that they can be further simplified. Indeed, the complex scalars are $K = N = 0$ and $L = 3\Psi_2^2$, confirming that we find this spacetime to be of Petrov type D, and we know that in this case, only Ψ_2 is non-zero, if built with the principal null directions. We demonstrate this through two tetrad rotations, see Section 2.5.2.1, first to make Ψ_0 vanish, such that the new scalars are

$$\tilde{\Psi}_\alpha = \{0,\ 0,\ -2\Psi_2,\ 3i\Psi_2,\ 3\Psi_2\}, \tag{B.5}$$

then to make the new $\tilde{\Psi}_4$ vanish, hence the final scalars are

$$\hat{\Psi}_\alpha = \{0,\ 0,\ -2\Psi_2,\ 0,\ 0\}. \tag{B.6}$$

This indeed leaves only $\hat{\Psi}_2 \neq 0$, and it has gained a factor of -2 through these rotations. This is the same result as Eq. (42) of (Meures and Bruni, 2011).

As expected, we have identified the spacetime to be of type D; however, should $E^2 = 0$, which is the case if $\beta_+ = 0$, then it would reduce to an FLRW metric, i.e. it would be of type O.

The Maple "PetrovType()" function will identify this spacetime as type I unless it is also provided with the following definition $Z(x, y, z, t) = 1 + \beta_+(z)\mathcal{F}(t) + \mathcal{A}\beta_+(z)(x^2 + y^2)$ (without needing to define β, $\mathcal{F}$ or $\mathcal{A}$), it then finds this spacetime to be of type D. For the other spacetimes, the classification we make by computing the invariants corroborates the classifications made by this function, where we only need to provide the metric as information.

B.2 A non-diagonal inhomogeneous test metric

With $\gamma = At(-2 + A^2t^2)$ the determinant of the spatial metric of Section 5.2.2, we find:

$$\begin{aligned}
{}^{(3)}R &= \frac{At^2}{2\gamma}\Big(t(\partial_z A)^2(2 + 3A^2t^2) - 4\gamma\partial_z\partial_z A\Big),\\
{}^{(4)}R &= \frac{A}{2\gamma^2}\Big((2 + 3A^2t^2)(-2A + t^3(\partial_z A)^2) - 4t^2\gamma\partial_z\partial_z A\Big),\\
E^{2\{n\}} &= \frac{1}{96\gamma^4}\Big(2A^4c_2^2\left(3A^2t^2 + 2\right) + c_2^2t^3(\partial_z A)^2\left(8A^3 + t(\partial_z A)^2\left(A^2t^2 + 3\right)\right)\\
&\quad + 4\gamma t^2\partial_z\partial_z A\left(4A^3c_2 + \left(A^2t^2 + 3\right)\left(c_2t(\partial_z A)^2 + \gamma\partial_z\partial_z A\right)\right)\Big)\\
B^{2\{n\}} &= \frac{5A^3t^3}{32\gamma^4}(\partial_z A)^2(2 + A^2t^2)^2,
\end{aligned} \tag{B.7}$$

where we simplify these expressions with the following substitution $c_2 = 2 - 3A^2t^2$.

Then using Einstein's equations we find $T_{\alpha\beta}$ for a non perfect fluid Eq. (2.41) (Ellis, Maartens, and MacCallum, 2012):

$$T_{\alpha\beta} = \rho^{\{n\}} n_\alpha n_\beta + p^{\{n\}} \gamma_{\alpha\beta} + 2q^{\{n\}}_{(\alpha} n_{\beta)} + \pi^{\{n\}}_{\alpha\beta}, \tag{B.8}$$

with the energy density $\rho^{\{n\}}$, pressure $p^{\{n\}}$, energy flux $q^{\{n\}}_\alpha$, and anisotropic pressure $\pi^{\{n\}}_{\alpha\beta}$ all expressed in the normal frame n^α. They can be identified following their definitions:

$$\begin{aligned}
\rho^{\{n\}} &= T^{\alpha\beta} n_\alpha n_\beta = \frac{At}{4\kappa\gamma^2}\Big(3A^2\gamma + t^2(\partial_z A)^2(2+3A^2t^2) - 4t\gamma\partial_z\partial_z A\Big), \\
p^{\{n\}} &= \frac{1}{3}\gamma_{\alpha\beta}T^{\alpha\beta}/3 \\
&= \frac{A}{12\kappa\gamma^2}\Big(4A + 3A^5t^4 + (2+3A^2t^2)(2A - t^3(\partial_z A)^2) + 4t^2\gamma\partial_z\partial_z A\Big), \\
q^{\{n\}}_\alpha &= -\gamma^\beta_\alpha T_{\beta\mu} n^\mu = \frac{At\partial_z A}{4\kappa\gamma^2}\Big(0,\ \ At(-6+A^2t^2),\ \ 2+A^2t^2,\ \ 2-7A^2t^2\Big), \\
\pi^{\{n\}}_{\alpha\beta} &= \gamma_{\alpha\mu}\gamma_{\beta\nu}T^{\mu\nu} - \frac{1}{3}\gamma_{\alpha\beta}\gamma_{\mu\nu}T^{\mu\nu} = \frac{1}{12\kappa\gamma^2}\begin{pmatrix} 0 & 0 & 0 & 0 \\ 0 & \pi_{xx} & \pi_{xy} & \pi_{xz} \\ 0 & \pi_{xy} & \pi_{yy} & \pi_{yz} \\ 0 & \pi_{xz} & \pi_{yz} & \pi_{zz} \end{pmatrix},
\end{aligned} \tag{B.9}$$

with the factorised components of $\pi^{\{n\}}_{\alpha\beta}$ expressed as below, with $c_1 = t^2(\partial_z A)^2(2-3A^2t^2) + 2t\gamma\partial_z\partial_z A$:

$$\begin{aligned}
\pi_{xx} &= 16A^3t + (3+A^2t^2)c_1 \\
\pi_{xy} &= A^2(4+3A^4t^4) + 4Atc_1 \\
\pi_{xz} &= A^2(4+3A^4t^4) + Atc_1 \\
\pi_{yy} &= 2A^3t(2+3A^2t^2) + (3+A^2t^2)c_1 \\
\pi_{yz} &= 6At(2-A^4t^2) + 3c_1 \\
\pi_{zz} &= 2A^3t(2+3A^2t^2) + (3-2A^2t^2)c_1.
\end{aligned} \tag{B.10}$$

Then, in computing the invariants to determine the Petrov type (too long to be included here), we find that I and J do not satisfy the requirements for this spacetime to be special, so it is of Petrov type I. Note that, should A be a constant along z, then ${}^{(3)}R = B^{2\{n\}} = 0$, and

$$I^3 - 27J^2 = \frac{A^{12}c_2^6}{2^{15}\gamma^{10}}. \tag{B.11}$$

Then, at the point in time where $c_2 = 0$, this spacetime would be of type O, with $E^{2\{n\}} = 0$.

B.3 Bianchi II Collins-Stewart

Here γ is the γ-law index of the perfect fluid, so the energy-stress tensor takes the form:

$$T_{\alpha\beta} = \rho^{\{u\}}((\gamma-1)g_{\alpha\beta} + \gamma u_\alpha u_\beta) \tag{B.12}$$

with $\rho^{\{u\}}$ given in Section 5.2.3. Then we obtain the following expressions:

$$\begin{aligned} {}^{(3)}R &= -\frac{s^2}{8\gamma^2 t^2} \\ {}^{(4)}R &= \frac{3\gamma^2 - 36\gamma + 44}{8\gamma^2 t^2} + {}^{(3)}R \\ E^2 &= \frac{(3\gamma-2)^2(5\gamma-6)^2}{384\gamma^4 t^4} \\ B^2 &= \frac{-3(\gamma-2)(3\gamma-2)^3}{128\gamma^4 t^4}. \end{aligned} \tag{B.13}$$

The only non-zero Weyl scalar is

$$\Psi_2 = \frac{(3\gamma-2)(6-5\gamma+3is)}{48\gamma^2 t^2}, \tag{B.14}$$

directly obtained with the scheme in Section 2.5.3, without further frame rotations. The invariants are then $I = 3\Psi_2^2$, $J = -\Psi_2^3$ and $K = L = N = 0$. Therefore this spacetime is of Petrov type D for both dust and radiation.

B.4 Bianchi VI tilted model

The spacetime from Section 5.2.4 has the following metric determinant $g = -k^2 t^{2(1+2s)}$, and we find the following expressions:

$$\begin{aligned} {}^{(3)}R &= \frac{-2}{k^2 t^2}, \\ {}^{(4)}R &= {}^{(3)}R + \frac{1}{2t^2}\Big(m^2c_1^2 + 4q^2 + 12s^2\Big), \\ E^{2\{n\}} &= \frac{1}{24k^4t^4}\Big[16 + 16k^2q^2\Big(-2 + k^2(q^2+3c_2^2)\Big) \\ &\quad + k^2m^2c_1^2\Big(16 + 4k^2m^2c_1^2 + k^2(11q^2 - 18qc_2 + 3c_2^2)\Big)\Big], \\ B^{2\{n\}} &= \frac{9m^2c_1^2 + 16c_2^2}{8k^2t^4}, \end{aligned} \tag{B.15}$$

where we use the parameter substitutions $c_1 = (q - s + 1)$ and $c_2 = (s - 1)$.

Although this spacetime follows a γ-law perfect fluid in a tilted frame, we work with the normal frame $n^\alpha = \{1,\ 0,\ 0,\ 0\}$, meaning that the stress-energy tensor takes the non-perfect fluid form, Eq. (2.41), with the following quantities:

$$\begin{aligned} \rho^{\{n\}} &= \frac{-1}{4\kappa k^2 t^2}\Big(4 + k^2(m^2c_1^2 + 4q^2 - 4s(s+2))\Big), \\ p^{\{n\}} &= \frac{1}{12k^2\kappa t^2}\Big(4 - k^2(3m^2c_1^2 + 12q^2 + 4s(5s-2))\Big), \\ q_\alpha^{\{n\}} &= \frac{-1}{2\kappa t}\Big(0,\ \ m^2c_1 + 4q,\ \ mc_1e^x/kt^{c_1},\ \ 0\Big), \\ \pi_{\alpha\beta}^{\{n\}} &= \frac{1}{6\kappa}\begin{pmatrix} 0 & 0 & 0 & 0 \\ 0 & \pi_{xx} & \pi_{xy} & 0 \\ 0 & \pi_{xy} & \pi_{yy} & 0 \\ 0 & 0 & 0 & \pi_{zz} \end{pmatrix}, \end{aligned} \tag{B.16}$$

with the factorised components to the anisotropic pressure:

$$\begin{aligned}
\pi_{xx} &= -8 - 8c_2k^2s + m^2(4 - k^2(-6c_2q + 3c_1^2m^2 + 3q^2 + 11s^2 - 14s + 3)),\\
\pi_{xy} &= \frac{me^x}{kt^{c_1}}(4 - k^2(3c_1^2m^2 + 3q^2 + 6q + 5s^2 - 8s + 3)),\\
\pi_{yy} &= \frac{e^{2x}}{k^2t^{2c_1}}(4 - k^2(3c_1^2m^2 + s(4c_1 + 8q))),\\
\pi_{zz} &= \frac{4t^{2(q+s-1)}}{k^2e^{2x}}(1 + k^2s(3q + s - 1)).
\end{aligned} \tag{B.17}$$

Computing the invariants, we find the spacetime to be of Petrov type I, in particular for $\gamma = 1.22$, $I^3 - 27J^2 \simeq 61.05t^{12}$.

B.5 Bianchi IV vacuum plane wave

As described by the title of this spacetime from Section 5.2.5, this is a vacuum solution, so $T_{\alpha\beta} = {}^{(4)}R = 0$, then we find ${}^{(3)}R = -2/t^2$, and $E^2 = B^2 = 1/2t^4$ and the complex scalars are all null: $I = J = K = L = N = 0$. Therefore this spacetime is of type N, as can be established by the Weyl scalars in the null principal direction $\Psi_\alpha = \{0,\ 0,\ 0,\ 0,\ t^{-2}\}$.

C - Constraints, error bars and convergence

The 3+1 decomposition of Einstein's field equations (Baumgarte and Shapiro, 2010) provide the Hamiltonian and momentum constraints, see Section 3.3.3:

$$\mathcal{H} = {}^{(3)}R + \frac{2}{3}K^2 - 2A^2 - 2\Lambda - 2\kappa\rho^{\{n\}} = 0, \quad \text{and} \quad \mathcal{M}^i = D_j^{\{n\}}\left(A^{ij} - \frac{2}{3}\gamma^{ij}K\right) - \kappa q^{\{n\}i} = 0, \tag{C.1}$$

with $q^{\{n\}i} = -\gamma^{ia}n^b T_{ab}$ the momentum density, and $D_j^{\{n\}}$ the spatial covariant derivative of γ_{ij}.

We estimate the accuracy of the initial conditions implemented by quantifying the violation of these constraints ($\mathcal{H}$ or $\mathcal{M}^i$) normalised with their relative energy scales (Mertens, Giblin, and Starkman, 2016; Macpherson, 2019):

$$[\mathcal{H}] = \left[\left({}^{(3)}R\right)^2 + \left(\frac{2}{3}K^2\right)^2 + \left(2A^2\right)^2 + \left(2\Lambda\right)^2 + \left(2\kappa\rho^{\{n\}}\right)^2\right]^{1/2}, \tag{C.2}$$

$$[\mathcal{M}] = \left[D_j^{\{n\}}(A^{ij})D_j^{\{n\}}(A_i^j) + \left(\frac{-2}{3}\right)^2 \gamma^{ij}D_j^{\{n\}}(K)D_i^{\{n\}}(K) + (-\kappa)^2 q^{\{n\}i}q_i^{\{n\}}\right]^{1/2}. \tag{C.3}$$

The momentum constraint is automatically satisfied at first order, so we first focus on the Hamiltonian constraint as presented in Fig. (C.1). This enables us to try different methods to set the initial conditions of the simulation and find the best approach.

Firstly, we consider pure FLRW simulations ($A_{pert} = 0$) in both the ΛCDM Eq. (4.29) and EdS Eq. (4.27) models. Their normalised $\mathcal{H}$, domain averaged over the whole simulation box, are presented as blue lines in Fig. (C.1). In both cases, we find a small error confirming these were implemented correctly.

Secondly, various methods of implementing the perturbation in the initial energy density are tried with $\rho^{\{n\}} = \rho_{IN}$. We show the impact of initially setting ρ_{IN} up to its first order as $\rho_{IN} = \bar{\rho}(1 + \delta^{(1)})$ using Eq. (6.4), this is the pink curve. Then, we show the impact of including higher order terms by defining ρ_{IN} with the Hamiltonian constraint Eq. (6.12), this is the dotted black line. Where all terms on the right-hand side of Eq. (6.12) are calculated in full from the definition of γ_{ij} and K_{ij}, Eq. (6.6) and Eq. (6.7). This shows a significant decrease in the initial error; this perturbation amplitude even matches the simulations without perturbations.

We highlight the importance of including the higher order terms consistently, with the purple dashed line, where ρ_{IN} is initially defined from the Hamiltonian constraint, but instead of being calculated in full from the metric, the 3-Ricci is provided using only the first order expression, Eq. (4.50). The error in the resulting simulation matches that of the simulation with only first-order terms. So

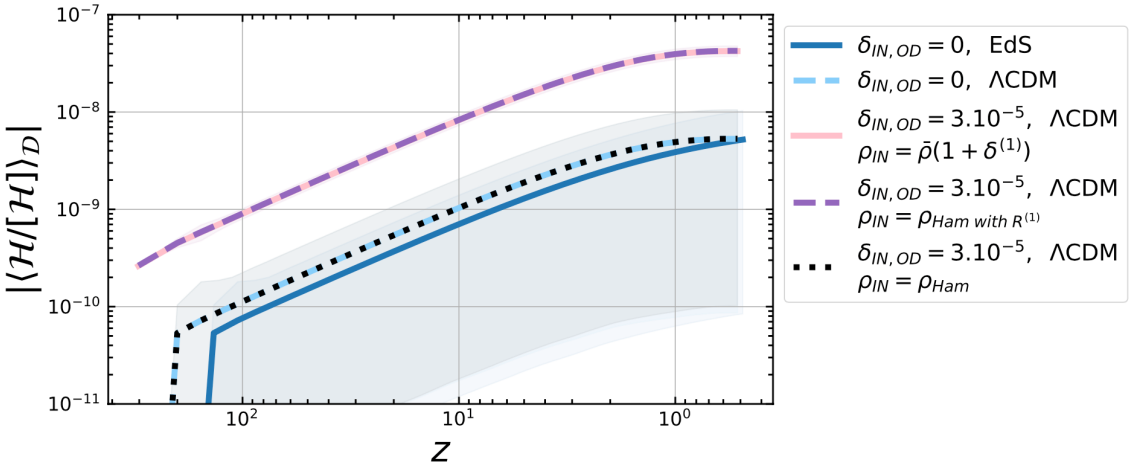

Figure C.1: Domain average violation to the Hamiltonian constraint normalised with its energy scale of 5 different simulations, versus the redshift z. The initial (IN) amplitude of density contrast δ at the peak of the over-density (OD) and the presence of Λ in the simulations is specified in the legend. When $\delta_{IN,\,OD} = 3 \times 10^{-5}$, the initial energy density can be defined as $\rho_{IN} = \bar{\rho}(1 + \delta^{(1)})$ (*pink full*), or as $\rho_{IN} = \rho_{Ham\ with\ R^{(1)}}$ (*purple dashed*) from the Hamiltonian constraint but with first order 3-Ricci scalar, Eq. (4.50). We find that a better definition is $\rho_{IN} = \rho_{Ham}$ (*black dotted*), calculated in full from the Hamiltonian constraint using the first order γ_{ij} and K_{ij}, Eq. (6.6) and Eq. (6.7), and the fully nonlinear 3-Ricci scalar of γ_{ij}. Here $\lambda_{pert} = 1821$Mpc and $z_{IN} = 302.5$ for ΛCDM initially and $\lambda_{pert} = 1206$Mpc and $z_{IN} = 205.4$ otherwise. Error bars, when visible, are indicated as shaded regions.

the best approach for our simulations corresponds to the dotted black line with ρ_{IN} obtained from the Hamiltonian constraint in full, which is what was used for this project.

The error bars on Fig. (C.1), and throughout, are obtained by using two other simulations of double grid size each, such that we have three simulations, each of 32^3, 64^3, and 128^3 data points. Consider the result $f_{\Delta x}$ from a simulation with grid size Δx; we have accompanying simulations of grid size $2\Delta x$ and $4\Delta x$ each having their respective solution $f_{2\Delta x}$ and $f_{4\Delta x}$. The error on $f_{\Delta x}$ is then (Alcubierre, 2008):

$$\epsilon_{\Delta x} = \frac{f_{2\Delta x} - f_{\Delta x}}{C - 1} \tag{C.4}$$

with the convergence

$$C = \frac{|f_{4\Delta x} - f_{2\Delta x}|}{|f_{2\Delta x} - f_{\Delta x}|} = 2^n \tag{C.5}$$

and n is the order of the FD approximation. Fourth-order schemes are used for the simulation evolution and in post-processing, see Section 3.6.1, Section 5.1.2 and Appendix A.

To check convergence in the simulations, we show in Fig. (C.2) the error in the normalised Hamiltonian and momentum constraints.

On the left panels, we plot their absolute value at different quartiles of the grid distribution, however this could be made more candid by tracking the evolution of the individual data points. Then, on the right, the average median is considered versus the resolution (Macpherson, Lasky, and Price, 2017), where the dashed lines correspond to the predicted truncation error from the FD schemes, that is $\propto N^{-n}$, indicative of the convergence order.

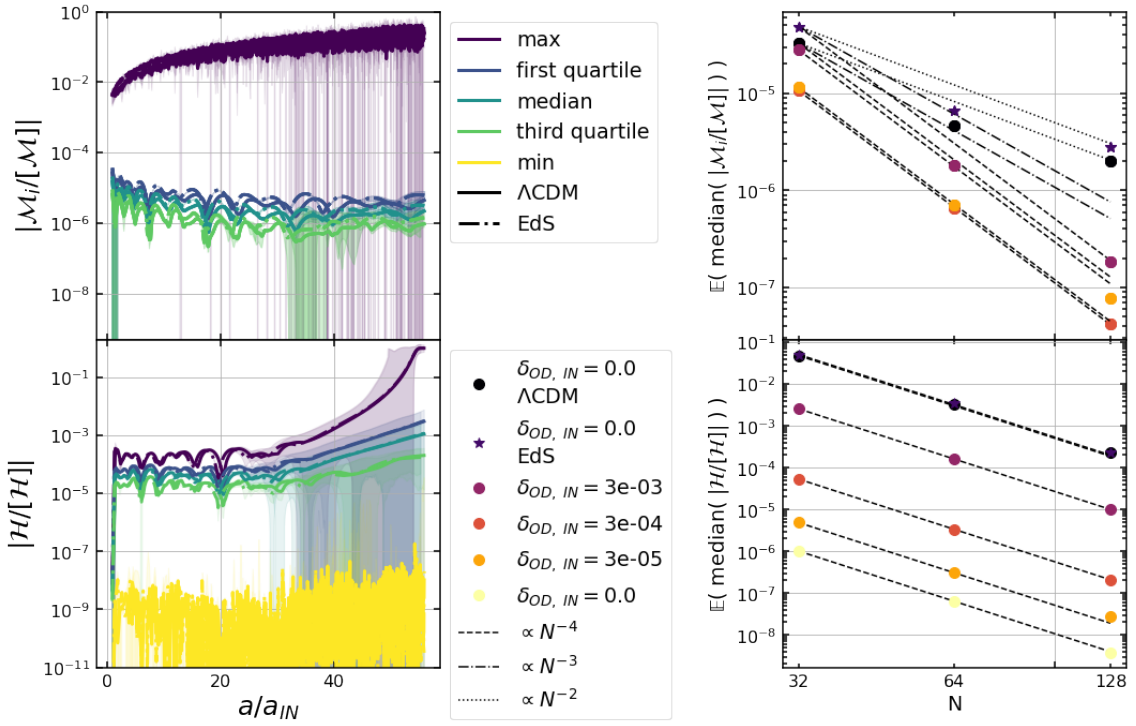

Figure C.2: *Left:* momentum (top) and Hamiltonian (bottom) constraint violation, normalised with their respective energy scale, measured at different quartiles of the data distribution during the evolution of the simulation. The simulation with Λ is indicated with full lines, while the one without is indicated with dot-dashed lines. The three momentum constraints $i = \{1,\ 2,\ 3\}$ are plotted with the same lines, but they are not distinguishable because they overlap. Error bars, when visible, are indicated as shaded regions. *Right:* average median of these constraints for simulations of different resolution (N^3 the number of data points) and amplitude of the initial (IN) density contrast at the peak of the over-density (OD) $\delta_{IN,\,OD}$. When perturbed, the energy density is initially fully defined from the Hamiltonian constraint. $\lambda_{pert} = 1821$Mpc and $z_{IN} = 302.5$ when $\Lambda \neq 0$ initially and $\lambda_{pert} = 1206$Mpc and $z_{IN} = 205.4$ otherwise.

For the Hamiltonian constraint, while the amplitude of the violation may increase as the perturbation amplitude increases, it continues to follow fourth-order convergence, as expected.

For the momentum constraint, while the same could be said for small perturbations, the top right panel of Fig. (C.2) shows a decreased convergence when $\delta_{IN,\,OD} = 0.03$. Indeed, the momentum constraint is only satisfied a first order, so in a nonlinear scenario, the solution tends towards a non-zero solution. However, the top left panel shows that while there is a violation of the momentum constraint, this does not grow throughout the simulation. The max curve may seem concerning, but this is because it is amplified by data points whose momentum energy scale is the numerical equivalent of zero; thus, the shape of the curve resembles numerical noise. In computing C, with Eq. (C.5), we find that the average convergence of the median of the normalised momentum constraint violation is $C \simeq 13.76$ for the case with Λ and $C \simeq 15.47$ for the case without, indicating that this solution has a $3.7 - 3.9$ order convergence towards a non-zero solution that does not grow during the simulation.

D - Numerically Integrating

The average of a scalar ϕ over a certain domain $\mathcal{D}^{\{n\}}$ on the hypersurface γ_{ij} is computed as:

$$\langle\phi\rangle_{\mathcal{D}^{\{n\}}} = \frac{\Delta x^3}{V} \sum_{\mathcal{D}^{\{n\}}} \phi\gamma^{1/2} \tag{D.1}$$

with γ the determinant of the spatial metric in our synchronous-comoving gauge and $\Delta x = \Delta y = \Delta z$ are the space coordinate intervals between grid points. V is the proper volume given by

$$V = \Delta x^3 \sum_{\mathcal{D}^{\{n\}}} \gamma^{1/2}. \tag{D.2}$$

The proper and comoving lengths along a grid line are calculated by

$$L_p = \Delta x \sum_{i=0}^{i_{max}} \gamma^{1/6} \qquad \text{and} \qquad L_c = \Delta x \sum_{i=0}^{i_{max}} 1, \tag{D.3}$$

since Δx is the comoving spatial coordinate element. In the background, the comoving length is related to the proper length simply by the scale factor: $L_p(t) = a(t)L_c$.

Computing L_p and L_c as in Eq. (D.3) is perfectly fine along the vertex direction because this direction is aligned with the grid. However, this is no longer the case in the face and edge directions, so a weighted integration is needed:

$$L_p = \Delta x \sum_{i=0}^{i_{max}} w\gamma^{1/6} \qquad \text{and} \qquad L_c = \Delta x \sum_{i=0}^{i_{max}} w \tag{D.4}$$

with the weight w in the range $0 \leqslant w \leqslant \sqrt{3}$. Each data point is in the centre of a cubic grid cell, so the value of this data point only applies to the section passing through this cell. $w\ \Delta x$ then represents the comoving length of the section contained in each cell. It is computed by finding the intersection between the integrated direction and the grid cells and then calculating the length between these intersection points.

On occasion, we integrate up to $K = 0$ see Section 6.3.3, or up to a given comoving radius see Section 6.3.4; in these cases, the last weight to be used is measured between the last intersection and this boundary point. In both these cases, the boundary point is found using a trilinear interpolation within this last cell.

The chosen averaging domain in Section 6.3.4 is a comoving sphere. Approximating a sphere on a grid can be done by only considering the grid points contained within the sphere; however, we refine this with a weighted integration:

$$\langle\phi\rangle_{\mathcal{D}^{\{n\}}} = \frac{\Delta x^3}{V} \sum_{\mathcal{D}^{\{n\}}} w\phi\gamma^{1/2} \qquad \text{and} \qquad V = \Delta x^3 \sum_{\mathcal{D}^{\{n\}}} w\gamma^{1/2}, \tag{D.5}$$

with $0 \leqslant w \leqslant 1$. Here $w\ \Delta x^3$ is the comoving volume of the part of the cubic grid cell that is included in the comoving sphere. The weight w is computed with the `sphereint` code (Munoz, 2023b), where the value of w depends on the number of cubic grid cell vertices contained in the sphere. If all eight are in the sphere $w = 1$, and if there are none $w = 0$. When the cell is partially within the sphere, we compute the intersecting points of the sphere and the cube edges, approximate the spherical boundary contained in the cube as a plane, and compute the volume of the corresponding geometrical shape. Most cases take the form of trirectangular tetrahedrons. That is clear when one cube vertex is in the sphere, but in other cases, the shape is extended to be a trirectangular tetrahedron, and then smaller trirectangular tetrahedrons are removed. When four cube vertices are in the sphere, there is a particular case where a truncated right square prism needs to be considered.

Bibliography

Abdalla, E. et al. (June 2022). "Cosmology intertwined: A review of the particle physics, astrophysics, and cosmology associated with the cosmological tensions and anomalies". In: *Journal of High Energy Astrophysics* 34, pp. 49–211. DOI: 10.1016/j.jheap.2022.04.002. arXiv: astro-ph/2203.06142 (cit. on pp. 48, 50).

Abramo, L. R. W., R. H. Brandenberger, and V. F. Mukhanov (Sept. 1997). "The Energy - momentum tensor for cosmological perturbations". In: *Physical Review D* 56.6, pp. 3248–3257. DOI: 10.1103/PhysRevD.56.3248. arXiv: gr-qc/9704037 (cit. on pp. 99, 102).

Acquaviva, V., N. Bartolo, S. Matarrese, and A. Riotto (Sept. 2003). "Gauge-invariant second-order perturbations and non-Gaussianity from inflation". In: *Nuclear Physics B* 667.1-2, pp. 119–148. DOI: 10.1016/s0550-3213(03)00550-9 (cit. on p. 93).

Adamek, J., C. Barrera-Hinojosa, M. Bruni, B. Li, H. J. Macpherson, and J. B. Mertens (July 2020). "Numerical solutions to Einstein's equations in a shearing-dust universe: a code comparison". In: *Classical and Quantum Gravity* 37.15, p. 154001. DOI: 10.1088/1361-6382/ab939b. arXiv: astro-ph/2003.08014 (cit. on pp. 65, 72, 73).

Adamek, J., C. Clarkson, D. Daverio, R. Durrer, and M. Kunz (Dec. 2018). "Safely smoothing spacetime: backreaction in relativistic cosmological simulations". In: *Classical and Quantum Gravity* 36.1, p. 014001. DOI: 10.1088/1361-6382/aaeca5. arXiv: astro-ph/1706.09309 (cit. on p. 61).

Adamek, J., C. Clarkson, R. Durrer, and M. Kunz (Feb. 2015). "Does small scale structure significantly affect cosmological dynamics?" In: *Physical Review Letter* 114.5, p. 051302. DOI: 10.1103/PhysRevLett.114.051302. arXiv: 1408.2741 (cit. on p. 60).

Adamek, J., D. Daverio, R. Durrer, and M. Kunz (Nov. 2013). "General relativistic N-body simulations in the weak field limit". In: *Physical Review D* 88.10, p. 103527. DOI: 10.1103/PhysRevD.88.103527. arXiv: astro-ph/1308.6524 (cit. on p. 42).

— (Mar. 2016a). "General relativity and cosmic structure formation". In: *Nature Physics* 12.4, pp. 346–349. DOI: 10.1038/nphys3673. arXiv: astro-ph/1509.01699 (cit. on pp. 72, 111).

— (July 2016b). "gevolution: a cosmological N-body code based on General Relativity". In: *Journal of Cosmology and Astroparticle Physics* 2016.7, pp. 53–53. DOI: 10.1088/1475-7516/2016/07/053. arXiv: astro-ph/1604.06065 (cit. on pp. 42, 72).

Adamek, J., R. Durrer, and M. Kunz (Nov. 2014). "N-body methods for relativistic cosmology". In: *Classical and Quantum Gravity* 31.23, p. 234006. DOI: 10.1088/0264-9381/31/23/234006. arXiv: 1408.3352 (cit. on p. 42).

Agazie, G. et al. (June 2023). "The NANOGrav 15 yr Data Set: Evidence for a Gravitational-wave Background". In: *The Astrophysical Journal Letters* 951.1, p. L8. DOI: 10.3847/2041-8213/acdac6. arXiv: astro-ph/2306.16213 (cit. on p. 2).

Alcubierre, M. (2008). *Introduction to 3+1 Numerical Relativity*. Oxford Science Publications. DOI: 10.1093/acprof:oso/9780199205677.001.0001 (cit. on pp. 10, 11, 19, 20, 24, 26, 29, 33, 34, 36, 38–41, 73, 76, 99, 100, 113, 129).

Alcubierre, M., G. Allen, B. Brügmann, E. Seidel, and W.-M. Suen (Nov. 2000). "Towards an understanding of the stability properties of the (3+1) evolution equations in General Relativity". In: *Physical Review D* 62.12, p. 124011. DOI: 10.1103/PhysRevD.62.124011. arXiv: gr-qc/9908079 (cit. on p. 38).

Alcubierre, M., A. de la Macorra, A. Diez-Tejedor, and J. M. Torres (2015). "Cosmological scalar field perturbations can grow". In: *Physical Review D* 92.6, p. 063508. DOI: 10.1103/PhysRevD.92.063508. arXiv: gr-qc/1501.06918 (cit. on p. 72).

Alcubierre, M. and M. D. Mendez (2011). "Formulations of the 3+1 evolution equations in curvilinear coordinates". In: *Gen. Rel. Grav.* 43, pp. 2769–2806. DOI: 10.1007/s10714-011-1202-x. arXiv: gr-qc/1010.4013 (cit. on p. 42).

Allnutt, J.A. (Nov. 1981). "A Petrov type-III perfect fluid solution of Einstein's equations". In: *General Relativity and Gravitation* 13.11, pp. 1017–1020. DOI: 10.1007/BF00756362 (cit. on p. 27).

Anderson, M., E. W. Hirschmann, S. L. Liebling, and D. Neilsen (Oct. 2006). "Relativistic MHD with adaptive mesh refinement". In: *Classical and Quantum Gravity* 23.22, p. 6503. DOI: 10.1088/0264-9381/23/22/025. arXiv: gr-qc/0605102 (cit. on p. 41).

Andrade, T. et al. (Dec. 2021). "GRChombo: An adaptable numerical relativity code for fundamental physics". In: *Journal of Open Source Software* 6.68, p. 3703. DOI: 10.21105/joss.03703. arXiv: gr-qc/2201.03458 (cit. on pp. 42, 72).

Angulo, R. E. and O. Hahn (Feb. 2022). "Large-scale dark matter simulations". In: *Living Reviews in Computational Astrophysics* 8.1. DOI: 10.1007/s41115-021-00013-z. arXiv: astro-ph/2112.05165 (cit. on p. 72).

Anninos, P. (Aug. 1998). "Plane-symmetric cosmology with relativistic hydrodynamics". In: *Physical Review D* 58.6, p. 064010. DOI: 10.1103/PhysRevD.58.064010 (cit. on pp. 33, 34).

Anninos, P., J. Massó, E. Seidel, W.-M. Suen, and J. Towns (Aug. 1995). "Three-dimensional numerical relativity: The evolution of black holes". In: *Physical Review D* 52.4, pp. 2059–2082. DOI: 10.1103/PhysRevD.52.2059 (cit. on p. 39).

Antoniadis, J. et al. (June 2023). *The second data release from the European Pulsar Timing Array III. Search for gravitational wave signals*. arXiv: astro-ph/2306.16214 (cit. on p. 2).

Arnowitt, R., S. Deser, and C. W. Misner (Dec. 1959). "Dynamical Structure and Definition of Energy in General Relativity". In: *Physical Review* 116.5, pp. 1322–1330. DOI: 10.1103/PhysRev.116.1322 (cit. on pp. 9, 29).

— (Aug. 2008). "Republication of: The dynamics of general relativity". In: *General Relativity and Gravitation* 40.9, pp. 1997–2027. DOI: 10.1007/s10714-008-0661-1 (cit. on pp. 73, 76, 100).

Aurrekoetxea, J. C., K. Clough, R. Flauger, and E. A. Lim (May 2020). "The Effects of Potential Shape on Inhomogeneous Inflation". In: *Journal of Cosmology and Astroparticle Physics* 2020.5, pp. 30–30. DOI: 10.1088/1475-7516/2020/05/030. arXiv: 1910.12547 (cit. on pp. 72, 91).

Aurrekoetxea, J. C., K. Clough, and E. A. Lim (July 2022). "CTTK: A new method to solve the initial data constraints in numerical relativity". arXiv: gr-qc/2207.03125 (cit. on p. 93).

Baiotti, L. and L. Rezzolla (Oct. 2006). "Challenging the paradigm of singularity excision in gravitational collapse". In: *Physical Review Letter* 97.14, p. 141101. DOI: 10.1103/PhysRevLett.97.141101. arXiv: gr-qc/0608113 (cit. on p. 40).

Baker, J. and M. Campanelli (Nov. 2000). "Making use of geometrical invariants in black hole collisions". In: *Physical Review D* 62.12, p. 127501. DOI: 10.1103/PhysRevD.62.127501. arXiv: gr-qc/0003031 (cit. on pp. 25, 26, 83).

Baker, J. G., J. Centrella, D.-I. Choi, M. Koppitz, and J. van Meter (2006). "Gravitational wave extraction from an inspiraling configuration of merging black holes". In: *Physical Review Letter* 96, p. 111102. DOI: 10.1103/PhysRevLett.96.111102. arXiv: gr-qc/0511103 (cit. on p. 41).

Bardeen, J. M. (Oct. 1980). "Gauge-invariant cosmological perturbations". In: *Physical Review D* 22.8, pp. 1882–1905. DOI: 10.1103/PhysRevD.22.1882 (cit. on pp. 64, 73).

Bardeen, J. M., P. J. Steinhardt, and M. S. Turner (Aug. 1983). "Spontaneous creation of almost scale-free density perturbations in an inflationary universe". In: *Physical Review D* 28.4, pp. 679–693. DOI: 10.1103/PhysRevD.28.679 (cit. on p. 93).

Barnes, A. (Sept. 2014). *Einstein Spacetimes with Constant Weyl Eigenvalues*. arXiv: gr-qc/1409.4300 (cit. on p. 25).

Barnes, A. and R. R. Rowlingson (July 1989). "Irrotational perfect fluids with a purely electric Weyl tensor". In: *Classical and Quantum Gravity* 6.7, pp. 949–960. DOI: 10.1088/0264-9381/6/7/003 (cit. on pp. 21, 81).

Barreira, A., C. Llinares, S. Bose, and B. Li (May 2016). "RAY-RAMSES: a code for ray tracing on the fly in N-body simulations". In: *Journal of Cosmology and Astroparticle Physics* 2016.05, pp. 001–001. DOI: 10.1088/1475-7516/2016/05/001. arXiv: astro-ph/1601.02012 (cit. on p. 72).

Barrera-Hinojosa, C. and B. Li (Jan. 2020a). "GRAMSES: a new route to general relativistic N-body simulations in cosmology. Part I. Methodology and code description". In: *Journal of Cosmology and Astroparticle Physics* 2020.1, p. 007. DOI: 10.1088/1475-7516/2020/01/007. arXiv: astro-ph/1905.08890 (cit. on pp. 42, 72, 118).

— (Apr. 2020b). "GRAMSES: a new route to general relativistic N-body simulations in cosmology. Part II. Initial conditions". In: *Journal of Cosmology and Astroparticle Physics* 2020.4, p. 056. DOI: 10.1088/1475-7516/2020/04/056. arXiv: astro-ph/2001.07968 (cit. on pp. 39, 42, 72).

Barrera-Hinojosa, C., B. Li, M. Bruni, and J. He (Jan. 2021). "Vector modes in ΛCDM: the gravitomagnetic potential in dark matter haloes from relativistic N-body simulations". In: *Monthly Notices of the Royal Astronomical Society* 501.4, pp. 5697–5713. DOI: 10.1093/mnras/staa4025. arXiv: astro-ph/2010.08257 (cit. on pp. 72, 74, 111, 118, 119).

Barrera-Hinojosa, C., B. Li, and Y-C. Cai (Dec. 2021). "Looking for a twist: probing the cosmological gravitomagnetic effect via weak lensing-kSZ cross-correlations". In: *Monthly Notices of the Royal Astronomical Society* 510.3, pp. 3589–3604. DOI: 10.1093/mnras/stab3657. arXiv: astro-ph/2109.02632 (cit. on pp. 72, 74, 111, 119).

Barrow, J. D. and J. Stein-Schabes (1984). "Inhomogeneous cosmologies with cosmological constant". In: *Physics Letters A* 103.6, pp. 315–317. DOI: 10.1016/0375-9601(84)90467-5 (cit. on pp. 74, 78, 81).

Bartolo, N., E. Komatsu, S. Matarrese, and A. Riotto (Nov. 2004). "Non-Gaussianity from inflation: Theory and observations". In: *Physics Reports* 402.3, pp. 103–266. DOI: 10.1016/j.physrep.2004.08.022. arXiv: astro-ph/0406398 (cit. on p. 62).

Baumgarte, T. W. and S. L. Shapiro (Dec. 1998). "Numerical integration of Einstein's field equations". In: *Physical Review D* 59.2, p. 024007. DOI: 10.1103/physrevd.59.024007. arXiv: gr-qc/9810065 (cit. on pp. 29, 36, 38, 100).

— (2010). *Numerical Relativity: Solving Einstein's Equations on the Computer*. Cambridge University Press. DOI: 10.1017/CBO9781139193344 (cit. on pp. 29, 31, 33–36, 99, 128).

Beetle, C. and L. M. Burko (Dec. 2002). "A Radiation scalar for numerical relativity". In: *Physical Review Letter* 89.27, p. 271101. DOI: 10.1103/PhysRevLett.89.271101. arXiv: gr-qc/0210019 (cit. on p. 27).

Bel, L. (Apr. 1958). "Définition d'une densité d'énergie et d'un état de radiation totale généralisée". In: *Comptes rendus hebdomadaires des séances de l'Académie des sciences Paris* 246.2. LINK, pp. 1015–1018 (cit. on p. 19).

Bentivegna, E. (Feb. 2017). "Automatically generated code for relativistic inhomogeneous cosmologies". In: *Physical Review D* 95.4, p. 044046. DOI: 10.1103/PhysRevD.95.044046. arXiv: gr-qc/1610.05198 (cit. on pp. 32–34, 91, 100).

Bentivegna, E. and M. Bruni (June 2016). "Effects of Nonlinear Inhomogeneity on the Cosmic Expansion with Numerical Relativity". In: *Physical Review Letter* 116.25, p. 251302. DOI: 10.1103/PhysRevLett.116.251302. arXiv: gr-qc/1511.05124 (cit. on pp. 42, 60, 72, 91, 96, 101, 103, 104).

Bentivegna, E., T. Clifton, J. Durk, M. Korzyński, and K. Rosquist (July 2018). "Black-hole lattices as cosmological models". In: *Classical and Quantum Gravity* 35.17, p. 175004. DOI: 10.1088/1361-6382/aac846. arXiv: gr-qc/1801.01083 (cit. on pp. 92, 112).

Bernardeau, F., S. Colombi, E. Gaztañaga, and R. Scoccimarro (Sept. 2002). "Large-scale structure of the Universe and cosmological perturbation theory". In: *Physics Reports* 367.1-3, pp. 1–248. DOI: 10.1016/S0370-1573(02)00135-7. arXiv: astro-ph/0112551 (cit. on p. 66).

Bernstein, D. H. (1993). "A Numerical Study of the Black Hole Plus Brill Wave Spacetime." PhD thesis. University of Illinois, Urbana-Champaign (cit. on p. 39).

Berti, E., V. Cardoso, and A. O. Starinets (July 2009). "Quasinormal modes of black holes and black branes". In: *Classical and Quantum Gravity* 26.16, p. 163001. DOI: 10.1088/0264-9381/26/16/163001. arXiv: gr-qc/0905.2975 (cit. on p. 62).

Berti, E., F. White, A. Maniopoulou, and M. Bruni (Apr. 2005). "Rotating neutron stars: an invariant comparison of approximate and numerical space–time models". In: *Monthly Notices of the Royal Astronomical Society* 358.3, pp. 923–938. ISSN: 0035-8711. DOI: 10.1111/j.1365-2966.2005.08812.x. arXiv: gr-qc/0405146 (cit. on pp. 27, 28).

Berti, E., K. Yagi, H. Yang, and N. Yunes (Apr. 2018). "Extreme Gravity Tests with Gravitational Waves from Compact Binary Coalescences: (II) Ringdown". In: *General Relativity and Gravitation* 50.5, p. 49. DOI: 10.1007/s10714-018-2372-6. arXiv: gr-qc/1801.03587 (cit. on p. 62).

Bertschinger, E. (May 1985a). "Self - similar secondary infall and accretion in an Einstein-de Sitter universe". In: *Astrophysical Journal Supplement Series* 58, p. 39. DOI: 10.1086/191028 (cit. on p. 117).

— (May 1985b). "Self-similar evolution of holes in an Einstein–de Sitter universe". In: *Astrophysical Journal Supplement Series* 58, p. 1. DOI: 10.1086/191027 (cit. on p. 117).

— (2000). *Cosmological Perturbation Theory and Structure Formation*. arXiv: astro-ph/0101009 (cit. on pp. 55, 56).

Bianchi, L. (1902). "Sui simboli a quattro indici e sulla curvatura di Riemann". In: *Atti della Accademia nazionale dei Lincei* 11 (5). LINK, pp. 3–7 (cit. on p. 9).

Bini, D., P. Carini, and R. T. Jantzen (Oct. 1995). "Relative observer kinematics in general relativity". In: *Classical and Quantum Gravity* 12.10, pp. 2549–2563. DOI: 10.1088/0264-9381/12/10/013 (cit. on pp. 19, 76).

Bini, D., A. Geralico, and R. T. Jantzen (Jan. 2023). "Petrov type I spacetime curvature: Principal null vector spanning dimension". In: *International Journal of Geometric Methods in Modern Physics* 20.5, p. 2350087. DOI: 10.1142/S0219887823500871. arXiv: gr-qc/2111.01283 (cit. on pp. 23, 25, 27, 61, 73).

Bolejko, K. (Dec. 2018). "Relativistic numerical cosmology with silent universes". In: *Classical and Quantum Gravity* 35.2, p. 024003. DOI: 10.1088/1361-6382/aa9d32. arXiv: astro-ph/1708.09143 (cit. on pp. 19, 42).

Bona, C., J. Massó, E. Seidel, and J. Stela (July 1995). "New Formalism for Numerical Relativity". In: *Physical Review Letter* 75.4, pp. 600–603. DOI: 10.1103/PhysRevLett.75.600 (cit. on p. 39).

Bond, J. R., L. Kofman, and D. Pogosyan (Apr. 1996). "How filaments are woven into the cosmic web". In: *Nature* 380, pp. 603–606. DOI: 10.1038/380603a0. arXiv: astro-ph/9512141 (cit. on p. 116).

Bondi, H. (Dec. 1947). "Spherically Symmetrical Models in General Relativity". In: *Monthly Notices of the Royal Astronomical Society* 107.5-6, pp. 410–425. DOI: 10.1093/mnras/107.5-6.410 (cit. on p. 71).

Bonnor, W. B. (Feb. 1995). "The electric and magnetic Weyl tensors". In: *Classical and Quantum Gravity* 12.2, pp. 499–502. DOI: 10.1088/0264-9381/12/2/018 (cit. on pp. 24, 73, 81, 111).

Bonnor, W. B. and W. Davidson (Sept. 1985). "Petrov type II perfect fluid spacetimes with vorticity". In: *Classical and Quantum Gravity* 2.5, pp. 775–780. DOI: 10.1088/0264-9381/2/5/017 (cit. on p. 27).

Bonvin, C., F. Lepori, S. Schulz, I. Tutusaus, J. Adamek, and P. Fosalba (June 2023). *A case study for measuring the relativistic dipole of a galaxy cross-correlation with the Dark Energy Spectroscopic Instrument*. arXiv: 2306.04213 (cit. on p. 2).

Boyle, M., D. Hemberger, et al. (Sept. 2019). "The SXS collaboration catalog of binary black hole simulations". In: *Classical and Quantum Gravity* 36.19, p. 195006. DOI: 10.1088/1361-6382/ab34e2. arXiv: 1904.04831 (cit. on p. 2).

Boyle, M., L. Lindblom, H. Pfeiffer, M. Scheel, and L. E. Kidder (2007). "Testing the accuracy and stability of spectral methods in numerical relativity". In: *Physical Review D* 75, p. 024006. DOI: 10.1103/PhysRevD.75.024006. arXiv: gr-qc/0609047 (cit. on p. 42).

Braden, J., M. C. Johnson, H. V. Peiris, and A. Aguirre (July 2017). "Constraining cosmological ultralarge scale structure using numerical relativity". In: *Physical Review D* 96.2, p. 023541. DOI: 10.1103/PhysRevD.96.023541. arXiv: astro-ph/1604.04001 (cit. on p. 72).

Brandenberger, R. H. (Oct. 2002). *Back Reaction of Cosmological Perturbations and the Cosmological Constant Problem*. DOI: 10.48550/ARXIV.HEP-TH/0210165. arXiv: hep-th/0210165 (cit. on pp. 99, 102).

Brandt, S. R. et al. (May 2020). "The Einstein Toolkit". LINK. DOI: 10.5281/zenodo.3866075 (cit. on pp. 41, 91, 92, 100, 115).

Brans, C. H. (Jan. 1965). "Invariant Approach to the Geometry of Spaces in General Relativity". In: *Journal of Mathematical Physics* 6.1, pp. 94–102. DOI: 10.1063/1.1704268 (cit. on p. 23).

Brown, D., P. Diener, O. Sarbach, E. Schnetter, and M. Tiglio (Feb. 2009). "Turduckening black holes: An analytical and computational study". In: *Physical Review D* 79.4, p. 044023. DOI: 10.1103/PhysRevD.79.044023. arXiv: gr-qc/0809.3533 (cit. on p. 100).

Brügmann, B. (1999). "Binary black hole mergers in 3-d numerical relativity". In: *International Journal of Modern Physics D* 8, p. 85. DOI: 10.1142/S0218271899000080. arXiv: gr-qc/9708035 (cit. on p. 41).

Bruni, M. (1991). "Covariant and gauge-invariant cosmological perturbations". PhD thesis. SISSA, Trieste (cit. on pp. 10, 13, 16, 33, 51, 55).

Bruni, M., P. K. S. Dunsby, and G. F. R. Ellis (Aug. 1992). "Cosmological perturbations and the physical meaning of gauge invariant variables". In: *The Astrophysical Journal* 395.Aug, pp. 34–53. DOI: 10.1086/171629 (cit. on pp. 14, 19, 63, 64, 73, 76, 93).

Bruni, M., G. F. R. Ellis, and P. K. S. Dunsby (Apr. 1992). "Gauge-invariant perturbations in a scalar field dominated universe". In: *Classical and Quantum Gravity* 9.4, pp. 921–946. DOI: 10.1088/0264-9381/9/4/010 (cit. on p. 63).

Bruni, M., L. Gualtieri, and C. F. Sopuerta (Jan. 2003). "Two-parameter nonlinear spacetime perturbations: Gauge transformations and gauge invariance". In: *Classical and Quantum Gravity* 20.3, pp. 535–556. DOI: 10.1088/0264-9381/20/3/310. arXiv: gr-qc/0207105 (cit. on p. 62).

Bruni, M., J. C. Hidalgo, N. Meures, and D. Wands (Mar. 2014). "Non-Gaussian initial conditions in ΛCDM: Newtonian, relativistic, and primordial contributions". In: *The Astrophysical Journal* 785.1, p. 2. DOI: 10.1088/0004-637X/785/1/2. arXiv: astro-ph/1307.1478 (cit. on pp. 55, 57, 58, 62, 65, 79, 91, 93–95, 102, 115).

Bruni, M., J. C. Hidalgo, and D. Wands (Sept. 2014). "Einstein's signature in cosmological large-scale structure". In: *The Astrophysical Journal Letters* 794.1, p. L11. DOI: 10.1088/2041-8205/794/1/L11. arXiv: astro-ph/1405.7006 (cit. on pp. 79, 91, 93, 94, 102, 115).

Bruni, M., R. Maartens, and C. G. Tsagas (Jan. 2003). "Magnetic field amplification in CDM anisotropic collapse". In: *Monthly Notices of the Royal Astronomical Society* 338, p. 785. DOI: 10.1046/j.1365-8711.2003.06095.x. arXiv: astro-ph/0208126 (cit. on p. 71).

Bruni, M., S. Matarrese, S. Mollerach, and S. Sonego (Sept. 1997). "Perturbations of space-time: Gauge transformations and gauge invariance at second order and beyond". In: *Classical and Quantum Gravity* 14.9, pp. 2585–2606. DOI: 10.1088/0264-9381/14/9/014. arXiv: gr-qc/9609040 (cit. on p. 62).

Bruni, M., S. Matarrese, and O. Pantano (Mar. 1995a). "A Local view of the observable universe". In: *Physical Review Letter* 74.11, pp. 1916–1919. DOI: 10.1103/PhysRevLett.74.1916. arXiv: astro-ph/9407054 (cit. on p. 118).

— (June 1995b). "Dynamics of silent universes". In: *The Astrophysical Journal* 445, pp. 958–977. DOI: 10.1086/175755. arXiv: astro-ph/9406068 (cit. on pp. 19, 118).

Bruni, M. and S. Sonego (Jan. 1999). "Observables and gauge invariance in the theory of nonlinear spacetime perturbations". In: *Classical and Quantum Gravity* 16.7, pp. L29–L36. DOI: 10.1088/0264-9381/16/7/101. arXiv: gr-qc/9906017 (cit. on pp. 62, 65).

Bruni, M., D. B. Thomas, and D. Wands (Feb. 2014). "Computing General Relativistic effects from Newtonian N-body simulations: Frame dragging in the post-Friedmann approach". In: *Physical Review D* 89.4, p. 044010. DOI: 10.1103/PhysRevD.89.044010. arXiv: astro-ph/1306.1562 (cit. on pp. 72, 74, 111, 118).

Buchert, T., H. van Elst, and A. Heinesen (Dec. 2023). "The averaging problem on the past null cone in inhomogeneous dust cosmologies". In: *General Relativity and Gravitation* 55.1, p. 7. DOI: 10.1007/s10714-022-03051-x. arXiv: gr-qc/2202.10798 (cit. on p. 65).

Buchert, T. and S. Räsänen (2012). "Backreaction in Late-Time Cosmology". In: *Annual Review of Nuclear and Particle Science* 62.1, pp. 57–79. DOI: 10.1146/annurev.nucl.012809.104435. arXiv: astro-ph/1112.5335 (cit. on pp. 59, 60).

Bull, P. et al. (June 2016). "Beyond ΛCDM: Problems, solutions, and the road ahead". In: *Physics of the Dark Universe* 12, pp. 56–99. DOI: 10.1016/j.dark.2016.02.001. arXiv: astro-ph/1512.05356 (cit. on p. 2).

Campanelli, M. and C. O. Lousto (May 1999). "Second order gauge invariant gravitational perturbations of a Kerr black hole". In: *Physical Review D* 59.12, p. 124022. DOI: 10.1103/PhysRevD.59.124022. arXiv: gr-qc/9811019 (cit. on p. 62).

Campanelli, M., C. O. Lousto, and Y. Zlochower (Apr. 2009). "Algebraic classification of numerical spacetimes and black-hole-binary remnants". In: *Physical Review D* 79.8, p. 084012. DOI: 10.1103/PhysRevD.79.084012. arXiv: gr-qc/0811.3006 (cit. on p. 92).

Carminati, J. and R. G. McLenaghan (Nov. 1991). "Algebraic invariants of the Riemann tensor in a four-dimensional Lorentzian space". In: *Journal of Mathematical Physics* 32.11, pp. 3135–3140. DOI: 10.1063/1.529470 (cit. on pp. 23, 73).

Cartan, E. (1946). *Leçons sur la Geometrie des Espaces de Riemann*. LINK. Gauthier-Villars, Paris (cit. on p. 23).

Chandrasekhar, S. (1992). *The Mathematical Theory of Black Holes*. Oxford University Press (cit. on pp. 26, 28, 70).

Chaurasia, S. V., T. Dietrich, and S. Rosswog (2021). "Black hole-neutron star simulations with the BAM code: First tests and simulations". In: *Physical Review D* 104.8, p. 084010. DOI: 10.1103/PhysRevD.104.084010. arXiv: gr-qc/2107.08752 (cit. on p. 41).

Cheong, P. C.-K., A. T.-L. Lam, H. H.-Y. Ng, and T. G. F. Li (2021). "Gmunu: paralleled, grid-adaptive, general-relativistic magnetohydrodynamics in curvilinear geometries in dynamical space –times". In: *Monthly Notices of the Royal Astronomical Society* 508.2, pp. 2279–2301. DOI: 10.1093/mnras/stab2606. arXiv: 2012.07322 (cit. on p. 42).

Cherubini, C., D. Bini, M. Bruni, and Z. Perjes (Oct. 2004). "Petrov classification of perturbed spacetimes: The Kasner example". In: *Classical and Quantum Gravity* 21.21, pp. 4833–4843. DOI: 10.1088/0264-9381/21/21/006. arXiv: gr-qc/0404075v1 (cit. on p. 21).

Cheung, M. H-Y. et al. (Feb. 2023). "Nonlinear effects in black hole ringdown". In: *Physical Review Letter* 130.8, p. 081401. DOI: 10.1103/PhysRevLett.130.081401. arXiv: gr-qc/2208.07374 (cit. on p. 62).

Choquet-Bruhat, Y (2015). *Introduction to General Relativity, Black Holes, and Cosmology*. Oxford University Press (cit. on p. 76).

Christoffel, E. B. (1869). "Ueber die Transformation der homogenen Differentialausdrücke zweiten Grades". In: *Journal für die reine und angewandte Mathematik*. LINK, p. 46 (cit. on p. 8).

Clarkson, C. A. (Dec. 2004). "Density fluctuations and gravity waves: A Covariant approach to gauge - invariant non-linear cosmological perturbation theory". In: *Physical Review D* 70.12. [Erratum: Phys.Rev.D 70, 129902 (2004)], p. 103524. DOI: 10.1103/PhysRevD.70.129902. arXiv: astro-ph/0311505 (cit. on p. 62).

Clausius, R. (1870). "XVI. On a mechanical theorem applicable to heat". In: *The London, Edinburgh, and Dublin Philosophical Magazine and Journal of Science* 40.265, pp. 122–127. DOI: 10.1080/14786447008640370 (cit. on p. 68).

Clifton, T., D. Gregoris, and K. Rosquist (Jan. 2017). "The magnetic part of the Weyl tensor, and the expansion of discrete universes". In: *General Relativity and Gravitation* 49.2, p. 30. DOI: 10.1007/s10714-017-2192-0. arXiv: gr-qc/1607.00775 (cit. on p. 74).

Clough, K., P. Figueras, H. Finkel, M. Kunesch, E. A. Lim, and S. Tunyasuvunakool (Dec. 2015). "GRChombo: Numerical relativity with adaptive mesh refinement". In: *Classical and Quantum Gravity* 32.24, p. 245011. DOI: 10.1088/0264-9381/32/24/245011. arXiv: gr-qc/1503.03436 (cit. on p. 42).

Clough, K. and E. A. Lim (2016). *Critical Phenomena in Non-spherically Symmetric Scalar Bubble Collapse*. arXiv: gr-qc/1602.02568 (cit. on p. 72).

Clough, K., E. A. Lim, B. S. DiNunno, W. Fischler, R. Flauger, and S. Paban (Sept. 2017). "Robustness of Inflation to Inhomogeneous Initial Conditions". In: *Journal of Cosmology and Astroparticle Physics* 2017.09, p. 025. DOI: 10.1088/1475-7516/2017/09/025. arXiv: hep-th/1608.04408 (cit. on pp. 72, 93).

Coley, A., J. M. Peters, and E. Schnetter (July 2021). "Geometric horizons in binary black hole mergers". In: *Classical and Quantum Gravity* 38.17, 17LT01. DOI: 10.1088/1361-6382/ac10ed. arXiv: gr-qc/2108.04210 (cit. on pp. 25, 26).

Collins, C. B. and J. M. Stewart (Sept. 1971). "Qualitative Cosmology". In: *Monthly Notices of the Royal Astronomical Society* 153.4, pp. 419–434. DOI: 10.1093/mnras/153.4.419 (cit. on p. 80).

Corman, M. and W. E. East (Dec. 2022). "Starting inflation from inhomogeneous initial conditions with momentum". arXiv: gr-qc/2212.04479 (cit. on p. 93).

D'Inverno, R. (1992). *Introducing Einstein's Relativity*. Oxford University Press (cit. on pp. 5, 113, 114).

D'Inverno, R. and R. Russell-Clark (Oct. 1971). "Classification of the Harrison metrics". In: *Journal of Mathematical Physics* 12.7, pp. 1258–1263. DOI: 10.1063/1.1665729 (cit. on pp. 23, 25, 26, 73).

Danehkar, A. (Aug. 2009). "On the Significance of the Weyl Curvature in a Relativistic Cosmological Model". In: *Modern Physics Letters A* 24, pp. 3113–3127. DOI: 10.1142/S0217732309032046. arXiv: physics.gen-ph/0707.2987 (cit. on p. 19).

— (June 2022). "Covariant Evolution of Gravitoelectromagnetism". In: *Universe* 8.6, p. 318. DOI: 10.3390/universe8060318. arXiv: gr-qc/2206.13946 (cit. on p. 19).

Darmois, G. (1927). *Les équations de la gravitation einsteinienne*. LINK. Gauthier-Villars, Paris (cit. on pp. 29, 38).

Daszuta, B., F. Zappa, W. Cook, D. Radice, S. Bernuzzi, and V. Morozova (2021). "GR-Athena++: Puncture Evolutions on Vertex-centered Oct-tree Adaptive Mesh Refinement". In: *Astrophys. J. Supp.* 257.2, p. 25. DOI: 10.3847/1538-4365/ac157b. arXiv: gr-qc/2101.08289 (cit. on p. 41).

Davis, T. M. and C. H. Lineweaver (2004). "Expanding Confusion: Common Misconceptions of Cosmological Horizons and the Superluminal Expansion of the Universe". In: *Publications of the Astronomical Society of Australia* 21.1, pp. 97–109. DOI: 10.1071/AS03040. arXiv: astro-ph/0310808 (cit. on p. 50).

de Jong, E., J. C. Aurrekoetxea, and E. A. Lim (Mar. 2022). "Primordial black hole formation with full numerical relativity". In: *Journal of Cosmology and Astroparticle Physics* 03.03, p. 029. DOI: 10.1088/1475-7516/2022/03/029. arXiv: 2109.04896 (cit. on p. 118).

de Jong, E., J. C. Aurrekoetxea, E. A. Lim, and T. França (June 2023). *Spinning primordial black holes formed during a matter-dominated era*. arXiv: 2306.11810 (cit. on p. 118).

de Sitter, W. (Nov. 1917). "On Einstein's Theory of Gravitation and its Astronomical Consequences. Third Paper." In: *Monthly Notices of the Royal Astronomical Society* 78.1, pp. 3–28. DOI: 10.1093/mnras/78.1.3 (cit. on p. 54).

Di Valentino, E., O. Mena, S. Pan, L. Visinelli, W. Yang, A. Melchiorri, D. F. Mota, A. G. Riess, and J. Silk (July 2021). "In the realm of the Hubble tension — a review of solutions". In: *Classical and Quantum Gravity* 38.15, p. 153001. DOI: 10.1088/1361-6382/ac086d. arXiv: astro-ph/2103.01183 (cit. on pp. 48, 50).

Dunsby, P. K. S., M. Bruni, and G. F. R. Ellis (Aug. 1992). "Covariant Perturbations in a multifluid cosmological medium". In: *The Astrophysical Journal* 395, pp. 54–73. DOI: 10.1086/171630 (cit. on pp. 14, 64, 93).

Eardley, D. M. and L. Smarr (Apr. 1979). "Time functions in numerical relativity: Marginally bound dust collapse". In: *Physical Review D* 19.8, pp. 2239–2259. DOI: 10.1103/PhysRevD.19.2239 (cit. on p. 38).

East, W. E., F. Pretorius, and B. C. Stephens (June 2012). "Hydrodynamics in full general relativity with conservative adaptive mesh refinement". In: *Physical Review D* 85.12, p. 124010. DOI: 10.1103/physrevd.85.124010. arXiv: gr-qc/1112.3094 (cit. on pp. 42, 72).

East, W. E., R. Wojtak, and T. Abel (Feb. 2018). "Comparing fully general relativistic and Newtonian calculations of structure formation". In: *Physical Review D* 97.4, p. 043509. DOI: 10.1103/PhysRevD.97.043509. arXiv: astro-ph/1711.06681 (cit. on pp. 72, 73, 91, 101, 103, 105).

East, W. E., R. Wojtak, and F. Pretorius (Nov. 2019). "Einstein-Vlasov Calculations of Structure Formation". In: *Physical Review D* 100.10, p. 103533. DOI: 10.1103/PhysRevD.100.103533. arXiv: astro-ph/1908.05683 (cit. on pp. 42, 72, 73, 101).

Einstein, A. (May 1916). "The Foundation of the General Theory of Relativity". In: *Annalen der Physik* 49. LINK, pp. 769–822 (cit. on pp. 1, 5, 12).

Einstein, A. (Feb. 1917). "Cosmological Considerations in the General Theory of Relativity". In: *Sitzungsberichte der Königlich Preußischen Akademie der Wissenschaften (Berlin)*. LINK, pp. 142–152 (cit. on pp. 12, 48, 54).

Einstein, A. and W. de Sitter (1932). "On the Relation between the Expansion and the Mean Density of the Universe". In: *Proceedings of the National Academy of Sciences* 18.3, pp. 213–214. DOI: 10.1073/pnas.18.3.213 (cit. on p. 55).

Einstein Toolkit (n.d.). URL: https://www.einsteintoolkit.org/ (cit. on pp. 41, 100).

Ellis, G. F. R. (Mar. 2009). "Republication of: Relativistic cosmology". In: *General Relativity and Gravitation* 41.3, pp. 581–660. DOI: 10.1007/s10714-009-0760-7 (cit. on pp. 13, 14, 19, 73, 92, 109).

Ellis, G. F. R. and M. Bruni (Sept. 1989). "Covariant and gauge-invariant approach to cosmological density fluctuations". In: *Physical Review D* 40.6, pp. 1804–1818. DOI: 10.1103/PhysRevD.40.1804 (cit. on pp. 63, 73, 93).

Ellis, G. F. R., M. Bruni, and J. Hwang (Aug. 1990). "Density Gradient - Vorticity Relation in Perfect Fluid Robertson-Walker Perturbations". In: *Physical Review D* 42.4, pp. 1035–1046. DOI: 10.1103/PhysRevD.42.1035 (cit. on pp. 15, 118).

Ellis, G. F. R. and H. van Elst (1999). "Cosmological models: Cargese lectures 1998". In: *NATO Science Series C* 541, pp. 1–116. DOI: 10.1007/978-94-011-4455-1_1. arXiv: gr-qc/9812046 (cit. on pp. 14, 109).

Ellis, G. F. R., R. Maartens, and M. A. H. MacCallum (2012). *Relativistic Cosmology*. Cambridge University Press. DOI: 10.1017/CBO9781139014403 (cit. on pp. 10, 11, 14–16, 19, 51, 52, 73, 92, 109, 110, 125).

Escrivà, A. and C.-M. Yoo (Oct. 2023). "Primordial Black Hole formation from overlapping cosmological fluctuations". arXiv: gr-qc/2310.16482 (cit. on p. 119).

Escrivà, Albert (Jan. 2020). "Simulation of primordial black hole formation using pseudo-spectral methods". In: *Physics of the Dark Universe* 27, p. 100466. DOI: 10.1016/j.dark.2020.100466. arXiv: gr-qc/1907.13065 (cit. on p. 42).

Fernando, M., D. Neilsen, H. Lim, E. Hirschmann, and H. Sundar (2019). "Massively Parallel Simulations of Binary Black Hole Intermediate-Mass-Ratio Inspirals". In: *SIAM Journal on Scientific Computing* 41.2, pp. C97–C138. DOI: 10.1137/18M1196972. arXiv: gr-qc/1807.06128 (cit. on p. 41).

Fidler, C., T. Tram, C. Rampf, R. Crittenden, K. Koyama, and D. Wands (Sept. 2016). "Relativistic interpretation of Newtonian simulations for cosmic structure formation". In: *Journal of Cosmology and Astroparticle Physics* 2016.09, pp. 031–031. DOI: 10.1088/1475-7516/2016/09/031. arXiv: astro-ph/1606.05588 (cit. on pp. 72, 118).

— (June 2017). "Relativistic initial conditions for N-body simulations". In: *Journal of Cosmology and Astroparticle Physics* 2017.06, pp. 043–043. DOI: 10.1088/1475-7516/2017/06/043. arXiv: astro-ph/1702.03221 (cit. on p. 118).

Font, J. A. (Aug. 2003). "Numerical Hydrodynamics in General Relativity". In: *Living Reviews in Relativity* 6.1, pp. 1433–8351. DOI: 10.12942/lrr-2003-4 (cit. on p. 100).

Fornberg, B. (1988). "Generation of finite difference formulas on arbitrarily spaced grids". In: *Mathematics of computation* 51, pp. 699–706. DOI: 10.1090/S0025-5718-1988-0935077-0 (cit. on pp. 44, 75).

Fourès-Bruhat, Y. (1952). "Théorème d'existence pour certains systèmes d'équations aux dérivées partielles non linéaires". In: *Acta Mathematica* 88, pp. 141–225. DOI: 10.1007/BF02392131 (cit. on pp. 29, 36, 39).

Friedmann, A. (Dec. 1922). "Über die Krümmung des Raumes". In: *Zeitschrift fur Physik* 10.1, pp. 377–386. DOI: 10.1007/BF01332580 (cit. on pp. 47, 48, 52, 53).

— (Dec. 1924). "Über die Möglichkeit einer Welt mit konstanter negativer Krümmung des Raumes". In: *Zeitschrift fur Physik* 21.1, pp. 326–332. DOI: 10.1007/BF01328280 (cit. on pp. 47, 48).

Gair, J. R. et al. (June 2023). "The Hitchhiker's Guide to the Galaxy Catalog Approach for Dark Siren Gravitational-wave Cosmology". In: *The Astronomical Journal* 166.1, p. 22. DOI: 10.3847/1538-3881/acca78. arXiv: gr-qc/2212.08694 (cit. on p. 2).

Garat, A. and R. H. Price (Jan. 2000). "Gauge invariant formalism for second order perturbations of Schwarzschild space-times". In: *Physical Review D* 61.4, p. 044006. DOI: 10.1103/PhysRevD.61.044006. arXiv: gr-qc/9909005 (cit. on p. 62).

Gerlach, U. H. and U. K. Sengupta (Sept. 1978). "Relativistic Equations for Aspherical Gravitational Collapse". In: *Physical Review D* 18.6, pp. 1789–1797. DOI: 10.1103/PhysRevD.18.1789 (cit. on p. 64).

Geshnizjani, G. and R. Brandenberger (Dec. 2002). "Back reaction and the local cosmological expansion rate". In: *Physical Review D* 66 (12), p. 123507. DOI: 10.1103/PhysRevD.66.123507. arXiv: hep-th/0310265 (cit. on pp. 99, 102).

Giacomazzo, B. and L. Rezzolla (2007). "WhiskyMHD: A New numerical code for general relativistic magnetohydrodynamics". In: *Classical and Quantum Gravity* 24, S235–S258. DOI: 10.1088/0264-9381/24/12/S16. arXiv: gr-qc/0701109 (cit. on p. 42).

Giblin, J. T., J. B. Mertens, and G. D. Starkman (June 2016). "Departures from the Friedmann-Lemaître-Robertston-Walker Cosmological Model in an Inhomogeneous Universe: A Numerical Examination". In: *Physical Review Letter* 116.25, p. 251301. DOI: 10.1103/PhysRevLett.116.251301. arXiv: gr-qc/1511.01105 (cit. on pp. 72, 96).

Giblin, J. T., J. B. Mertens, G. D. Starkman, and C. Tian (Sept. 2019a). "Cosmic expansion from spinning black holes". In: *Classical and Quantum Gravity* 36.19, p. 195009. DOI: 10.1088/1361-6382/ab3bf2. arXiv: gr-qc/1903.01490 (cit. on p. 42).

— (Jan. 2019b). "Limited Accuracy of Linearized Gravity". In: *Physical Review D* 99.2, p. 023527. DOI: 10.1103/PhysRevD.99.023527. arXiv: astro-ph/1810.05203 (cit. on pp. 39, 61, 72, 73, 101).

Gillessen, S., F. Eisenhauer, S. Trippe, T. Alexander, R. Genzel, F. Martins, and T. Ott (2009). "Monitoring stellar orbits around the Massive Black Hole in the Galactic Center". In: *Astrophys. J.* 692, pp. 1075–1109. DOI: 10.1088/0004-637X/692/2/1075. arXiv: 0810.4674 (cit. on p. 1).

Giusti, A. and V. Faraoni (Feb. 2021). "Turnaround physics beyond spherical symmetry". In: *Physical Review D* 103 (4), p. 044049. DOI: 10.1103/PhysRevD.103.044049. arXiv: gr-qc/1911.05130 (cit. on p. 71).

Gleiser, R. J., C. O. Nicasio, R. H. Price, and J. Pullin (Feb. 2000). "Gravitational radiation from Schwarzschild black holes: The Second order perturbation formalism". In: *Physics Reports* 325.2, pp. 41–81. DOI: 10.1016/S0370-1573(99)00048-4. arXiv: gr-qc/9807077 (cit. on p. 62).

Goldberg, S. R., T. Clifton, and K. A. Malik (Feb. 2017). "Cosmology on all scales: a two-parameter perturbation expansion". In: *Physical Review D* 95.4, p. 043503. DOI: 10.1103/PhysRevD.95.043503. arXiv: astro-ph/1610.08882 (cit. on p. 62).

Goldwirth, D. S. and T. Piran (June 1990). "Inhomogeneity and the Onset of Inflation". In: *Physical Review Letter* 64.24, pp. 2852–2855. DOI: 10.1103/PhysRevLett.64.2852 (cit. on p. 72).

Goobar, A. et al. (June 2023). "Uncovering a population of gravitational lens galaxies with magnified standard candle SN Zwicky". In: *Nature Astronomy*. DOI: 10.1038/s41550-023-01981-3. arXiv: 2211.00656 (cit. on p. 1).

Goodale, T., G. Allen, G. Lanfermann, J. Massó, T. Radke, E. Seidel, and J. Shalf (2003). "The Cactus Framework and Toolkit: Design and Applications". *High Performance Computing for Computational Science — VECPAR 2002*. Ed. by J. M. L. M. Palma, A. A. Sousa, J. Dongarra, and V. Hernández. Vol. 2565. Berlin, Heidelberg: Springer, pp. 197–227. ISBN: 978-3-540-36569-3. DOI: 10.1007/3-540-36569-9_13 (cit. on pp. 92, 100).

Goode, S. W. (May 1989). "Analysis of spatially inhomogeneous perturbations of the FRW cosmologies". In: *Physical Review D* 39.10, pp. 2882–2892. DOI: 10.1103/PhysRevD.39.2882 (cit. on p. 64).

Goode, S. W. and J. Wainwright (Dec. 1982). "Singularities and evolution of the Szekeres cosmological models". In: *Physical Review D* 26 (12), pp. 3315–3326. DOI: 10.1103/PhysRevD.26.3315 (cit. on pp. 78, 79).

Gosenca, M., J. Adamek, C. T. Byrnes, and S. Hotchkiss (Dec. 2017). "3D simulations with boosted primordial power spectra and ultracompact minihalos". In: *Physical Review D* 96.12, p. 123519. DOI: 10.1103/PhysRevD.96.123519. arXiv: 1710.02055 (cit. on p. 72).

Gourgoulhon, E. (2007). *3+1 formalism and bases of numerical relativity*. arXiv: gr-qc/0703035 (cit. on pp. 29, 99).

Grandclément, P. (May 2010). "Kadath: A Spectral solver for theoretical physics". In: *J. Comput. Phys.* 229.9, pp. 3334–3357. DOI: 10.1016/j.jcp.2010.01.005. arXiv: gr-qc/0909.1228 (cit. on p. 41).

Grasso, M. and E. Villa (Dec. 2021). "BiGONLight: light propagation with bilocal operators in numerical relativity". In: *Classical and Quantum Gravity* 39.1, p. 015011. DOI: 10.1088/1361-6382/ac35aa. arXiv: gr-qc/2107.06306 (cit. on pp. 65, 78).

Grasso, M., E. Villa, M. Korzy'nski, and S. Matarrese (Aug. 2021). "Isolating nonlinearities of light propagation in inhomogeneous cosmologies". In: *Physical Review D* 104.4, p. 043508. DOI: 10.1103/PhysRevD.104.043508. arXiv: astro-ph/2105.04552 (cit. on p. 65).

Gressel, H. A. and M. Bruni (June 2018). "$f_N L - g_N L$ mixing in the matter density field at higher orders". In: *Journal of Cosmology and Astroparticle Physics* 2018.6, p. 016. DOI: 10.1088/1475-7516/2018/06/016. arXiv: astro-ph/1712.08687 (cit. on p. 62).

Gunn, J. E. and J. R. III Gott (Aug. 1972). "On the Infall of Matter Into Clusters of Galaxies and Some Effects on Their Evolution". In: *The Astrophysical Journal* 176, p. 1. DOI: 10.1086/151605 (cit. on pp. 65, 66, 91, 103, 104).

Gunnarsen, L., S. Hisa-Aki, and M. Kei-Ichi (1995). "A 3+1 method of finding principal null directions". In: *Classical and Quantum Gravity* 12.1, pp. 133–140. DOI: 10.1088/0264-9381/12/1/011 (cit. on p. 76).

Harvey, A. and D. Tsoubelis (May 1977). "Exact Bianchi IV cosmological model". In: *Physical Review D* 15.10, pp. 2734–2737. DOI: 10.1103/PhysRevD.15.2734 (cit. on p. 80).

Harvey, A., D. Tsoubelis, and B. Wilsker (Oct. 1979). "Bianchi IV metric with electromagnetic field". In: *Physical Review D* 20.8, pp. 2077–2078. DOI: 10.1103/PhysRevD.20.2077 (cit. on p. 80).

Hawke, I. and J. M. Stewart (June 2002). "The dynamics of primordial black-hole formation". In: *Classical and Quantum Gravity* 19.14, p. 3687. DOI: 10.1088/0264-9381/19/14/310 (cit. on p. 118).

Hawking, S. W. (Aug. 1966). "Perturbations of an Expanding Universe". In: *The Astrophysical Journal* 145, p. 544. DOI: 10.1086/148793 (cit. on pp. 18, 19, 63, 73, 75, 92, 95, 109).

Heinesen, A. and H. J. Macpherson (Mar. 2022). "A prediction for anisotropies in the nearby Hubble flow". In: *Journal of Cosmology and Astroparticle Physics* 2022.3, p. 57. DOI: 10.1088/1475-7516/2022/03/057. arXiv: astro-ph/2111.14423 (cit. on pp. 74, 92, 112, 118).

Hilbert, D. (1915). "Die Grundlagen der Physik". In: *Nachrichten von der Gesellschaft der Wissenschaften zu Göttingen – Mathematisch-Physikalische Klasse* 3, pp. 395–407. DOI: 10.1007/978-1-4020-4000-9_43 (cit. on p. 12).

Hilditch, D., A. Weyhausen, and B. Brügmann (Mar. 2016). "Pseudospectral method for gravitational wave collapse". In: *Physical Review D* 93.6, p. 063006. DOI: 10.1103/PhysRevD.93.063006. arXiv: gr-qc/1504.04732 (cit. on p. 41).

Hogan, P. A. and G.F.R. Ellis (Jan. 1997). "Propagation of information by electromagnetic and gravitational waves in cosmology". In: *Classical and Quantum Gravity* 14.1A, A171–A188. DOI: 10.1088/0264-9381/14/1A/015 (cit. on p. 111).

Hubble, E. (Apr. 1929). "A relation between distance and radial velocity among extra-galactic nebulae". In: *Proceedings of the National Academy of Sciences of the United States of America* 15.3, pp. 168–173. DOI: 10.1073/pnas.15.3.168 (cit. on pp. 47, 50).

Hui, L. and E. Bertschinger (Nov. 1996). "Local approximations to the gravitational collapse of cold matter". In: *The Astrophysical Journal* 471.1, p. 1. DOI: 10.1086/177948. arXiv: astro-ph/9508114 (cit. on p. 118).

Husa, S., I. Hinder, and C. Lechner (June 2006). "Kranc: a Mathematica package to generate numerical codes for tensorial evolution equations". In: *Computer Physics Communications* 174.12, pp. 983–1004. DOI: 10.1016/j.cpc.2006.02.002 (cit. on p. 100).

Imbiriba, B., J. Baker, D.-I. Choi, J. Centrella, D. R. Fiske, J. D. Brown, J. R. van Meter, and K. Olson (2004). "Evolving a puncture black hole with fixed mesh refinement". In: *Physical Review D* 70, p. 124025. DOI: 10.1103/PhysRevD.70.124025. arXiv: gr-qc/0403048 (cit. on p. 41).

Ip, H. Y. and F. Schmidt (Feb. 2017). "Large-Scale Tides in General Relativity". In: *Journal of Cosmology and Astroparticle Physics* 2017.02, p. 025. DOI: 10.1088/1475-7516/2017/02/025. arXiv: astro-ph/1610.01059 (cit. on p. 118).

Jain, B. and E. Bertschinger (Jan. 1993). "Nonlinear effects due to the coupling of long wave modes". *Cosmic Velocity Fields*. Ed. by F. Bouchet and M. Lachieze-Rey. Vol. 9, p. 553. DOI: 10.48550/arXiv.astro-ph/9309040. arXiv: astro-ph/9309040 (cit. on p. 117).

Jain, B. and E. Bertschinger (Jan. 1996). "Selfsimilar evolution of cosmological density fluctuations". In: *Astrophysical Journal* 456, p. 43. DOI: 10.1086/176625. arXiv: astro-ph/9503025 (cit. on p. 117).

Jordan, P., W. Beiglböck, K. Bichteler, W. Budich, W. Kundt, and M. Trümper (Jan. 1964). *Contributions to actual problems of General Relativity*. Airforce Report, University of Hamburg. LINK (cit. on pp. 18, 73, 75, 92).

Karlhede, A. (Sept. 1980). "A review of the geometrical equivalence of metrics in general relativity". In: *General Relativity and Gravitation* 12.9, pp. 693–707. DOI: 10.1007/BF00771861 (cit. on pp. 23, 73).

Kerr, R. P. (Sept. 1963). "Gravitational Field of a Spinning Mass as an Example of Algebraically Special Metrics". In: *Physical Review Letter* 11.5, pp. 237–238. DOI: 10.1103/PhysRevLett.11.237 (cit. on p. 27).

Kidder, L. E., M. A. Scheel, S. A. Teukolsky, E. D. Carlson, and G. B. Cook (2000). "Black hole evolution by spectral methods". In: *Physical Review D* 62, p. 084032. DOI: 10.1103/PhysRevD.62.084032. arXiv: gr-qc/0005056 (cit. on p. 42).

Killing, W. (1892). "Ueber die Grundlagen der Geometrie". In: *Journal für die reine und angewandte Mathematik* 109. LINK, pp. 121–186 (cit. on p. 11).

King, A. R. and G. F. R. Ellis (Sept. 1973). "Tilted homogeneous cosmological models". In: *Communications in Mathematical Physics* 31.3, pp. 209–242. DOI: 10.1007/BF01646266 (cit. on pp. 19, 76).

Kinnersley, W. (May 1969). "Type D Vacuum Metrics". In: *Journal of Mathematical Physics* 10, pp. 1195–1203. DOI: 10.1063/1.1664958 (cit. on p. 27).

Kodama, H. and M. Sasaki (Jan. 1984). "Cosmological Perturbation Theory". In: *Progress of Theoretical and Experimental Physics* 78, pp. 1–166. DOI: 10.1143/PTPS.78.1 (cit. on pp. 55, 58, 64).

Kofman, L. and D. Pogosian (Mar. 1995). "Equations of gravitational instability are nonlocal". In: *Astrophysical Journal* 442, pp. 30–38. DOI: 10.1086/175419. arXiv: astro-ph/9403029 (cit. on p. 118).

Kokkotas, K. D. and B. G. Schmidt (Sept. 1999). "Quasinormal modes of stars and black holes". In: *Living Reviews in Relativity* 2.1, p. 2. DOI: 10.12942/lrr-1999-2. arXiv: gr-qc/9909058 (cit. on p. 62).

Korzyński, M., I. Hinder, and E. Bentivegna (Aug. 2015). "On the vacuum Einstein equations along curves with a discrete local rotation and reflection symmetry". In: *Journal of Cosmology and Astroparticle Physics* 2015.8, pp. 25–25. DOI: 10.1088/1475-7516/2015/08/025. arXiv: gr-qc/1505.05760 (cit. on pp. 74, 112).

Kou, X-X., J. B. Mertens, C. Tian, and S-Y. Zhou (June 2022). "Gravitational waves from fully general relativistic oscillon preheating". In: *Physical Review D* 105.12, p. 123505. DOI: 10.1103/PhysRevD.105.123505. arXiv: gr-qc/2112.07626 (cit. on p. 72).

Kurki-Suonio, H., J. Centrella, R. A. Matzner, and J. R. Wilson (Jan. 1987). "Inflation From Inhomogeneous Initial Data in a One-dimensional Back Reacting Cosmology". In: *Physical Review D* 35, pp. 435–448. DOI: 10.1103/PhysRevD.35.435 (cit. on p. 72).

Landau, L. D. and E. M. Lifshitz (1975). *The Classical Theory of Fields*. Vol. 2. Reed Education and Professional Publishing Ltd (cit. on p. 24).

Landau, R. H., M. J. Páez, and C. C. Bordeianu (2007). *Computational Physics*. Wiley-VCH Verlag GmbH & Co. KGaA (cit. on pp. 43, 45).

Langlois, D. and F. Vernizzi (May 2010). "A geometrical approach to nonlinear perturbations in relativistic cosmology". In: *Classical and Quantum Gravity* 27.12, p. 124007. DOI: 10.1088/0264-9381/27/12/124007. arXiv: astro-ph/1003.3270 (cit. on p. 93).

Lemaître, G. (Mar. 1931). "Expansion of the universe, A homogeneous universe of constant mass and increasing radius accounting for the radial velocity of extra-galactic nebulae". In: *Monthly Notices of the Royal Astronomical Society* 91.5, pp. 483–490. DOI: 10.1093/mnras/91.5.483 (cit. on pp. 47, 48).

— (1933). "L'Univers en expansion". In: *Annales de la Société Scientifique de Bruxelles* A.LIII, pp. 51–85 (cit. on pp. 47, 48, 71).

Lenzi, M. and C. F. Sopuerta (Oct. 2021). "Master functions and equations for perturbations of vacuum spherically symmetric spacetimes". In: *Physical Review D* 104.8, p. 084053. DOI: 10.1103/PhysRevD.104.084053. arXiv: gr-qc/2108.08668 (cit. on p. 62).

Lepori, F., S. Schulz, J. Adamek, and R. Durrer (Sept. 2023). "The halo bias for number counts on the light cone from relativistic N-body simulations". In: *Journal of Cosmology and Astroparticle Physics* 2, p. 36. DOI: 10.1088/1475-7516/2023/02/036. arXiv: astro-ph/2209.10533 (cit. on p. 72).

Lewis, A. and A. Challinor (June 2006). "Weak gravitational lensing of the CMB". In: *Physics Reports* 429.1, pp. 1–65. DOI: 10.1016/j.physrep.2006.03.002. arXiv: astro-ph/0601594 (cit. on pp. 26, 59, 73).

Lie, S. (1888). *Theory of Transformation Groups I*. Leipzig: B. G. Teubner. DOI: 10.1007/978-3-662-46211-9. arXiv: math/1003.3202 (cit. on p. 10).

LIGO Scientific Collaboration and Virgo Collaboration (Feb. 2016). "Observation of Gravitational Waves from a Binary Black Hole Merger". In: *Physical Review Letter* 116.6, p. 061102. DOI: 10.1103/physrevlett.116.061102. arXiv: gr-qc/1602.03837 (cit. on p. 2).

Linder, E. V. and R. N. Cahn (Dec. 2007). "Parameterized beyond-Einstein growth". In: *Astroparticle Physics* 28.4, pp. 481–488. DOI: 10.1016/j.astropartphys.2007.09.003. arXiv: astro-ph/0701317 (cit. on p. 66).

Löffler, F. et al. (May 2012). "The Einstein Toolkit: a community computational infrastructure for relativistic astrophysics". In: *Classical and Quantum Gravity* 29.11, p. 115001. arXiv: gr-qc/1111.3344 (cit. on pp. 41, 91, 100, 115).

Loutrel, N., J. L. Ripley, E. Giorgi, and F. Pretorius (May 2021). "Second Order Perturbations of Kerr Black Holes: Reconstruction of the Metric". In: *Physical Review D* 103.10, p. 104017. DOI: 10.1103/PhysRevD.103.104017. arXiv: gr-qc/2008.11770 (cit. on p. 62).

Lu, T. H., K. Ananda, C. Clarkson, and R. Maartens (Feb. 2009). "The cosmological background of vector modes". In: *Journal of Cosmology and Astroparticle Physics* 2009.2, p. 23. DOI: 10.1088/1475-7516/2009/02/023. arXiv: astro-ph/0812.1349 (cit. on p. 56).

Lucie-Smith, L., H. V. Peiris, A. Pontzen, B. Nord, and J. Thiyagalingam (n.d.). *Deep learning insights into cosmological structure formation*. DOI: 10.48550/ARXIV.2011.10577. arXiv: 2011.10577 (cit. on p. 117).

Lynden-Bell, D. (May 1967). "Statistical mechanics of violent relaxation in stellar systems". In: *Monthly Notices of the Royal Astronomical Society* 136.1, pp. 101–121. DOI: 10.1093/mnras/136.1.101 (cit. on p. 72).

Lyth, D. H. (Apr. 1985). "Large-scale energy-density perturbations and inflation". In: *Physical Review D* 31.8, pp. 1792–1798. DOI: 10.1103/PhysRevD.31.1792 (cit. on pp. 62, 91, 94).

Lyth, D. H., K. A. Malik, and M. Sasaki (May 2005). "A General proof of the conservation of the curvature perturbation". In: *Journal of Cosmology and Astroparticle Physics* 2005.5, p. 004. DOI: 10.1088/1475-7516/2005/05/004. arXiv: astro-ph/0411220 (cit. on p. 62).

Ma, C. and E. Bertschinger (Dec. 1995). "Cosmological Perturbation Theory in the Synchronous and Conformal Newtonian Gauges". In: *The Astrophysical Journal* 455, p. 7. DOI: 10.1086/176550. arXiv: astro-ph/9506072 (cit. on pp. 55, 57).

Maartens, R. and B. A. Bassett (Mar. 1998). "Gravito-electromagnetism". In: *Classical and Quantum Gravity* 15.3, pp. 705–717. DOI: 10.1088/0264-9381/15/3/018. arXiv: gr-qc/9704059 (cit. on pp. 19, 73, 92, 109).

Maartens, R., G. F. R. Ellis, and S. T. C. Siklos (July 1997). "Local freedom in the gravitational field". In: *Classical and Quantum Gravity* 14.7, pp. 1927–1936. DOI: 10.1088/0264-9381/14/7/025. arXiv: gr-qc/9611003 (cit. on p. 118).

Maartens, R., T. Gebbie, and G. F. R. Ellis (Mar. 1999). "Covariant cosmic microwave background anisotropies. 2. Nonlinear dynamics". In: *Physical Review D* 59.8, p. 083506. DOI: 10.1103/PhysRevD.59.083506. arXiv: astro-ph/9808163 (cit. on pp. 24, 62).

Macpherson, H. J. (2019). "Inhomogeneous cosmology in an anisotropic Universe". PhD thesis. Monash Centre for Astrophysics, School of Physics and Astronomy. arXiv: astro-ph/1910.13380 (cit. on pp. 60, 101, 128).

— (Mar. 2023). "Cosmological distances with general-relativistic ray tracing: framework and comparison to cosmographic predictions". In: *Journal of Cosmology and Astroparticle Physics* 3, p. 19. DOI: 10.1088/1475-7516/2023/03/019. arXiv: astro-ph/2209.06775 (cit. on pp. 65, 72).

Macpherson, H. J. and A. Heinesen (July 2021). "Luminosity distance and anisotropic sky-sampling at low redshifts: a numerical relativity study". In: *Physical Review D* 104.2, p. 023525. DOI: 10.1103/PhysRevD.104.023525. arXiv: astro-ph/2103.11918 (cit. on pp. 2, 42).

Macpherson, H. J., P. D. Lasky, and D. J. Price (Mar. 2017). "Inhomogeneous cosmology with numerical relativity". In: *Physical Review D* 95.6, p. 064028. DOI: 10.1103/physrevd.95.064028. arXiv: astro-ph/1611.05447 (cit. on pp. 64, 72, 91, 129).

— (Sept. 2018). "The trouble with Hubble: Local versus Global Expansion Rates in Inhomogeneous Cosmological Simulations with Numerical Relativity". In: *The Astrophysical Journal* 865.1, p. L4. DOI: 10.3847/2041-8213/aadf8c. arXiv: astro-ph/1807.01714 (cit. on p. 72).

Macpherson, H. J., D. J. Price, and P. D. Lasky (Mar. 2019). "Einstein's Universe: Cosmological structure formation in numerical relativity". In: *Physical Review D* 99.6, p. 063522. DOI: 10.1103/PhysRevD.99.063522. arXiv: astro-ph/1807.01711 (cit. on p. 60).

Magnall, S. J., D. J. Price, P. D. Lasky, and H. J. Macpherson (July 2023). "Inhomogeneous Cosmology using General Relativistic Smoothed Particle Hydrodynamics coupled to Numerical Relativity". arXiv: gr-qc/2307.15194 (cit. on pp. 72, 91, 101, 118).

Maldacena, J. (May 2003). "Non-gaussian features of primordial fluctuations in single field inflationary models". In: *Journal of High Energy Physics* 2003.05, pp. 013–013. DOI: 10.1088/1126-6708/2003/05/013. arXiv: astro-ph/0210603 (cit. on p. 93).

Malik, K. A. and D. R. Matravers (Sept. 2008). "A Concise Introduction to Perturbation Theory in Cosmology". In: *Classical and Quantum Gravity* 25.19, p. 193001. DOI: 10.1088/0264-9381/25/19/193001. arXiv: astro-ph/0804.3276 (cit. on p. 62).

Malik, K. A. and D. Wands (May 2009). "Cosmological perturbations". In: *Physics Reports* 475.1, pp. 1–51. DOI: 10.1016/j.physrep.2009.03.001. arXiv: astro-ph/0809.4944 (cit. on pp. 55–57, 62, 91, 93, 115).

Maplesoft (2019). *Maple*. Version 2019. Waterloo, Ontario. URL: https://hadoop.apache.org (cit. on pp. 21, 74, 80, 81, 123).

Marra, V., E.W. Kolb, S. Matarrese, and A. Riotto (Dec. 2007). "On cosmological observables in a swiss-cheese universe". In: *Physical Review D* 76.12, p. 123004. DOI: 10.1103/PhysRevD.76.123004. arXiv: astro-ph/0708.3622 (cit. on p. 71).

Matarrese, S., S. Mollerach, and M. Bruni (July 1998). "Second order perturbations of the Einstein-de Sitter universe". In: *Physical Review D* 58.4, p. 043504. DOI: 10.1103/PhysRevD.58.043504. arXiv: astro-ph/9707278 (cit. on p. 62).

Matarrese, S., O. Pantano, and D. Saez (Feb. 1993). "General-relativistic approach to the nonlinear evolution of collisionless matter". In: *Physical Review D* 47.4, pp. 1311–1323. DOI: 10.1103/PhysRevD.47.1311 (cit. on p. 118).

— (Jan. 1994a). "General relativistic dynamics of irrotational dust: Cosmological implications". In: *Physical Review Letter* 72.3, pp. 320–323. DOI: 10.1103/PhysRevLett.72.320. arXiv: astro-ph/9310036 (cit. on p. 118).

— (Dec. 1994b). "A Relativistic approach to gravitational instability in the expanding Universe: Second order Lagrangian solutions". In: *Monthly Notices of the Royal Astronomical Society* 271.3, pp. 513–522. DOI: 10.1093/mnras/271.3.513. arXiv: astro-ph/9403032 (cit. on p. 118).

Matte, A. (1953). "Sur De Nouvelles Solutions Oscillatoires Des Equations De La Gravitation". In: *Canadian Journal of Mathematics* 5, pp. 1–16. DOI: 10.4153/CJM-1953-001-3 (cit. on pp. 18, 24, 73, 75, 92, 109).

Maxwell, J. C. (Jan. 1865). "VIII. A dynamical theory of the electromagnetic field". In: *Philosophical Transactions of the Royal Society of London* 155, pp. 459–512. DOI: 10.1098/rstl.1865.0008 (cit. on p. 18).

McIntosh, C. B. G., R. Arianrhod, S. T. Wade, and C. Hoenselaers (June 1995). "Electric and magnetic Weyl tensors: classification and analysis". In: *Classical and Quantum Gravity* 11.6, pp. 1555–1564. DOI: 10.1088/0264-9381/11/6/019/meta (cit. on pp. 24, 73).

Meringolo, C. and S. Servidio (2021). "Aliasing instabilities in the numerical evolution of the Einstein field equations". In: *Gen. Rel. Grav.* 53.10, p. 95. DOI: 10.1007/s10714-021-02865-5. arXiv: gr-qc/2108.00786 (cit. on p. 42).

Mertens, J. B., J. T. Giblin, and G. D. Starkman (June 2016). "Integration of inhomogeneous cosmological spacetimes in the BSSN formalism". In: *Physical Review D* 93.12, p. 124059. DOI: 10.1103/physrevd.93.124059. arXiv: gr-qc/1511.01106 (cit. on pp. 41, 72, 128).

Meures, N. and M. Bruni (June 2011). "Exact nonlinear inhomogeneities in ΛCDM cosmology". In: *Physical Review D* 83.12, p. 123519. DOI: 10.1103/PhysRevD.83.123519. arXiv: astro-ph/1103.0501 (cit. on pp. 78, 79, 81, 89, 124).

— (Jan. 2012). "Redshift and distances in a \LambdaCDM cosmology with non-linear inhomogeneities". In: *Monthly Notices of the Royal Astronomical Society* 419, p. 1937. DOI: 10.1111/j.1365-2966.2011.19850.x. arXiv: astro-ph/1107.4433 (cit. on pp. 78, 79, 81).

Milillo, I., D. Bertacca, M. Bruni, and A. Maselli (2015). "Missing link: A nonlinear post-Friedmann framework for small and large scales". In: *Physical Review D* 92.2, p. 023519. DOI: 10.1103/PhysRevD.92.023519. arXiv: gr-qc/1502.02985 (cit. on pp. 74, 111).

Milne, E. A. (1935). *Relativity Gravitation and World - Structure*. LINK. Oxford Clarendon Press (cit. on p. 53).

Misner, C. W., K. S. Thorne, and J. A. Wheeler (2017). *Gravitation*. Princeton University Press (cit. on p. 5).

Mitman, K. et al. (Feb. 2023). "Nonlinearities in black hole ringdowns". In: *Physical Review Letter* 130.8, p. 081402. DOI: 10.1103/PhysRevLett.130.081402. arXiv: gr-qc/2208.07380 (cit. on p. 62).

Mo, H., F. van den Bosch, and S. White (2010). *Galaxy Formation and Evolution*. Cambridge University Press. DOI: 10.1017/CBO9780511807244 (cit. on pp. 48, 65, 66, 69, 71, 91, 103, 104, 115).

Mollerach, S. and S. Matarrese (Oct. 1997). "Cosmic microwave background anisotropies from second order gravitational perturbations". In: *Physical Review D* 56.8, pp. 4494–4502. DOI: 10.1103/PhysRevD.56.4494. arXiv: astro-ph/9702234 (cit. on p. 62).

Monaco, P. (1997). "The Cosmological Mass Function". PhD thesis. SISSA, Trieste. arXiv: astro-ph/9710085 (cit. on pp. 65, 71, 91, 115, 118).

Mösta, P., B. C. Mundim, J. A. Faber, R. Haas, S. C. Noble, T. Bode, F. Löffler, C. D. Ott, C. Reisswig, and E. Schnetter (Nov. 2013). "GRHydro: a new open-source general-relativistic magnetohydrodynamics code for the Einstein toolkit". In: *Classical and Quantum Gravity* 31.1, p. 015005. DOI: 10.1088/0264-9381/31/1/015005. arXiv: gr-qc/1304.5544 (cit. on p. 100).

Mukhanov, V. F., L. R. W. Abramo, and R. H. Brandenberger (Mar. 1997). "Backreaction Problem for Cosmological Perturbations". In: *Physical Review Letter* 78 (9), pp. 1624–1627. DOI: 10.1103/PhysRevLett.78.1624. arXiv: gr-qc/9609026v1 (cit. on pp. 99, 102).

Munoz, R. L. (2022). `EBWeyl`. URL: https://github.com/robynlm/ebweyl (cit. on pp. ix, 73–77, 88, 89, 92, 100, 109, 112, 115, 116).

— (2023a). `ICPertFLRW`. URL: https://github.com/robynlm/ICPertFLRW (cit. on pp. ix, 92, 95, 100, 115).

— (2023b). `sphereint`. URL: https://github.com/robynlm/sphereint (cit. on pp. ix, 100, 108, 132).

Munoz, R. L. and M. Bruni (June 2023a). "EBWeyl: a Code to Invariantly Characterize Numerical Spacetimes". In: *Classical and Quantum Gravity* 40.13, p. 135010. DOI: 10.1088/1361-6382/acd6cf. arXiv: gr-qc/2211.08133 (cit. on pp. ix, 3, 74, 75, 92, 109, 112, 115, 116).

— (June 2023b). "Structure formation and quasispherical collapse from initial curvature perturbations with numerical relativity simulations". In: *Physical Review D* 107.12, p. 123536. DOI: 10.1103/PhysRevD.107.123536. arXiv: astro-ph/2302.09033 (cit. on pp. ix, 3, 73, 89).

Musco, I. (Dec. 2019). "Threshold for primordial black holes: Dependence on the shape of the cosmological perturbations". In: *Physical Review D* 100.12, p. 123524. DOI: 10.1103/PhysRevD.100.123524. arXiv: gr-qc/1809.02127 (cit. on p. 93).

Musco, I., J. C. Miller, and A. G. Polnarev (Oct. 2009). "Primordial black hole formation in the radiative era: Investigation of the critical nature of the collapse". In: *Classical and Quantum Gravity* 26.23, p. 235001. DOI: 10.1088/0264-9381/26/23/235001. arXiv: gr-qc/0811.1452 (cit. on p. 72).

Musco, I., J. C. Miller, and L. Rezzolla (Mar. 2005). "Computations of primordial black hole formation". In: *Classical and Quantum Gravity* 22.7, pp. 1405–1424. DOI: 10.1088/0264-9381/22/7/013. arXiv: gr-qc/0412063 (cit. on p. 42).

Musco, I. and T. Papanikolaou (2022). "Primordial black hole formation for an anisotropic perfect fluid: Initial conditions and estimation of the threshold". In: *Physical Review D* 106.8, p. 083017. DOI: 10.1103/PhysRevD.106.083017. arXiv: gr-qc/2110.05982 (cit. on p. 118).

Nakamura, K. (Jan. 2007). "Second-order gauge invariant cosmological perturbation theory: Einstein equations in terms of gauge invariant variables". In: *Progress of Theoretical Physics* 117.1, pp. 17–74. DOI: 10.1143/PTP.117.17. arXiv: gr-qc/0605108 (cit. on p. 62).

Nakamura, T., K. Oohara, and Y. Kojima (Jan. 1987). "General Relativistic Collapse to Black Holes and Gravitational Waves from Black Holes". In: *Progress of Theoretical Physics Supplement* 90, pp. 1–218. DOI: 10.1143/PTPS.90.1 (cit. on pp. 29, 36, 38, 100).

Navarro, J. F., C. S. Frenk, and S. D. M. White (May 1996). "The Structure of Cold Dark Matter Halos". In: *The Astrophysical Journal* 462, p. 563. DOI: 10.1086/177173. arXiv: astro-ph/9508025 (cit. on p. 72).

Nerozzi, A., C. Beetle, M. Bruni, L. M. Burko, and D. Pollney (July 2005). "Towards wave extraction in numerical relativity: The quasi-Kinnersley frame". In: *Physical Review D* 72, p. 024014. DOI: 10.1103/PhysRevD.72.024014. arXiv: gr-qc/0407013 (cit. on p. 28).

Nerozzi, A., M. Bruni, V. Re, and L. M. Burko (Feb. 2006). "Towards a wave-extraction method for numerical relativity: IV. Testing the quasi-Kinnersley method in the Bondi-Sachs framework". In: *Physical Review D* 73, p. 044020. DOI: 10.1103/PhysRevD.73.044020. arXiv: gr-qc/0507068 (cit. on p. 28).

Newman, E. and R. Penrose (Dec. 1962). "An Approach to Gravitational Radiation by a Method of Spin Coefficients". In: *Journal of Mathematical Physics* 3.3, pp. 566–578. DOI: 10.1063/1.1724257 (cit. on pp. 20, 26).

Newton, I. (1687). *Philosophiæ Naturalis Principia Mathematica*. Jussu Societatis Regiae ac Typis Joseph Streater (cit. on pp. 1, 5, 67).

Nichols, D. A. et al. (Dec. 2011). "Visualizing spacetime curvature via frame-drag vortexes and tidal tendexes: General theory and weak-gravity applications". In: *Physical Review D* 84.12, p. 124014. DOI: 10.1103/PhysRevD.84.124014. arXiv: gr-qc/1108.5486 (cit. on p. 119).

Noh, H. and J-C. Hwang (May 2004). "Second-order perturbations of the Friedmann world model". In: *Physical Review D* 69.10, p. 104011. DOI: 10.1103/PhysRevD.69.104011. arXiv: astro-ph/0305123 (cit. on p. 62).

Osano, B., C. Pitrou, P. Dunsby, J-P. Uzan, and C. Clarkson (Apr. 2007). "Gravitational waves generated by second order effects during inflation". In: *Journal of Cosmology and Astroparticle Physics*

2007.4, p. 003. DOI: 10.1088/1475-7516/2007/04/003. arXiv: gr-qc/0612108 (cit. on p. 62).

Ota, A., H. J. Macpherson, and W. R. Coulton (2022). "Covariant transverse-traceless projection for secondary gravitational waves". In: *Physical Review D* 106.6, p. 063521. DOI: 10.1103/PhysRevD.106.063521. arXiv: gr-qc/2111.09163 (cit. on p. 62).

Owen, R. (June 2010). "Degeneracy measures for the algebraic classification of numerical spacetimes". In: *Physical Review D* 81.12, p. 124042. DOI: 10.1103/PhysRevD.81.124042. arXiv: gr-qc/1004.3768 (cit. on pp. 26, 92).

Owen, R. et al. (Apr. 2011). "Frame-dragging vortexes and tidal tendexes attached to colliding black holes: Visualizing the curvature of spacetime". In: *Physical Review Letter* 106.15, p. 151101. DOI: 10.1103/PhysRevLett.106.151101. arXiv: gr-qc/1012.4869 (cit. on pp. 74, 92).

Pace, F., C. Schimd, D. F. Mota, and A. Del Popolo (Sept. 2019). "Halo collapse: virialization by shear and rotation in dynamical dark-energy models. Effects on weak-lensing peaks". In: *Journal of Cosmology and Astroparticle Physics* 2019.9, pp. 60–60. DOI: 10.1088/1475-7516/2019/09/060. arXiv: astro-ph/1811.12105 (cit. on p. 72).

Palenzuela, C., B. Miñano, D. Viganò, A. Arbona, C. Bona-Casas, A. Rigo, M. Bezares, C. Bona, and J. Massó (2018). "A Simflowny-based finite-difference code for high-performance computing in numerical relativity". In: *Classical and Quantum Gravity* 35.18, p. 185007. DOI: 10.1088/1361-6382/aad7f6. arXiv: 1806.04182 (cit. on p. 42).

Pani, P. (Sept. 2013). "Advanced Methods in Black-Hole Perturbation Theory". In: *International Journal of Modern Physics A* 28.22n23, p. 1340018. DOI: 10.1142/S0217751X13400186. arXiv: gr-qc/1305.6759 (cit. on pp. 62, 63).

Pareja, M. J. and M. A. H. MacCallum (July 2006). "Local freedom in the gravitational field revisited". In: *Classical and Quantum Gravity* 23.15, pp. 5039–5048. DOI: 10.1088/0264-9381/23/15/019. arXiv: gr-qc/0605075 (cit. on p. 118).

Passamonti, A., M. Bruni, L. Gualtieri, A. Nagar, and C. F. Sopuerta (Apr. 2006). "Coupling of radial and axial non-radial oscillations of compact stars: Gravitational waves from first-order differential rotation". In: *Physical Review D* 73.8, p. 084010. DOI: 10.1103/PhysRevD.73.084010. arXiv: gr-qc/0601001 (cit. on p. 62).

Passamonti, A., M. Bruni, L. Gualtieri, and C. F. Sopuerta (Jan. 2005). "Coupling of radial and non-radial oscillations of relativistic stars: Gauge-invariant formalism". In: *Physical Review D* 71.2, p. 024022. DOI: 10.1103/PhysRevD.71.024022. arXiv: gr-qc/0407108 (cit. on p. 62).

Passamonti, A., N. Stergioulas, and A. Nagar (Apr. 2007). "Gravitational Waves from Nonlinear Couplings of Radial and Polar Nonradial Modes in Relativistic Stars". In: *Physical Review D* 75.8, p. 084038. DOI: 10.1103/PhysRevD.75.084038. arXiv: gr-qc/0702099 (cit. on p. 62).

Peacock, J. A. (1999). *Cosmological Physics*. Cambridge University Press. DOI: 10.1017/CBO9780511804533 (cit. on pp. 47, 65, 69, 91, 103, 104, 115).

Peebles, P. J. E. (1980). *The large-scale structure of the universe*. Princeton University Press (cit. on pp. 48, 50, 66, 94).

— (Dec. 1982). "Large-scale background temperature and mass fluctuations due to scale-invariant primeval perturbations". In: *The Astrophysical Journal* 263, pp. L1–L5. DOI: 10.1086/183911 (cit. on p. 48).

Penrose, R. (1960). "A spinor approach to general relativity". In: *Annals of Physics* 10.2, pp. 171–201. DOI: 10.1016/0003-4916(60)90021-X (cit. on p. 25).

Penzias, A. A. and R. W. Wilson (July 1965). "A Measurement of excess antenna temperature at 4080-Mc/s". In: *The Astrophysical Journal* 142, pp. 419–421. DOI: 10.1086/148307 (cit. on p. 47).

Petrov, A. Z. (Aug. 2000). "The Classification of Spaces Defining Gravitational Fields". In: *General Relativity and Gravitation* 32.8, pp. 1665–1685. DOI: 10.1023/A:1001910908054 (cit. on pp. 23, 25, 112).

Pettinari, G. W., C. Fidler, R. Crittenden, K. Koyama, and D. Wands (Apr. 2013). "The intrinsic bispectrum of the Cosmic Microwave Background". In: *Journal of Cosmology and Astroparticle Physics* 2013.4, p. 003. DOI: 10.1088/1475-7516/2013/04/003. arXiv: astro-ph/1302.0832 (cit. on p. 62).

Pirani, F. A. E. (Feb. 1957). "Invariant Formulation of Gravitational Radiation Theory". In: *Physical Review* 105 (3), pp. 1089–1099. DOI: 10.1103/PhysRev.105.1089 (cit. on p. 26).

Pitrou, C., T. S. Pereira, and J-P. Uzan (July 2015). "Weak-lensing by the large scale structure in a spatially anisotropic universe: theory and predictions". In: *Physical Review D* 92.2, p. 023501. DOI: 10.1103/PhysRevD.92.023501. arXiv: astro-ph/1503.01125 (cit. on p. 62).

Planck Collaboration (Sept. 2020). "Planck 2018 results". In: *Astronomy & Astrophysics* 641, A5. DOI: 10.1051/0004-6361/201833910. arXiv: astro-ph/1907.12875 (cit. on pp. 48, 55, 101).

Plebański, J. and A. Krasiński (2006). *An introduction to General Relativity and Cosmology*. Cambridge University Press. DOI: 10.1017/CBO9780511617676 (cit. on pp. 7, 25).

Porth, O., H. Olivares, Y. Mizuno, Z. Younsi, L. Rezzolla, M. Moscibrodzka, H. Falcke, and M. Kramer (May 2017). "The black hole accretion code". In: *Computational Astrophysics and Cosmology* 4.1, p. 1. DOI: 10.1186/s40668-017-0020-2. arXiv: gr-qc/1611.09720 (cit. on p. 41).

Pound, A. and B. Wardell (2020). "Black hole perturbation theory and gravitational self-force". *Handbook of Gravitational Wave Astronomy*. ed C. Bambi, S. Katsanevas, K. D. Kokkotas. Springer Singapore, pp. 1–119. DOI: 10.1007/978-981-15-4702-7_38-1 (cit. on p. 62).

Press, W. H. and P. Schechter (Feb. 1974). "Formation of Galaxies and Clusters of Galaxies by Self-Similar Gravitational Condensation". In: *The Astrophysical Journal* 187, pp. 425–438. DOI: 10.1086/152650 (cit. on pp. 70, 71).

Pueblas, S. and R. Scoccimarro (Aug. 2009). "Generation of vorticity and velocity dispersion by orbit crossing". In: *Physical Review D* 80.4, p. 043504. DOI: 10.1103/PhysRevD.80.043504. arXiv: astro-ph/0809.4606 (cit. on p. 118).

Quintana-Miranda, E., P. Monaco, and L. Tornatore (Apr. 2023). "GRGADGET: an N-body TreePM relativistic code for cosmological simulations". In: *Monthly Notices of the Royal Astronomical Society : Letters* 522.4, pp. 5238–5253. DOI: 10.1093/mnras/stad1174. arXiv: astro-ph/2301.11854 (cit. on p. 118).

Rácz, G., L. Dobos, R. Beck, I. Szapudi, and I. Csabai (July 2017). "Concordance cosmology without dark energy". In: *Monthly Notices of the Royal Astronomical Society : Letters* 469.1, pp. L1–L5. DOI: 10.1093/mnrasl/slx026. arXiv: astro-ph/1607.08797 (cit. on p. 72).

Rácz, G., I. Szapudi, I. Csabai, and L. Dobos (June 2021). "The anisotropy of the power spectrum in periodic cosmological simulations". In: *Monthly Notices of the Royal Astronomical Society* 503.4, pp. 5638–5645. DOI: 10.1093/mnras/stab874. arXiv: astro-ph/2006.10399 (cit. on p. 97).

Rampf, C., E. Villa, D. Bertacca, and M. Bruni (Oct. 2016). "Lagrangian theory for cosmic structure formation with vorticity: Newtonian and post-Friedmann approximations". In: *Physical Review D* 94.8, p. 083515. DOI: 10.1103/PhysRevD.94.083515. arXiv: gr-qc/1607.05226 (cit. on p. 111).

Rasera, Y. et al. (May 2022). "The RayGalGroupSims cosmological simulation suite for the study of relativistic effects: An application to lensing-matter clustering statistics". In: *Astronomy & Astrophysics* 661, A90. DOI: 10.1051/0004-6361/202141908. arXiv: astro-ph/2111.08745 (cit. on p. 72).

Raychaudhuri, A. (May 1955). "Relativistic Cosmology. I". In: *Physical Review* 98.4, pp. 1123–1126. DOI: 10.1103/PhysRev.98.1123 (cit. on pp. 16, 53).

Reardon, D. J. et al. (June 2023). "Search for an Isotropic Gravitational-wave Background with the Parkes Pulsar Timing Array". In: *The Astrophysical Journal Letters* 951.1, p. L6. DOI: 10.3847/2041-8213/acdd02. arXiv: astro-ph/2306.16215 (cit. on p. 2).

Rekier, J., I. Cordero-Carrión, and A. Füzfa (Jan. 2015). "Fully relativistic non-linear cosmological evolution in spherical symmetry using the BSSN formalism". In: *Physical Review D* 91.2, p. 024025. DOI: 10.1103/PhysRevD.91.024025. arXiv: gr-qc/1409.3476 (cit. on pp. 42, 72).

Rendall, A. D. (2008). *Partial Differential Equations in General Relativity*. Oxford UNiversity Press (cit. on pp. 29, 36).

Ricci, M. M. G. and T. Levi-Civita (Mar. 1900). "Méthodes de calcul différentiel absolu et leurs applications". In: *Mathematische Annalen* 54, pp. 125–201. DOI: 10.1007/BF01454201 (cit. on pp. 5, 7, 8).

Riemann, B. (1868). "Ueber die Hypothesen, welche der Geometrie zu Grunde liegen". In: *Abhandlungen der Königlichen Gesellschaft der Wissenschaften in Göttingen*. LINK, p. 133 (cit. on p. 8).

Riess, A. G., A. V. Filippenko, et al. (Sept. 1998). "Observational Evidence from Supernovae for an Accelerating Universe and a Cosmological Constant". In: *The Astrophysical Journal* 116.3, p. 1009. DOI: 10.1086/300499. arXiv: gr-qc/1409.3476 (cit. on p. 47).

Riess, A. G., W. Yuan, et al. (July 2022). "A Comprehensive Measurement of the Local Value of the Hubble Constant with 1 km s-1 Mpc-1 Uncertainty from the Hubble Space Telescope and the SH0ES Team". In: *The Astrophysical Journal Letters* 934.1, p. L7. DOI: 10.3847/2041-8213/ac5c5b. arXiv: astro-ph/2112.04510 (cit. on p. 48).

Ripley, J. L., N. Loutrel, E. Giorgi, and F. Pretorius (May 2021). "Numerical computation of second order vacuum perturbations of Kerr black holes". In: *Physical Review D* 103.10, p. 104018. DOI: 10.1103/PhysRevD.103.104018. arXiv: gr-qc/2010.00162 (cit. on p. 62).

Robertson, H. P. (Nov. 1935). "Kinematics and World-Structure". In: *The Astrophysical Journal* 82, p. 284. DOI: 10.1086/143681 (cit. on p. 48).

— (Apr. 1936a). "Kinematics and World-Structure II." In: *The Astrophysical Journal* 83, p. 187. DOI: 10.1086/143716 (cit. on p. 48).

— (May 1936b). "Kinematics and World-Structure III." In: *The Astrophysical Journal* 83, p. 257. DOI: 10.1086/143726 (cit. on p. 48).

Robinson, I. and A. Trautman (Feb. 1962). "Some spherical gravitational waves in general relativity". In: *Proceedings of the Royal Society of London. A.* 265, pp. 463–473. DOI: 10.1098/rspa.1962.0036 (cit. on p. 27).

Rosquist, K. and R. T. Jantzen (Jan. 1985). "Exact power law solutions of the Einstein equations". In: *Physics Letters A* 107.1, pp. 29–32. DOI: 10.1016/0375-9601(85)90240-3 (cit. on p. 80).

Rosswog, S., F. Torsello, and P. Diener (2023). *The Lagrangian Numerical Relativity code SPHINCS_BSSN_v1.0*. arXiv: gr-qc/2306.06226 (cit. on pp. 42, 72).

Rovelli, C. (Feb. 1991). "What is observable in classical and quantum gravity?" In: *Classical and Quantum Gravity* 8.2, p. 297. DOI: 10.1088/0264-9381/8/2/011 (cit. on pp. 65, 73).

Rubin, V. C. and W. K. Jr. Ford (Feb. 1970). "Rotation of the Andromeda Nebula from a Spectroscopic Survey of Emission Regions". In: *The Astrophysical Journal* 159, p. 379. DOI: 10.1086/150317 (cit. on p. 48).

Ruchlin, I., Z. B. Etienne, and T. W. Baumgarte (Mar. 2018). "SENR/NRPy+: Numerical relativity in singular curvilinear coordinate systems". In: *Physical Review D* 97.6, p. 064036. DOI: 10.1103/PhysRevD.97.064036. arXiv: gr-qc/1712.07658 (cit. on p. 100).

Saga, S., A. Taruya, and S. Colombi (Aug. 2022). "Cold dark matter protohalo structure around collapse: Lagrangian cosmological perturbation theory versus Vlasov simulations". In: *Astronomy & Astrophysics* 664, A3. DOI: 10.1051/0004-6361/202142756. arXiv: astro-ph/2111.08836 (cit. on pp. 72, 91).

Sahni, V. and P. Coles (Nov. 1995). "Approximation methods for non-linear gravitational clustering". In: *Physics Reports* 262.1, pp. 1–135. DOI: 10.1016/0370-1573(95)00014-8. arXiv: astro-ph/9505005 (cit. on pp. 65–67, 69, 91, 115, 118).

Schiesser, W. E. (1991). *The Numerical Method of Lines: Integrating of Partial Differential Equations*. Elsevier Science (cit. on p. 44).

Schmidt, A. S., S. D. M. White, F. Schmidt, and J. Stücker (Sept. 2018). "Cosmological N-Body Simulations with a Large-Scale Tidal Field". In: *Monthly Notices of the Royal Astronomical Society* 479.1, pp. 162–170. DOI: 10.1093/mnras/sty1430. arXiv: astro-ph/1803.03274 (cit. on p. 117).

Schneider, P. (2015). *Extragalactic Astronomy and Cosmology*. Springer Berlin, Heidelberg. DOI: 10.1007/978-3-642-54083-7 (cit. on pp. 47, 50).

Schnetter, E., S. H. Hawley, and I. Hawke (Feb. 2004). "Evolutions in 3D numerical relativity using fixed mesh refinement". In: *Classical and Quantum Gravity* 21.6, p. 1465. DOI: 10.1088/0264-9381/21/6/014. arXiv: gr-qc/0310042 (cit. on p. 100).

Schwarzschild, K. (Jan. 1916). "On the gravitational field of a mass point according to Einstein's theory". In: *Sitzungsberichte der Königlich Preussischen Akademie der Wissenschaften* 1. LINK, pp. 189–196. arXiv: physics/9905030 (cit. on pp. 27, 70).

SCIAMA (n.d.). URL: http://www.sciama.icg.port.ac.uk/ (cit. on p. 100).

Sheth, R. K. and G. Tormen (Sept. 1999). "Large-scale bias and the peak background split". In: *Monthly Notices of the Royal Astronomical Society* 308.1, pp. 119–126. DOI: 10.1046/j.1365-8711.1999.02692.x. arXiv: astro-ph/9901122 (cit. on p. 71).

Shibata, M. (2015). *Numerical Relativity*. World Scientific Publishing Company. DOI: 10.1142/9692 (cit. on pp. 20, 21, 26, 29, 33–35, 43, 73, 76, 99).

Shibata, M. and T. Nakamura (Nov. 1995). "Evolution of three-dimensional gravitational waves: Harmonic slicing case". In: *Physical Review D* 52.10, pp. 5428–5444. DOI: 10.1103/PhysRevD.52.5428 (cit. on pp. 29, 36, 100).

Shibata, M. and M. Sasaki (1999). "Black hole formation in the Friedmann universe: Formulation and computation in numerical relativity". In: *Physical Review D* 60, p. 084002. DOI: 10.1103/PhysRevD.60.084002. arXiv: gr-qc/9905064 (cit. on pp. 93, 118).

Slurm (n.d.). URL: https://slurm.schedmd.com/documentation.html (cit. on p. 100).

Smarr, L. and J. W. Jr. York (May 1978a). "Kinematical conditions in the construction of spacetime". In: *Physical Review D* 17.10, pp. 2529–2551. DOI: 10.1103/PhysRevD.17.2529 (cit. on pp. 38–40).

— (Apr. 1978b). "Radiation gauge in general relativity". In: *Physical Review D* 17.8, pp. 1945–1956. DOI: 10.1103/PhysRevD.17.1945 (cit. on p. 39).

Sobral-Blanco, D. and C. Bonvin (2021). "Measuring anisotropic stress with relativistic effects". In: *Physical Review D* 104.6, p. 063516. DOI: 10.1103/PhysRevD.104.063516. arXiv: astro-ph/2102.05086 (cit. on p. 64).

Sonego, S. and M. Bruni (Apr. 1998). "Gauge dependence in the theory of nonlinear space-time perturbations". In: *Communications in Mathematical Physics* 93.1, pp. 209–218. DOI: 10.1007/s002200050325. arXiv: gr-qc/9708068 (cit. on p. 62).

Sopuerta, C. F., M. Bruni, and L. Gualtieri (Sept. 2004). "Nonlinear N parameter space-time perturbations: Gauge transformations". In: *Physical Review D* 70.6, p. 064002. DOI: 10.1103/PhysRevD.70.064002. arXiv: gr-qc/0306027 (cit. on p. 62).

Sopuerta, C. F., R. Maartens, G. F. R. Ellis, and W. M. Lesame (June 1999). "Nonperturbative gravitomagnetic fields". In: *Physical Review D* 60.2, p. 024006. DOI: 10.1103/PhysRevD.60.024006. arXiv: gr-qc/9809085 (cit. on p. 118).

Sopuerta, C. F. and N. Yunes (Sept. 2009). "Extreme and Intermediate-Mass Ratio Inspirals in Dynamical Chern-Simons Modified Gravity". In: *Physical Review D* 80.6, p. 064006. DOI: 10.1103/PhysRevD.80.064006. arXiv: gr-qc/0904.4501 (cit. on p. 62).

Springel, V., C. S. Frenk, and S. D. M. White (Apr. 2006). "The large-scale structure of the Universe". In: *Nature* 440.7088, pp. 1137–1144. DOI: 10.1038/nature04805. arXiv: astro-ph/0604561 (cit. on p. 48).

Staelens, F., J. Rekier, and A. Füzfa (Apr. 2021). "Universality of the spherical collapse with respect to the matter type : the case of a barotropic fluid with linear equation of state". In: *General Relativity and Gravitation* 53.4, p. 38. DOI: 10.1007/s10714-021-02804-4. arXiv: gr-qc/1912.00677 (cit. on p. 72).

Stephani, H., D. Kramer, M. MacCallum, C. Hoenselaers, and E. Herlt (2003). *Exact Solutions of Einstein's Field Equations*. Cambridge University Press. DOI: 10.1017/CBO9780511535185 (cit. on pp. 9, 20, 21, 23–27, 73, 80, 81, 83, 92, 112, 113).

Stewart, J. M. (July 1990). "Perturbations of Friedmann-Robertson-Walker cosmological models". In: *Classical and Quantum Gravity* 7.7, pp. 1169–1180. DOI: 10.1088/0264-9381/7/7/013 (cit. on p. 64).

Stewart, J. M. and M. Walker (Oct. 1974). "Perturbations of Space-Times in General Relativity". In: *Proceedings of the Royal Society of London. A.* 341.1624, pp. 49–74. DOI: 10.1098/rspa.1974.0172 (cit. on pp. 26, 28, 61, 63, 73, 93).

Szekeres, P. (1965). "The Gravitational compass". In: *Journal of Mathematical Physics* 6, pp. 1387–1391. DOI: 10.1063/1.1704788 (cit. on pp. 26, 28, 114).

— (Feb. 1975). "A Class of Inhomogeneous Cosmological Models". In: *Communications in Mathematical Physics* 41.1, pp. 55–64. DOI: 10.1007/BF01608547 (cit. on pp. 27, 74, 78, 81).

Talebian-Ashkezari, A., N. Ahmadi, and A. A. Abolhasani (Mar. 2018). "δ M formalism: a new approach to cosmological perturbation theory in anisotropic inflation". In: *Journal of Cosmology and Astroparticle Physics* 2018.3, p. 001. DOI: 10.1088/1475-7516/2018/03/001. arXiv: gr-qc/1609.05893 (cit. on p. 62).

Teukolsky, S. A. (Oct. 1973). "Perturbations of a rotating black hole. 1. Fundamental equations for gravitational electromagnetic and neutrino field perturbations". In: *The Astrophysical Journal* 185, pp. 635–647. DOI: 10.1086/152444 (cit. on pp. 26–28, 63).

The Event Horizon Telescope Collaboration (Apr. 2019a). "First M87 Event Horizon Telescope Results. I. The Shadow of the Supermassive Black Hole". In: *The Astrophysical Journal Letters* 875.1, p. L1. DOI: 10.3847/2041-8213/ab0ec7. arXiv: astro-ph/1906.11238 (cit. on p. 1).

— (2019b). "First M87 Event Horizon Telescope Results. V. Physical Origin of the Asymmetric Ring". In: *The Astrophysical Journal Letter* 875.1, p. L5. DOI: 10.3847/2041-8213/ab0f43. arXiv: astro-ph/1906.11242 (cit. on p. 2).

— (2022). "First Sagittarius A* Event Horizon Telescope Results. I. The Shadow of the Supermassive Black Hole in the Center of the Milky Way". In: *The Astrophysical Journal Letters* 930.2, p. L12. DOI: 10.3847/2041-8213/ac6674 (cit. on p. 1).

Thierfelder, M., S. Bernuzzi, and B. Brügmann (2011). "Numerical relativity simulations of binary neutron stars". In: *Physical Review D* 84, p. 044012. DOI: 10.1103/PhysRevD.84.044012. arXiv: gr-qc/1104.4751 (cit. on p. 41).

Thomas, D. B., M. Bruni, K. Koyama, B. Li, and G-B. Zhao (July 2015). "f(R) gravity on non-linear scales: The post-Friedmann expansion and the vector potential". In: *Journal of Cosmology and Astroparticle Physics* 07, p. 051. DOI: 10.1088/1475-7516/2015/07/051. arXiv: gr-qc/1503.07204 (cit. on pp. 72, 74).

Thomas, D. B., M. Bruni, and D. Wands (July 2015). "The fully non-linear post-Friedmann frame-dragging vector potential: Magnitude and time evolution from N-body simulations". In: *Monthly Notices of the Royal Astronomical Society* 452.2, pp. 1727–1742. DOI: 10.1093/mnras/stv1390. arXiv: astro-ph/1501.00799 (cit. on pp. 72, 74, 111, 118, 119).

Thomas, M. W. and E. Schnetter (2010). *Simulation Factory: Taming application configuration and workflow on high-end resources*. DOI: 10.48550/ARXIV.1008.4571. arXiv: cs/1008.4571 (cit. on p. 100).

Tian, C., S. Anselmi, M. F. Carney, J. T. Giblin, J. B. Mertens, and G. D. Strakman (Apr. 2020). "On the question of measuring spatial curvature in an inhomogeneous universe". In: *Physical Review D* 103.8, p. 083513. DOI: 10.1103/PhysRevD.103.083513. arXiv: astro-ph/2010.07274 (cit. on p. 73).

Tian, C., M. F. Carney, J. B. Mertens, and G. Starkman (Mar. 2022). "Accurate relativistic observables from postprocessing light cone catalogs". In: *Physical Review D* 105.6. DOI: 10.1103/physrevd.105.063511. arXiv: astro-ph/2110.00893 (cit. on p. 72).

Tolman, R. C. (Feb. 1934). "Effect of Inhomogeneity on Cosmological Models". In: *Proceedings of the National Academy of Sciences* 20.3, pp. 169–176. DOI: 10.1073/pnas.20.3.169 (cit. on p. 71).

Torres, J. M., M. Alcubierre, A. Diez-Tejedor, and D. Núñez (Dec. 2014). "Cosmological nonlinear structure formation in full general relativity". In: *Physical Review D* 90.12, p. 123002. DOI: 10.1103/PhysRevD.90.123002. arXiv: gr-qc/1409.7953 (cit. on pp. 42, 72).

Torsello, F., M. Kocic, M. Högås, and E. Mörtsell (2020). "Covariant BSSN formulation in bimetric relativity". In: *Classical and Quantum Gravity* 37.2. [Erratum: Class.Quant.Grav. 37, 079501 (2020)], p. 025013. DOI: 10.1088/1361-6382/ab56fc. arXiv: gr-qc/1904.07869 (cit. on p. 29).

Tsagas, C. G., A. Challinor, and R. Maartens (May 2008). "Relativistic cosmology and large-scale structure". In: *Physics Reports* 465.2, pp. 61–147. DOI: 10.1016/j.physrep.2008.03.003. arXiv: astro-ph/0705.4397 (cit. on p. 62).

Tyson, J. A., F. Valdes, and R. A. Wenk (Jan. 1990). "Detection of Systematic Gravitational Lens Galaxy Image Alignments: Mapping Dark Matter in Galaxy Clusters". In: *The Astrophysical Journal Letters* 349, p. L1. DOI: 10.1086/185636 (cit. on p. 1).

Umeh, O. (2022). "The art of building a smooth cosmic distance ladder in a perturbed universe". In: *Journal of Cosmology and Astroparticle Physics* 08.08, p. 023. DOI: 10.1088/1475-7516/2022/08/023. arXiv: 2201.11089 (cit. on p. 2).

— (Mar. 2023). *Vorticity generation in cosmology and the role of shell crossing*. arXiv: 2303.08782 (cit. on p. 2).

Villa, E. and C. Rampf (Jan. 2016). "Relativistic perturbations in ΛCDM: Eulerian & Lagrangian approaches". In: *Journal of Cosmology and Astroparticle Physics* 2016.1. [Erratum: JCAP 05, E01 (2018)], p. 030. DOI: 10.1088/1475-7516/2016/01/030. arXiv: gr-qc/1505.04782 (cit. on p. 62).

Vittorio, N. (2018). *Cosmology*. CRC Press, Taylor & Francis Group. DOI: 10.1201/b22176 (cit. on pp. 49, 52–54, 65–67, 69, 71, 91, 103, 104, 115).

Voss, A. (June 1880). "Zur Theorie der Transformation quadratischer Differentialausdrücke und der Krümmung höherer Mannigfaltigkeiten". In: *Mathematische Annalen* 16, pp. 129–179. DOI: 10.1007/BF01446384 (cit. on p. 9).

Wainwright, J. and G. F. R. Ellis (1997). *Dynamical Systems in Cosmology*. Cambridge University Press. DOI: 10.1017/CBO9780511524660 (cit. on pp. 19, 80, 81).

Wald, R. M. (1984). *General Relativity*. The University of Chicago Press. DOI: 10.7208/chicago/9780226870373.001.0001 (cit. on pp. 5, 23, 70, 76).

Walker, A. G. (June 1937). "On Milne's Theory of World-Structure". In: *Proceedings of the London Mathematical Society* s2-42.1, pp. 90–127. DOI: 10.1112/plms/s2-42.1.90 (cit. on p. 48).

Wang, L. and P. J. Steinhardt (Dec. 1998). "Cluster Abundance Constraints for Cosmological Models with a Time-varying, Spatially Inhomogeneous Energy Component with Negative Pressure". In: *The Astrophysical Journal* 508.2, pp. 483–490. DOI: 10.1086/306436 (cit. on pp. 66, 94).

Weinberg, S. (1972). *Gravitation and Cosmology: Principles and Applications of the General Theory of Relativity*. John Wiley and Sons (cit. on pp. 5, 8, 61).

Weyl, H. (Sept. 1918). "Reine Infinitesimalgeometrie". In: *Mathematische Zeitschrift* 2.3-4, pp. 384–411. DOI: 10.1007/BF01199420 (cit. on pp. 5, 9, 18).

White, M. J (Dec. 2002). "The Mass function". In: *Astrophys. J. Suppl.* 143.2, p. 241. DOI: 10.1086/342752. arXiv: astro-ph/0207185 (cit. on p. 71).

White, S. D. M. and M. J. Rees (July 1978). "Core condensation in heavy halos: a two-stage theory for galaxy formation and clustering." In: *Monthly Notices of the Royal Astronomical Society* 183.3, pp. 341–358. DOI: 10.1093/mnras/183.3.341 (cit. on p. 72).

Will, C. M. (Dec. 2014). "The Confrontation between General Relativity and Experiment". In: *Living Reviews in Relativity* 17.4. DOI: 10.12942/lrr-2014-4. arXiv: gr-qc/1403.7377 (cit. on p. 2).

Wilson, J. R. (Apr. 1972). "Numerical Study of Fluid Flow in a Kerr Space". In: *The Astrophysical Journal* 173.2, pp. 431–438. DOI: 10.1086/151434 (cit. on p. 34).

— (1979). "A numerical method for relativistic hydrodynamics". *Sources of Gravitational Radiation*. Ed. by L. L. Smarr. Cambridge University Press, pp. 423–445 (cit. on p. 34).

Wylleman, L., A. Coley, D. McNutt, and M. Aadne (Nov. 2019). "Observer-based invariants for cosmological models". In: *Classical and Quantum Gravity* 36.23, p. 235018. DOI: 10.1088/1361-6382/ab52a7. arXiv: gr-qc/2007.15915 (cit. on pp. 23, 73).

Xu, H. et al. (June 2023). "Searching for the Nano-Hertz Stochastic Gravitational Wave Background with the Chinese Pulsar Timing Array Data Release I". In: *Research in Astronomy and Astrophysics* 23.7, p. 075024. DOI: 10.1088/1674-4527/acdfa5. arXiv: astro-ph/2306.16216 (cit. on p. 2).

Yamamoto, T., M. Shibata, and K. Taniguchi (2008). "Simulating coalescing compact binaries by a new code SACRA". In: *Physical Review D* 78, p. 064054. DOI: 10.1103/PhysRevD.78.064054. arXiv: gr-qc/0806.4007 (cit. on p. 42).

Yoo, C-M., T. Harada, and H. Okawa (Apr. 2017). "3D Simulation of Spindle Gravitational Collapse of a Collisionless Particle System". In: *Classical and Quantum Gravity* 34.10, p. 105010. DOI: 10.1088/1361-6382/aa6ad5. arXiv: gr-qc/1611.07906 (cit. on pp. 42, 72).

— (Aug. 2020). "Threshold of Primordial Black Hole Formation in Nonspherical Collapse". In: *Physical Review D* 102.4. [Erratum: Phys.Rev.D 107, 049901 (2023)], p. 043526. DOI: 10.1103/PhysRevD.102.043526. arXiv: gr-qc/2004.01042 (cit. on p. 118).

Yoo, C.-M., T. Ikeda, and H. Okawa (Mar. 2019). "Gravitational Collapse of a Massless Scalar Field in a Periodic Box". In: *Classical and Quantum Gravity* 36.7, p. 075004. DOI: 10.1088/1361-6382/ab06e2. arXiv: gr-qc/1811.00762 (cit. on p. 72).

Yoo, J. and R. Durrer (Sept. 2017). "Gauge-transformation properties of cosmological observables and its application to the light-cone average". In: *Journal of Cosmology and Astroparticle Physics* 2017.9, pp. 16–16. DOI: 10.1088/1475-7516/2017/09/016. arXiv: astro-ph/1705.05839 (cit. on p. 65).

York, J. W. Jr. (Apr. 1973). "Conformatlly invariant orthogonal decomposition of symmetric tensors on Riemannian manifolds and the initial value problem of general relativity". In: *Journal of Mathematical Physics* 14.4, pp. 456–464. DOI: 10.1063/1.1666338 (cit. on p. 29).

— (Jan. 1979). "Kinematics and Dynamics of General Relativity". *Workshop on Sources of Gravitational Radiation*. Ed. by L. L. Smarr. Cambridge University Press, pp. 83–126 (cit. on pp. 36, 38, 100).

Zakhary, E. and C. B. G. McIntosh (May 1997). "A Complete Set of Riemann Invariants". In: *General Relativity and Gravitation* 29.5, pp. 539–581. DOI: 10.1023/A:1018851201784 (cit. on pp. 23, 73).

Zel'dovich, Y. B. (Mar. 1970). "Gravitational instability: An approximate theory for large density perturbations". In: *Astronomy & Astrophysics* 5, pp. 84–89 (cit. on p. 71).

FORM UPR16

Research Ethics Review Checklist

Please include this completed form as an appendix to your thesis (see the Research Degrees Operational Handbook for more information

UNIVERSITY OF PORTSMOUTH

Postgraduate Research Student (PGRS) Information			**Student ID:**	951147
PGRS Name:	Robyn Louise Munoz			
Department:	ICG	**First Supervisor:**	Marco Bruni	
Start Date: (or progression date for Prof Doc students)				

Study Mode and Route:					
Part-time	☐	MPhil	☐	MD	☐
Full-time	X	PhD	X	Professional Doctorate	☐

Title of Thesis:	Cosmological simulations of large-scale structures in numerical relativity
Thesis Word Count: (excluding ancillary data)	43383

If you are unsure about any of the following, please contact the local representative on your Faculty Ethics Committee for advice. Please note that it is your responsibility to follow the University's Ethics Policy and any relevant University, academic or professional guidelines in the conduct of your study

Although the Ethics Committee may have given your study a favourable opinion, the final responsibility for the ethical conduct of this work lies with the researcher(s).

UKRIO Finished Research Checklist:
(If you would like to know more about the checklist, please see your Faculty or Departmental Ethics Committee rep or see the online of the full checklist at: https://ukrio.org/publications/code-of-practice-for-research

a)	Have all of your research and findings been reported accurately, honestly and within a reasonable time frame?	YES X NO ☐
b)	Have all contributions to knowledge been acknowledged?	YES X NO ☐
c)	Have you complied with all agreements relating to intellectual property, publication and authorship?	YES X NO ☐
d)	Has your research data been retained in a secure and accessible form and will it remain so for the required duration?	YES X NO ☐
e)	Does your research comply with all legal, ethical, and contractual requirements?	YES X NO ☐

Candidate Statement:

I have considered the ethical dimensions of the above named research project, and have successfully obtained the necessary ethical approval(s)

Ethical review number(s) from Faculty Ethics Committee (or from NRES/SCREC):	ETHIC-2019-1452

If you have *not* submitted your work for ethical review, and/or you have answered 'No' to one or more of questions a) to e), please explain below why this is so:

Signed *(PGRS)*:	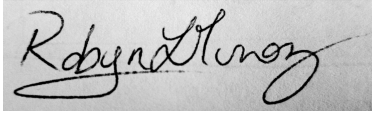	**Date:** 6th July 2023